In memoriam of Academician Andrei ANDRIESH, the Founder of Noncrystalline Semiconductor School in the Republic of Moldova

24.10.1933-7.04.2012

Academician Andrei ANDRIESH, the third president of the Academy of Sciences of Moldova (1989-2004), Doctor habilitate in physics and mathematics, twice Laureate of the State Award in Science and Production died on April 7, 2012. The scientific community in Moldova and abroad has lost a valuable scientist, a man of great humanity, and a citizen with love to this country, the founder of the scientific school on noncrystalline semiconductors.

Academician Andrei Andriesh was born on October 24, 1933 in Chisinau. He graduated from the Physics and Mathematics Faculty at the Moldova State University of Chisinau (1956) and PhD in the Ioffe Physical Technical Institute in St. Petersburg (1962). Internationally renowned scientist in the fields of optoelectronics and noncrystalline semiconductor, personality of a vast erudition and culture, academician Andrei Andriesh devoted its entire life to the Academy of Sciences of Moldova. His scientific carrier began with different positions of researcher at the Institute of Mathematics and Physics (1962-1964), Scientific Secretary (1964-1971), head of laboratory (1971-1993) and director of the Center for Optoelectronics of the

Institute of Applied Physics of the Academy of Sciences (since 1994). He held the most important administrative positions in the Academy of Sciences: General Scientific Secretary (1984-1989) and president of the Academy of Sciences (1989-2004). In 2004 he was elected honorary president of the Academy of Sciences of Moldova.

Academician Andrei Andriesh was the founder of scientific school in physics of noncrystalline semiconductors. The noncrystalline semiconductors present a new group of materials with physical properties different from crystalline semiconductors due to the disordered structure of atomic network in these materials. This group includes chalcogenide glasses, which are transparent in the infrared region and are promising for different applications in photonics and optoelectronics.

Academician Andrei Andriesh had the honor to work under leadership of Prof. B.T. Kololmiets, Academician R. Grigorovici, Prof. S. Ovshischy, and Prof. N. Mott—Nobel Laureate in the field of noncrystalline semiconductors. Academician Andrei Andriesh was an initiator of systematic investigations of photoelectric and optical properties of chalcogenide glasses, the light propagation in optical waveguides, the photoinduced optical phenomena, including nonlinear effects, in the R. Moldova. Due to the significant scientific results obtained in this field with his coauthors, in 2001 for the second time, he became the Laureate of the State Prize of the R. Moldova in science, techniques, and production, and the winner of the "Stanford R.Ovshinsky" Award of Excellence in the field of chalcogenides in 2005.

In the Center of Optoelectronics, the basic physical properties of chalcogenide glasses have been being studied. It was demonstrated that the spectrum of localized states and energy distribution can be modified through varying the chalcogenide glass composition, temperature and light irradiation. For the first time, there was carried out a complex experimental study of the transient processes of the dispersive transport, photoconductivity and photoinduced optical absorption, the specific features of which are determined by the non-equilibrium carriers and the spectrum of the localized states. In the case of dispersive transport, a theoretical model of multiple trapping of charge carriers was developed, which allowed explaining the experimental results and features of the drift in chalcogenide glasses, photoinduced absorption, photoconductivity, and non-linear phenomena.

Under the supervision of Academician Andrei Andriesh, in the Center of Optoelectronics, the search for and development of novel methods of recording the optical and holographic information, as well as effective media for optical registration, were carried out. At present, the holograms of various types (rainbow holograms, focused image holograms, Fourier holograms, volume holograms) are formed with high diffraction efficiency, large scene depth, and dimensions of 0.5 mm^2 to 140 cm^2. A technology process for preparing a metal matrix for multiplication of patterns from a hologram origin was developed. The study of the structural transformations in thin films of vitreous semiconductors stimulated by low-energy electron irradiation presents interest from the practical point of view for the formation of phase and relief diffraction elements with submicron period for various optoelectronic applications.

In the last years of activities, academician Andrei Andriesh initiated the development and investigation of the new organic/inorganic nanostructured composite materials. Nanostructured composite materials are very attractive for the future implementation of new photonic and optoelectronic devices. Actually, the definition of nanocomposite materials has significantly broadened; it includes a large variety of systems and structures, such as one-dimensional, two-dimensional (metal oxides, metal phosphates, chalcogenides), three-dimensional, and amorphous materials. The main efforts were focused on the ability to control nanoscale structures with the

required physical and optical characteristics through innovational synthesizing approaches. The luminescent composites based on lanthanide complexes have attracted much attention due to scientific interest as well as for the wide variety of application in photonics and optoelectronics: planar optical amplifiers, solar cells, light emitting diodes, gas selective sensors, photonic devices, etc. Academician Andrei Andriesh was an author and coauthor of about 500 scientific papers and 30 patents. They include "Vitreous Arsenic Sulfide and it's alloys" (1981), "Nonstationary Currents in Disordered Solids" (1983), "The Vitreous Semiconductors in the Photoelectric Systems of Recording of Optical Information" (1988), "Physics of Chalcogenide Glasses" (1996), etc. He contributed to training of highly skilled scientists, including 17 doctors and 8 doctors habilitate.

Academician Andrei Andriesh was a Member of the Engineering Academy of the Russian Federation, Corresponding Member of the Austrian Society Albert Schweitzer-Gesellschaft Modling, Member of the European Academy of Arts, Honorable Member of the Romanian Academy of Sciences, President SPIE-Moldova Society, Honorable Member of the American-Romanian Academy, and Doctor Honoris Causa of the Polytechnic University from Bucharest.

Academician Andrei Andriesh essentially contributed to the elaboration and development of the Informational Infrastructure Strategy and the implementation of Academic network development projects in Moldova by RENAM (Research and Education Networking Association in Moldova) with support of the NATO Science Committee and European Commission.

Academician Andrei Andriesh was awarded with the title „Om Emerit", he was the winner of the Award „C. Miculescu" of the Romanian Academy of Sciences, the Medal „Insigna de Onoare", „Ordinul Republicii", „Academician S. I. Vavilov", etc. His productive research activities in the field of noncrystalline semiconductors, creativity, and directed actions are an example for young researchers and encourage them to discoveries of new materials, photonic and optoelectronic devices.

In memoriam of Doctor Evgenii S. Moskalenko
05.05.1963–12.03.2012

Doctor Evgenii S. Moskalenko, experimental physicist, came originally from the Republic of Moldova being born in Chisinau on May 5, 1963. He graduated from the Leningrad State University in 1986 and received his candidatus scientiarum degree in 1991 being doctoral student of the Ioffe Physical-Technical Institute (PTI) of the Russian Academy of Sciences in St. Petersburg, where he was working the following 20 years up till his sudden decease on March 12, 2012. The last 10 years, being a senior scientific collaborator of PTI, he simultaneously took part, as an invited researcher, in the investigations of the optical properties of semiconductor nanostructures in the frame of the Department of Physics and Measurement Technology of the Linkoping University in Sweden. He is the author of 64 papers in referred journals, the list of which is attached, as well as of 62 conference articles.

The head of the Department of Physics and Measurement Technology of the Linkoping University in Sweden Professor Per Olof Holtz has written the following comments in memory of Evgenii S. Moskalenko.

> "It was beyond doubt that Evgenii became an important and valuable member of our group during these 12 years. First of all, he was indeed a brilliant physicist, who strongly contributed to our interpretation and improved understanding of the properties of the quantum dots. He forwarded his ideas and achieved results in a congenial way. Evgenii was a person with a great curiosity, who could work exceptionally hard and with purposefulness and great excitement to reach the goal. I did value his experience, strengths, capability as exhibited in his work throughout the years.

He also made a significant contribution in the supervision of several PhD students. The impact made by Evgenii in the way he forwarded his extensive knowledge and experience to my students was invaluable and highly appreciated by the students."

E.S. Moskalenko: List of Publications. ***Papers in referred journals***

1. A.V. Akimov, A.A. Kaplyanskii, and E.S. Moskalenko, "Phonon hot spot in Cuprous Oxide crystals", Physics of the Solid State, 29, 1058, (1987).
2. A.V. Akimov, A.A. Kaplyanskii, V.V. Krivolapchuk, and E.S. Moskalenko, "Manifestation of the matastable localized hole states in slow kinetics of the edge luminescence of n-GaAs", JETP Lett., 46, 42, (1987).
3. A.V. Akimov, A.A. Kaplyanskii, E.S. Moskalenko, and R.A. Titov, "Exciton drag by heat phonon pulses in silicon", Sov. Phys. JETP, 67, 2348-2355, (1988).
4. A.V. Akimov, A.A. Kaplyanskii, E.S. Moskalenko, "Exciton drag by heat pulses in silicon" in: Phonons 89, ed. S. Hunklinger (World Scientific, Singapure), 1260-1263, 1990.
5. A.V. Akimov, A.A. Kaplyanskii, and E.S. Moskalenko, "Nonequilibrium terahertz range acoustic phonons and luminescence of excitons in semiconductors", in: Laser Optics in Condenced Matter vol. 2, ed. E. Garmire, A.A. Maradudin, K.K. Rebane, Plenum Press, N.Y., London, 37-46, 1990.
6. A.V. Akimov, A.A. Kaplyanskii, E.S. Moskalenko, "Luminescence study of exciton drag by acoustic phonons in silicon", J. Luminescence, 45, 135-139, (1990).
7. A.V. Akimov, A.A. Kaplyanskii, J. Kochka, E.S. Moskalenko, and J. Stuchlik, "Scattering of Terahertz phonons in amorphous Si and Ge", Sov. Phys. JETP, 73 (4), 742-748, (1991).
8. A.V. Akimov, S.A. Basun, S.P. Feofilov, A.A. Kaplyanskii, and E.S. Moskalenko, "Luminescence study of nonequilibrium phonons in noncrystalline solids", Bull. Acad. Sci. USSR, Phys. Ser., 56, 26-37, (1991).
9. A.V. Akimov, A.A. Kaplyanskii, and E.S. Moskalenko, "Phonon wind on excitons in silicon", Physica B, 169, 382-387, (1991).
10. A.V. Akimov, L.J. Challis, E.S. Moskalenko, C. Mellor, and J. Cooper, "Phonon emission from the first and second subbands of a two-dimensional electron gas in silicon detected by exciton luminescence", Phys. Rev. B, 45, 11387-11390, (1992).
11. A.A. Kaplyanskii, A.V. Akimov, S.A. Basun, S.P. Feofilov, E.S. Moskalenko, J. Kocka, and J. Stuchlik, "Optical studies of high-frequency nonequilibrium phonons in noncrystalline solids", J. Luminescence, 53, 7-14, (1992).
12. A.V. Akimov, A.A. Kaplyanskii, and E.S. Moskalenko, "Investigation using phonon detection by exciton luminescence", in: Phonon Scattering in condensed matter VII, ed. M. Meissner, R.O. Pohl, Springer-Verlag, 101-104, 1993.
13. A.V. Akimov, L.J. Challis, E.S. Moskalenko, C. Mellor, and J. Cooper, "Luminescence detection of phonons emitted from the first and second sub-bands of a 2-DEG in silicon", in: Phonon Scattering in condensed matter VII, ed. M. Meissner, R.O. Pohl, Springer-Verlag, 371-372, 1993.
14. E.S. Moskalenko, A.V. Akimov, A.L. Zhmodikov, A.A. Kaplyanskii, T.S. Cheng, O.H. Huhges, L.J. Challis, "Nonequilibrium phonon heating of the two-dimensional exciton gases in GaAs/AlGaAs quantum wells", Physics of the Solid State, 36, 1668-1672, (1994).

15. E.S. Moskalenko, A.L. Zhmodikov, A.V. Akimov, A.A. Kaplyanskii, L.J. Challis, T.S. Cheng, O.H. Huhges, "Phonon heating of the two-dimensional exciton gases in GaAs/AlGaAs quantum wells", Annalen der Phyzik, 4, 127-135, (1995).
16. A.V. Akimov, E.S. Moskalenko, L.J. Challis, and A.A. Kaplyanskii, "Interaction of phonons with 2D exciton gas", Physica B, 219&220, 9-12, (1996).
17. F.F. Ouali, N.N. Zinov'ev, L.J. Challis, A.V. Akimov, D.N. Hill, E.S. Moskalenko, F.W. Sheard, and M. Henini, "Phonon-assisted tunneling in GaAs/AlGaAs resonant tunneling devices", Physica B, 219&220, 19-21, (1996).
18. E.S. Moskalenko, A.V. Akimov, A.A. Kaplyanskii and A.L. Zhmodikov, L.J. Challis, T.S. Cheng and C.T. Foxon, "Effect of nonequilibrium phonons on exciton states in interruption grown GaAs/AlGaAs quantum wells", Physica B, 219&220, 59-61, (1996).
19. D.A. Mazurenko, A.V. Akimov, E.S. Moskalenko, A.L. Zhmodikov, A.A. Kaplyanskii, L.J. Challis, T.S. Cheng and C.T. Foxon, "Tunnelling of direct and indirect excitons in slightly asymmetric double quantum wells", Acta Physica Polonica A, 90, 895-898, (1996).
20. E.S. Moskalenko, D.N. Hill, F.F. Ouali, L.J. Challis, W. Sheard, M. Henini, "Magnetic Field Studies of phonon-assisted tunneling in a delta-doped double barrier resonant tunneling device", 12-th International Conference "High Magnetic Fields in the Physics of Semiconductors II", eds. G. Landwehr and W. Ossau, World Scientific, Singapore, vol. 1, 453-456, 1996.
21. A.V. Akimov, E.S. Moskalenko, A.L. Zhmodikov, D.A. Mazurenko, A.A. Kaplyanskii, L.J. Challis, T.S. Cheng, "Luminescence of Excitons in Slightly Asymmetric Double Quantum Wells", Physics of the Solid State, 39 (3), 649-653, (1997).
22. A.V. Akimov, A.A. Kaplyanskii, D.A. Mazurenko, E.S. Moskalenko, A.L. Zhmodikov, L.J. Challis, T.S. Cheng, C.T. Foxon, "Exciton tunnelling induced by nonequilibrium phonons in lightly asymmetric double quantum wells", Phys. Stat. Sol. (b), 204, 400-403, (1997).
23. D.N. Hill, S.A. Cavill, A.V. Akimov, F.F. Ouali, E.S. Moskalenko, L.J. Challis, A.J. Kent, F.W. Sheard, P. Kral, M. Henini, "Studies of phonon-assisted tunnelling in a doped double barrier resonant tunnelling device", Phys. Stat. Sol. (b), 204, 431, (1997).
24. V.V. Krivolapchuk, D.A. Mazurenko, E.S. Moskalenko, N.K. Poletaev, A.L. Zhmodikov, T.S. Cheng, C.T. Foxon, "Anomalous influence of magnetic field on the indirect exciton in GaAs/AlGaAs double quantum wells", Physics of the Solid State, 40 (5), 737-739, (1998).
25. V.V. Krivolapchuk, E.S. Moskalenko, A.L. Zhmodikov, T.S. Cheng, C.T. Foxon, "Manifestation of collective properties of spatially indirect excitons in GaAs/AlGaAs asymmetric double quantum wells", Physics of the Solid State, 41 (2), 291-295, (1999).
26. V.V. Krivolapchuk, E.S. Moskalenko, A.L. Zhmodikov, T.S. Cheng, C.T. Foxon, "Collective properties of spatially indirect excitons in asymmetric GaAs/AlGaAs double quantum wells", Solid State Commun., 111, 49-54, (1999).
27. V.V. Krivolapchuk, E.S. Moskalenko, A.L. Zhmodikov, "A giant shot of radiation intensity as eventual evidence of Bose-Einstein condensation of excitons in double quantum wells in GaAs/AlGaAs", Nanotechnology, 11, 246-251, (2000).
28. E.S. Moskalenko, V.V. Krivolapchuk, A.L. Zhmodikov, "Giant burst of the emission line intensity of spatially indirect excitons in GaAs/AlGaAs double quantum wells", Physics of the Solid State, 42 (8), 1535, (2000).
29. E.S. Moskalenko, K.F. Karlsson, P.O. Holtz, B. Monemar, W.V. Shoenfeld, J.M. Garsia, P.M. Petroff, "The influence of the excitation energy on the charged exciton formation in self-assembled InAs quantum dots", Phys. Rev. B, 64, 085302-1–085302-6, (2001).

30. K.F. Karlsson, E.S. Moskalenko, P.O. Holtz, B. Monemar, W.V. Shoenfeld, J.M. Garsia, P.M. Petroff, ”Temperature influence on optical charging of self-assembled InAs/GaAs semiconductor quantum dots”, Appl. Phys. Lett., 78, 2952-2954, (2001).
31. V.V. Krivolapchuk, E.S. Moskalenko, A.L. Zhmodikov, ”Features of the indirect exciton luminescence line in GaAs/AlGaAs double quantum wells”, Phys. Rev. B, 64, 045313-1–045313-6, (2001).
32. K.F. Karlsson, E.S. Moskalenko, P.O. Holtz, B. Monemar, W.V. Schoenfeld, J.M. Garcia, and P.M. Petroff, ”Optical charging of self-assembled InAs/GaAs quantum dots”, Physica Scripta T, 101, 140-143, (2002).
33. K.F. Karlsson, E.S. Moskalenko, P.O. Holtz, B. Monemar, W.V. Schoenfeld, J.M. Garcia, P.M. Petroff, ”Carrier Diffusion in the Barrier Enabling Formation of Charged Excitons in InAs/GaAs Quantum Dots”, Acta Physica Polonica A, 100, 387-395, (2001).
34. K.F. Karlsson, E.S. Moskalenko, P.O. Holtz, B. Monemar, W.V. Schoenfeld, J.M. Garcia, and P.M. Petroff; ”The influence of carrier diffusion on the formation of charged excitons in InAs/GaAs quantum dots”, Physica E, 13, 101-104, (2002).
35. E.S. Moskalenko, K.F. Karlsson, P.O. Holtz, B. Monemar, W.V. Schoenfeld, J.M. Garcia, P.M. Petroff, “The formation of the charged exciton complexes in self-assembled InAs single quantum dots”, Journal of Applied Physics, 92, 6787-6793, (2002).

36. E.S. Moskalenko, K.F. Karlsson, P.O. Holtz, B. Monemar, W.V. Schoenfeld, J.M. Garcia, P.M. Petroff, “An acceptor-induced threshold energy for the optical charging of InAs single quantum dots”, Phys. Rev. B, 66, 195332-1–195332-11, (2002).

37. K.F. Karlsson, P.O. Holtz, E.S. Moskalenko, B. Monemar, W.V. Schoenfeld, J.M. Garcia, P.M. Petroff, ”Effective tuning of the charge state of single In(Ga)As/GaAs quantum dots by below barrier band gap excitation”, Surface Science, 532-535, 843-847, (2003).

38. E.S. Moskalenko, V. Donchev, K.F. Karlsson, P.O. Holtz, B. Monemar, W.V. Schoenfeld, J.M. Garcia, P.M. Petroff, “The effect of an additional infrared excitation on the luminescence efficiency of a single InAs/GaAs quantum dot”, Phys. Rev. B, 68, 155317-1–155317-14, (2003).

39. V. Donchev, K.F. Karlsson, E.S. Moskalenko, P.O. Holtz, B. Monemar, W.V. Schoenfeld, J.M. Garcia, P.M. Petroff, “Temperature study of the photoluminescence of a single InAs/GaAs quantum dot”, Phys. Stat. Sol. (c), 1 (3), 608-611, (2004).
40. E.S. Moskalenko, K.F. Karlsson, V. Donchev, P.O. Holtz, B. Monemar, W.V. Schoenfeld, P.M. Petroff, “Effective optical manipulation of the charge state and emission intensity of the InAs/GaAs quantum dots by means of additional infrared illumination”, Appl. Phys. Lett., 85, 754-756, (2004).
41. E.S. Moskalenko, K.F. Karlsson, V. Donchev, P.O. Holtz, W.V. Schoenfeld P.M. Petroff, “The effect of an additional infrared laser on the carrier collection efficiency of InAs quantum dots”, Appl. Phys. Lett., 84, 4896-4898, (2004).
42. E.S. Moskalenko, K.F. Karlsson, V. Donchev, P.O. Holtz, W.V. Schoenfeld, P.M. Petroff, “Effect of the electric field on the carrier collection efficiency of InAs quantum dots”, Physics of the Solid State, 47 (11), 2154, (2005).
43. E.S. Moskalenko, K.F. Karlsson, V. Donchev, P.O. Holtz, B. Monemar, W.V. Schoenfeld, P.M. Petroff, ”Effects of separate carrier generation on the emission properties of InAs/GaAs quantum dots”, Nano Letters, 5 (11), 2117-2122, (2005).
44. V. Donchev, E.S. Moskalenko, K.F. Karlsson, P.O. Holtz, B. Monemar, W.V. Schoenfeld,

J.M. Garcia, P.M. Petroff, "Enhancement of the photoluminescence intensity of a single InAs/GaAs quantum dot by separate generation of electrons and holes", Physics of the Solid State, 48 (10), 1993, (2006).
45. V.V. Krivolapchuk, A.A. Zhmodikov, E.S. Moskalenko, "Exciton condensate emission in double quantum wells", Physics of the Solid State, 48 (1), 150, (2006).
46. E.S. Moskalenko, M. Larsson, W.V. Schoenfeld, P.M. Petroff, P.O. Holtz, "Carrier transport in self organized InAs/GaAs quantum dot structures as studied by single dot spectroscopy", Phys. Rev. B, 73, 155336-1–155336-5, (2006).
47. M. Larsson, E.S. Moskalenko, L.A. Larsson, P.O. Holtz, C. Verdozzi, C.-O. Almbladh, "Magnetic field effects on optical and transport properties in InAs/GaAs quantum dots", Phys. Rev. B, 74, 245312-1–245312-8, (2006).
48. E.S. Moskalenko, K.F. Karlsson, M. Larsson, P.O. Holtz, B. Monemar, W.V. Schoenfeld, P.M. Petroff, "The effect of the external electric field on the luminescence intensity of InAs/GaAs quantum dots", Nano. Letters, 7 (1), 188-193, (2007).

49. E.S. Moskalenko, M. Larsson, K.F. Karlsson, P.O. Holtz, B. Monemar, W.V. Schoenfeld, P.M. Petroff, "The effect of the external lateral electric field on the luminescence intensity of InAs/GaAs quantum dots", Physics of the Solid State, 49 (10), 1995, (2007).

50. P.O. Holtz, E.S. Moskalenko, M. Larsson, K.F. Karlsson, W.V. Schoenfeld, P.M. Petroff, "Effects of External Fields on the Excitonic Emission from Single InAs/GaAs Quantum Dots", Microelectronics Journal, 39, 331-334, (2008).

51. E.S. Moskalenko, L.A. Larsson, M. Larsson, P.O. Holtz, W.V. Schoenfeld, P.M. Petroff, "Effective tuning of the charge state of a single InAs/GaAs quantum dot by an external magnetic field", Phys. Rev. B, 78, 075306, (2008).

52. E.S. Moskalenko, L.A. Larsson, M. Larsson, P.O. Holtz, W.V. Schoenfeld, P.M. Petroff, "Comparative magneto-photoluminescence study of ensembles and of individual InAs quantum dots", Nano Letters, 9, 353, (2009).

53. E.S. Moskalenko, L.A. Larsson, and P.O. Holtz, "Spin Polarization of the Neutral Exciton in a Single InAs Quantum Dot at Zero Magnetic Field", Phys. Rev. B, 80, 193413, (2009).
54. V.F. Agekyan, P.O. Hotz, E.S. Moskalenko, A.Yu. Serov, N.G. Filisofov, "Magnetic field affected energy transfer of the band states into 3d-shell of Mn^{2+} in CdMgTe matrix with CdMnTe nano layers", Physics of the Solid State, 52 (1), 28, (2009).
55. R.V. Kuzmin, V.V. Krivolapchuk, E.S. Moskalenko and M.M. Mezdrogina, "Fluctuations of emission intensity of exciton Bose-Condensate in GaAs/$Al_{0.33}Ga_{0.67}As$ double quantum wells", Physics of the Solis State, 52 (6), 1184, (2010).
56. E.S. Moskalenko, L.A. Larsson and P.O. Holtz, "Manipulating the spin polarization of excitons in a single quantum dot by optical means", Appl. Phys. Letters, 98, 071906-071908, (2011).
57. E.S. Moskalenko, L.A. Larsson and P.O. Holtz, "Spin polarization of neutral excitons in quantum dots: the role of the carrier collection area", Nanotechnology, 21, 345401, (2010).
58. E.S. Moskalenko, L.A. Larsson and P.O. Holtz, "Spin polarization of the neutral exciton in a single quantum dot", Superlattices and Microstructures, 49 (3), 294-299, (2011).
59. L.A. Larsson, M. Larsson, E.S. Moskalenko, and P.O. Holtz "Temperature and magnetic field effects on the transport controlled charge state of a single quantum dots", Nanoscale Res. Lett., 5, 1150-1155, (2010).

60. E.S. Moskalenko and N.K. Poletaev, "Circular polarization of photoluminescence in GaAs/AlGaAs quantum wells in its dependence on sample growth conditions", Physics of the Solid State, 53 (2), 398-403, (2011).

61. M.M. Mezdrogina, E.S. Moskalenko, and Yu.V. Kozhanova, "Influence of the magnetic field and measurement temperature on the shape of microphotoluminescence spectra of Eu-doped InGaN/GaN quantum-well structures", Physics of the Solid State, 53 (8), 1680-1688, (2011).

62. E.S. Moskalenko, L.A. Larsson and P.O. Holtz, "Circularly polarized emission from ensembles of InAs/GaAs quantum dots", Journal of Appl. Phys., 110, 013510, (2011).

63. V.F. Agekyan, P.O. Holz, G. Karczewski, V.N. Katz, E.S. Moskalenko, A.Yu. Serov, and N.G. Filosofov, "Magnetoluminescence of CdTe/MnTe/CdMgTe Heterostructures with Ultrathin MnTe Layers", Semiconductors, 45, 10, 1301–1305, (2011).

64. M.M. Mezdrogina, M.V. Eremenko, S.M. Golubenko, and E.S. Moskalenko, "Influence of Nanoparticles and Thin Layers of Gold, Europium Phthalocyanine, and Erbium Nanoparticles on the Formation of Luminescence Spectra of Structures with InGaN/GaN Quantum Wells", Physics of the Solid State, 54, 1, 194–201, (2012).

OPTICAL ORIENTATION AND SPIN POLARIZATION OF THE ELECTRONS AND NUCLEI IN SEMICONDUCTOR QUANTUM DOTS

S. A. Moskalenko[1], I. V. Podlesny[1], B. V. Novikov[2], and Ig. A. Lelyakov[1]

[1]*Institute of Applied Physics, Academy of Sciences of Moldova, Academiei str. 5, Chisinau, MD-2028 Republic of Moldova*
[2]*Department of Solid State Physics, Institute of Physics, St. Petersburg State University, Ulyanovskaya str. 1, Petrodvorets, St. Petersburg, 198504 Russia*

(Received 16 May 2012)

A short review of the results concerning the optical orientation and spin polarization effects in semiconductor quantum dots obtained by a group of investigators of the Department of Physics and Measurement Technology of the Linkoping University in Sweden with the participation of Evgenii S. Moskalenko is written below in his memory.

The possibility of polarizing the nuclei in a metal by an electron spin system in equilibrium was first pointed out by Overhauser [1]. The spin polarization effects of the localized electrons in semiconductor quantum dots (QDs) can be understood on the base of investigations initiated by Dyakonov and Perel [2] and prolonged in a series of theoretical [3-8] and experimental investigations [9-12], which elaborated the basic concepts in this field. They were performed and prolonged in numerous further investigations including [13-18]. Most of these effects belong to the optical orientation phenomena arising under the action of the circularly polarized laser radiation including the spin polarization of electrons and nuclei and optical alignment of excitons in semiconductors.

The interest in electron spin polarization effects in QDs is due to the fact that they are not subjected to classical spin relaxation mechanisms known for free carriers [9]. The recent theoretical studies [2-7] predict that the dominant mechanism of electron spin relaxation in QDs at low temperatures is due to its hyperfine interaction with nuclei.

The comparison with the experiments confirms this point of view. The long spin dephasing time of an electron in a QD suggests elaborating a model of quantum bit on this ground [9]. The influence of the electron spin polarization on the spins of nuclei takes place through the hyperfine Fermi constant interaction, which is described by Hamiltonian (2) in [4]:

$$H_{hf} = \frac{\mathrm{v}_0}{2}\sum_j A^j \left|\Psi(\vec{R}_j)\right|^2 \left(\hat{I}_\alpha^j \cdot \hat{\sigma}_\alpha\right), \tag{1}$$

where the sum goes over all nuclei in the QD, v_0 is the volume of the unit cell, $\Psi(\vec{R}_j)$ is the electron envelope wave function at the *j*-th nucleus, $\hat{I}_\alpha$ and $\hat{\sigma}_\alpha$ are the spin projections on the coordinate axes $\alpha = x, y, z$. The electron spin in a QD interacts with a large but finite number of nuclei $N_L \approx 10^3 - 10^5$ [9]. The constant of the Fermi contact interaction A^j has the expression [4]:

$$A^j = \frac{16\pi\mu_B\mu_j}{3I^j}\left|U_c(\vec{R}_j)\right|^2. \tag{2}$$

It includes the Bohr magneton μ_B, the nuclear magnetic moment μ_j, and the periodic part

$U_c(\vec{R}_j)$ of the electron Bloch wave function at the point $\vec{R}_j$. As a result of the nuclear spin polarization, a nuclear hyperfine magnetic field $\vec{B}_N$ arises. It is known as Overhauser field. Its value $\vec{B}_N$ can be determined from equation (3) in [4]:

$$\mu_B g_e \vec{B}_N = v_0 \left\langle \sum_j A^j \left|\Psi(\vec{R}_j)\right|^2 \vec{I}^{\,j} \right\rangle. \tag{3}$$

The symbol $\langle\ \rangle$ denotes the quantum mechanical average over the nuclei wave functions, and g_e is the electron Lande *g*-factor. The magnitude and direction of this field are randomly distributed over the ensemble of QDs. The density distribution function has a Gaussian probability [4]:

$$W(B_N) = \frac{1}{\pi^{3/2}\Delta_B^3} \exp\left[\frac{-B_N^2}{\Delta_B^2}\right]. \tag{4}$$

The parameter Δ_B determines the dispersion of the density distribution.

The equation of motion of the spin $\vec{S}$ in a fixed magnetic field is given by equation (9) in [4], which describes the coherent electron spin precession in a single QD due to the magnetic field $\vec{B}_N$ oriented in the unit vector $\vec{n}$ direction giving rise to the precession frequency ω_e equal to

$$\omega_e = \frac{\mu_B g_e B_N}{\hbar}; \qquad \vec{n} = \frac{\vec{B}_N}{B_N}. \tag{5}$$

Each electron spin is moving in the frozen fluctuation of the nuclear hyperfine magnetic field $\vec{B}_N$ in its own QD. But these fields are randomly distributed among the dots of the ensemble. Averaging the coherent precession over the magnetic field distribution (4) the ensemble averaged time dependence (10) in [4] was obtained:

$$\left\langle \vec{S}(t) \right\rangle = \frac{\vec{S}_0}{3}\left\{1+2\left[1-2\left(\frac{t}{T_\Delta}\right)^2\right]\exp\left[-\left(\frac{t}{T_\Delta}\right)^2\right]\right\}, \tag{6}$$

where $\vec{S}_0$ is the initial spin. It consists of two terms. One of them is a constant $\vec{S}_0/3$, whereas the other term describes the Gaussian decreasing dependence with the dephasing time T_Δ related with the dispersion parameter Δ_B by formula (11) in [4]:

$$T_\Delta = \frac{\hbar}{\mu_B |g_e| \Delta_B}. \tag{7}$$

This spin dephasing mechanism in the frozen fluctuation model with the inhomogeneous broadening of the local magnetic fields B_N is termed as spin relaxation [2-5, 9]. For repeated measurements on a single quantum dot the hyperfine interaction has the same effect as for an ensemble with the same time dependence. The Overhauser field in its turn influences the electron spin. This influence is measured by the Zeeman effect with energy $\hbar\omega_e$ known as Overhauser shift [2, 3]. The electron spin creates its own magnetic field $\vec{B}_e$ known as Knight field [2, 3]. Merkulov, Efros, and Rosen [4] analyzed three main processes, which determine the electron spin relaxation. One of them is the precession of the electron spin around the Overhauser hyperfine field with the frequency ω_e (5). The second process is the precession of the nuclear spin around

the Knight field $\vec{B}_e$. Its frequency ω_n is determined by

$$\omega_n \approx \frac{B_e \mu_n}{\hbar}, \qquad \mu_n = \hbar \gamma I,$$

where μ_n is the nuclear magnetic moment, γ is the gyromagnetic ratio, and I is the nuclear spin. The third process is determined by the precession of the spins of nuclei around the magnetic fields created by another neighbour nuclei. This process is due to the dipole-dipole interaction between the nuclear spins and can be characterized by the frequency ω_{d-d}.

Supposing the number of nuclei in a QD equal to $N_L \cong 10^5$ in [9] the values $\omega_e \approx 10^{10} s^{-1}$, $\omega_h \approx 10^7 s^{-1}$ and $\omega_{d-d} \approx 10^3 s^{-1}$ were estimated. These so different frequencies permitted introducing the adiabatic hypothesis into the calculations considering that the electron precession takes place under the condition of the frozen nuclear spins, because they do not succeed to change their orientation during the precession period of the electrons. The value of the Overhauser shift with the precession frequency $\omega_c \approx 10^{10} s^{-1}$ is two order of magnitude smaller than the thermal energy kT at $T = 10$ K. The possibility to observe the hyperfine electron-nuclei interaction effects under these conditions is a wonderful event in condensed matter physics. It is due to the small spin-spin nuclear interaction, which is equivalent to a very low effective nuclear spin temperature in comparison with the lattice temperature related with the orbital motion of the nuclei and with their phonon branches of the spectrum.

Braun et al. [9] have investigated the spin time dynamics of positively charged X^+ excitons in InAs/GaAs QDs by cw and time-resolved photoluminescence (PL) spectroscopy. The excitons X^+ consist of one electron and two holes forming a spin singlet. The exchange interaction between the electron and the holes is canceled in the X^+ ground state. Under these conditions, the analysis of the circular polarization of the X^+ luminescence probes directly the spin polarization of the electron. If the excitation pulse is circularly polarized, for example σ^+, and the luminescence intensity is recorded in the copolarized I^+ and in the counterpolarized I^- geometry as regards the excitation laser, then the degree ρ_c of the PL circular polarization is determined as [9]:

$$\rho_c = \frac{I^+ - I^-}{I^+ + I^-}. \tag{8}$$

Merkulov et al. [4] and Semenov et al. [6] have predicted that the electron spin dephasing induced by the inhomogeneous broadening of the nuclear field B_N can be suppressed in an external magnetic field $\vec{B}_{ext}$, which must be larger than the dispersion Δ_B. In Ref. [9] assuming the electron *g*-factor as $|g_e| = 0.8$ [10] the dispersion Δ_B was determined as equal to 28 mT, whereas the dephasing time T_Δ as 500 ps. It was shown that the spin polarization decays within the first 800 ps down to 1/3 of its initial value. After that, the polarization remains stable with no measurable decay on the radiative lifetime scale [9], in full accordance with the theoretical description [4]. The application of a small external magnetic field $\vec{B}_{ext} =$ 100 mT is very unusual in nonmagnetic semiconductors, as was underlined in [4]. As was mentioned in [9], the photogenerated electrons in the undoped QDs feel a strong effective magnetic field due to exchange interaction with the holes [9, 10]. This exchange field has the order of magnitude of a few Teslas, much stronger than the Overhauser fields. In the case of X^- excitons with two

electrons and one hole, the total spin of electrons is zero and no effect of hyperfine interaction was observed [9, 11]. The hole spin in *p*-type valence band does not interact with nuclei [9, 12]. In a series of papers published by the Linkoping University group of investigators [13-18] it was established that even for the case of neutral excitons, a nonzero nuclear magnetic field builds up in the In(Ga)As/GaAs QDs. To explain these experimental observations, the exciton formation in a QDs was considered as a process of separated capture of electrons and holes, rather than a mechanism according to which the electron and hole are captured into the QD as an entity. This variant takes place in experiments where the electrons and holes are created in the wetting layer (WL) on the surface of which the QDs are situated, and not directly into the QDs. The charge carriers undergo a transport in the WL prior to the capture into the QDs. The transport and capture processes are characterized by the parameter $\Delta\tau_{e-h}$, which denoted the difference in the capture times of electrons and holes into the QDs. These processes taking place under the influence of electric and magnetic fields were studied in [19-38]. According to [16-18], the electrons are captured first because of their smaller effective mass. The efficiency of the dynamic nuclear polarization by spin-oriented electrons depends on the fraction of time $\Gamma_e = \Delta\tau_{e-h}/\tau_{rc}$, where τ_{rc} is the recycling time, i.e., the average time between two adjacent events of exciton formation in QDs. $\vec{B}_N$ and ρ_c are predicted to be directly proportional to τ_{rc}^{-1} as in fact was observed in experiments. Electron is alone in the QD during $\Delta\tau_{e-h}$ and can then polarize the nuclei. Within a certain number of recycling events, the nuclear field builds up. As a result, the electron spin $\vec{S}$ is influenced not only by a "destructive" magnetic field $\vec{B}_{exch}$ arising due to the exchange electron-hole interaction, but also by the "stabilizing" nuclear field $\vec{B}_N$ [13-17]. It is the joint influence of both of these factors that determine the value of the projection of $\vec{S}$ onto the *z* axis, and hence ρ_c, as measured in the experiment. The present model is very similar to that developed for the exciton pseudospin and the role of $\vec{B}_{ext}$ is played by $\vec{B}_N$. The model adopted in [13-17] based on the separate capture of electrons and holes into the QDs is widely accepted, as one can see from [39, 40]. The studies of the denser ensembles of the same-type QDs performed in crossed internal electric and external magnetic fields, have directly demonstrated that the capture process of electrons and holes into the QDs should in fact be separately considered [15, 16]. In [13-17] a high degree of spin polarization is achieved for the neutral exciton at a zero external magnetic field in individual InAs QDs excited by circularly polarized laser radiation and studied by micro-photoluminescence (μ-PL) methods.

A high degree of polarization $\rho_c \approx 60\%$ observed in the case of a neutral exciton is a remarkable event, because it is well known that the bright states $|+1\rangle$ and $|-1\rangle$ of the heavy-hole neutral exciton are mixed due to in-plane asymmetry of a QD. The electron-hole pair state $|+1\rangle$ is created by electron spin projection $|s_z\rangle = |-1/2\rangle$ and heavy-hole moment projection $|j_z\rangle = |+3/2\rangle$, whereas the state $|-1\rangle$ by the states $|s_z\rangle = |+1/2\rangle$ and $|j_z\rangle = |-3/2\rangle$. The states $|+1\rangle$ and $|-1\rangle$ are mixed forming two linearly polarized states $|x\rangle$ and $|y\rangle$, which emit light along the $\langle 110\rangle$ and $\langle 1\underline{1}0\rangle$ crystallographic directions and are split by the anisotropic e-h exchange interaction energy $\hbar\omega_{exch}$. At external magnetic field $\vec{B}_{ext} = 0$, the neutral exciton is expected to reveal two orthogonal linearly polarized components of the PL spectrum and only at

elevated values of $\vec{B}_{ext}$ parallel to *z* axis the mixed states $|x\rangle$ and $|y\rangle$ will transform into the pure $|+1\rangle$ and $|-1\rangle$ states giving rise to circular-polarized emission [13].

Upon excitation with linearly-polarized light σ^x at $\vec{B}_{ext}=0$, two orthogonal and linearly polarized PL lines separated by $\hbar\omega_{exch}=25\,\mu\text{eV}$ were in fact monitored [13, 14]. Following the exciton pseudospin model proposed in [8, 41] the anisotropic e-h exchange interaction is viewed as an in-plane magnetic field $\vec{B}_{exch}$ perpendicular to axis *Oz*. The precession period of the exciton pseudospin around the field $\vec{B}_{exch}$ equals to $T_{exch}=2\pi/\omega_{exch}\approx 160\,\text{ps}$ [13, 14].

Taking into account that the exciton decay time equals $\tau_d=800\,\text{ps}$, one may conclude that the exciton pseudospin will accomplish many turns around $\vec{B}_{exch}$ before recombination. Hence ρ_c being proportional to the projection of the exciton pseudospin onto the *z* axis is predicted to be negligible. An external magnetic field of sufficient strength applied in Faraday geometry $\vec{B}_{ext}\,||\,Oz$ will restore the polarization of the neutral exciton because of the decoupling of the $|+1\rangle$ and $|-1\rangle$ states. This decoupling in the condition $\left|\vec{B}_{ext}\mu_B g_{ex}\right|>\hbar\omega_{exch}$, where g_{ex} is the neutral exciton *g*-factor and $\mu_B=58\,\mu\text{eV/T}$ is the Bohr magneton, will give rise to nonvanishing values of ρ_c. In the vector model [8, 41, 13] the application of $\vec{B}_{ext}$ initiates the precession of the exciton pseudospin around the total magnetic field $\vec{B}_{tot}=\vec{B}_{ext}+\vec{B}_{exch}$ as is represented in Fig. 1 in [13]. This precession leads to a nonzero value of $\left|\vec{S}_z^{ex}\right|$ and hence to $\rho_c\neq 0$. Despite $\vec{B}_{ext}=0$, at the circularly polarized excitation of the InAs QDs, the obvious energy separation of about 50 μeV was recorded between the σ^+ and σ^- components of the PL spectrum [13]. It was the signature of the appearance of an effective magnetic field $\vec{B}_N$ in a sample with a projection onto the *z* axis. When the excitation helicity was reversed the polarization-resolved PL components exchange their spectral positions, clearly demonstrating that $\vec{B}_N$ has reversed its direction. The contribution of $\left|\vec{B}_N^z\right|$ to the Zeeman splitting was estimated as 42 μeV. The build-up time of the $\vec{B}_N$ was measured in [13, 14] using the light with alternating σ^+ and σ^- polarizations with frequency *f*, whereas the detection of the PL components was performed within the time intervals corresponding to only σ^+ and σ^- excitation windows. The polarization degree ρ_c remains approximately the same for $f\lesssim 100Hz$, and the time $\Delta\tau\simeq 10\text{ms}$ was sufficient for $\vec{B}_N$ to be build-up. The value $\left|\vec{B}_N^z\right|$ determining ρ_c was estimated to be on the order of a few Teslas. To understand the origin of $\vec{B}_N$ in [13] a concept of dynamical polarization of lattice nuclei by optically oriented electrons was employed following [1-7] discussed above. As in the case of X^+ exciton studied by Braun et al. in [9], in the case of X^0 exciton in the In(Ga)As/GaAs QDs, the interaction between a single electron and a large number 10^4-10^5 of nuclei results in a dynamical nuclear spin polarization leading to the appearance of the spin-oriented nuclei. As was mentioned above, the equivalent effective magnetic field $\vec{B}_N$ acting on the electron localized in the QD gives rise to the Overhauser shift defined as $\Delta E=\left|B_N^z\mu_B g_{ex}\right|$. Adopting $|g_{ex}|=0.5-0.6$ and

$\Delta E = 42\ \mu\text{eV}$ in [13], the value $\left|\vec{B}_N^z\right| = (1.2-1.4)\ \text{T}$ was evaluated to be in satisfactory agreement with previous estimations [42, 43]. To explain the experimentally observed fact that a relatively strong nuclear magnetic field was build-up in the QD even for the case of a neutral exciton at $\vec{B}_{ext} = 0$, in [13-15] the preceding steps to the formation of the exciton were considered. They are related with the processes of separate capture of electrons and holes as was demonstrated in many previous publications [15, 19-30]. The capture times $\tau_{e(h)}$ for electrons and holes excited into the wetting layer (WL) could be estimated as $\tau_{e(h)} = L_{e(h)}/V_{e(h)}$. Here $L_{e(h)}$ corresponds to collection lengths for individual charged carriers into the QD. V_e and V_h are their velocities in the WL plane. As was deduced earlier [12], they are $V_e = 1.6\cdot 10^7\ \text{cm/s}$ and $V_h = 3.1\cdot 10^6\ \text{cm/s}$. For experimental conditions with the QD located within the area of the laser spot, the value $L_e = L_h = 1\ \mu\text{m}$ can be assumed and hence the difference in the capture times $\Delta\tau_{e-h}$ equals 26 ps. It is an expected time rise for the PL in the QD. According to this concept adopted in [13-15] before the recombination of an exciton, the QD is assumed to be populated with only one electron for 26 ps. This value is smaller than the average time τ_{rc} between two subsequent exciton formation events. The recycling τ_{rc} is supposed to be comparable with the exciton decay time $\tau_d \approx 800\ \text{ps}$. When the parameter $\Delta\tau_{e-h}$ is decreased by exciting directly in the QD with the photon energy smaller than excitation energy of the WL, the gradual reduction of ρ_c was observed [13-15]. The nuclear spins being polarized continue to conserve their polarization at least 10^{-3} s and in this period of time the Overhauser magnetic field is build-up being continuously supplied by other spin polarized electrons appearing successively in the QD under the influence of the circularly polarized laser radiation. A strongly coupled electron-nuclear spin system gives rise to two effective magnetic fields: a nuclear Overhauser field $\vec{B}_N$ acting upon the electrons ant the electron magnetic field $\vec{B}_e$ called the Knight field acting upon the nuclei [2-4]. The typical local effective magnetic fields $\vec{B}_L$ have the magnitudes of about $B_L \approx (0.1-0.3)\ \text{mT}$ [2-4]. They are caused by the nuclear spin-spin interactions and lead to the disappearance of the optically oriented nuclear spins. If $\left|\vec{B}_e\right| > \left|\vec{B}_L\right|$ a dynamic nuclear polarization is predicted at $\vec{B}_{ext} = 0$. To determine the value of $\left|\vec{B}_e\right|$ one can represent the average interaction energy of an electron spin $\vec{S}$ with *N* nuclei as the nuclear spin energy in an effective electron field $\vec{B}_e$ as follows:

$$A\left(\vec{I}_{av}\cdot\vec{S}\right) = -N\hbar\gamma\left(\vec{I}_{av}\cdot\vec{B}_e\right);\ \vec{B}_e = -\frac{\vec{S}\cdot A}{N\hbar\gamma};\ B_e = b\left|S_z\right|;$$
$$b = \frac{A}{N\hbar\gamma};\ \mu_n = \hbar\gamma I. \tag{9}$$

Here γ is the gyromagnetic ratio, μ_n is the magnetic moment of nucleus with spin *I*. I_{av} is the average spin of nuclei, *A* is the hyperfine contact interaction constant.

For the parameters $N = 5\cdot 10^4$, $A = 56\ \mu\text{eV}$, $\gamma = 5.86\cdot 10^7\ \text{T}^{-1}\text{s}^{-1}$ the constant *b* was estimated as $b = 30\ \text{mT}$. At $\left|S_z\right| = 1/2$ the Knight magnetic field equals $B_e = 15\ \text{mT}$, which is well

above the typical magnitude of B_L. This fact justifies the assumption that an essential $\left|\vec{B}_N\right|$ could be developed in the QD at $\vec{B}_{ext} = 0$ under the conditions described in [13-18].

To better understand the photoluminescence (PL) from the self-assembled InAs QDs (QDs) its dependence on some parameters, such as excitation power, pump-photon energy, crystal temperature [19-22], and the role of acceptor impurities [23, 24] were investigated.

Two new lines red-shifted relative to the ground state energy were identified as charged exciton complexes X^- and X^{--}.

It was observed that the PL spectra are very sensitive to the excitation energy and crystal temperature due to the effective diffusivity of photogenerated particles, which depends essentially on the excess excitation photon energy over the barrier band gap energy. The oscillating dependence of the QD exciton PL intensity on the photon excitation energy was explained in terms of the phonon relaxation processes [19-22]. The excess energy of the photogenerated carriers is released by the emission of LO phonons. If the excess energy exactly fits with an integer number of $\hbar\omega_{LO}$ phonons, it is quickly released, whereby the carriers become motionless at the band gap edge energy shortly after generation. It leads to low effective diffusivity. The carriers with higher diffusivity are moving in a spatially large region and can achieve the capturing centers. Due to different masses the excess energy is distributed in a non-equal way between the electrons and the heavy-holes, which results in different diffusivities. The capture centers primarily trap the high diffusivity carriers. Subsequently the attraction of low diffusivity carriers of opposite charge is increased by the Coulomb interaction [19-22]. The acceptor-induced threshold energy for the optical charging of InAs single QDs was observed [23, 24]. This threshold energy lies in the interval between the wetting layer ground state energy and the GaAs barrier energy and it is ascribed to the quantum transitions between the acceptor states and the conduction band states in GaAs [23, 24].

The use of an infrared laser excitation in addition to the optical excitation permitted to effectively manipulate the emission efficiency of the QDs [25-27]. At low temperatures the supplementary charges created by the infrared laser lead to the screening of the built-in electric fields, which play an important role in the carrier capture mechanism. The influence of the separate generation of the excess electrons and holes into the QDs at dual-laser excitation was investigated in [31, 32]. New interesting results concerning the properties of the self-assembled InAs/GaAs QDs were obtained subjecting the samples to the action of the external lateral electric field as well as of the magnetic field perpendicular and parallel to the wetting layer (WL) [32, 38]. When an external lateral electric field was applied, a considerable enhancement of the PL intensity of the QDs was observed. This severalfold increase depends on the magnitudes of the external electric field and the internal built-in electric fields. The latter could be altered by an additional infrared illumination of the sample. At low temperatures the magnetic field perpendicular to the layer alters the in-plane transport properties due to the localization of the carriers in the WL potential fluctuations. The decreased transport in the WL leads to a reduced capture in the QDs and consequently to a weakened dot-related emission. In addition, with increasing fields oriented parallel to the growth direction and perpendicular to the layer, i.e., in Faraday geometry, the redistribution of the intensities of the spectral lines was observed.

Conclusions

It has been established that, even for the case of neutral excitons, a nonzero nuclear magnetic field is building up in the In(Ga)As/GaAs QDs when the electrons and holes are photo-generated on the surface of the wetting layer and not directly into the QDs [13-18]. To explain these experimental observations, the exciton formation in QDs was considered as a process of the separated capture of electrons and holes, rather than a mechanism according to which an electron and a hole are captured into the QD as an entity [19-38].

References

[1] A.W. Overhauser, Phys. Rev., 92, 411, (1953).
[2] M.I. Dyakonov and V.I. Perel in *Optical Orientation* edited by F. Meier and B.P. Zakharchenya (North-Holland, Amsterdam, 1984) chap. 2; Zh. Eksp. Teor. Fiz., 68, 1514, (1975).
[3] Optical Orientation. Edited by F. Meier and B.P. Zakharchenya (North-Holland, Amsterdam, 1984) chap. 3-10.
[4] A. Merkulov, Al.L. Efros, and M. Rosen, Phys. Rev. B, 65, 205309, (2002).
[5] A. Khaetskii and Yu.V. Nazarov, Phys. Rev. B, 61, 12639, (2000).
[6] Y. Semenov et al., Phys. Rev. B, 67, 733010, (2003).
[7] T. Takagahara, Phys. Rev. B, 62, 16840, (2000).
[8] E.L. Ivchenko, Pure Appl. Chem., 67, 463, (1995).
[9] P.F. Braun et al., Phys. Rev. Lett., 94, 116601, (2005).
[10] M. Bayer et al., Phys. Rev. Lett., 82, 1748, (1999).
[11] R.J. Warburton et al., Nature (London), 405, 926, (2000).
[12] E.I. Gryncharova et al., Sov. Phys. Semicond., 11, 997, (1977).
[13] E.S. Moskalenko, L.A. Larsson, and P.O. Holtz, Phys. Rev. B, 80, 193413, (2009).
[14] E.S. Moskalenko, L.A. Larsson, and P.O. Holtz, J. Appl. Phys., 110, 013510, (2011).
[15] E.S. Moskalenko, L.A. Larsson, M. Larsson, P.O. Holtz, W.V. Schoenfeld, and P.M. Petroff, Nano Lett., 9, 353, (2009).
[16] E.S. Moskalenko, L.A. Larsson, and P.O. Holtz, Nanotechnology, 21, 345401, (2010).
[17] E.S. Moskalenko, L.A. Larsson, and P.O. Holtz, Superlattices and Microstructures, 49, 294, (2011).
[18] L.A. Larsson, E.S. Moskalenko, and P.O. Holtz, Applied Phys. Lett., 98, 071906, (2011).
[19] E.S. Moskalenko, K.F. Karlsson, P.O. Holtz, and B. Monemar, Phys. Rev. B, 64, 085302, (2001).
[20] K.F. Karlsson, E.S. Moskalenko, P.O. Holtz, B. Monemar, W.V. Schoenfeld, et al., Appl. Phys. Lett., 78, 2952, (2001).
[21] K.F. Karlsson, E.S. Moskalenko, P.O. Holtz, B. Monemar, W.V. Schoenfeld, J.M. Garcia, and P.M. Petroff, Acta physica Polonica, 100, 387, (2001).
[22] K.F. Karlsson, E.S. Moskalenko, P.O. Holtz, B. Monemar, W.V. Schoenfeld, J.M. Garcia, and P.M. Petroff, Physica E, 13, 101, (2002).
[23] E.S. Moskalenko, K.F. Karlsson, P.O. Holtz, B. Monemar, W.V. Schoenfeld, J.M. Garcia, and P.M. Petroff, Phys. Rev. B, 66, 195332, (2002).
[24] K.F. Karlsson, E.S. Moskalenko, P.O. Holtz, B. Monemar, W.V. Schoenfeld, J.M. Garcia, and P.M. Petroff, Surface Science, 532-535, 843, (2003).
[25] E.S. Moskalenko, V. Donchev, K.F. Karlsson, P.O. Holtz, B. Monemar, W.V. Schoenfeld,

J.M. Garcia, and P.M. Petroff, Phys. Rev. B, 68, 155317, (2003).
[26] V. Donchev, K.F. Karlsson, E.S. Moskalenko, P.O. Holtz, B. Monemar, W.V. Schoenfeld, J.M. Garcia, and P.M. Petroff, Phys. Stat. Sol (c), 1, 608, (2004).
[27] E.S. Moskalenko, K.F. Karlsson, V. Donchev, P.O. Holtz, B. Monemar, and W.V. Schoenfeld, Appl. Phys. Lett., 85, 754, (2004).
[28] E.S. Moskalenko, K.F. Karlsson, V. Donchev, P.O. Holtz, W.V. Schoenfeld, et al., Appl. Phys. Lett., 84, 4896, (2004).
[29] E.S. Moskalenko, K.F. Karlsson, V. Donchev, P.O. Holtz, W.V. Schoenfeld, and P.M. Petroff, Physics of the Solid State, 47, 2154, (2005).
[30] E.S. Moskalenko, K.F. Karlsson, V. Donchev, P.O. Holtz, B. Monemar, W.V. Schoenfeld, and P.M. Petroff, Nano Lett., 5, 2117, (2005).
[31] V. Donchev, E.S. Moskalenko, K.F. Karlsson, P.O. Holtz, B. Monemar, W.V. Schoenfeld, J.M. Garcia, and P.M. Petroff, Physics of the Solid State, 48, 1993, (2006).
[32] E.S. Moskalenko, M.A. Larsson, W.V. Schoenfeld, P.M. Petroff, and P.O. Holtz, Phys. Rev. B, 73, 155336, (2006).
[33] M.A. Larsson, E.S. Moskalenko, L.A. Larsson, P.O. Holtz, C. Verdozzi, C.O. Almbadh, W.V. Schoenfeld, and P.M. Petroff, Phys. Rev. B, 74, 245312, (2006).
[34] E.S. Moskalenko, M. Larsson, K.F. Karlsson, P.O. Holtz, B. Monemar, W.V. Schoenfeld, and P.M. Petroff, Nano Lett., 7, 183, (2007).
[35] E.S. Moskalenko, M. Larsson, K.F. Karlsson, P.O. Holtz, B. Monemar, W.V. Schoenfeld, and P.M. Petroff, Physics of the Solid State, 49, 1995, (2007).
[36] E.S. Moskalenko, L.A. Larsson, M. Larsson, P.O. Holtz, W.V. Schoenfeld, and P.M. Petroff, Phys. Rev. B, 78, 075306, (2008).
[37] E.S. Moskalenko, L.A. Larsson, M. Larsson, P.O. Holtz, W.V. Schoenfeld, and P.M. Petroff, Nano Lett., 9, 353, (2009).
[38] L.A. Larsson, M. Larsson, E.S. Moskalenko, and P.O. Holtz, Nanoscale Res. Lett., 5, 1150, (2010).
[39] J. Urayama et al., Phys. Rev. Lett., 86, 4930, (2001).
[40] E.C. Le Ru et al., Phys. Rev. B, 67, 245318, (2003).
[41] R.I. Dzhioev et al., Phys. Rev. B, 56, 13405, (1997).
[42] A.I. Tartakovskii et al., Phys. Rev. Lett., 98, 026806, (2007).
[43] P. Maletinskii et al., Phys. Rev. B, 75, 035409, (2007).

THE NAMBU-GOLDSTONE MODES OF BOSE-EINSTEIN CONDENSED TWO-DIMENSIONAL MAGNETOEXCITONS

S. A. Moskalenko[1], M. A. Liberman[2], E. V. Dumanov[1], B. V. Novikov[3], E. S. Kiselyova[4], and F. Cerbu[1]

[1] *Institute of Applied Physics of the Academy of Sciences of Moldova, Academiei str. 5, Chisinau, MD2028 Republic of Moldova*
[2] *Department of Physics, Uppsala University, Box 530, Uppsala, SE-751 21Sweden*
[3] *Department of Solid State Physics, Institute of Physics, St. Petersburg State University, Ulyanovskaya str. 1., Petrodvorets, St. Petersburg, 198504 Russia*
[4]*Moldova State University, Mateevici str. 60, Chisinau, MD-2009 Republic of Moldova*
e-mail: dum@phys.asm.md

(Received 30 March 2012)

Abstract

The collective elementary excitations of the two-dimensional (2D) electron-hole systems in a strong perpendicular magnetic field are discussed from the point of view of the Bogoliubov [1] and Goldstone [2] theorems concerning the many-body Hamiltonian with continuous symmetries, continuously degenerate ground states, forming a ring of minima on the energy scale in dependence on the phase of the field operator. This system due to the quantum fluctuations does select a concrete ground state with a fixed phase of the field operator forming a ground state with a spontaneously broken continuous symmetry [1-3]. The collective excitation of this new ground state related only with the changes of the field operator phase without changing its amplitude leads to the quantum transitions along the ring of the minima and does not need excitation energy in the long wavelength limit. This type of gapless excitations is referred to as Nambu-Goldstone modes [2-8]. They are equivalent to massless particles in the relativistic physics. The concrete realization of these theorems in the case of 2D magnetoexcitons with direct implications of the plasmon-type excitations side by side with the exciton ones is discussed below in terms of the Bogoliubov [1] theory of quasiaverages.

1. Introduction: The Bogoliubov's Theory of the Quasiaverages

Bogoliubov [1] demonstrated his concept of quasiaverages by using the ideal Bose-gas model with the Hamiltonian

$$H = \sum_k \left(\frac{\hbar^2 k^2}{2m} - \mu \right) a_k^\dagger a_k \,, \tag{1}$$

here $a_k^\dagger$, a_k are the Bose operators of creation and annihilation of particles, and μ is their chemical potential.
The occupation numbers of the particles are

$$N_0 = \frac{1}{e^{-\beta\mu} - 1}; \;\; N_k = \frac{1}{e^{\beta\left(\frac{\hbar^2 k^2}{2m} - \mu\right)} - 1}, \tag{2}$$

where $\mu \le 0$ and $\beta = 1/kT$.

In the normal state, the density of particles in the thermodynamic limit at $\mu = 0$ becomes $n = 2.612\left(mk_BT\right)^{3/2}/\left(2\pi\hbar^2\right)^{3/2}$. At this point, the Bose-Einstein condensation occurs and a finite value of the density of condensed particles appears in the thermodynamic limit

$$n_0 = \lim_{V\to\infty}\frac{N_0}{V};\quad \mu = -k_BT\ln\left(1+\frac{1}{N_0}\right) \tag{3}$$

The operators $a_0^\dagger$ and a_0 asymptotically become $c-$numbers, when their commutator

$$\left[\frac{a_0}{\sqrt{V}},\frac{a_0^\dagger}{\sqrt{V}}\right] = \frac{1}{V} \tag{4}$$

asymptotically tends to zero and their product is equal to n_0. One can then write

$$\frac{a_0^\dagger}{\sqrt{V}} \to \sqrt{n_0}e^{i\alpha};\quad \frac{a_0}{\sqrt{V}} \to \sqrt{n_0}e^{-i\alpha} \tag{5}$$

On the other hand, the regular averages of the operators $a_0^\dagger$ and a_0 in Hamiltonian (1) are exactly equal to zero. It is the consequence of the commutativity of the operator H and the operator of the total particle number N as follows

$$\hat{N} = \sum_k a_k^\dagger a_k;\quad [H,\hat{N}] = 0. \tag{6}$$

As a result, the operators H is invariant with respect to the unitary transformation

$$U = e^{i\hat{N}\phi} \tag{7}$$

with an arbitrary angle ϕ. This invariance is called gradient invariance of the first kind or gauge invariance. When ϕ does not depend on the coordinate x, we have the global gauge invariance and in the case $\phi(x)$ it is named as local gauge invariance [2-8] or gauge invariance of the second kind.

The invariance (7) implies $H = U^\dagger HU;\ U^\dagger a_0 U = e^{i\phi}a_0$, which leads to the following average value

$$\langle a_0\rangle \cong Tr\left(a_0e^{-\beta H}\right) = Tr\left(a_0Ue^{-\beta H}U^\dagger\right) = Tr\left(U^\dagger a_0Ue^{-\beta H}\right) = e^{i\phi}\langle a_0\rangle;$$

$$\left(1-e^{i\phi}\right)\langle a_0\rangle = 0$$

The selection rules arise

$$\langle a_0\rangle = 0;\quad \langle a_0^\dagger\rangle = 0 \tag{8}$$

because ϕ is an arbitrary angle. The regular average (8) can also be obtained from asymptotical expressions (5) if they are integrated over the angle α. This apparent contradiction can be resolved if Hamiltonian (1) is completed by an additional term

$$-\nu\left(a_0^\dagger e^{i\varphi} + a_0e^{-i\varphi}\right)\sqrt{V},\quad \nu > 0, \tag{9}$$

where φ is a fixed angle and ν an infinitesimal value.

The new Hamiltonian has the form

$$H_{\nu,\phi} = \sum_k\left(\frac{\hbar^2k^2}{2m}-\mu\right)a_k^\dagger a_k - \nu\left(a_0^\dagger e^{i\varphi} + a_0e^{-i\varphi}\right)\sqrt{V}\ . \tag{10}$$

It does not conserve the condensate number. Now the regular average values of the

operators $a_0^\dagger$ and a_0 over the Hamiltonian $H_{\nu,\phi}$ differ from zero, i.e., $\langle a_0 \rangle_{H\varphi} \neq 0$ and $\langle a_0^\dagger \rangle_{H\varphi} \neq 0$. The definition of the quasiaverages designated by $< a_0 >$ is the limit of the regular average $\langle a_0 \rangle_{H\varphi}$ when ν tends to zero

$$< a_0 >= \lim_{\nu \to 0} \langle a_0 \rangle_{H_{\nu,\varphi}} . \tag{11}$$

It is important to emphasize that the limit $\nu \to 0$ must be effectuated after the thermodynamic limit $V \to \infty$, $N_0 \to \infty$. In the thermodynamic limit, μ is also infinitesimal, and it is possible to choose the ratio of two infinitesimal values μ and ν to give a finite value

$$-\frac{\nu}{\mu} = \sqrt{n_0} . \tag{12}$$

To calculate the regular average $\langle a_0 \rangle_{H_{\nu,\varphi}}$ one needs to represent the Hamiltonian (10) $H_{\nu,\phi}$ in a diagonal form with the aid of the canonical transformation over the amplitudes

$$a_0 = -\frac{\nu}{\mu} e^{i\varphi} \sqrt{V} + \alpha_0; \;\; a_k = \alpha_k; \;\; k \neq 0 . \tag{13}$$

In terms of the new variables the Hamiltonian $H_{\nu,\phi}$ takes the form

$$H_{\nu,\phi} = -\mu \alpha_0^\dagger \alpha_0 + \sum_k \left(\frac{\hbar^2 k^2}{2m} - \mu \right) \alpha_{\vec{k}}^\dagger \alpha_{\vec{k}} + \frac{\nu^2 V}{\mu} . \tag{14}$$

In the diagonal representation (14), the regular average value $\langle \alpha_0 \rangle_{H_{\nu,\varphi}}$ exactly equals zero, while the value $\langle a_0 \rangle_{H_{\nu,\varphi}}$ equals the first term on the right-hand side of formulas (13).

As a result, the quasiaverage $< a_0 >$ is

$$< a_0 >= \lim_{\nu \to 0} \langle a_0 \rangle_{H_{\nu,\varphi}} = \sqrt{N_0} e^{i\varphi} . \tag{15}$$

It depends on the fixed angle φ and does not depend on ν. The spontaneous global gauge symmetry breaking was implied when the phase φ of the condensate amplitude in Hamiltonian (10) was fixed.

When the interaction between the particles is taken into account, these differences appear for other amplitudes as well. They give rise to the renormalization of the energy spectrum of the collective elementary excitations. In such a way, the canonical transformation

$$a_k = \sqrt{N_0} \delta_{k,0} e^{i\varphi} + \alpha_k \tag{16}$$

introduced for the first time by Bogoliubov [1] in his theory of superfluidity, has a quantum-statistical foundation within the framework of the quasiaverage concept. At $T = 0$ the quasiaverage $< a_0 >$ coincides with the average over the quantum-mechanical ground state, which is a coherent macroscopic state [9].

The phenomena related with the spontaneous breaking of the continuous symmetry play an important role in statistical physics. The first contributions in this direction belonging to Nambu [3], Goldstone [2], Higgs [4], and Weinberg [5] were stimulated under the influence of the theory of superconductivity originated by Bardeen, Cooper, and Schrieffer [6] and refined by Bogoliubov [1]. Some elements of these concepts, such as the coherent macroscopic state with a given fixed phase and the displacement canonical transformation of the field operator describing the Bose-Einstein condensate, were introduced by Bogoliubov in the microscopical theory of

superfluidity [1] and were generalized in his theory of quasiaverages [1] noted above.

The brief review of the gauge symmetries, their spontaneous breaking, Goldstone and Higgs effects will be presented below following the Ryder's monograph [7] and Berestetskii's lectures [8].

2. The Goldstone's Theorem

Goldstone demonstrated his main idea considering a simple model of a complex scalar Bose field, which in classical description has the Lagrangian

$$L = \left(\frac{\partial \phi^*}{\partial x_\mu}\right)\left(\frac{\partial \phi}{\partial x^\mu}\right) - m^2\phi^*\phi - \lambda\left(\phi^*\phi\right)^2 . \tag{17}$$

The potential energy $V(\phi)$ has the form

$$V(\phi) = m^2\phi^*\phi + \lambda\left(\phi^*\phi\right)^2; \;\; \lambda > 0, \tag{18}$$

where m^2 is regarded as a parameter only, rather than a mass term, λ is the parameter of self-interaction, whereas the denotations x_μ and x^μ mean

$$x^\mu = (ct, \vec{x}); \;\; x_\mu = (ct, -\vec{x}); \tag{19}$$

Lagrangian is invariant under the global gauge transformation

$$\phi = e^{i\Lambda}\phi'; \;\; L(\phi) = L(\phi'); \;\; \Lambda - \text{constant} . \tag{20}$$

It has a global gauge symmetry. The ground state is obtained by minimizing the potential as follows

$$\frac{\partial V(\phi)}{\partial \phi} = m^2\phi^* + 2\lambda\phi^*\left|\phi\right|^2 . \tag{21}$$

The interest presents the case $m^2 < 0$, when the minima are situated along the ring

$$\left|\phi\right|^2 = -\frac{m^2}{2\lambda} = a^2; \;\; \left|\phi\right| = a; \;\; a > 0 . \tag{22}$$

The function $V(\phi)$ is shown in Fig. 1 being plotted against two real components of the field ϕ_1 and ϕ_2.

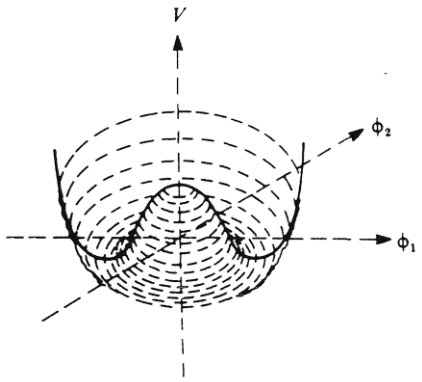

Fig. 1. The potential $V(\phi)$ with the minima at $\left|\phi\right| = a$ and a local maximum at $\phi = 0$.

There is a set of degenerate vacua related to each other by rotation. The complex scalar field can be expressed in terms of two scalar real fields, such as $\rho(x)$ and $\theta(x)$, in polar

coordinates representation or in Cartesian decomposition as follows

$$\phi(x) = \rho(x)e^{i\theta(x)} = \left(\phi_1(x) + i\phi_2(x)\right)\frac{1}{\sqrt{2}}. \tag{23}$$

The Bogoliubov-type canonical transformation breaking the global gauge symmetry was written as

$$\phi(x) = a + \frac{\phi_1'(x) + i\phi_2'(x)}{\sqrt{2}} = (\rho'(x) + a)e^{i\theta'(x)}. \tag{24}$$

The new particular vacuum state has the average $\langle\phi\rangle_0 = a$ with the particular vanishing vacuum expectation values $\langle\phi_1'\rangle_0 = \langle\phi_2'\rangle_0 = \langle\rho'\rangle_0 = \langle\theta'\rangle_0 = 0$. It means the selection of one vacuum state with infinitesimal phase $\theta' \to 0$. As was mentioned in [7], the physical fields are the excitations above the vacuum. They can be realized by performing perturbations about $|\phi| = a$. Expanding Lagrangian (17) in series on the infinitesimal perturbations θ', ρ', ϕ_1', ϕ_2' ignoring the constant terms, we will obtain

$$L = \frac{1}{2}\left(\partial_\mu\phi_1'\right)\left(\partial^\mu\phi_1'\right) + \frac{1}{2}\left(\partial_\mu\phi_2'\right)\left(\partial^\mu\phi_2'\right) - 2\lambda a^2\phi_1'^2 - \sqrt{2}\lambda\phi_1'\left(\phi_1'^2 + \phi_2'^2\right) - \frac{\lambda}{4}\left(\phi_1'^2 + \phi_2'^2\right)^2 \tag{25}$$

or in polar description

$$\begin{aligned} L = &\left(\partial_\mu\rho'\right)\left(\partial^\mu\rho'\right) + \left(\rho' + a\right)^2\left(\partial_\mu\theta'\right)\left(\partial^\mu\theta'\right) - \\ &-\left[\lambda\rho'^4 + 4a\lambda\rho'^3 + 4\lambda a^2\rho'^2 - \lambda a^4\right] \end{aligned} \tag{26}$$

Neglecting the cubic and quartic terms, we will see that there are the quadratic terms only of the type $4\lambda a^2\rho'^2$ and $2\lambda a^2\phi_1'^2$, but there are not quadratic terms proportional to θ'^2 and $\phi_2'^2$. If we compare these Lagrangians with relativistic physics, we can conclude that the field components ϕ_1' and ρ' represent massive particles and dispersion laws with energy gap, whereas the field components ϕ_2' and θ' represent the massless particles and gapless energy spectrum.
The main Goldstone results can be formulated as follows

$$\begin{aligned} &m_{\rho'}^2 = 4\lambda a^2, \;\; m_{\phi_1'}^2 = 2\lambda a^2; \\ &m_{\theta'}^2 = 0; \;\; m_{\phi_2'}^2 = 0; \end{aligned} \tag{27}$$

The spontaneous breaking of the global gauge symmetry takes place due to the influence of the quantum fluctuations. They transform the initial field ϕ with two massive real components ϕ_1 and ϕ_2, and a degenerate ground state with the minima forming a ring into another field with one massive and other massless components, the ground state of which has a well defined phase without initial symmetry.

The elementary excitations above the new ground state changing the value $\langle\rho\rangle = a$ are massive. It costs the energy to displace ρ' against the restoring forces of the potential $V(\rho)$. But there are no restoring forces corresponding to displacements along the circular valley $|\phi| = a$ formed by initial degenerate vacua.

Hence, for angular excitations θ' of wavelength, λ we have $\omega \sim \lambda^{-1} \to 0$ as $\lambda \to \infty$. The dispersion law is $\omega \sim ck$ and the particles are massless [7]. The θ' particles are known as the Goldstone bosons. This phenomenon is general and takes place in any order of perturbation theory. The spontaneous breaking of a continuous symmetry not only of the type as a global

gauge symmetry but also of the type of rotational symmetry entails the existence of massless particles referred to as Goldstone particles or Nambu-Golstone gapless modes. These statements are known as Goldstone theorem. Its affirms that there exists a gapless excitation mode when a continuous symmetry is spontaneously broken. The angular excitations θ' are analogous to the spin waves. The latter represent a slow spatial variation of the direction of magnetization without changing of its absolute value. Since the forces in a ferromagnetic are of short range, it requires a very little energy to excite this ground state. So, the frequency of the spin waves has the dispersion law $\omega = ck$. As was mentioned by Ryder [7], this argument breaks down if there are long-range forces like, for example, the $1/r$ Coulomb force. In this case, we deal with the maxwellian gauge field with local depending on x gauge symmetry instead of global gauge symmetry considered above.

The case of Goldstone field ϕ and of a maxwellian field with local gauge symmetry will be discussed below. But before it, a specific application of the above statement will be demonstrated following References [10-16], where the spinor Bose-Einstein condensates are discussed.

3. The Bogoliubov Excitations and the Nambu-Goldstone Modes

The above formulated theorems can be illustrated using the specific example of the Bose-Einstein condensed sodium atoms ^{23}Na in an optical-dipole trap following the investigations of Murata, Saito and Ueda [10] on the one side and of Uchino, Kobayashi and Ueda [11] on the other side. There are many other references in this direction, among which, we can mention [12-17]. The sodium atoms ^{23}Na have a spin $f = 1$ of the hyperfine interaction and obey the Bose statistics. The interacting bosons with $f = 1$ have a resultant spin F with the values $F = 0,1,2$. The contact hard-core interaction constant $g_F = 4\pi\hbar^2 a_F / M$ are characterized by s-wave scattering lengths a_F, which are different from zero for $F = 0$ when two atomic spins form a singlet, and for $F = 2$, when they form a quintuplet. The constant g_0 and g_2 enter into the combinations $c_0 = (g_0 + 2g_2)/3$ and $c_1 = (g_2 - g_0)/3$ which determine the Hamiltonian. The description of the atomic Bose gas in an optical-dipole trap is possibly in the plane-wave representation due to the homogeneity and the translational symmetry of the system. It means that the components of the Bose field operator $\psi_m(\vec{r})$ can be represented in the form:

$$\psi_m(\vec{r}) = \frac{1}{\sqrt{V}} \sum_k a_{km} e^{i\vec{k}\vec{r}} \tag{28}$$

where a_{km} is the annihilation operator with a wave vector $\vec{k}$ and a magnetic quantum number m, which in the case $f = 1$ takes three values 1, 0, -1. V is the volume of the system. The spinor Bose-Einstein condensates were realized experimentally by the MIT group [12] in different spin combinations using the sodium atoms ^{23}Na in a hyperfine spin states $\left| f = 1, m_f = -1 \right\rangle$ in a magnetic trap and then transforming them to an optical-dipole trap formed by a single infrared laser. The Bose-Einstein condensates were found to be long-lived. Some arguments concerning the metastable long-lived states were formulated. They may appear if the energy barriers, which prevent the system from a direct evolving toward its ground states, do exist. If the thermal energy needed to overcome these barriers is not available, the metastable state may be long-lived and these events are commonly encountered. Even the Bose-Einstein condensates in the dilute atomic

gases also arise due to the metastability. More so, in the gases with attractive interactions the Bose-Einstein condensates may be metastable against the collapse just due to the energy barriers [12]. Bellow we will discuss the Bogoliubov-type collective elementary excitations arising over the metastable long-lived ground states of the spinor-type Bose-Einstein condensates (BEC-tes) following [10, 11], so as to demonstrate the formation of the Nambu-Goldstone modes.

The Hamiltonian considered in [10] is given by formulas (3) and (4), and has the form

$$H = \sum_{\vec{k},m} \left(\varepsilon_{\vec{k}} - pm + qm^2 \right) a^{\dagger}_{\vec{k}m} a_{\vec{k}m} + \frac{c_0}{2V} \sum_{\vec{k}} : \hat{\rho}^{\dagger}_{\vec{k}} \hat{\rho}_{\vec{k}} : + \frac{c_1}{2V} \sum_{\vec{k}} : \hat{f}^{\dagger}_{\vec{k}} \hat{f}_{\vec{k}} : \tag{29}$$

Here the denotations were used

$$\begin{aligned}
&\varepsilon_k = \frac{\hbar^2 k^2}{2M}; \;\; c_0 = (g_0 + 2g_2)/3; \;\; c_1 = (g_2 - g_0)/3 \\
&\hat{\rho}_{\vec{k}} = \sum_{\vec{q},m} a^{\dagger}_{\vec{q},m} a_{\vec{q}+\vec{k},m}; \;\; \hat{\vec{f}} = (\hat{f}^x, \hat{f}^y, \hat{f}^z); \\
&\hat{\vec{f}}_{\vec{k}} = \sum_{q,m,n} \hat{\vec{f}}_{mn} a^{\dagger}_{q,m} a_{q+k,m} \\
&\hat{f}^x = \begin{vmatrix} 0 & 1 & 0 \\ 1 & 0 & 1 \\ 0 & 1 & 0 \end{vmatrix} \frac{1}{\sqrt{2}}; \;\; \hat{f}^y = \begin{vmatrix} 0 & -1 & 0 \\ 1 & 0 & -1 \\ 0 & 1 & 0 \end{vmatrix} \frac{i}{\sqrt{2}}; \;\; \hat{f}^z = \begin{vmatrix} 1 & 0 & 0 \\ 0 & 0 & 0 \\ 0 & 0 & -1 \end{vmatrix}
\end{aligned} \tag{30}$$

The repeated indices are assumed to be summed over 1,0,-1. The symbol $::$ denotes the normal ordering of the operators. The coefficient p is the sum of the linear Zeeman energy and of the Lagrangian multiplier, which is introduced to set the total magnetization in the z direction to a prescribed value. This magnetization is conserved due to the axisymmetry of the system in a magnetic field. q is the quadratic Zeeman effect energy, which is positive in the case of spin $f = 1$ ^{23}Na and ^{87}Rb atoms. The spin-spin interaction is ferromagnetic-type with $c_1 < 0$ for the $f = 1$ ^{87}Rb atoms and is antiferromagnetic-type with $c_1 > 0$ for the $f = 1$ ^{23}Na atoms [10]. Taking into account the fact that in many experimental situations the linear Zeeman effect can be ignored and the quadratic Zeeman effect term q can be manipulated experimentally, in [11] the both cases of positive and negative q at $p = 0$ were investigated for the spin -1 and spin -2 Bose-Einstein condensates (BECs). We will confine ourselves to the review of some spinor phases with spin -1 discussed in [11] so as to demonstrate the relations between the Nambu-Goldstone(NG) modes of the Bogoliubov energy spectra and the spontaneous breaking of the continuous symmetries. The description of the excitations is made in [10, 11] in the number-conserving variant of the Bogoliubov theory [1]. There is no need to introduce the chemical potential as a Lagrangian multiplier in order to adjust the particle number to a prescribed value.

The BEC takes place on a superposition state involving the single-particle states with wave vector $\vec{k} = 0$ and different magnetic quantum numbers

$$\left| \xi \right\rangle = \sum_m \xi_m a^{\dagger}_{0,m} \left| vac \right\rangle; \;\; \sum_m \left| \xi_m \right|^2 = 1 \tag{31}$$

The order parameter has a vector form and consists of three components: $\vec{\xi} = (\xi_1, \xi_0, \xi_{-1})$. The vacuum state $\left| vac \right\rangle$ means the absence of the atoms. The ground state wave function of the BEC-ed atoms is given by formula (8) of [11]

$$\left|\psi_g\right\rangle = \frac{1}{\sqrt{N!}}\left(\sum_{m=-f}^{f}\xi_m a_{0,m}^{\dagger}\right)^N \left|vac\right\rangle \tag{32}$$

In the mean-field approximation the operators $a_{0,m}^{\dagger}$, $a_{0,m}$ are replaced by the $c-$umbers $\xi_m\sqrt{N_0}$, where N_0 is the number of the condensed atoms. After this substitution, the initial Hamiltonian loses its global gauge symmetry and does not commute any longer with the operator $\hat{N}$. The order parameters ξ_m are chosen so as to minimize the expectation value of the new Hamiltonian as well as of its ground state and satisfy the normalization condition $\sum_m \left|\xi_m\right|^2 = 1$. To keep the order parameter of each phase unchanged, it is necessary to specify the combination of the gauge transformation and spin rotations [11]. This program was carried out in [18-21].

The initial Hamiltonian (29) in the absence of the external magnetic field has the symmetry $U(1)\times SO(3)$ representing the global gauge symmetry $U(1)$ and the spin-rotation symmetry $SO(3)$. The generators of these symmetries are referred to as symmetry generators and have the form

$$\begin{aligned}\hat{N} &= \int d\vec{x}\hat{\psi}_m^{\dagger}(x)\hat{\psi}_m(x) = \sum_{\vec{k},m} a_{\vec{k},m}^{\dagger} a_{\vec{k},m} \\ \hat{F}^j &= \int d\vec{x}\hat{\psi}_m(x) f_{mn}^j \hat{\psi}_n(x);\ \ j = x, y, z\end{aligned} \tag{33}$$

Unlike the $SO(3)$ symmetry group with three generators $\hat{F}^x$, $\hat{F}^y$ and $\hat{F}^z$, the $SO(2)$ symmetry group has only one generator $\hat{F}^z$ which describes the spin rotation around the z axis and looks as follows:

$$\hat{F}^z = \sum_{\vec{k},m} m a_{\vec{k},m}^{\dagger} a_{\vec{k},m} \tag{34}$$

In the presence of an external magnetic field, the symmetry of the Hamiltonian is $U(1)\times SO(2)$. The breaking of the continuous symmetries means the breaking of their generators. The number of the broken generators (BG) is denoted as N_{BG}. It equals 4 in the case of $U(1)\times SO(3)$ symmetry and to 2 in the case of $U(1)\times SO(2)$ symmetry.

The phase transition of the spinor Bose gas from the normal state to the Bose-Einstein condensed state was introduced mathematically into Hamiltonian (29) using the Bogoliubov displacement canonical transformation, when the single-particle creation and annihilation operators with a given wave vector $\vec{k}$, for example $\vec{k} = 0$, were substituted by the macroscopically $c-$numbers describing the condensate formation. The different superpositions of the single-particle states determine the structure of the finally established spinor phases [11]. Nielsen and Chadha [17] formulated a theorem which establishes the relation between the number of the Nambu-Goldstone modes, which must be present between the amount of the collective elementary excitations, which appear over the ground state of the system, if it is formed as a result of the spontaneous breaking of the N_{BG} continuous symmetries. The number of NG modes of the first type with linear (odd) dispersion law in the limit of long wavelengths denoted as N_I being accounted once, and the number N_{II} of the NG modes of the second type with quadratic (even) dispersion law at small wave vectors, being accounted twice give rise to the expression $N_I + 2N_{II}$, which is equal to or greater than the number N_{BG} of the broken symmetry

generators. The theorem is [17]

$$N_I + 2N_{II} \geq N_{BG} \tag{35}$$

It was verified in [11] for multiple examples of the spin -1 and spin -2 Bose-Einstein condensate phases. In the case of spin -2 nematic phases, the special Bogoliubov modes that have linear dispersion relation but do not belong to the NG modes were revealed. The Bogoliubov theory of the spin -1 and spin -2 Bose-Einstein condensates (BECs) in the presence of the quadratic Zeeman effect was developed by Uchino, Kobayashi and Ueda [11] taking into account the Lee, Huang, Yang (LHY) corrections to the ground state energy, pressure, sound velocity and quantum depletion of the condensate. Many phases that can be realized experimentally were discussed to examine their stability against the quantum fluctuations and the quadratic Zeeman effect. The relations between the numbers of the NG modes and of the broken symmetry generators were verified. A brief review of the results concerning the spin -1 phases of [11] is presented below so as to demonstrate, using these examples, the relations between the Bogoliubov excitations and the Nambu-Goldstone modes.

The first example is the ferromagnetic phase with $c_1 < 0$, $q < 0$ and the vector order parameter

$$\vec{\xi}^F = (1,0,0) \tag{36}$$

The modes with $m = 0$ and $m = -1$ are already diagonalized, whereas the mode $m = 1$ is diagonalized by the standard Bogoliubov transformation. The Bogoliubov spectrum is given by formulas (33) and (34) of [11] repeated below

$$E_{\vec{k},1} = \sqrt{\varepsilon_{\vec{k}}(\varepsilon_{\vec{k}} + 2\eta(c_0 + c_1))};\ E_{\vec{k},0} = \varepsilon_{\vec{k}} - q;\ E_{\vec{k},-1} = \varepsilon_{\vec{k}} - 2c_1 n \tag{37}$$

The $E_{\vec{k},1}$ mode is massless. In the absence of a magnetic field when $q = 0$, the mode $m = 0$ is also massless with the quadratic dispersion law. The initial symmetry of the Hamiltonian before the phase transition is $U(1) \times SO(3)$, whereas the final, remaining symmetry after the process of BEC is the symmetry of the ferromagnetic i.e. $SO(2)$. From the four initial symmetry generators $\hat{N}$, $\hat{F}^x$, $\hat{F}^y$ and $\hat{F}^z$ remains only the generator $\hat{F}^z$ of the $SO(2)$ symmetry. The generators $\hat{F}^x$ and $\hat{F}^y$ were broken by the ferromagnet phase, whereas the gauge symmetry operator $\hat{N}$ was broken by the Bogoliubov displacement transformation. The number of the broken generators $\hat{N}$, $\hat{F}^x$, $\hat{F}^y$ is three, i.e., $N_{BG} = 3$. In this case $N_I = 1$, $N_{II} = 1$ and $N_I + 2N_{II} = 3$, being equal to $N_{BG} = 3$. The equality $N_I + 2N_{II} = N_{BG}$ takes place. In the presence of an external magnetic field, with $q \neq 0$, the initial symmetry before the phase transition is $U(1) \times SO(2)$ with two generators $\hat{N}$ and $\hat{F}^z$, whereas after the BEC and the ferromagnetic phase formation the remained symmetry is $SO(2)$. Only one symmetry generator $\hat{N}$ was broken. It means $N_{BG} = 1$, $N_I = 1$ and $N_{II} = 0$. The equality $N_I + 2N_{II} = N_{BG}$ also takes place.

For $m = 1$ Bogoliubov mode to be stable, the condition $(c_0 + c_1) > 0$ is required. It ensures the mechanical stability of the meanfield ground state. Otherwise, the compressibility would not be positive definite and the system would become unstable against collapse. In the case $q > 0$, $c_1 > 0$ and $(c_0 + c_1) < 0$ the state would undergo the Landau instability for the $m = 0$ and $m = -1$ modes with quadratic spectra and the dynamical instability for the $m = 1$ mode with a linear spectrum (36)[11].

There are two polar phases. One with the parameters

$$\vec{\xi}^{P} = (0,1,0); \;\; q > 0; \;\; q + 2nc_1 > 0 \tag{38}$$

and the other with the parameters

$$\vec{\xi}^{P'} = \frac{1}{\sqrt{2}}(1,0,1); \;\; q < 0; \;\; c_1 > 0 \tag{39}$$

These two polar phases have two spinor configurations which are degenerate at $q = 0$ and connect other by $U(1) \times SO(3)$ transformation. However, for nonzero q the degeneracy is lifted and they should be considered as different phases. This is because the phase P has a remaining symmetry $SO(2)$, whereas the phase P' is not invariant under any continuous transformation. The number of NG modes is different in each phase and the low-energy behavior is also different. Following formulas (40)-(42) of [11] the density fluctuation operator a_{kd} and the spin fluctuation operators a_{k,f_x} and a_{k,f_y} were introduced

$$a_{kd} = a_{k,0}; \;\; a_{k,f_x} = \frac{1}{\sqrt{2}}(a_{k,1} + a_{k,-1}); \;\; a_{k,f_y} = \frac{i}{\sqrt{2}}(a_{k,1} - a_{k,-1}); \tag{40}$$

Their Bogoliubov energy spectra are

$$E_{\vec{k},d} = \sqrt{\varepsilon_{\vec{k}}(\varepsilon_{\vec{k}} + 2c_0)}; \;\; E_{\vec{k},f_j} = \sqrt{(\varepsilon_{\vec{k}} + q)(\varepsilon_{\vec{k}} + q + 2nc_1)}; \tag{41}$$

In the presence of an external magnetic field, the initial symmetry is $U(1) \times SO(2)$, whereas after the BEC and the formation of the phase P with $q \neq 0$ the remaining symmetry is also $SO(2)$. Only the symmetry $U(1)$ and its generator $\hat{N}$ were broken during the phase transition. It means we have in this case $N_{BG} = 1$, $N_I = 1$ and $N_{II} = 0$. The equality $N_I + 2N_{II} = N_{BG}$ holds. Density mode is massless because the $U(1)$ gauge symmetry is spontaneously broken in the mean-field ground state, while the transverse magnetization modes f_x and f_y are massive for non zero q, since the rotational degeneracies about the x and y axes do not exist being lifted by the external magnetic field. In the limit of infinitesimal $q \to 0$ nevertheless nonzero, the transverse magnetization modes f_x and f_y become massless. It occurs because before the BEC in the absence of an external magnetic field the symmetry of the spinor Bose gas is $U(1) \times SO(3)$, whereas after the phase transition it can be considered as a remaining symmetry $SO(2)$. The generators $\hat{N}$, $\hat{F}^x$, $\hat{F}^y$ were broken, whereas the generator $\hat{F}^z$ remained. In this case we have $N_{BG} = 3$, $N_I = 3$ and $N_{II} = 0$ the equality looks as $3 = 3$.

In the polar phase P' with the parameters (39) the density and spin fluctuation operators were introduced by formulas (57)-(59) [11]

$$a_{kd} = \frac{1}{\sqrt{2}}(a_{k,1} + a_{k,-1}); \;\; a_{k,f_x} = a_{k,0}; \;\; a_{k,f_y} = \frac{i}{\sqrt{2}}(a_{k,1} - a_{k,-1}); \tag{42}$$

with the Bogoliubov energy spectra described by formulas (65)-(67) [11]:

$$E_{\vec{k},d} = \sqrt{\varepsilon_{\vec{k}}(\varepsilon_{\vec{k}} + 2nc_0)}; \;\; E_{\vec{k},f_x} = \sqrt{(\varepsilon_{\vec{k}} - q)(\varepsilon_{\vec{k}} - q + 2nc_1)}; \;\; E_{\vec{k},f_z} = \sqrt{\varepsilon_{\vec{k}}(\varepsilon_{\vec{k}} + 2nc_1)} \tag{43}$$

At $q < 0$ in contrast to the case $q > 0$ one of the spin fluctuation mode $E_{\vec{k},f_z}$ becomes massless. The initial symmetry of the system is $U(1) \times SO(2)$. It has the symmetry generators $\hat{N}$ and $\hat{F}^z$. They are completely broken during the phase transition. After the phase transition and the P'

phase formation there are not any symmetry generators. The number of the broken generator is 2 ($N_{BG}=2$), whereas the numbers N_I and N_{II} are 2 and 0, respectively. As in the previous cases, the equality occurs in the Nielsen and Chadha rule. For the Bogoliubov spectra to be real the condition $q<0$, $c_0>0$ and $c_1>0$ must be satisfied, otherwise, the state $\vec{\xi}^{P'}$ will be dynamically unstable.

Side by side with the spinor-type three-dimensional (3D) atomic Bose-Einstein condensates in the optical traps, we will discuss also the case of the Bose-Einstein condensation of the two-dimensional (2D) magnetoexcitons in semiconductors [22-25]. The collective elementary excitations in these conditions were investigated in [26-31]

The starting Hamiltonian (10) in [30] has two continuous symmetries. One is the gauge global symmetry $U(1)$ and another one is the rotational symmetry $SO(2)$. The resultant symmetry is $U(1)\times SO(2)$. The gauge symmetry is generated by the operator $\hat{N}$ of the full particle number, when it commutes with the Hamiltonian. It means that the Hamiltonian is invariant under the unitary transformation $\hat{U}(\varphi)$ as follows

$$\hat{U}(\varphi)\hat{H}\hat{U}^{-1}(\varphi)=\hat{H};\ \ \hat{U}(\varphi)=e^{i\hat{N}\varphi};\ \ [\hat{H},\hat{N}]=0 \tag{44}$$

The operator $\hat{N}$ is referred to as symmetry generator. The rotational symmetry $SO(2)$ is generated by the rotation operator $\hat{C}_z(\varphi)$ which rotates the in-plane wave vectors $\vec{Q}$ on the arbitrary angle φ around z axis, which is perpendicular to the layer plane and is parallel to the external magnetic field. Coefficients $W_{\vec{Q}}$, $U(\vec{Q})$ and $V(\vec{Q})$ in formulas (6) and (9) of [30] depend on the square wave vector $\vec{Q}$ which is invariant under the rotations $\hat{C}_z(\varphi)$. This fact determines the symmetry $SO(2)$ of the Hamiltonian (10). The gauge symmetry of Hamiltonian (10) [30] after the phase transition to the Bose-Einstein condensation (BEC) state is broken as it follows from expression (16) of [30]. In terms of the Bogoliubov theory of quasiaverages, it contains a supplementary term proportional to $\tilde{\eta}$. The gauge symmetry is broken because this term does not commute with the operator $\hat{N}$. More so, this term is not invariant under the rotations $\hat{C}_z(\varphi)$, because the in-plane wave vector $\vec{k}$ of the BEC is transformed into another wave vector rotated by the angle φ in comparison with the initial position. The second continuous symmetry is also broken. In such a way, the installation of the Bose-Einstein condensation state with arbitrary in-plane wave vector $\vec{k}$ leads to the spontaneous breaking of the both continuous symmetries. We will discuss the more general case $\vec{k}\neq 0$ considering the case $\vec{k}=0$ as a limit $\vec{k}\to 0$ of the cases with small values $k \ll 1$. One can remember, that the supplementary terms in Hamiltonian (10) of [30] describing the influence of the ELLs are actual in the range of small values $kl<0.5$. Above we established that the number of the broken generators (BGs) denoted as N_{BG} equals to two ($N_{BG}=2$). Now we will discuss the number of the Nambu-Goldstone modes in a given system. Following the Goldstone's theorem in the systems with spontaneously broken continuous symmetries over the new ground states, there are some branches of the collective elementary excitations with gapless dispersion laws in the range of long wave-lengths. They are referred to as Nambu-Goldstone modes and can be compared with the massless particles in the relativistic physics. The Goldstone's theorem can be demonstrated considering a system described by the

complex scalar Bose field $\phi(x) = \rho(x)e^{i\theta(x)}$ with the potential energy $V(\varphi)$ which has a nonlinear dependence on ϕ in the form of a Mexican hat with the maximum at a point $\phi = 0$ and with the minimal values forming a ring with the radius of the hat a. The minimal potential energy values in the classical description determine the energies of the ground states or, in other words, the vacua of the system. They are strongly degenerated in dependence on the phase θ of the full operator. But under the influence of the quantum fluctuations between the manifold of vacua, one specific vacuum can be selected, for example, with the phase $\theta = 0$. In this case, the excitations of the system over the new vacuum state $\theta = 0$ transiting it to an adjacent vacuum state with infinitesimal $\theta \neq 0$ but lying on the vacuum ring will not need a finite amount of energy in the long wavelengths limit. The branch of the elementary excitations related only with the changes of the phases θ, but with unchanged value of radius a, is gapless in the range of small wave vectors. Another branch of excitations related with the changes of the radius a of the ring need finite amount of energy and are gapped. They are compared with the massive particles in relativistic physics. The Nambu-Goldstone modes are classified as being of the first type (I) when their dispersion law is linear (odd) in dependence on the wave vector and of the second type (II) when this dependence is quadratic (even). Nielsen and Chadha [17] formulated a theorem, which establishes the relation between the numbers N_I and N_{II} of both types Nambu-Goldstone(NG) modes and the number of the broken symmetry generators N_{BG}. If affirms that the number of first type NG modes N_I being accounted once and the number of second type NG modes N_{II} being accounted twice is equal or prevails the number of broken generators N_{BG}. The theorem looks as follows:

$$N_I + 2N_{II} \geq N_{BG} \tag{45}$$

As was shown above, the spontaneous symmetry breaking yields Nambu-Goldstone modes, which play a crucial role in determining low-energy behavior of various systems [5, 32-37]. The Goldstone theorem guarantees that the NG modes do not acquire mass at any order of quantum corrections. Nevertheless, sometimes soft modes appear, which are massless in the zeroth order, but become massive due to quantum corrections. They were introduced by Weinberg [5], who showed that these modes emerge if the symmetry of an effective potential of the zeroth order is higher than that of the gauge symmetry, and the idea was invoked to account for the emergence of low-mass particles in relativistic physics. Following [32] now these modes are referred to as quasi-Nambu-Goldstone modes, in spite of the fact that their initial name introduced by Weinberg was pseudo-modes instead of quasi-modes. Georgi and Pais [33] demonstrated that the quasi-NG modes also occur in cases in which the symmetry of the ground state is higher than that of the Hamiltonian [32]. This type of the quasi-Nambu-Goldstone modes is believed to appear, for example, in the weak-coupled limit of A phase of ^{3}He [37, 38].

4. The Quasi-Nambu-Goldstone Modes in the Bose-Einstein Condensates

The authors of [32] underlined that the spinor BEC are ideal systems to study the physics of the quasi-NG modes, because these systems have a great experimental manipulability and well established microscopic Hamiltonian.

It was shown in [32] that the quasi-NG modes appear in a spin-2 nematic phase. In the nematic condensate, three phases, each of which has a different symmetry, are energetically

degenerate to the zeroth order [36] and the zeroth order solution has a rotational symmetry $SO(5)$, whereas the Hamiltonian of the spin-2 condensate has a rotational symmetry $SO(3)$. By applying the Bogoliubov theory of the BEC under the assumption that the $\vec{k}=0$ components of the field operators are macroscopically occupied, it was shown that the order parameter of the nematic phase has an additional parameter independent on the rotational symmetry.

The ground state symmetry of the nematic phase to a zeroth order approximation is broken by quantum corrections, thereby making the quasi-NG modes massive. The breaking of the $SO(5)$ symmetry occurs. The number n of the quasi-NG modes was determined by Georgi and Pais [33] in the form of a theorem. It was explained and represented in [32] as follows:

$$n=\dim(\tilde{M})-\dim(M) \tag{46}$$

where $\tilde{M}$ is the surface on which the effective potential assumes its minimal values to the zeroth order and $\dim(\tilde{M})$ is the dimension of this surface. The dimension $\dim(M)$ determines the number of the NG modes. This implies that M is a submanifold of $\tilde{M}$ and n is the dimension of the complementary space of M inside $\tilde{M}$ [32].

In the case considered by Goldstone, the dimension of the ring is 1 and the number of the NG modes is 1; this leads to the absence of the quasi-NG modes $(n=0)$. Returning to the case of 2D magnetoexcitons in the BEC state with wave vector $\vec{k}$ different from zero $(\vec{k}\neq 0)$ described by Hamiltonian (16) of [30], one can remember that the both continuous symmetries existing in the initial form (10) [30] were lost. It happened due the presence of the term $\tilde{\eta}(d_{\vec{k}}^{\dagger}+d_{\vec{k}})$ in the frame of the Bogoliubov theory of quasiaverages. Nevertheless, the energy of the ground state as well as the self-energy parts $\Sigma_{ij}(P,\omega)$, which determine the energy spectrum of the collective elementary excitations depend only on the modulus of the wave vector $\vec{k}$ and do not depend at all on its direction. All these expressions have a rotational symmetry $SO(2)$, in spite of the fact that Hamiltonian (16) of [30] has lost it. In our mind we have the condition described by Georgi and Pais [33] favoring the emergence of the quasi-NG modes. We are explaining the existence of the gapped, massive exciton-type branches of the collective elementary excitations obtained in our calculations just by these considerations.

References

[1]N.N.Bogoliubov, Selected works, vol 2, 3, New-York: Gordon and Breach Sci. Publ., 1990-1991.
[2]J.Goldstone, Nuovo Cimento, 19, 154 (1961).
[3]Y.Nambu, Phys.Rev., 117, 648 (1960); Phys. Rev. Lett., 4, 380 (1960).
[4]P.Higgs, Phys. Rev., 145, 1156 (1966).
[5]S.Weinberg, Phys.Rev.Lett., 29, 1698 (1972).
[6]J.Bardeen, L.N.Cooper, and J.R.Schrieffer, Phys.Rev., 106, 162 (1957).
[7]L.H.Ryder, Quantum Field Theory, Cambridge University Press, Cambridge, (1966), 502 p.
[8]V.B.Berestetskii, The lecture: Spontaneous Breaking of the Symmetry and the Goldstone's Effect, Published in the collection of lectures, "Elementary Particles. Part 1", edited by the Institute of the Theoretical and Experimental Physics. Atomizdat, Moscow, 1973 (in Russian).

[9]S.A.Moskalenko and D.W.Snoke, "Bose-Einstein Condensation of Excitons and Biexcitons and Coherent Nonlinear Optics with Excitons," Cambridge University Press, Cambridge UK, New York USA, (2000), 415 p.
[10] K.Murata, H.Saito, and M.Ueda, Phys.Rev.A, 75, 013607 (2007).
[11] Sh.Uchino, M.Kobayashi, and M.Ueda, Phys.Rev.A, 81, 063632 (2010).
[12] H.-J.Miesner, D.M.Stamper-Kurn, J.Stenger, S.Inouye, A.P.Chikkatur, and W.Ketterle, Phys.Rev.Lett., 82, 2228 (1999).
[13] Sh. Uchino, M.Kobayashi, M.Nitta, Phys.Rev.Lett., 105, 230406 (2010).
[14] M.Ueda, Phys.Rev.A, 63, 013601 (2000).
[15] W.-J. Huang and S.-C. Gou, Phys.Rev.A, 59, 4608 (1999).
[16] Tin-Lun Ho, Phys.Rev.Lett., 81, 742 (1998).
[17] H.B.Nielsen and Chadha, Nucl.Phys. B, 105, 445 (1976).
[18] G.W.Semenoff and F.Zhou, Phys.Rev.Lett., 98, 100401 (2007).
[19] H.Makela, Y.Zhang, and k-A Suominen, J.Phys. A: Math.Gen., 36, 8555 (2003).
[20] F.Zhou, Phys.Rev.Lett., 87, 080401 (2001).
[21] J.L.Song, G.W.Semenoff, and F.Zhou, Phys.Rev.Lett., 98, 160408 (2007).
[22] I.V.Lerner and Yu.E.Lozovik, Zh. Eksp. Teor. Fiz. 78, 1167 (1980); I.V.Lerner and Yn.E.Lozovik, J. Low Temper. Phys. 38, 333 (1980); I.V.Lerner and Yn.E.Lozovik, Zh. Eksp. Teor. Fiz. 80, 1488 (1981) [Sov.Phys.-JETP 53, 763 (1981)].
[23] D.Paquet, T.M.Rice, and K.Ueda, Phys. Rev. B, 32, 5208 (1985).
[24] S.A.Moskalenko, M.A.Liberman, D.W.Snoke, and V. Botan, Phys. Rev. B, 66, 245316 (2002).
[25] S.A.Moskalenko, M.A.Liberman, P.I.Khadzhi, E.V.Dumanov, Ig.V.Podlesny, and V.Botan, Sol. State Comm., 140/5, 236 (2006); S.A.Moskalenko, M.A.Liberman, P.I.Khadzhi, E.V.Dumanov, Ig.V.Podlesny, and V.Botan, Physica E, 39, 1, 137 (2007).
[26] S.A.Moskalenko, M.A.Liberman, V.V.Botan, E.V.Dumanov, and Ig.V.Podlesny, Mold. J. of Phys. Scien., 4(2), 142 (2005).
[27] S.A.Moskalenko, M.A.Liberman, and E.V.Dumanov, J. of Nanoelectron. and Optoelectron., 4, 52 (2009).
[28] S.A.Moskalenko, M.A.Liberman, E.V.Dumanov, and Ig.V.Podlesny, Intern. J. of Quantum Chem., 110(1), 177 (2010).
[29] S.A.Moskalenko, M.A.Liberman, E.V.Dumanov, S.S.Rusu, and I.Sanduleac, Mold. J. of Phys. Scien., 9, 16 (2010).
[30] S.A.Moskalenko, M.A.Liberman, D.W.Snoke, E.V.Dumanov, S.S. Rusu, and F.Cerbu, J. of Phys.: Cond. Matt. (in press).
[31] E.V.Dumanov, M.A.Liberman, S.A.Moskalenko, B.V.Novikov, and S.S.Rusu, Phys. Stat. Solid.(b), (in press).
[32] S.Uchino, M.Kobayashi, M.Nitta, and M.Ueda, Phys.Rev.Lett., 105, 230406 (2010).
[33] H.Georgi and A.Pais, Phys.Rev.D, 12, 508 (1975).
[34] S.Uchino, T.Otsuka, and M.Ueda, Phys.Rev.A, 78, 023609 (2008).
[35] C.V.Ciobanu, S.-K.Yip and Tin-Lin Ho, Phys.Rev.A, 61, 033607 (2000).
[36] R.Barnett, A.Turner, and E.Demler, Phys.Rev.Lett, 97, 180412 (2006).
[37] J.Pang et al. arXiv:1010 (1986).
[38] G.E.Volovik, The Universe in a Helium Droplet, Oxford University, New York, 2003.

MICROSTRUCTURE AND MECHANICAL PROPERTIES OF TERNARY FLAKY SEMICONDUCTING COMPOUNDS

D. Grabco, O. Shikimaka, V. Zhitar

Institute of Applied Physics, Academy of Sciences of Moldova, Academiei str. 5, Chisinau, MD-2028 Republic of Moldova
e-mail: grabco@phys.asm.md

(Received 10 December 2011)

Abstract

Multicomponent sulfides $ZnIn_2S_4$, $Zn_3In_2S_6$, and $CoGaInS_4$ were obtained, and their mechanical properties (microhardness, plasticity, and brittleness) were studied. It was shown that the deformation peculiarities of the investigated compounds are connected with the specific layered crystalline structure.

1. Introduction

Ternary flaky semiconducting compounds are a promising material for the modern micro- and optoelectronics [1-4]. New multicomponent sulfides, such as three-packet $ZnIn_2S_4$ and single-packet $Zn_3In_2S_6$ crystal polytypes, as well as the $CoGaInS_4$ compound, are typical representatives of this class of crystals. Various devices have been elaborated on their basis. The compounds of the $Zn_xIn_2S_{3+x}$ type show high photosensitivity and intensive luminescence and can be used as effective ultraviolet detectors, solar cells, etc. The $CoGaInS_4$ crystals are of interest due to application as antiferromagnetic materials [2-5].

For the successful utilization of these materials, it is necessary to know their mechanical properties. Some features of plastic deformation observed using the microindentation and scratching methods are presented in this work.

2. Experimental

The compounds were obtained from the vapor phase by the method proposed earlier [5]. This technique makes it possible to grow the crystals in the form of thin hexagonal layered plates with dimensions of ~(20 × 12 × 0.8) mm^3. Single crystals were confined by the (0001) and (0110) faces. Atom coordinates and structure parameters are in accordance with the results reported in [6, 7].

The thin grown steps can be seen under optical and electron microscopic investigations of all studied ternary semiconductor compounds. At the same time, the growing features of hexagons were sometimes noticed on the as-grown surface of the $Zn_xIn_2S_{3+x}$ samples (Fig. 1). These hexagons probably begin to form from the helicoidal dislocations existing in the crystal volume and outgoing on the growth surface and build up a new growth layer of the crystal structure. Structurally perfect single crystals have a low dislocation density ($N_d = 10^2$, cm^{-2}) and are superior to the ZnS crystals in stability [8]; it was also observed that ternary flaky semiconducting compounds exhibit specific mechanical properties [4].

A PMT-3 microhardness tester supplied with a rotating device was used for the crystal

deformation and for the determination of microhardness via penetration (H_V) and sclerometric (H_S) methods. A Vickers' diamond pyramid was used for these experiments. The load (P) applied to the indenter was varied between 0.01 and 0.5 N. The hardness values were determined using the standard formulae [9]. A device for registration of acoustic emission (AE) signals was applied for the determination of crystal brittleness.

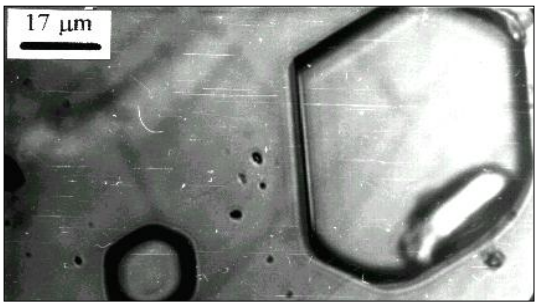

Fig. 1. As-grown hexagons on the $ZnIn_2S_4$ (0001) plane.

3. Results and Discussion

One of the unusual mechanical properties of the investigated flaky compounds is the inconstant microhardness values. They are dependent on the load applied to the indenter, and the *H(P)* dependences exhibit a nonmonotonous behavior. The microhardness increases in the range from low to middle loads (0.03÷0.2N). Here the microhardness values change in the intervals between 0.2÷0.5 *GPa*, 0.25÷0.5 *GPa*, and 0.17÷0.3 G*Pa* for $ZnIn_2S_4$, $Zn_3In_2S_6$, and $CoGaInS_4$, respectively. The microhardness reaches its maximal values at definite loads and then begins to decrease with a further increase in load. It was observed that the critical load value for the maximal H depends on the sample thickness (h). The microhardness values begin to decrease if the deformation depth reaches approximately one-half the sample thickness (0.5h). After that, the H_V values begin to diminish.

In order to understand the above behavior of the microhardness vs. load dependence, it is necessary to investigate the surface relief in the indentation neighborhood via varying the load.

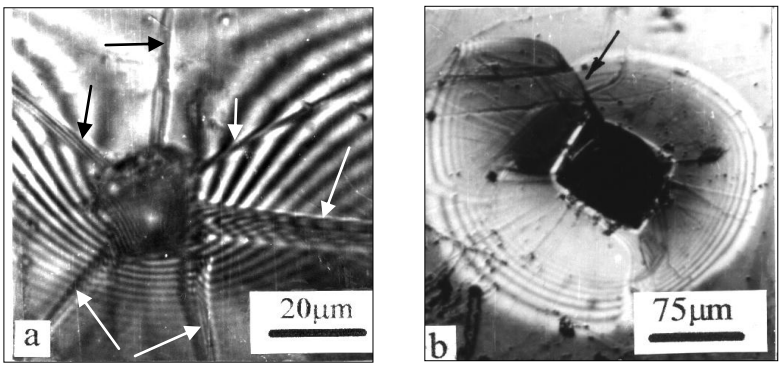

Fig. 2. $ZnIn_2S_4$ crystal, plane (0001): (a) interference around indentation. P = 0.3N; (b) circle-like deformation near by indentation. P=0.2N. (Twins are marked by arrows).

It was noticed that the surface is essentially modified near the indentations (Fig. 2) and scratches: the crystal exhibits a tendency to the local lowering of the surface which increases while approaching the indentations or the scratches. The lowering is intensified with load increase, too. So, the indentations obtained at P>0.1 N look in interference regime as situated in a pit (Fig. 2a).

The elastoplastic local flexure of the crystals under heavy loads on the indenter is so deep that conical hills of the forced out materials can be seen on the opposite side of the specimen. This is very well observed in the form of the concentric rings in the interference regime (Fig. 3). Sometimes the spontaneous (natural) interference generated by the crystal lamination at the indenter penetration is observed around the indentations (Fig. 2b). In some cases, the material lamination is accompanied by the appearance of twins (marked by arrows in Fig. 2).

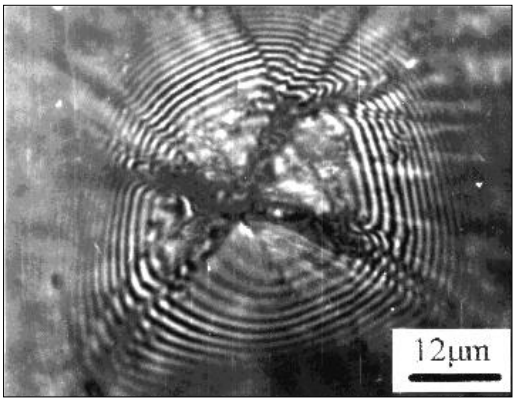

Fig. 3. Conical hill of the forced out material on the opposite side of the deformed $Zn_3In_2S_6$ crystal in the interference regime; (0001) plane; P = 0.5N.

It was established that the contribution of the twinning mechanism in microindentation process increases with increasing load (cf. Figs. 2b and 2a). A similar deformation has been previously found on the (111) plane of the bismuth type semimetals, which possess layer-like structure [9]. At the same time, unlike semimetals, the frail mechanism takes part in the deformation of ternary flaky compounds side by side with twinning one. However, the fragile destruction of the materials arises only in a thin superficial layer (~0.4% of the thickness of the deformed zone). This result indicates a good quality of crystals and their high strength properties.

The microstructure investigation showed that the tendency to twinning mechanism is more pronounced for $Zn_xIn_2S_{3+x}$ crystals. Tendency of the flaky compounds to twinning and frail destruction was also studied by (AE) method (table).

AE signals appearing under indentation. (N_1 and N_2 are the number of signals registered at the loading and unloading stages, respectively)

Crystal	P, N	N_1	N_2	$\Delta N = N_1 - N_2$
$CoGaInS_4$	0.1	700	2600	1900
	0.2	1180	4200	3020
$Zn_3In_2S_6$	0.1	430	1800	1370
	0.2	440	2180	1740

It is evident from the table that deformation of the $CoGaInS_4$ crystals is accompanied by the appearance of a greater number of signals than in the case of $Zn_3In_2S_6$. This indicates the smaller destruction of $Zn_3In_2S_6$ crystals as compared with $CoGaInS_4$ ones. Also, one can see that both the fragile destruction and twinning processes play a greater role when the crystals are unloaded, i.e., during crystal relaxation.

Thus, the results of the investigation of microstructure and mechanical properties of $Zn_xIn_2S_{3+x}$ and $CoGaInS_4$ indicate some specific peculiarities of their deformation. It was noticed that several mechanisms of deformation of flaky ternary compounds take place under the action of a concentrated load on the (0001) plane. They are: bending of crystal layers in the C-axis direction; plastic deformation by the twinning mechanism, brittle-plastic deformation of indentation and scratch surface with the formation of a nanostructural modification of the material in the contact zone and with the generation of thin cracks out of the contact region.

The existence of the nanostructure in the contact zone was observed under studying a very thin superficial layer after deformation. Just below it, mainly plastic indentations and scratches appear; this can be associated with either a local plastic compaction of the structure layers or a contribution of dislocation deformation mechanism.

4. Conclusion

The good-quality single crystals of the $Zn_xIn_2S_{3+x}$ and $CoGaInS_4$ ternary flaky semiconductor compounds were obtained. The strength and plastic properties of these crystals were studied, and the main mechanisms of deformation under the action of a concentrated load were proposed. It was shown that the specific deformation of multinary compounds takes place due to their stratified crystalline structure.

References

[1] V. Grivickas, V. Bikbajevas, M.I. Tarasik, and A.K. Fedotov, Lithuanian Journal of Physics, 46, 1, 67 (2006).

[2] D. Grabco, O. Shikimaka, V. Zhitar', S. Muntean, and G. Volodina, Mold. J. Phys. Sci., 3, 2, 178, (2004).

[3] M.A. Herman, Semiconductor Superlattices, Berlin: Akademie. Translated under the title Poluprovodnikovye sverkhreshetki, Moscow, Mir, 1989.

[4] D.Z. Grabko, N.A. Palistrant, G.G. Zaitseva, V.F. Zhitari, and S.I. Radautsan. Semiconductor Conference, CAS '98 Proceedings. 1998, **2,** p. 471.

[5] C. Batlistoni, L. Gastaldi, G. Matlogno, et. al., Sol. St. Com. 61**,** 1, 43 (1987).

[6] J. Moon-Seog and K. Wha-Tek, Appl. Phys. Lett. 70**,** 4, 484 (1997).

[7] H. Haeuseler, Mat. Res. Bull. 21**.** 709 (1986).

[8] V.F. Zhitar, N.I. Andreievskaya, and E.D. Arama, Neorg. Mater. 28, 9, 2007, (1992).

[9] D.Z. Grabko, Yu.S. Boyarskaya, and M.P. Dintu, Mechanical Properties of the Bi Type Semimetals. Shtiintsa, Kishinev, 1982, 132 p.

TRANSPORT PROPERTIES OF Cu_2ZnSnS_4

M. Guc[1], K. G. Lisunov[2], A. Nateprov, S. Levcenko, V. Tezlevan, and E. Arushanov

Institute of Applied Physics, Academy of Sciences of Moldova, Academiei str. 5, Chisinau, MD-2028 Republic of Moldova

[1]*e-mail: gmax@phys.asm.md*, [2] *kgl-official@rambler.ru*

(Received 16 December 2011)

Abstract

Temperature dependence of the resistivity, $\rho(T)$, of five single crystalline p-Cu_2ZnSnS_4 samples is investigated in the interval of $T \sim 300–10$ K. Below ~200 K, $\rho(T)$ exhibits an activated behavior obeying the Mott variable-range hopping conductivity law between ~130–150 K and ~30–70 K. Analysis of the experimental data yields relative acceptor concentration values. In addition, the values of dielectric permittivity, width of the acceptor band, and density of the localized states are estimated.

1. Introduction

Recently, promising quaternary Cu_2ZnSnS_4 compound absorber layers have attracted considerable interest [1–8]. It is believed that these materials, due to their low cost and low-toxic and abundant elements [1], are alternative of more expensive $CuIn_{1-x}Ga_xSe_2$ thin-film solar cell absorber materials, showing at present a high conversion efficiency of ~20 % [2]. Thin-film solar cells of Cu_2ZnSnS_4 with efficiency exceeding 9% have been fabricated so far [3]. This compound is also interesting as a wide-gap *p*-type thermoelectric material [8] as well as a photoelectrode for H_2 evolution from water [9–11].

Cu_2ZnSnS_4 crystallizes into two different structures, kesterite with space group $I\bar{4}$ and stannite (space group $I\bar{4}2m$) modifications, having 4 Cu, 2 Zn, 2 Sn, and 8 S atoms per unit cell and differing by 4 and 3 inequivalent bonds of S atoms, respectively [12, 13]. On the other hand, the disordered (mixed) structure has been observed as well [13, 14]. The point is that the total energies of both modifications are found to be very close, which favors the formation of a disordered structure with a more random distribution of Cu and Zn on cation positions, although the kesterite structure has a lower energy [13].

First-principles calculations of the electronic structure [13] and of a series of intrinsic defects and defect complexes [15], as well as investigations of the phase stability and defect formation in Cu_2ZnSnS_4 [16], were performed. The effective electron and hole masses, the fundamental band gap energy and high-frequency dielectric constant, κ_∞, were evaluated. Namely, for holes of the topmost valence band, the transversal effective mass values of $m_\perp = 0.71$ and 0.33 and the longitudinal effective mass values of $m_\parallel = 0.22$ and 0.84, for kesterite and stannite structures, respectively, were obtained (in units of free electron mass, m_0) [13]. Those of κ_∞ ranging from 6.5 to 7.1 were found to be less anisotropic and having closer values for both modifications of Cu_2ZnSnS_4 [13].

Photoluminescence of Cu_2ZnSnS_4 single crystals [17, 18] and films [19] was studied. Defect recombination model with a shallow donor below the conduction band (~ 5 meV) and two

shallow acceptors above the valence band, with energies $E_1 = 10 \pm 5$ meV and $E_2 \approx 30 \pm 5$ meV, was proposed [18]. Assuming an exciton binding energy of 10 meV, the value of the band gap $E_g = 1.519$ eV at 10 K was found [18].

The transport properties of Cu_2ZnSnS_4 polycrystalline thin films were investigated [4–7, 19], establishing the *p*-type conductivity but concentrating mainly on the resistivity data in the interval around the room temperature. On the other hand, the expected high degree of the microscopic lattice disorder favours a hopping charge transfer, which makes it important to study the low-temperature conductivity of the single-crystalline material.

Here, we present the resistivity measurements of p-Cu_2ZnSnS_4 single crystals in the temperature interval between 10–300 K and the analysis of low-temperature resistivity data. The purpose of the work is to investigate the hopping conductivity of the compound and to determine the microscopic properties of the localized carriers as well as some important macroscopic parameters of p-Cu_2ZnSnS_4.

2. Experimental

Single crystals of Cu_2ZnSnS_4 were grown by chemical vapor transport using iodine as a transport agent. The grown process was done in an evacuated quartz horizontal ampoule from the stoichiometric melt of high-purity precursors Cu, Zn, Sn, and S. The evaporation temperature was kept at 850^o C, the grown temperature was 800^o C, and the concentration of iodine was 5 mg/cm^3. The energy dispersive X-ray microanalysis (EDX) was used to analyze the degree of stoichiometry of the investigated crystals. EDX measurements yield a slight excess of Sn and S, the composition ratios being Cu/(Zn + Sn) ≈ 0.98, Zn/Sn ≈ 0.86, S/metals ≈ 1.045. All crystals exhibited *p*-type conductivity. The difference in composition ratio of samples studied is about 3% corresponding to the accuracy of our EDX measurements.

Resistivity, ρ (*T*), was measured using the van der Pauw method in a range of 10–300 K. The contacts were made with a silver paste, and the results do not depend on surface treatment. It is evident from Fig. 1 that all the investigated p-Cu_2ZnSnS_4 samples exhibit an activated conductivity below $T \sim 200$ K.

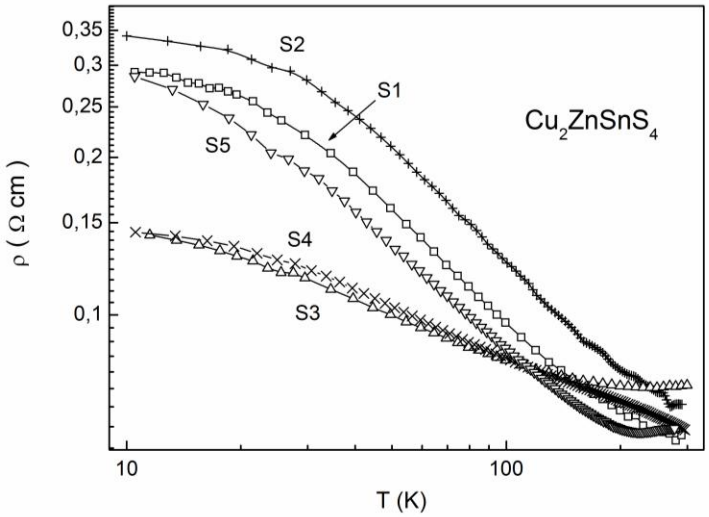

Fig. 1. Temperature dependence of the resistivity in the investigated samples S1– S5.

3. Theoretical background

A detailed analysis of the low-temperature data in Fig. 1 is performed using a universal expression for the resistivity of weakly doped crystalline semiconductors in the domain of the hopping charge transfer [20, 21]:

$$\rho(T) = A_p T^m \exp\left[\left(\frac{T_{0p}}{T}\right)^{1/p}\right]. \quad (1)$$

Here A_p is the prefactor constant, $p = 1$ refers to hopping over only the nearest-neighboring sites or the NNH conductivity, $p = 4$ describes the Mott type of the variable-range hopping (VRH) conductivity regime, $p = 2$ the Shklovskii-Efros VRH conduction mechanism, T_{0p} is the characteristic hopping temperature and $m = 1/p$ [21]. Transition from the NNH to the VRH conduction regime takes place when it becomes energetically favorable for electrons to jump beyond the nearest-neighboring sites [20, 21]. This situation is usually stimulated by lowering the temperature or increasing the microscopic disorder [20, 21]. The Mott VRH regime takes place in the case where the electron correlation effects can be neglected, resulting in a constant nonzero value, g (μ), of the density of the localized states (DOS) around the Fermi level, μ [20]. The Shklovskii-Efros VRH conduction sets in the case where the Coulomb interactions between the electrons become important and lead to a parabolic dependence of the DOS, g (ε) ~ (ε – μ)^2, within an energy interval of the Coulomb gap, (μ – Δ, μ + Δ) [21]. The higher ratio of Δ/W, where W is half width of the impurity band (for briefness, below it is referred to simply as "width of the band"), implies the increased importance of the Coulomb correlations and stimulates the onset of the Shklovskii-Efros VRH conduction at higher temperatures.

The characteristic temperature at $p = 1$ is written usually as $T_{01} = E_{act} / k$, where E_{act} is the NNH activation energy, whereas for the VRH conductivity ($p = 4$ and 2) the expressions

$$T_{04} = \frac{\beta_4}{kg(\mu)a^3} \quad \text{and} \quad T_{02} = \frac{\beta_2 e^2}{\kappa k a} \quad (2)$$

are valid, respectively. In Eq. (2) $\beta_4 = 21$ and $\beta_2 = 2.8$ are numerical constants, κ is the dielectric permittivity, and a is the localization radius of charge carriers [21], which is sensitive to proximity to the metal-insulator transition (MIT). This is given by the expression

$$a = a_0 (1 - N/N_c)^{-\nu}, \quad (3)$$

where a_0 is the localization radius far from the MIT, $\nu \approx 1$ is a critical exponent, N is the concentration of sites involved in the hopping (acceptors in the case of p-Cu_2ZnSnS_4), and N_c is the critical concentration of the MIT [22]. Parameters a_0 and N_c are interrelated with the Mott universal criterion [20]:

$$N_c^{1/3} a_0 \approx 0.25. \quad (4)$$

At this point, it is important to mention another expression describing proximity of a system to the MIT:

$$a \sim | \mu - E_c |^{-\nu}, \quad (3')$$

which is referred to as the Anderson MIT in the impurity band with coexisting localized and extended states separated by the mobility threshold, E_c [20].

The type of the hopping conductivity can be determined with Eq. (1) by linearization of ρ (T) in coordinates of ln ($\rho T^{-1/p}$) vs. $T^{-1/p}$ or analyzing the local activation energy [21]:

$$E_{loc}(T) = \frac{d[\ln \rho(T)]}{d(kT)^{-1}}. \quad (5)$$

Introducing E_{loc} (T), Eq. (1) can be presented in the following form

$$\ln[E_{loc}/(kT)+m] = \ln(1/p) + (1/p)\ln T_{0p} + (1/p)\ln(1/T)\,, \qquad (6)$$

where $m = 1/p$ [see remarks to Eq. (1)]. Namely, by putting m = 1, 1/2 or 1/4 in the left-hand side of Eq. (6), from the linear part of the plots of $\ln[E_{loc}/(kT) + m]$ vs. $\ln(1/T)$ one should obtain p = 1, 2 or 4, respectively, provided that one of the above discussed three hopping conduction regimes takes place.

4. Analysis and discussion

4.1. Identification of the conductivity mechanism

Using at first the method of linearization of ρ (T) with Eq. (1) and taking different tentative values of p = 1, 4, and 2, we find the best linearity of the plots shown in Fig. 2 implying that p = 4 and the Mott VRH conductivity is established unambiguously in all the investigated samples. The linear fit of the plots in Fig. 2 yields the values of A_4 and T_{04}, as well as those of T_v and T_m (the onset and the lowest temperature of the Mott VRH conduction interval, respectively), which are listed in Table 1.

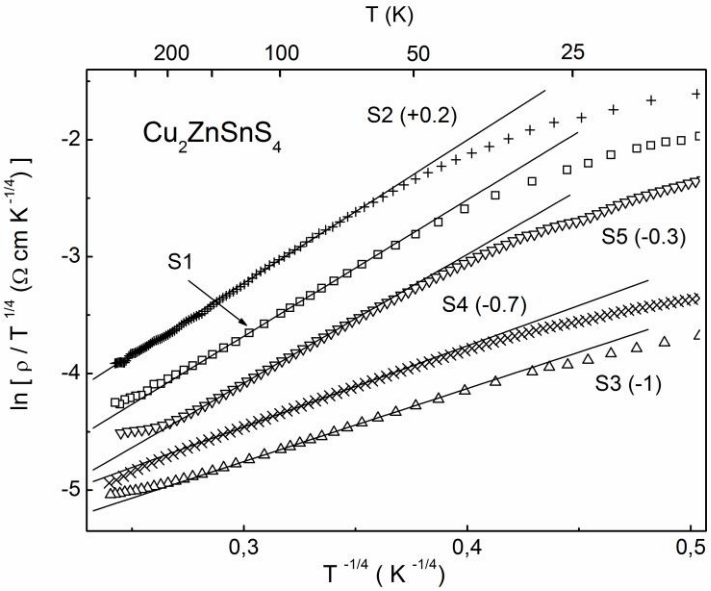

Fig. 2. Plots of ln ($\rho/T^{1/4}$) vs. $T^{-1/4}$ for the investigated samples S1– S5. For convenienc, the plots for samples S2 – S5 are shifted along the vertical axis by the values shown in parenthesis. The straight lines are linear fits.

Figure 3 shows that the Mott regime of the VRH conduction is supported by the plots of ln [$E_{loc}/(kT)$ + 1/4] vs. ln 1/T for samples S1, S4 and S5. The straight lines are drawn for p = 4 yielding the values of $T_0 \approx 19.2\times10^4$, 2.28×10^3, and 1.47×10^4 K; $T_v \approx$ 122, 133, and 145 K; and $T_m \approx$ 63, 68, and 85 K for samples S1, S4, and S5, respectively, which are very close to the respective data in Table 1. It is important to mention that the strong variation of the values of T_{04} in our samples is attributed, according to Eqs. (2) and (3), to a proximity to the MIT rather than to large variation of g (μ). In fact, if N is close to N_c, only a small scattering of N can cause an appreciable variation of a and lead to the large scattering of $T_{04} \sim a^{-3}$. On the other hand, strong

changes of g (μ) in the samples obtained with the same preparation method are unlikely.

Table 1. Prefactor constant (A_4), the onset (T_v) and lowest (T_m) temperatures of the Mott VRH conduction regime, the Mott VRH characteristic temperature (T_{04}) and the bandwidth parameter (W_0) of the investigated p-Cu_2ZnSnS_4 samples

Sample No.	A_4 (Ω cm $K^{-1/4}$)	T_v (K)	T_m (K)	T_{04} (K)	W_0 (meV)
1	7.60×10^{-4}	130	50	1.86×10^{4}	38.6
2	8.29×10^{-4}	150	55	2.24×10^{4}	45.1
3	3.59×10^{-3}	133	32	1.52×10^{3}	21.0
4	2.92×10^{-3}	132	65	2.31×10^{3}	23.2
5	8.31×10^{-4}	151	77	1.48×10^{4}	40.9

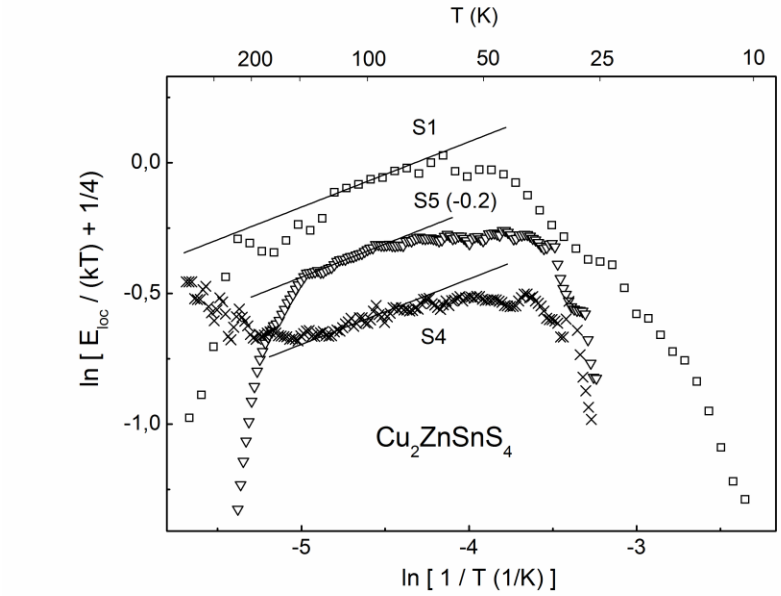

Fig. 3. Plots of ln [E_{loc} / (kT) + 1/4] vs. ln (1/T) for samples S1, S4, and S5. The plot for S4 is shifted by − 0.2 units along the vertical axis for convenience. The straight lines correspond to the constant slope of 1/p = ¼.

4.2. Model of the acceptor band

An important parameter $W_0 = k\,(T_v^3 T_{04})^{1/4}$ connected to the width of the impurity band, W, is exhibited in Table 1, as well. In fact, as shown by Mott [20], the VRH conduction takes place within an optimum energy stripe (μ – E_M, μ + E_M), where the Mott energy is given by the relation $E_M(T) = kT\,\xi_c(T)$ and the percolation threshold for the Mott VRH regime by the expression $\xi_c(T) = (T_{04}/T)^{1/4}$ [21]. Hence, at the onset VRH temperature, T_v, one finds

E_M (T_v) = k ($T_v^3 T_{04}$)$^{1/4}$ = W_0. On the other hand, a criterion of transition to the Mott VRH conduction at $T = T_v$ can be written as $<\Delta E> \approx <\Delta E_M>$, where $<\Delta E>$ is the mean difference of the electron energy during hopping and $<\Delta E_M>$ is the mean difference of the electron energy within the Mott optimum stripe. Suppose first a case of intermediate degree of the compensation, $K \sim 1/2$, when μ is lying close to the center of the impurity band. Then one finds $<\Delta E> \approx 1/2\ (2W) \approx W$, $<\Delta E_M> \approx 1/2\ (2E_M) \approx E_M$, and the criterion above leads at $T = T_v$ to the relation $W\,|_{K \sim 1/2} \approx W_0$ [21]. On the other hand, for the case of a weak compensation, $K << 1$, μ lies close to the band edge, $\mu = W - \delta$, which gives similarly: $<\Delta E> \approx W + \delta/2$, $<\Delta E_M> \approx E_M/2 + \delta/2$ and $W\,|_{K << 1} \approx W_0/2$, provided that $\delta << W_0$. Above we take into account that, for $K << 1$, almost half of the Mott optimum stripe lies outside the impurity band, which has a definite sense if the band can be characterized with clear-cut edges (e.g., this is strictly substantiated for the rectangular DOS shape).

Hence, it follows from Table 1 that the typical width of the acceptor band in our samples, expected to lie between $W \sim W_0/2$ and W_0 (depending on K), is comparable with the values of the acceptor levels, $E_1 \approx 10$ meV and $E_2 \approx 30$ meV found in Cu_2ZnSnS_4 [18] (see Introduction). This implies a high microscopic disorder in the investigated samples and a strong broadening of the acceptor levels E_1 and E_2 into the wide acceptor bands, where the band widths should be connected mainly to disorder. Under these conditions, these bands are strongly overlapped, and it is reasonable to treat them as a single band, as shown in the left panel of Fig. 4. Then the energy of the peak or center of the unified band can be found approximately as $E_0 \approx (E_1 + E_2)/2 \approx 20$ meV.

Next, the resulting broad band under conditions of proximity to the MIT should possess also a wide interval of extended states around the center and two intervals of the localized states shifted to the band edges or tails [20], as shown schematically in the right panel of Fig. 4 where the localized states are hatched. Therefore, the position of μ near the center of the band and an intermediate degree of the compensation can be excluded in our case, otherwise the activated conduction would not be observed. On the other hand, strong compensation and position of μ near the left-hand band edge in Fig. 4 are unlikely, because proximity to the MIT means a closeness of μ to the left mobility edge, $-E_c$. However, in this case, the interval ($-E_c$, E_c) of the extended states at $T = 0$ would be free of holes, which suggests that, at low temperatures, there occurs a strong domination of the conduction, connected to activation of the holes into the interval ($-E_c$, E_c) rather than hopping charge transfer [20]. This type of conductivity yields the dependence of $\rho(T)$ differing considerably from the Mott VRH conduction but resembling the NNH conduction [20], where $p = 1$, and $E_{act} = |\mu - E_c|$ in Eq. (1) would be very small, strongly stimulating this type of conductivity. Since no signs of this mechanism is observed in our case, it is reasonable to suppose that $K << 1$ and μ lies inside the right-hand interval of the localized states, as shown in the right of Fig. 4. To proceed further and obtain important numerical results, we approximate the DOS of the acceptor band with a rectangular shape shown by the dashed line in the right panel of Fig. 4. This considerably simplifies the subsequent analysis but brings an additional error discussed later. Eventually, we neglect δ and put $\mu \approx W \approx W_0/2$ in the numerical analysis below.

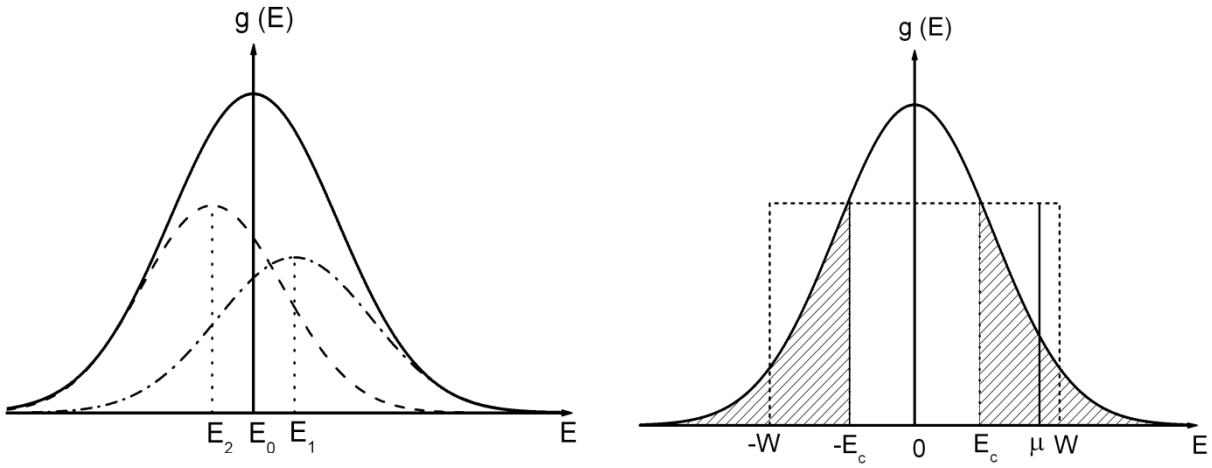

Fig. 4. Left panel: plots of g (E) for two strongly overlapped impurity bands with peaks at energies E_1 (dash-dot line) and E_2 (solid line). The solid line represents the plot of DOS vs. energy of the unified impurity band having a peak at E_0 (schematically). Right panel: image of DOS vs. energy of the unified band containing the extended states between the mobility edges – E_c and E_c and the localized states outside them, shown by the hatched area (solid line). The dashed line represents the approximation of the DOS with a rectangular shape (schematically).

4.3. Numerical analysis of the temperature parameters

Using (1), (3), and (4), putting $g(\mu) \approx N/(2W)$, where $W \approx W_0/2 \approx (1/2)k\,(T_v^{\,3}T_{04})^{1/4}$, we find the equation

$$\left(\frac{T_{04}}{T_v}\right)^{1/4} \approx 4\beta_4^{1/3}\left(\frac{N}{N_c}\right)^{1/3}\left(1-\frac{N}{N_c}\right)^{\nu}, \qquad (7)$$

which yields, at $\nu \approx 1$ and with the data of T_{04} and T_v in Table 1, the values of the N/N_c ratio and those of a/a_0 listed in Table 2. The values of $N/N_c \sim 0.72$–0.84 and a/a_0, which were found with N/N_c and Eq. (3) at $\nu \approx 1$ and lying appreciably above unity (Table 2), are consistent with proximity of the acceptor system in the investigated samples to the MIT, as has been supposed above.

Table 2. Localization radius in units of that far from the MIT (a/a_0) and in units of the Bohr radius (a/a_B), the relative acceptor concentration (N/N_c), the width of the acceptor band (W), the mobility threshold (E_c) and the DOS (g (μ)) in the investigated p-Cu_2ZnSnS_4 samples

Sample No.	a/a_0	a/a_B	N/N_c	W (meV)	E_c (meV)	$g(\mu)$ (10^{16} mev^{-1}cm^{-3})
1	3.6	3.9	0.72	19.3	15.4	4.1
2	3.5	3.2	0.72	22.5	17.2	3.5
3	6.4	8.9	0.84	10.5	9.5	8.8
4	5.8	7.8	0.83	11.6	10.3	7.9
5	3.9	3.7	0.74	20.4	16.1	4.0

The value of $a_0 \approx \hbar/(2mE_0)^{1/2}$ [21] can be calculated approximately by putting $E_0 \approx 20$ meV (see *Section 4.2*) and treating m as a mean effective mass of the holes, $m \approx \left(m_\perp^2 m_\parallel\right)^{1/3}$ [21]. Using the data of $m_\perp$ and $m_\parallel$ in Cu_2ZnSnS_4 [13] (see Introduction), we find $m = 0.47 \pm 0.02$; that is, for both modifications of Cu_2ZnSnS_4, m is varied insignificantly, which yields $a_0 \approx 20$ Å.

On the other hand, the relation $a_0 \approx a_B$ is fulfilled for shallow hydrogen-like impurity levels [20, 21], where

$$a_B = \hbar^2\kappa_0/(me^2) \tag{8}$$

is the Bohr radius and κ_0 is the static dielectric permittivity far from the MIT. Therefore, the $a/a_B \approx a/a_0$ ratio can be calculated independently with Eq. (3'), written in the form

$$a/a_B \approx (\mu/E_c - 1)^{-\nu}, \tag{9}$$

putting $\nu \approx 1$, $\mu \approx W \approx W_0/2$ (*see Section 4.2*) and using the expression [20]

$$E_c \approx W - \frac{V_0^2}{4(z-1)J}. \tag{10}$$

In Eq. (10) $z \approx 6$ is the number of nearest neighbors in the acceptor system, V_0 represents a scale of scattering of the hole energy due to the microscopic disorder [20], and $J = J_0 \exp(-R/a_B)$ is the overlap integral. Here $R \approx (4\pi N/3)^{-1/3}$ is half of the mean distance between the acceptors, and the prefactor J_0 can be written as

$$J_0 \approx \frac{e^2}{\kappa_0 a_B}\left[\frac{3}{2}\left(1+\frac{R}{a_B}\right)+\frac{1}{6}\left(\frac{R}{a_B}\right)^2\right], \tag{11}$$

similar to [20] but differing by the introduction of κ_0 in the denominator of Eq. (11). This modification of the original expression of Eq. (11) is important, because a system of disordered sites in vacuum was considered in [20], whereas a corresponding system of impurity sites in semiconductors exists in media of the host lattice [21]. Eventually, taking into account the presumed main reason for broadening of the acceptor states into the acceptor bands connected to the lattice disorder (see *Section 4.2*), one can put $V_0 \approx 2W \approx W_0$ [20]. Hence, we can evaluate the ratio of a/a_B with Eqs. (8–11) using a single adjustable parameter, κ_0, to fit a/a_B to the data of a/a_0 in Table 2 by minimizing the standard deviation.

However, an important detail should be discussed preliminary. It follows from Tables 1 and 2 that the values of W in samples S3 and S4 are ~2 times lower than in S1, S2, and S5, whereas $2W \approx W_0$ is close to the difference of $E_2 - E_1 \approx 20$ meV. This means that the overlap of the bands generated by broadening of the levels E_2 and E_1 is appreciably smaller in S3 and S4, which worsens the applicability of our model of a single acceptor band to these samples and makes the fitting procedure less accurate in the case where the data of these samples are involved.

Therefore, at first, we fit the values of a/a_0 with a/a_B only for samples S1, S2, and S5, yielding $\kappa_0 \approx 17$, $a_B \approx 19$ Å, $E_B \approx 22$ meV, and $E_H \approx 27$ meV, where $E_B = \hbar^2/(2ma_B^2)$ and $E_H \approx 5e^2/(8\kappa_0 a_B)$ are the Bohr energy and the Hubbard on-site correlation energy of the shallow hydrogen-like impurity, respectively [20, 21]. The values of a/a_B calculated with Eq. (9) are displayed in Table 2 as well as those of E_c evaluated with Eq. (10). We can see a reasonable agreement between a/a_0 and a/a_B in S1, S2, and S5, which is worsening for S3 and S4 as can be expected from the preliminary discussion above. Next, N_c can be found with the Mott criterion, $N_c^{1/3}a_B \approx 0.25$, which gives $N_c \approx 2.2\times10^{18}$ cm^{-3}. Eventually, the data of N/N_c from Table 2 yield those of N and the values of W from Table 2 permits the evaluation of $g(\mu) \approx N/(2W)$, which is shown in Table 2.

In the case where all the data of a/a_0 in Table 2 are involved in the fitting with a/a_B, we find $\kappa_0 \approx 19$, $a_B \approx 22$ Å, $E_B \approx 18$ meV and $E_H \approx 22$ meV. The parameters a/a_B, E_c, N_c and g (μ) are comparable with the corresponding previous data. On the other hand, now E_B, representing the centre of the acceptor band, is found to be systematically smaller than W in samples S1, S2, and S5 (Table 5), which however are expected to follow better the model formulated in *Section 4.2*. This issue is in line with the preliminary discussion above. Therefore, the numerical values of the parameters obtained by fitting of a/a_0 only for S1, S2, and S5 look preferable.

4.4. Discussion

First of all, we should mention the proximity of $E_0 \approx 20$ meV guessed in *Section 4.2* and $a_0 \approx 20$ Å connected to E_0 (see *Section 4.3*) with those of $E_B \approx 22$ meV and $a_B \approx 19$ Å, respectively, evaluated within a more strict procedure above. Next, we pay attention to the similarity of $E_H \approx 27$ meV and the difference of $E_2 - E_1 \approx 20$ meV. The latter points out a possible nature of the two acceptor bands centered at E_1 and E_2 in Cu_2ZnSnS_4 as Hubbard-like bands. These bands appear via spin-splitting of the acceptor level due to the Hubbard correlation or repulsion of two holes with opposite spins localized on the same level [20]. However, broadening of these bands should be attributed mainly to the microscopic disorder rather than to an overlap of acceptor states. This can also be substantiated in another way. In fact, using the expressions of E_B and E_H at the end of *Section 4.3*, taking into account the relations $E_1 = E_B - E_H/2$ and $E_2 = E_B + E_H/2$, we find that $E_1 \approx E_B (1 - 5/8) \approx 8$ meV and $E_2 \approx E_B (1 + 5/8) \approx 35$ meV, where only the results of the present work (i.e., the above value of E_B) were used. Hence, it is evident that our values of E_1 and E_2 almost coincide with $E_1 = 10 \pm 5$ meV and $E_2 = 30 \pm 5$ meV found in [18], which makes it quite probable to regard the two acceptor bands in Cu_2ZnSnS_4 as Hubbard-like bands. At this point, the relation $E_0 \approx (E_1 + E_2)/2$ utilized in *Section 4.2* acquires a more strict meaning.

Concerning the applicability of the rectangular approximation of the DOS (right panel in Fig. 4) in general, it is supported by broadness of the acceptor band but is worsened by the position of μ close to the band edge. In fact, it is evident from the right panel of Fig. 4 that $g(\mu)$ can be appreciably smaller for a more realistic DOS (shown schematically with the solid line) than for the rectangular DOS (dashed line). At this point, the values of $g(\mu)$ found here should be regarded rather as some typical or mean values characterizing the acceptor band of strongly disordered Cu_2ZnSnS_4. Similar inference looks reasonable with respect to the values of N/N_c and a/a_0, which are interrelated. However, their uncertainty should be evidently smaller than that of $g(\mu)$ above, because Eq. (2), which is important for the analysis, yields $T_{04} \sim [g\ (\mu)]^{-1}$ but $T_{04} \sim a^{-3}$. This considerably reduces the error of a caused by the rectangular approximation of the DOS as well as the error of the other parameters obtained by fitting of a/a_0 with a/a_B. At this point, the validity of E_B and a_B being close to E_0 and a_0, respectively, has been already estimated above. The obtained value of κ_0 requires an independent substantiation, which is better to perform through optical measurements. Here we can only mention that κ_0 looks reasonable obeying the expected relation of $\kappa_0 > \kappa_\infty$ (see Introduction).

Finally, we discuss deviations of $\rho(T)$ from the Mott behavior visible in Fig. 2 and especially in Fig. 3. The high-temperature deviation is attributable to the NNH conductivity or to the band conduction connected to the thermal excitation of the holes into the valence band. Due to the relatively large value of E_B or E_0 the first out of these reasons looks preferable, although the final conclusion at this point requires further substantiation. On the other hand, it is well

known that, in many doped semiconductors, the violation of the Mott VRH conduction regime with lowering T is attributed to the onset of the Shklovskii-Efros VRH conductivity [22–24]. However, this should lead to the formation of the second slope, with $p = 1/2$, of the plots in Fig. 3, which is not observed down to at least ~25 K in S4 and S5 and down to 10 K in S1. At this point, it is possible to estimate the onset temperature of the Shklovskii-Efros behavior of $\rho(T)$ as follows. The value of the Coulomb gap can be obtained through the expression $\Delta \approx e^2/(\kappa R_A)$ [21], where $\kappa \approx \kappa_0 \ (a/a_0)^2$ [22] and $R_A = 2R$ is the mean distance between the acceptors, yielding $\Delta \approx 0.2 - 0.6$ meV. Hence, the low value of the Δ/W ratio shifts the onset of the Shklovskii-Efros VRH conduction regime to low temperature T_{v2}, which can be obtained with the expression $\Delta \approx 0.5\, k\, (T_{v2}\, T_{02})^{1/2}$ [21], where T_{02} can be evaluated with the second of Eqs. (2). Eventually, we find $T_{v2} \approx 4–7$ K lying below the lowest temperature of 10 K used in this work. This suggests a broad intermediate interval, where both VRH conduction mechanisms make a comparable contribution to $\rho(T)$, which therefore cannot be characterized by Eq. (1) with any definite value of p.

5. Conclusions

We have studied the low-temperature conductivity of p-Cu_2ZnSnS_4 single crystals. The Mott variable-range hopping conduction is established within a broad temperature interval. Analysis of the resistivity data under conditions of the proximity to the Anderson metal-insulator transition and presumed low degree of compensation has yielded typical values of width of the acceptor band, the acceptor concentration, and the density of the localized states in the acceptor band as well as the localization and the Bohr radii of the holes and the dielectric permittivity far from the MIT. The results give evidence for a high degree of microscopic disorder in the studied p-Cu_2ZnSnS_4 samples.

Acknowledgments

Financial supports from STCU # *5402* and from IRSES PVICOKEST – 269167 projects are acknowledged.

References

[1] J.J. Scragg, P.J. Dale, L.M. Peter, G. Zoppi, and I. Forbes, Phys. Stat. Sol. b 245, 1772 (2008).
[2] I. Repins, M.A. Contreras, B. Egaas., C. DeHart, J. Scharf, C.L. Perkins, B. To, and R. Noufi, Prog. Photovolt. Res. Appl. 16, 235 (2008).
[3] T.K. Todorov, K.B. Reuter, and D.B. Mitzi, Adv. Mater. 22, 1 (2010).
[4] H. Kataghiri, N. Ishigaki, T. Ishida, and K. Saito, Jpn. J. Apl. Phys. 40, 500 (2001).
[5] Y. Kumar, G. Babu, P. Bhaskar, and V. Raja, Sol. Energ. Mat. Sol. C. 93, 1230 (2009).
[6] Y.B. Kumar, P. Bhaskar, G. Babu, and V. Raja, Phys. Stat. Sol. a 207, 149 (2010).
[7] J. Seol, S. Lee, J. Lee, H. Nam, and K. Kim, Sol. Energ. Mat. Sol. C. 75, 155 (2003).
[8] M.-L. Liu, Fu-Q. Huang, Li-D. Chen, and I-W. Chen, Appl. Phys. Lett 94, 202103 (2009).
[9] I. Tsuji, Y. Shimodaira, H. Kato, H. Kobayashi, and A. Kudo, Chem. Mater. 22, 1402 (2010).
[10] S. Ikeda, T. Nakamura, T. Harada, and M. Matsumura, Phys. Chem. Chem. Phys. 12, 13943 (2010).
[11] D. Yokoyama, T. Minegishi, K. Jimbo, T. Hisatomi, G. Ma, M. Katayama, J. Kubota, H.

Katagiri, and K. Domen, Appl. Phys. Express 3, 101202 (2010).
[12] S. Schorr, H.-J. Hoebler, and M. Tovar, Eur. J. Mineral. 19, 65 (2007).
[13] C. Persson, J. Appl. Phys. 107, 053710 (2010).
[14] S. Schorr, Thin Solid Films 515, 5985 (2007).
[15] S. Chen, X.G. Gong, A. Walsh, and Su-H. Wei, Applied Physics Letters 96, 021902 (2010).
[16] A. Nagoya, R. Asahi, R. Wahl, and G. Kresse, Phys. Rev. B 81, 113202 (2010).
[17] K. Tanaka, Y. Miyamoto, H. Uchiki, K. Nakazawa, and H. Araki, Phys. Stat. Sol. a 203, 2891 (2006).
[18] Hönes K., Zscherpel E., Scragg J., and Siebentritt S., Physica B: Condens. Matter 404, 4949 (2009)
[19] J.P. Leitao, N.M. Santos, P.A. Fernandes, P.M. Salome, A.F. P da Cunha, J.C. Gonzalez, G.M. Ribeiro, and F.M. Matinaga, Phys. Rev. B 84, 024120 (2011).
[20] N. Mott and E.A.Davies, Electron Processes in Non-Crystalline Materials, Clarendon, Oxford, 1979; Mott N. F., Metal–Insulator Transitions, Taylor and Francis, London, 1990.
[21] B.I. Shklovskii, and A.L. Efros, Electronic Properties of Doped Semiconductors, Springer, Berlin, 1984.
[22] T.G. Castner, Hopping Transport in Solids, Ed. M. Pollak and B. Shklovskii, North-Holland, Amsterdam, p 3, 1991.
[23] E. Arushanov, K.G. Lisunov, H. Vinzelberg, G. Behr, J. Schumann, and O. Schmidt, J. Appl. Phys. 104, 053720 (2008).
[24] K.G. Lisunov, H. Vinzelberg, E. Arushanov, and J. Schumann, Semicond. Sci. Technol. 26, 095001 (2011).

CHARACTERISTIC MODELING OF A DIODE DETECTOR BASED ON A SEMICONDUCTOR (Bi-Sb)/SUPERCONDUCTOR (NbN) HETEROJUNCTION WITH SURFACE STATES

Ia. Kerner

Institute of Electronic Engineering and Nanotechnologies "D. Gitsu"
Academy of Sciences of Moldova
Academiei str. 3/3, Chisinau, MD-2028 Republic of Moldova
e-mail: iacov@nano.asm.md

(Received 15 February 2012)

Abstract

Diode detectors (DDs) are widely used in electronic information and communication systems. In this study, a numerical modeling of the electric potential distribution and current passing in contacts of niobium nitride (NbN) with a bismuth-antimony (Bi-Sb) semiconductor alloy was performed.

Earlier, we have studied the case in which the surface states were in thermodynamic equilibrium with a semiconductor. In this article, an opposite situation is studied, when the surface states are in thermodynamic equilibrium with a superconductor. The possibility to design diode detectors based on these contacts that operate at temperatures (T) of liquid helium 4.2 K and 1 K is explored. The dependences of current responsivity (CR), voltage responsivity (VR), and noise equivalent power (NEP) on signal frequency (f) are analyzed. The obtained results are compared with literature data. DDs operating at the temperature of liquid nitrogen (T = 77.4 K) and liquid helium are considered.

A comparison with the available literature data shows that the proposed DDs can be 10÷100 times better. The physical reasons of these advantages are discussed. It is shown that unique properties of Bi-Sb alloys and especially of $Bi_{0.88}Sb_{0.12}$ alloy make these alloys very promising materials for cryoelectronics.

1. Introduction

Diode detectors (DDs) play an important role in radio technique and electronics. The use of high frequencies (above 1 GHz) stimulated a careful study of Schottky barrier diodes. These diodes involve quick-acting metal-semiconductor contacts [1].

A further improvement in their parameters was achieved due to a decrease in the working temperature. This direction was named cryoelectronics [2]; it gives the possibility to increase the nonlinearity of current-voltage dependences and current responsivity. Thermal noise power decreases too. For example, DDs based on Pb-pGaAs contacts were prepared [3, 4]. At a signal frequency of f = 9 GHz and T= 4.2 K, these diodes had CR ≈ 500 A/W and noise equivalent power 5×10^{-15} W/$\sqrt{Hz}$. At the same frequency and T = 1 K, there parameters were: CR ≈ 2500 A/W and noise equivalent power 5.4×10^{-16} W/$\sqrt{Hz}$. In addition, deep cooling allows using the materials with a small energy gap width but with a high mobility of electrons, such as solid solutions Bi-Sb [2, 5].

After the discovery of high temperature superconductors (HTSCs), the possibilities to use

HTSCs in cryoelectronics were studied too. At the liquid nitrogen temperature T = 77 K and signal frequency f = 37.5 GHz, the respective structures exhibited a voltage responsivity of 3000 V/W [6]. Further studies [7] made it possible to design structures with VR = 5000 V/W and noise equivalent power NEP = 2×10^{-12} W/$\sqrt{Hz}$ at a signal frequency of f = 31 GHz and a temperature of T = 77 K. According to our publication [8], the DDs based on HTSC-InSb contacts can have CR ≈ 40 A/W, VR ≈ 10^6 V/W and NEP ≈ 8×10^{-15} W/$\sqrt{Hz}$ at T = 77.4 K and f = 10 GHz. At the same temperature and f = 30 GHz, these DDs can exhibit CR ≈ 15 A/W, VR ≈ 3.5×10^5 V/W and NEP ≈ 2×10^{-14} W/$\sqrt{Hz}$.

On the other hand, an oxidation of the semiconductor in HTSC-semiconductor contacts often occurs, because oxygen is an integral part of a HTSC. In addition, cooling to the liquid nitrogen temperature 77.4 K may be insufficient to obtain good parameters of DDs. In this situation, taking into account the rapid development of cryogenics, the study of DDs based on conventional superconductor–semiconductor contacts seems to be a relevant problem. Usually, these DDs operate at liquid helium temperatures (T ≤ 4.2 K). In this study, a numerical modeling of electrical potential distribution and current passing in contacts of niobium nitride with a bismuth-antimony semiconductor alloy was performed for the case in which the surface states are in thermodynamic equilibrium with a superconductor.

2. Results and discussion

Contacts of semiconductor solid solution $Bi_{0.88}Sb_{0.12}$ with NbN were considered, because, according to our results [9], these contacts seem to have the best parameters. Round flat contacts with a contact area (S) of 10 μ^2 and 1 μ^2 were studied. Earlier, we have studied the case in which the surface states were in thermodynamic equilibrium with a semiconductor [9, 10]. In this article, an opposite situation is studied, when the surface states are in thermodynamic equilibrium with a superconductor (according to [1, 2, 11], this situation can also take place). Material properties were taken from [12, 13]. Results of calculations are shown in Figs. 1-3. In all figures, a logarithmic scale for X-axes is used. An exponential form is often used for numbers of axes.

Figs. 1-3 show that current and voltage responsivities decrease and NEP increases at the frequencies more 10 GHz. At these frequencies, the negative role of barrier capacity is revealed, and it begins to shunt the nonlinear contact resistance. On the other hand, at high frequencies, the contact capacity resistance becomes comparable with ohm spreading resistance. The current redistribution occurs; it leads to a reduction in the rectified current, and DD parameters become worse.

According to Figs. 1-3, the reduction of the contact area can sufficiently improve these parameters (compare curves 1 and 2, 3 and 4 in these figures). Taking into account the small surface area, these contacts may be regarded as point contacts [1]. In this case, the barrier capacity is proportional to S, and ohm spreading resistance is proportional to $S^{-1/2}$ [1]. In this situation, when the contact area decreases, the capacity resistance increases faster than the ohm spreading resistance. Therefore, the redistribution of applied variable voltage occurs, the contact voltage increases, and DD parameters become good. With a decrease in the contact area, the contact differential resistance and voltage responsivity increase. On the other hand, noise current and noise equivalent power decrease (see Figs. 2, 3).

In addition, a decrease in the working temperature from 4.2 K to 1 K can sufficiently improve these parameters. On the one hand, nonlinearity of the current–voltage characteristics sufficiently increases, which leads to an increase in the current responsivity, voltage

responsivity, and noise equivalent power [1-3]. On the other hand, noise current decreases, and this effect provides with an additional reduction in noise equivalent power [1-4].

A comparison with our data [10] shows that, in the case in which the surface states are in thermodynamic equilibrium with a superconductor, DDs based on Bi-Sb can have very good parameters.

For comparison, our results [14] for HTSC-semiconductor contacts are presented in Figs. 4 and 5.

Taking into account results [3, 4, 6-8], we can conclude that contacts with Bi-Sb give the possibility to considerably improve DD parameters. They are much more effective than HTSC-superconductor contacts [6-8, 14]. In addition, they are better than contacts with GaAs [3, 4] operating at liquid helium temperature.

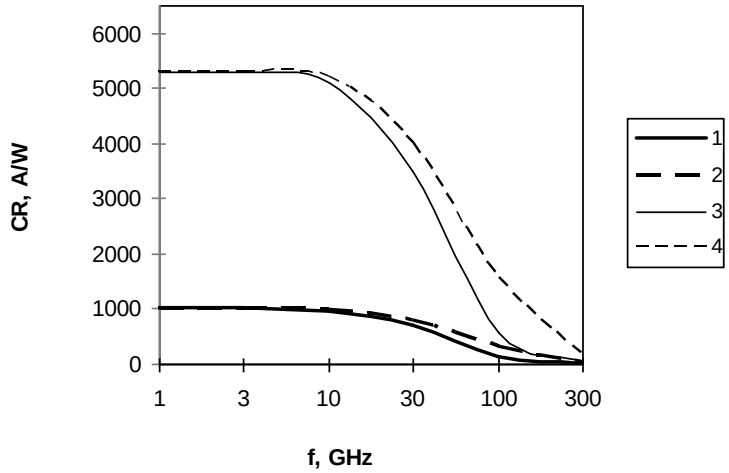

Fig. 1. Calculated current responsivity dependence on signal frequency in the contacts with $Bi_{0.88}Sb_{0.12}$. The legend inscriptions correspond to the following data:
(1) T = 4.2 K, S = 10 μ^2, (**2**) T = 4.2 K, S = 1 μ^2, (**3**) – T = 1 K, S = 10 μ^2, and (**4**) T = 1 K, S = 1 μ^2

The main advantages of Bi-Sb are as follows:

(i) Small barrier heights due to a narrow energy gap. This fact provides a high CVD nonlinearity and a high current responsivity.

(ii) High mobility of electrons, which reduces ohm resistance and improves frequency properties.

(iii) Low barrier capacity, due to small barriers heights and small effective masses of electrons, which also improves frequency properties.

These unique properties of Bi-Sb alloys and especially of $Bi_{0.88}Sb_{0.12}$ alloy make these alloys very promising materials for cryoelectronics.

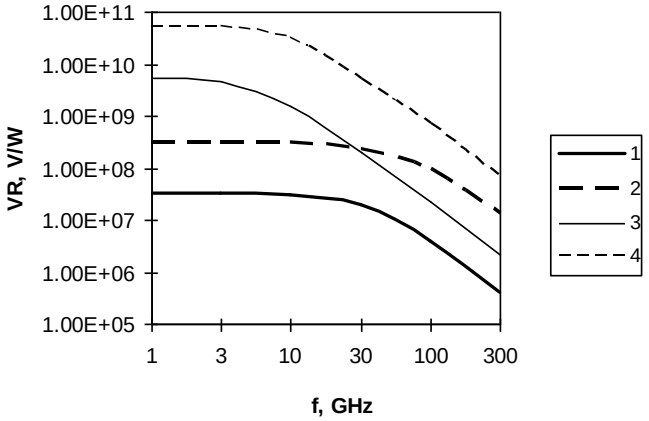

Fig. 2. Calculated voltage responsivity dependence on signal frequency. The legend inscriptions and other data are similar to those in Fig. 1.

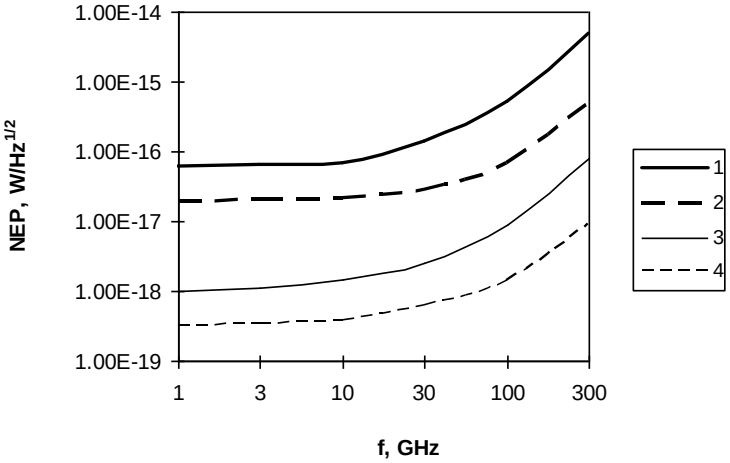

Fig. 3. Calculated noise equivalent power dependence on signal frequency. The legend inscriptions and other data are similar to those in Fig. 1.

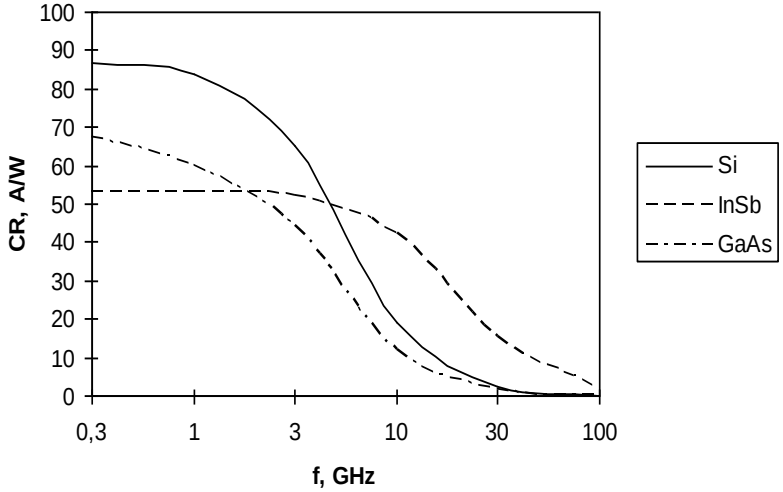

Fig. 4. Calculated current responsivity dependence on signal frequency for HTSC-semiconductor contacts (the semiconductor substance is shown in legend inscriptions). T = 77.4 K.

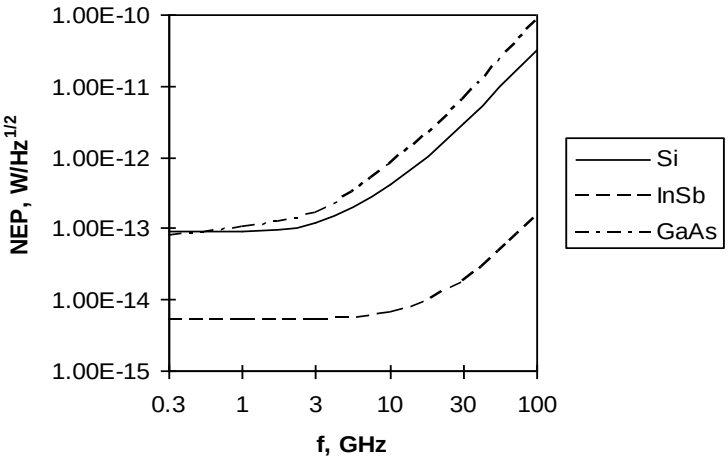

Fig. 5. Calculated noise equivalent power dependence on signal frequency for HTSC-semiconductor contacts. The legend inscriptions and other data are similar to those in Fig. 4. T = 77.4 K.

3. Conclusion

A comparison with the data of [3, 4, 9, 10] shows that, in the case in which the surface states are in thermodynamic equilibrium with a superconductor, the proposed DDs can have the current responsivity 2 times higher and noise equivalent power 50 times less than the ones in existing DDs (at the same temperature and signal frequency). In addition, they can exhibit very high voltage responsivity.

Contact area reduction can sufficiently improve the frequency properties, noise equivalent power, and especially voltage responsivity.

This fact suggests that contacts with Bi-Sb are promising.

References

[1] V.I. Striha, E.V. Buzaneva, and I.A. Radzievsky, Semiconductor devices with Schottky barrier. Physics, technology, application [in Russian], Sov. Radio, Moscow, 1974, 248 p.
[2] V.N. Alfeev, Superconductors, semiconductors and paraelectrics in cryoelectronics [in Russian], Sov. Radio, Moscow, 1979, 408 p.
[3] M. Mc Call, M.F. Millea, and A.H. Silver, Applied Physics Letters, 23, 5, 263 (1973)
[4] M. Mc Call, M.F. Millea, A.H. Silver, et al., IEEE Transactions on Magnetics, 13, 1, 221 (1977).
[5] V.G. Alekseeva, T.M. Lifshits, E.G. Chirkova, and A.Ia. Shul'man, Radio technique and Electronics [in Russian], 23, 9, 1926 (1978).
[6] V.A. Kulikov, L.V. Matveets, A.Iu. Serebryakov, et al., Pis'ma v JTF [Letters in Journal of Technical Physics – in Russian], 15, 20, 74 (1989).
[7] L.S. Kuz'min, V. N. Okhrimenko, E. S. Soldatov, and A. N. Tavkhelidze, Sverhprovodimost` [Superconductivity– in Russian], 3, 11, 2650 (1990).
[8] Ia.I. Kerner, Moldavian Journal of the Physical Sciences, 5, 3-4, 360 (2006).

[9] Ia.I. Kerner, in: 2nd Int. Conf. "Telecommunications, Electronics and Informatics". Chisinau, Moldova, May 15-18, 2008. Proceedings, UTM, Chisinau, 2, 59 (2008).
[10] Ia. I. Kerner, in: Proceedings of the 7th International Conference on "Microelectronics and Computer Science", September 22-24, 2011, Chisinau, Moldova, U.T.M., Chisinau, 37 (2011).
[11] E. H. Rhoderick, Metal–Semiconductor Contacts, Clarendon Press, Oxford, 1978, 208 p.
[12] D.V. Gitsu, I.M. Holban, V.G. Kantser, and F.M. Munteanu, Transport phenomena in bismuth and its alloys [in Russian], Shtiintsa, Kishinev, 1983, 266 p.
[13] Tables of the physical values. Reference book [in Russian]. Ed. by acad. I.K. Kikoin, Atomizdat, Moscow, 1976, 1006 p.
[14] Ia.I. Kerner, in: Proceeding of the 3rd Int. Conf. "Telecommunications, Electronics and Informatics", Chisinau, Moldova, May 20-23, 2010, UTM, Chisinau, 1, 268 (2010).

OPTICAL PROPERTIES OF SOME $[(As_2S_3)_{0.5}:(As_2Se_3)_{0.5}]_{1-x}:Sn_x$ CHALCOGENIDE GLASSES

O. V. Iaseniuc

Institute of Applied Physics, Academy of Sciences of Moldova,
Academiei str. 5, Chisinau, MD-2028 Republic of Moldova
e-mail: oxygena08@rambler.ru

(Received 27 February 2012)

Abstract

The transmission spectra of bulk and thin films of $[(As_2S_3)_{0.5}:(As_2Se_3)_{0.5}]_{1-x}:Sn_x$ in the visible and near infrared (IR) regions were investigated. The doping of $As_2(S, Se)_3$ chalcogenide glass with tin impurities essentially reduces the absorption bands of S-H (Se-H) and H_2O located at $\nu = 5190$ cm^{-1} and $\nu = 3617$ cm^{-1}, respectively. The amorphous $[(As_2S_3)_{0.5}:(As_2Se_3)_{0.5}]_{1-x}:Sn_x$ thin films exhibit photoinduced effects under the light irradiation with photon energy above the optical band gap ($h\nu \geq Eg$), which makes them promising materials for registration of optical and holographic information. The modification of optical parameters (optical band gap Eg, absorption coefficient α, refractive index n) under light irradiation and heat treatment of amorphous thin films with different amounts of Sn was studied. The relaxation of photodarkening effect in amorphous $[(As_2S_3)_{0.5}:(As_2Se_3)_{0.5}]_{1-x}:Sn_x$ thin films, which is described by the stretch exponential function $T(t)/T(0) = A_0+Aexp[-(t-t_0)/\tau]^{(1-\alpha)}$, was also investigated.

1. Introduction

Chalcogenide glasses of the As-S-Se system exhibit photostructural transformations, and are promising materials for registration media, for fabrication of diffractive elements, and other optoelectronic applications [1-3]. It is well known that the optical properties (absorption coefficient α, refractive index n, optical band gap Eg) depend on the glass composition. In the last years, a special attention has been devoted to the influence on the photostructural transformation in amorphous thin films doped with metal impurity [4-6]. It was shown that the Sn impurity introduced in the As_2Se_3, AsSe, and Sb_2S_3 glass network reduces the photodarkening effect [4, 5, 7]. According to Mössbauer spectroscopy of ^{119}Sn in the As_2Se_3:Sn glassy system, new tetrahedral $Sn(Se_{1/2})_4$ and quasi-octahedral SnSe structural units, which influence the photostructural transformations, can be formed [5]. The advantages of application of amorphous (As_2S_3):(As_2Se_3) and (As_2S_3):(As_2Se_3):Sn as gas sensors and for registration of optical information were shown in [8-10]. Some optical properties of $(As_2S_{1.5}Se_{1.5})_{0.99}:Sn_{0.01}$ were reported in [11]. In the present paper, we report the optical transmission spectra and the modification of optical parameters (optical band gap Eg, absorption coefficient α, refractive index n) under light irradiation and heat treatment of amorphous $[(As_2S_3)_{0.5}:(As_2Se_3)_{0.5}]_{1-x}:Sn_x$ thin films with different amounts of Sn. The relaxation of photodarkening effect under light exposure was also investigated.

2. Experimental

The bulk chalcogenide glasses $[(As_2S_3)_{0.5}:(As_2Se_3)_{0.5}]_{1-x}:Sn_x$ ($0 \le x \le 0.1$) were prepared from the elements of 6N (As, Se, Sn) purity by a conventional melt quenching method. The thin-film samples with a thickness of d = 0.5÷3 μm were prepared by flash thermal vacuum evaporation of the synthesized initial glasses onto glass substrates held at T_{subs} = 100°C. For optical transmission spectra measurements, a UV/VIS (λ = 300÷800 nm), the 61 NIR (λ = 800÷3500 nm) Specord's CARLZEISS Jena production and Spectrum 100 FTIR Spectrometer (PerkinElmer) (λ = 1280÷25000 nm) were used. For calculation of the optical constants from the transmission spectra, we used the method proposed by Swanepoel and Tauc [12, 13] and the computer program PARAV-V1.0 (www.chalcogenide.eu.org) [14]. To initiate photostructural transformations in thin-film samples, continuous He-Ne lasers (λ = 633 nm, P = 0.6 mW and λ = 540 nm, P = 0.75 mW) were used as a source of light exposure.

3. Results and discussion

The mid-IR transmission spectra of As_2S_3 and some $[(As_2S_3)_{0.5}:(As_2Se_3)_{0.5}]_{1-x}:Sn_x$ bulk glasses are shown in Fig.1 and, as in the case of vitreous As_3S_3 doped with metals [15], are characterized by several well-resolved absorption bands. For vitreous As_2S_3, these bands are located at frequencies of ν = 5190 cm^{-1} (S-H), ν = 3617-3522 cm^{-1} (H_2O), ν = 2482 cm^{-1} (S-H), ν = 1857 cm^{-1} (As-H), ν = 1597 cm^{-1} (H_2O), and ν = 1003 cm^{-1} (As_2O_3), and are summarized in Table 1. The characteristic absorption bands for pure As_2S_3 at ν = 5190, 3617, 3522, 1857, and 1597 cm^{-1} are significantly reduced upon doping with Sn. At the same time, for the $[(As_2S_3)_{0.5}:(As_2Se_3)_{0.5}]_{0.98}:Sn_{0.02}$ glass, additional absorption bands appear at ν = 5190 cm^{-1} 3194, 2026, and 1493 1500 cm^{-1}. The observed changes upon doping in the mid infrared region are most likely related to interactions of a portion of the introduced metal ion impurities with the inherent impurities of the host glass, such as hydrogen and oxygen atoms. These interactions result in the reduction of the relative intensity of bands associated with O-H, S-H, As-O, and As-H bonds in the parent glass.

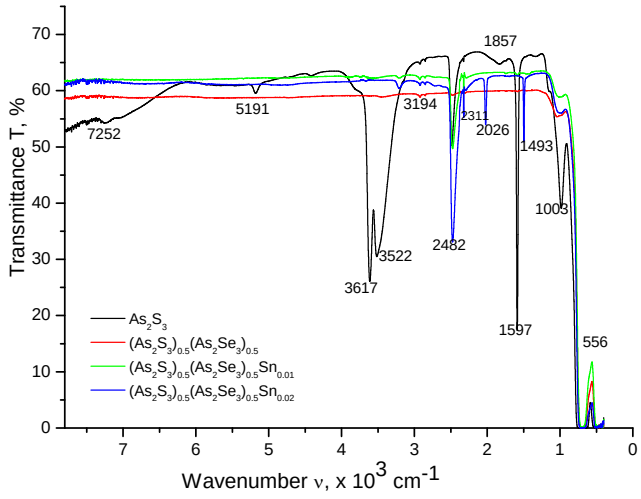

Fig.1. Transmission spectra of bulk samples of $[(As_2S_3)_{0.5}:(As_2Se_3)_{0.5}]_{1-x}:Sn_x$ glasses.

Fig. 2 shows the typical transmission spectra for some compositions of amorphous glass $[(As_2S_3)_{0.5}:(As_2Se_3)_{0.5}]_{1-x}:Sn_x$ thin films. From the transmission spectra T = f(λ), using the expressions:

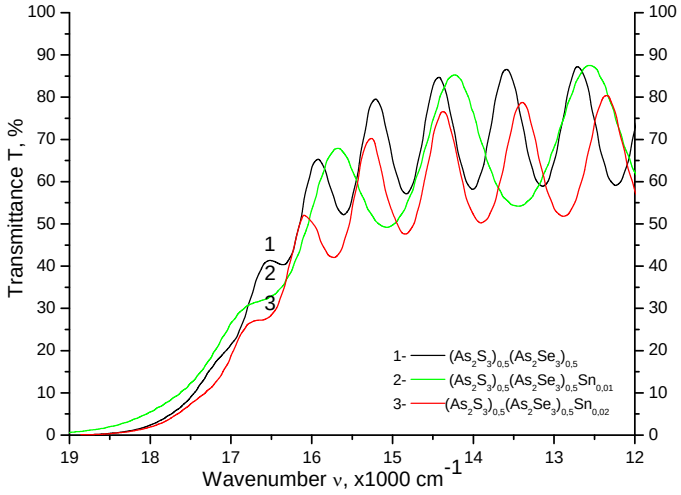

Fig.2. Transmission spectra of some amorphous $[(As_2S_3)_{0.5}:(As_2Se_3)_{0.5}]_{1-x}:Sn_x$ thin films.

$\alpha = \frac{1}{d}\ln\frac{(1-R)^2}{T}, n = \left[M + (M^2 - n_s^2)^{1/2}\right]^{1/2}$, where $M = \frac{2n_s}{T_m} - \frac{n_s^2+1}{2}$ and the dependence $(\alpha h\nu)^{1/2} = A(h\nu - Eg)$, we calculated the absorption coefficient α, the refractive index n, and the value of the optical band gap *Eg*, respectively. Here *d* is the thickness of the sample (measured with a Linnik interferometer), *R* is the reflection, n_s is the refractive index of glass substrate, T_m is the experimental values of transmission minimum points of particular fringes of transmission spectra, and *A* is a constant.

In chalcogenide glasses, the absorption edge is broader than in crystalline analogues, and this is caused by a broad energy distribution of electronic states in the band gap due to disorder and defects. The absorption edge in the high absorption region ($\alpha > 10^4$ cm^{-1}) is described by the quadratic function

$$\alpha \propto \frac{1}{h\nu}(h\nu - E_g)^2 , \quad (1)$$

and when plotted in the Tauc co-ordinates (α·hν)1/2 vs. (hν) [16] gives the value of the optical band gap *Eg* determined as the energy difference between the onsets of exponential tails of the allowed conduction bands [17].

Figure 3 represents the absorption spectra in the Tauc co-ordinates $(\alpha h\nu)^{1/2} = A(h\nu - Eg)$. The Sn impurities in the $(As_2S_3)_{0.5}:(As_2Se_3)_{0.5}$ increase the absorption coefficient α and decrease the optical band gap Eg, as was observed in the case of the amorphous AsSe:Sn films [18]. These peculiarities indicate that the tin impurities in chalcogenide glasses induce a broadening of the electronic tail states in the conduction bands and shift the Urbach edge in the red region of the spectrum. This broadening of the electronic tail states can be attributed to the formation of new

tetrahedral structural units containing Sn [5], which leads to an additional structural disorder to that existing in the matrix of chalcogenide glass.

Table 1. Assignments of characteristic vibration bands for vitreous As_2S_3 and $[(As_2S_3)_{0.5}:(As_2Se_3)_{0.5}]_{1-x}:Sn_x$ bulk glasses

Bond	Position (cm^{-1})	As_2S_3	x = 0	x = 0.01	x = 0.02
Unidentified	7252	7252	–	–	–
S-H (Se-H)	5190	5190	–	–	–
H_2O	3617	3617	–	–	–
H_2O	3522	3522	–	–	–
-S-H-	3194	–	–	–	3194
-S-H-(Se-H-)	2482	2482	–	2482	2482
CO_2	2311	–	–	2311	2311
-C-O-S-	2026	–	–	–	2026
-As-H-	1857	1857	–	–	–
H_2O	1597	1597	–	–	–
CS_2	1493	–	–	–	1493
AsO (As_2O_3)	1003	1003	1003	1003	1003

Figure 4 represents the dispersion curves of the refractive index $n = f(\lambda)$. It is evident that an increase in the tin content in amorphous glass $[(As_2S_3)_{0.5}:(As_2Se_3)_{0.5}]_{1-x}:Sn_x$ thin films increases the refractive index *n*. The values of the refractive index n at the wavelength λ = 633 nm are presented in Table 2. Figure 4 and Table 2 show that a sharp increase in the refractive index *n* takes place upon the introduction of 10 at % (or x=0.1) Sn in the $(As_2S_3)_{0.5}:(As_2Se_3)_{0.5}$ host glass.

Table 2. Optical parameters α, Eg^{opt}, and *n* for some amorphous $[(As_2S_3)_{0.5}:(As_2Se_3)_{0.5}]_{1-x}:Sn_x$ thin films

Nr.	Film composition	$\alpha \cdot 104$, cm^{-1} ($h\nu$ = 2.3 eV)	Eg^{opt}, eV, ±0.01	n (λ = 633 nm), ±0.02
1	$(As_2S_3)_{0.5}:(As_2Se_3)_{0.5}$	2.44	1.96	2.52
2	$[(As_2S_3)_{0.5}:(As_2Se_3)_{0.5}]_{0.99}:Sn_{0.01}$	3.17	1.90	2.70
3	$[(As_2S_3)_{0.5}:(As_2Se_3)_{0.5}]_{0.98}:Sn_{0.02}$	3.07	1.94	2.74

The relaxation of the relative optical transmission $T/T_0 = f(t)$ under light exposure (λ = 633 nm) for amorphous $[(As_2S_3)_{0.5}:(As_2Se_3)_{0.5}]_{1-x}:Sn_x$ thin films is shown in Fig. 5. At a constant light intensity, the presented dependences characterize the decay of the film optical transmittance with the increase in the dose of absorbed photons. To obtain a unified basis for comparison of the transmission relaxation T(t)/T(0) curves, we used the so-called stretched exponential presentation for the relaxation curves in the form

$$T(t)/T(0) = A_0 + A\exp[-(t-t_0)/\tau]^{(1-\beta)}, \quad (2)$$

Here *t* is the exposure time, τ is the apparent time constant, *A* characterizes the exponent

amplitude, t_0 and A_0 are the initial coordinates, and α is the dispersion parameter ($0<\beta<1$).

For the obtained relaxation curves, a rather wide scatter of parameters is observed for samples of the different composition. For doped samples, this dispersion can be caused by the fact that the concentration and distribution uniformity of the impurity is not adequately preserved along the film at deposition. But the relaxation curves are significantly different in the case of nondoped $(As_2S_3)_{0.5}$:$(As_2Se_3)_{0.5}$ as well. The main cause is the difference in thickness. For these samples, the effect of interference of light reflected at the front and rear film boundaries significantly changes the amount of absorbed light leading to a strong dependence of photodarkening at a fixed laser wavelength on film thickness [5].

The photodarkening phenomenon in chalcogenide glass films under illumination has no plain explanation up to now in spite of detailed investigation and a series of models advanced for interpretation of it. The red shift of the absorption edge, which indicates the narrowing of the optical gap of the film at photodarkening, is believed to be due to the broadening of the valence band, the top of which is formed mainly by states of lone-pare electrons of the chalcogen atom. Several models have been put forward to substantiate this broadening with a particular individual atom regarded as an initial object of photoexcitation [19, 20]. Recently, a novel model for photodarkening in a-$As_2Se(S)_3$ has been proposed [21, 22], in which photoexcited charge carriers in extended states are considered to be responsible for photodarkening.

A comparison of the parameters of the relaxation curves for the samples deposited at different incident angles has shown that, in the considered limits of distance from the center over the evaporator, the greatest effect of photodarkening is observed for the central samples, in contrast to the results reported in the literature for obliquely deposited films [20]. The slight decrease in the photodarkening amplitude with the distance from the center is due to the decrease in the film thickness.

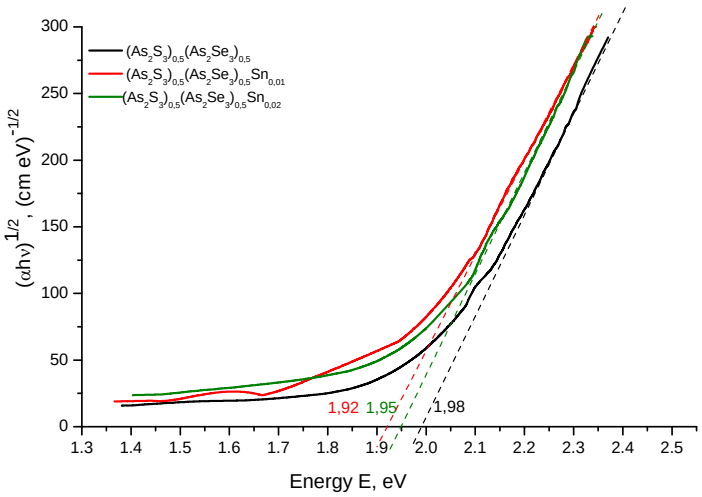

Fig. 3. Absorption spectra in the Tauc coordinates $(\alpha\ h\nu)^{1/2} = A(h\nu - Eg)$.

Unlike the previous conceptions, the new model takes into account the layered cluster structure of a chalcogenide glass. During exposure, the layer is negatively charged due to the capture of photoexcited electrons, and repulsive forces are built between the layers. These forces cause an enlargement in the interlayer distance (leading to photoexpansion) and slip motion along

the layers. The last mentioned process alters the interaction of lone-pair electrons between the layers leading to a photodarkening effect. Earlier, in his structural model proposed for explanation of photodarkening phenomena, M. Popescu [23] has pointed out that distortion in the second and third coordination spheres should be taken into account as important factors.

The model of Shimakawa et al. [21, 22] offers a good basis for consideration of the effect on photodarkening of impurity atoms with coordination different from that of the host glass atoms, as in the case of tin. The foreign metal atoms provide bridging between the layers and hence reduce the slip motion, thus hindering the photodarkening. We suggest that this consideration is applicable in the case of tin impurity in amorphous $[(As_2S_3)_{0.5}:(As_2Se_3)_{0.5}]_{1-x}:Sn_x$ thin films.

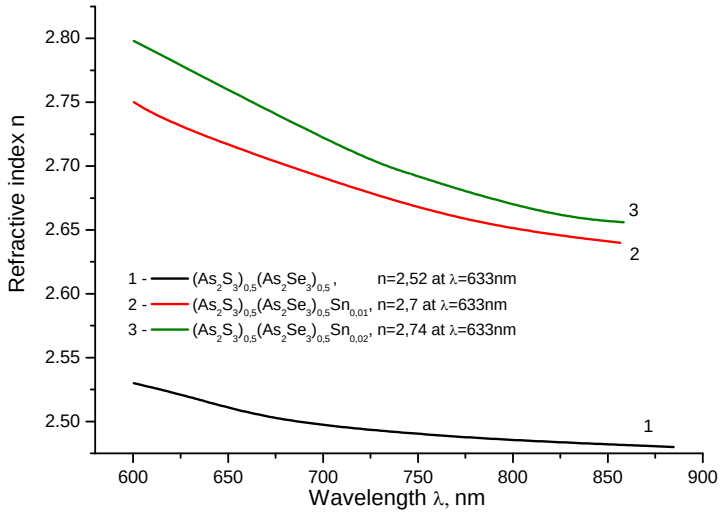

Fig. 4. Dispersion curves n = f(λ) for amorphous $[(As_2S_3)_{0.5}:(As_2Se_3)_{0.5}]_{1-x}:Sn_x$ thin films.

In the absence of tin, the arsenic chalcogenide glass is formed of corrugated and disordered layer domains with some correlation between them. This correlation leads to a rather compact packing with low inter-configurational distance. Upon the introduction of Sn, due to the tetrahedral disposal of the sp3 bonds with the chalcogens, the dopant atom inserted in the network increases the thickness of the layered configuration as revealed by the significant shift of the FSDP towards lower angles. This insertion corresponds, in fact, to the introduction of the structural units of the type $SnSe_2$ in the network. The effect is greater for higher dopant content but only up to a certain concentration, because further the separation of the reciprocally ordered configurations is interrupted by increasing interconnection between layers followed by the transition to three-dimensionally (3D) connected network. The transition is preceded by the appearance of structural units of the SnSe type. Then, the direct consequence of this transition will be shown in the intensity of the FSDP, which gradually disappears. The interruption of the two-dimensional structure and transition is probably due to a more ionic nature of the Sn-Se bonds.

The ionic component gives a higher structural mobility in the network and therefore a higher instability of the glass. Thus, we can expect that the tin impurity strongly affects the

network of the host glass inducing changes in both short-range and medium-range order; in particular, they have a significant effect on the structural layers and the pattern of their relative motion. This fact clearly indicates a strong retardation of the slip motion of the structure layers due to the presence of impurity. Since tin tends to form directional bonds when introduced in the host glass, and especially during the annealing process, some bridging bonds should appear between the layers. The structure of the glasses that contains a tin impurity requires, therefore, some excess slip forces, i.e., leads to greater exposition doses and time constants. Furthermore, the formation of clusters, such as of the $SnSe_2$ type, can decrease the density of lone-pair defects typical for AsSe and AsS (i.e., D-centers) thus lowering the charge state of the layers and, finally, the photodarkening.

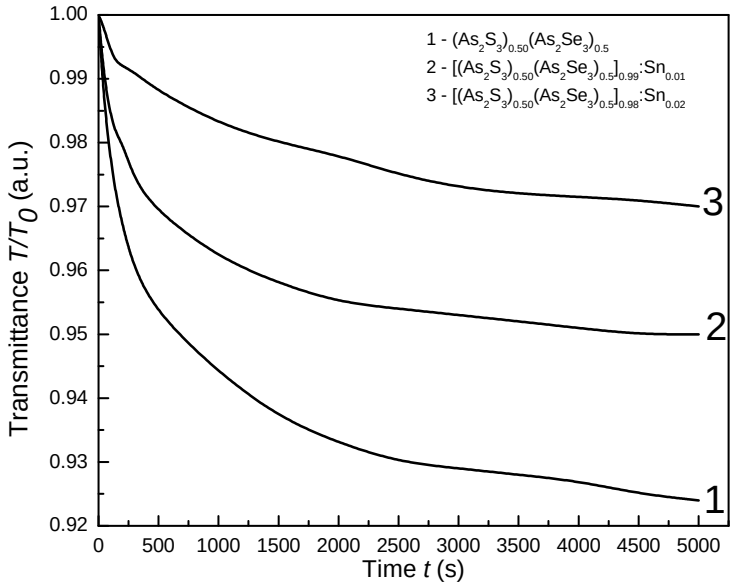

Fig. 5. Relaxation curves of photodarkening $T/T_0 = f(t)$ for amorphous $[(As_2S_3)_{0.5}:(As_2Se_3)_{0.5}]_{1-x}:Sn_x$ thin films.

The fact that the photodarkening kinetics can be described by a stretched exponential can be regarded as an indication of dispersion in the kinetic mechanism, i.e., the time dependence of the process rate [24]. The data suggest that the formation of photoinduced absorption is limited by a dispersive process with the exponent $\alpha \cong 0.5$. In our case, it is the dispersive nature of hole transport that can cause the dispersive nature of relaxation after photogeneration. In fact, the transport of photoexcited holes is included in the model at the stage at which the layer clusters are charged due to the capture of charge carriers. Charge transport in chalcogenide glasses is known as highly dispersive due to a wide distribution of capture times in multiple-trapping process [25]. For a-As_2Se_3-like glasses, the dispersive parameter α of hole transport is close to 0.5 in accordance with the value found from the stretched exponential presentation of photodarkening kinetics [5]. The fact that α is increasing with the addition of metal impurities indicates that the dispersion of the transport is decreased. In general, this is agreement with both the stabilization of structure and the expected alteration of defect center density.

4. Conclusion

The doping of $As_2(S, Se)_3$ chalcogenide glass with tin impurities essentially reduces the absorption bands of S-H (Se-H) and H2O located at $\nu = 5190$ cm^{-1} and $\nu = 3617$ cm^{-1}, respectively. The reduction in the optical gap of As_2Se_3 glass upon alloying Sn, most likely, results from a broadening of the valence band. The top of the valence band in these glasses has a contribution from chalcogen S(Se) lone-pair electrons. The modification of optical parameters (optical band gap Eg, absorption coefficient α, refractive index n) under light irradiation of amorphous thin films with different amount of Sn was investigated. The relaxation of photodarkening effect in amorphous $[(As_2S_3)_{0.5}:(As_2Se_3)_{0.5}]_{1-x}:Sn_x$ thin films is described by the stretch exponential function $T(t)/T(0) = A_0+Aexp[-(t-t_0)/\tau^{](1-\beta)}$. The main feature of the photodarkening effect in the samples under study is that the tin impurities suppressed the photodarkening.

Acknowledgments

The work is supported by the National Institutional Project no. 11.817.05.03A. The author is kindly grateful to Drs. V.E. Tazlavan and E.P. Colomeico for sample preparation; to Drs. I.A. Cojocaru, D.F. Felix, and A.Yu. Meshalkin for optical measurements; and Prof. M.S. Iovu for valuable discussion, critical reading of this paper, and his interest in this work.

References

[1] Stronski A.V., Vlcek M., Kostyukevych S.A., et al., Semicond. Phys., Quantum Electron. Optoelectron., 5(3), 284-287 (2002).
[2] Gerbreders A. and Teteris J., J. Optoelectron. Adv. Mater., 9(10), 3164-3166 (2007).
[3] Reinfelde M. and Teterism J., J. Optoelectron. Adv. Mater., 13(12), 1531-1533 (2011).
[4] Iovu M.S., Shutov S.D., and Popescu M., J. Non-Cryst. Solids, 924-928 (2002).
[5] Boolchand P., Georgiev D.G., and Iovu M.S., Chalcogenide Lett., 2(4), 27-34 (2005).
[6] Iovu M.S., Boolchand P., and Georgiev D.G., J. Optoelectron. Adv. Mater., 7(2), 763-770 (2005).
[7] Iovu M.S., Harea D.V., and Colomeico E.P., J. Optoelectron. Adv. Mater., 10(4), 862-866 (2008).
[8] Corsac O., Neamtu S., and Nasedchina N., Studia Universitatis, Revista Stiintifica a Universitatii de Stat din Moldova, Seria Stiinte ale Naturii, 1, 304-306 (2007).
[9] Dmitriev S., Goglidze T., Dementiev I., Pocatilov E., Lad R., and Vetelino J., Studia Universitatis, Revista Stiintifica a Universitatii de Stat din Moldova, Seria Stiinte ale Naturii, 1, 315-318 (2007).
[10] Zhidkov Yu., Korshak O., Prilepov V., Nyamtsu S., and Kiritsa A., Studia Universitatis, Revista Stiintifica a Universitatii de Stat din Moldova, Seria Stiinte ale Naturii, 1, 162-165 (2009).
[11] Iaseniuc O., Andriesh A., and Abashkin A., Mold. J. Phys. Sci., 4, 349-355 (2010).
[12] Tauc J., The Optical Properties of Solids, North-Holland, Amsterdam, 1970.
[13] Swanepoel R., J. Phys. E: Sci. Instrum., 16, 1214-1242 (1983).
[14] Ganjoo A. and Golovchak R., J. Optoelectron. Adv. Mater., 10(6), 1328-1332 (2008).
[15] Iovu M.S., Shutov S.D.,.Andriesh A.M, Kamitsos E.I., Varsamis C.P.E., Furniss D., Seddon A.B., and Popescu M., J. Optoelectron. Adv. Mater., 3(2), 443-454 (2001).
[16] Wood D.L. and Tauc J., Phys. Rev., B5, 3144-3151 (1972).

[17] Chacorn V. and Haneman D., Solid State Commun., 65(7), 609-611(1988).
[18] Iovu M., Syrbu N.N., Shutov S.D., Vasiliev I.A., Rebeja S., Colomeico E., Popescu M., and Sava F., Phys. Stat. Solidi A, 175(2), 623-629 (1999).
[19] Pfeiffer G., Paesler M.A., and Agarwal S.C., J. Non-Cryst. Solids, 130, 111-143 (1991)
[20] Shimakawa K., Kolobov A., and Elliot S.R., Adv. Phys., 44(6), 775-788 (1995).
[21] Shimakawa K., Yoshida N., Ganjoo A., Kuzukawa Y., and Singh J., Philos. Mag. Lett., 77, 153-158 (1998).
[22] Ganjoo A., Yoshida N., and Shimakawa K., Photoinduced Changes on the Structural and Electronic Properties of Amorphous Semiconductors, Recent Research Developments in Applied Physics, ed. M. Kawasaki, N. Ashgritz, and R. Anthony, Research Signpost, Trivandrum, 2, 129-150 (1999).
[23] Popescu M., J. Non-Cryst. Solids, 90, 533-536 (1987).
[24] Gisom D.L., Gingerich M.T, and Frieble E.J., Phys. Rev. Lett., 71, 1019-1022 (1993).
[25] Pfister G. and Sher H., Adv. Phys., 27, 747-798 (1978).

LOW-TEMPERATURE LUMINESCENCE OF NANOSIZED $SrAl_2O_4:Eu^{2+}$

M. Nazarov [1,2*], A. Nor Nazida[1], S. C. M. Calyn[1], N. M. A. Aziz[3], and M.N Ahmad-Fauzi [1]

[1]*School of Materials and Mineral Resources Engineering, University Sains Malaysia, Engineering Campus, 14300 Nibong Tebal, Pulau Pinang, Malaysia*
[2] *Institute of Applied Physics, Academiei str. 5, Chisinau, MD-2028 Republic of Moldova*
[3]*Advanced Materials Research Centre, SIRIM Berhad, 09000 Kulim, Kedah, Malaysia*
** e-mail: nazarov@eng.usm.my*

(Received 24 April 2012)

Abstract

A stoichiometric $SrAl_2O_4:Eu^{2+}$ nanosized powder was synthesized by a combustion method using urea at 500°C and calcination at 1000ºC. The luminescence properties were investigated and two luminescence bands at 450 nm and 512 nm were observed at lower temperatures. This luminescence in the green region corresponds to transitions of Eu^{2+} from $4f^6 5d^1 \rightarrow 4f^7$. For the first time, an analysis of the electron-vibrational interaction and crystal field splitting of the Eu^{2+} 5d states has been performed for the considered system. The parameters of Stokes shift, Huang–Rhys factor, zero-phonon line position, and effective phonon energy were investigated and determined.

1. Introduction

The alkali earth aluminates phosphor doped with rare earth ions are functional inorganic materials with strong luminescence in the blue to red regions of the spectrum [1-3]. These materials have attracted much attention for various studies which are generally used for numerous applications in display devices, signage, medical application, emergency rescue guidance system, storage devices, and many more [4]. These phosphors have been regarded as excellent phosphors due to their highly efficient luminescence centers contributed by activator, Eu^{2+} ions.
The spectra and wavelength positions of the emission bands depend on the hosts changing from near-UV to red and mostly interpreted due to the crystal field splitting of 5*d* level. Crystal field theory describes the energy levels based on symmetry coordination (e.g., monoclinic and orthorhombic) within a given crystal environment. With increasing crystal field strength, the 5*d* state becomes lower than the $4f^7$ state, and it produces the luminescence from $5d \rightarrow 4f$ transition. This scenario shifts the emission band or luminescence color of Eu^{2+} ions to longer wavelength [5]. These transitions typically involve the vibrational modes and emissions exhibiting a Stokes shift [6]. The detailed study of Stokes shift is very important to better understand the luminescence mechanism and also to improve the luminescence properties.

The $4f^6 5d$ state of Eu^{2+} is very sensitive to the change of crystal field strength, which leads to splitting the main levels into sublevels depending on the strength of the host. This sensitivity can be discussed in detail for emission spectral properties in $SrAl_2O_4:Eu^{2+}$ crystals at low temperatures. Moreover, the experimental results at low temperatures published in sparse papers are often in contradiction and need more careful examinations.

The main goal of this research is to continue studying the properties of nanosized $SrAl_2O_4:Eu^{2+}$ at low temperatures and to determine the main electron-vibronic parameters of the

investigated system. This paper reports the photoluminescence (PL) results and crystal field splitting studies. We have estimated the Stokes shift, the Huang-Rhys factor, the energy of an effective phonon interacting with the Eu^{2+} 5d states, and the zero-phonon line (ZPL) position for $SrAl_2O_4:Eu^{2+}$.

2. Experimental

2.1 Sample Preparation

$SrAl_2O_4:Eu^{2+}$ phosphor was prepared by combustion synthesis. The following starting materials were used: Aluminium nitrate ($Al(NO_3)_3.9H_2O$; Systerm, 98%), strontium nitrate ($Sr(NO_3)_2$; Aldrich, 99%), europium oxide (Eu_2O_3; Aldrich, 99.99%) and urea ($CO(NH_2)_2$; Systerm, 99%). Small amounts of acid boric (H_3BO_3; Fisher, 100.04%) were used as a flux and small amounts of urea were used as a reducer and fuel. Each raw material $Al(NO_3)_3.9H_2O$, $Sr(NO_3)_2$, H_3BO_3 and $CO(NH_2)_2$ was dissolved into deionized water, and Eu_2O_3 was dissolved with a minimum amount of the HNO_3 solution to be converted into $Eu(NO_3)_3$. The two solutions were mixed together and stirred using a magnetic bar for several hours at 75°C to obtain a viscous gel solution. White combustion ash was obtained in 3-5 min by combusting the precursor gel at a temperature of 500°C. The final pigment synthesis is performed by heating the combustion ash at 1000°C in a weak reductive atmosphere for 2 h to obtain the $SrAl_2O_4:Eu^{2+}$ phosphor. A weak reductive atmosphere was created by using a graphite crucible to inhibit further oxidation.

2.2 Characterization techniques

The photoluminescence spectra of this phosphor were characterized by using a setup shown in Fig. 1. The excitation and luminescence spectra were recorded using a Horiba Jobin Yvon Spectrometer (iHR 550) coupled to a R928 Hamamatsu photomultiplier (FL-1073). A 450 W Xe lamp combined with a Horiba Jobin Yvon monochromator (FL1005) was used as the excitation source. The setup allows selecting a specific excitation wavelength and also an emission scanning range up to the second order of the wavelength. An ARS DE-202AE closed cycle helium flow cryostat is installed into the sample chamber for low temperature studies. This system gives the possibility to carry out experiments at low temperatures up to 10 K. The sample powder was glued to an aluminum sample holder using silver paste and positioned at 45° to the incoming excitation beam.

In PL measurements, each sample was excited by a 325-nm excitation wavelength. The emission slit was set at 1 mm, respectively, to avoid intensity saturation at the detector. After reaching the specific temperature, we waited for 30 min before measurement to ensure temperature stability between the sensor attached at the sample holder and the heat station of the cryostat (Fig. 2). Data acquisition in this setup is controlled by the Fluor-Essence software. Once the emission light is recorded by the detector, the optical signal is digitized and corrected to improve the detector response.

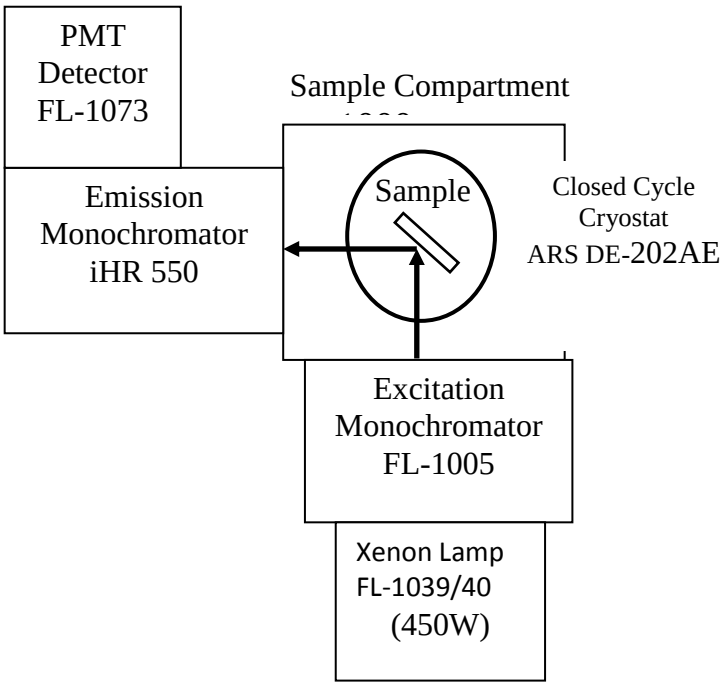

Fig. 1. Schematic diagram of Horiba Jobin Yvon Spectrometer (iHR 550).

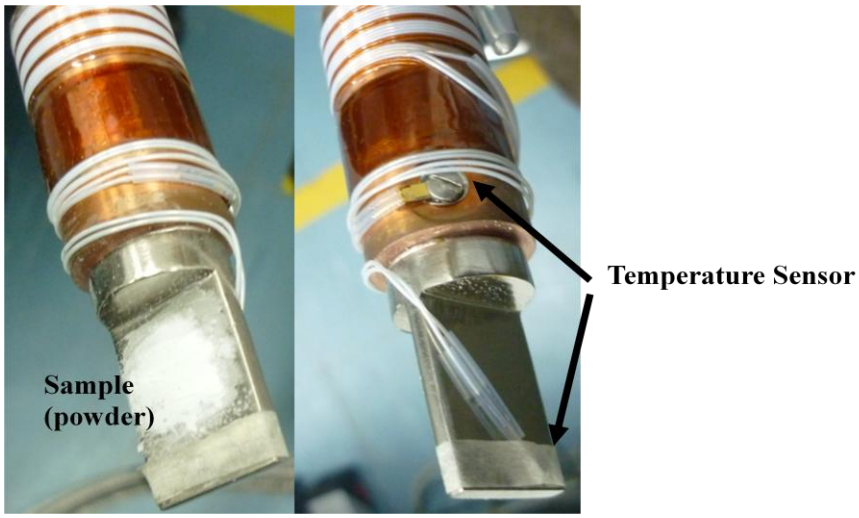

Fig. 2. Sample holder and temperature detector for measuring at a lower temperature.

3. Results and Discussion

3.1 Estimation of electron-vibrational interaction parameters

Theoretically, there are three parameters that represent the electron-vibrational interaction between the impurity ions and their surrounding. The first parameter is the Stokes shift ΔE_s which corresponds to the energy difference between the first absorption and emission peaks. The second is the Huang-Rhys factor S, i.e., the mean number of the emitted phonons accompanying the optical transitions. This value is proportional to ΔE_s. The last one is the effective phonon energy

ħ*w*.

The classical description cannot satisfactorily explain emission spectral shapes and nonradiative transition probabilities. The single configuration coordinate model based on quantum mechanics was used to fit the emission band of considered phosphors (Fig. 3).

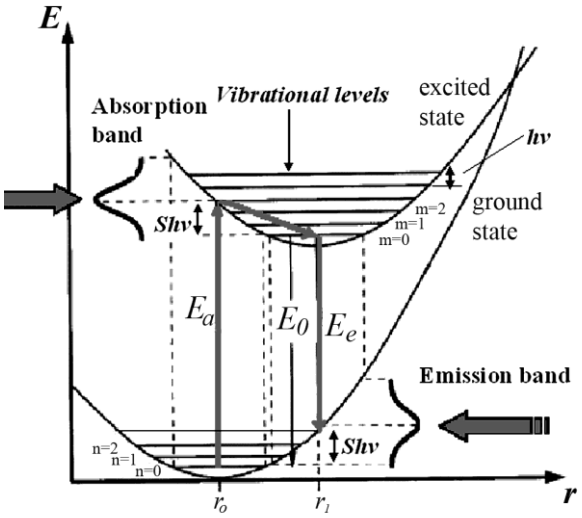

Fig. 3. Configuration diagram.

Since the 4*f*-shell is well shielded, the electron-vibrational (vibronic) interaction within this shell is negligible so that the intensities of the vibronic satellites corresponding to 4*f*-4*f* transitions are small. On the contrary, 4*f*-5*d* transitions give rise to the broad vibronic bands whose shape-function can be described by the normalized "Pekarian" type spectral distribution [7]:

$$F(\Omega)=exp\left[-\frac{a}{2}Coth\left(\frac{p\hbar\omega}{2kT}\right)\right]\sum_{-\infty}^{\infty}exp\left(\frac{p\hbar\omega}{2kT}\right)I_p\left(\frac{a}{2Sinh\left(\frac{\hbar\omega}{2kT}\right)}\right)\delta(\Omega-\Omega_0-p\omega). \qquad (1)$$

In Eq.(1) $I_p(x)$ is the modified Bessel function that represents a series of the discrete lines, a is the so-called heat release parameter (shift of the dimensionless vibrational coordinate after photon absorption), $\delta(\Omega-\Omega_0-p\omega)$ is the Dirac δ-function that describes an individual non-broadened vibrational line of the dimensional frequency $p=(\Omega-\Omega_0)/\omega$, Ω_0 is the frequency of the zero-phonon line, ω is the frequency of the active vibrational mode, and k the Boltzmann constant. If the dispersion zone of the lattice vibrations is taken into account, the shape function is smoothed, which is achieved by replacing the δ-function by the Gaussian or Lorentzian bands.

This equation can be resolved mathematically, and it shows the general tendency of decreasing the maximum of intensity with increasing temperature (Fig. 4) that is in good agreement with our experimental data (Fig. 7). The effect of decreasing integrated PL intensity in real experiments can be explained by thermal quenching. It means that at high temperature both non-radiative and radiative transitions are present, while at low temperature the non-radiative transitions are negligible.

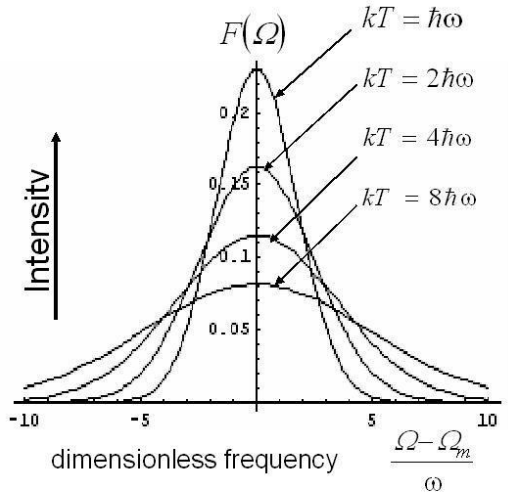

$a = Q_0^2 = 3$

Fig. 4. Temperature dependence of the absorption band within the semiclassical approximation.

In the case of low temperature Pekarian can be simplified. In fact, in this case $Sinh(\hbar\omega/2kT) \approx (1/2)exp(\hbar\omega/kT)$, $exp\left(-\frac{a}{2}Coth\frac{\hbar\omega}{2kT}\right) \approx exp\left(-\frac{a}{2}\right)$, and the modified Bessel function can be represented as a series in terms of the argument $a\,e^{-\frac{p\hbar\omega}{2kT}}$:

$$I_p\left(a\,e^{-\frac{\hbar\omega}{2kT}}\right) \approx \left[\left(\frac{a}{2}\right)^p \frac{1}{p!} + \left(\frac{a}{2}\right)^{p+2} \frac{1}{(p+1)!} e^{-\frac{\hbar\omega}{kT}}\right] e^{-\frac{p\hbar\omega}{2kT}}. \quad (2)$$

In decomposition (2) small terms $o\left[a\,e^{-\frac{\hbar\omega}{2kT}}\right]^4$ (and high order terms) are neglected, which is justified when the temperature is low enough $(kT \le \hbar\omega)$ and the vibronic coupling is not too strong. Combining (1) and (2), one can obtain the following low temperature approximation for the band profile of the vibronic band:

$$F(\Omega) = e^{-\frac{a}{2}}\left[\sum_{p=0}^{\infty}\left(\frac{a}{2}\right)^p \frac{1}{p!} + \sum_{p=-1}^{\infty}\left(\frac{a}{2}\right)^{p+2} \frac{1}{(p+1)!} e^{-\frac{\hbar\omega}{kT}}\right]\delta(\Omega - \Omega_0 - p\omega). \quad (3)$$

This expression describes a discrete set of the vibronic lines (each represented by a corresponding δ-function) and therefore reflects the quantum properties of the vibrations. The dispersion of the vibrations makes the discrete structure smooth. Therefore, one can omit the δ-functions and the required summations and consider that intensity of the band in (3) as a function of the continuous parameter *p*.

At temperature T=0 K from this equation, we obtain a well known transition probability given by the simple relation [5]:

$$F(p) = \frac{e^{-S} \cdot S^P}{p!} \quad (4)$$

where S=a/2 is the Pekar- Huang-Rhys factor.

Usually, only this term in (4) that is the Poisson type distribution is taken into account for

the band shapes at low temperatures. From the physical point of view, this means absorption (emission) originating from the fundamental vibronic level in the initial electron-vibrational state.

The knowledge of Huang-Rhys-Pekar factor allows us to determine the Stokes shift:

$$\Delta Es = (2S - 1) \cdot \hbar\omega \tag{5}$$

The temperature variation of the full width at half maximum (FWHM) can be described by using the configuration coordinate model (Fig. 3) and the Boltzmann distribution according to the following equation proposed by Henderson [8]:

$$\Gamma(T) = \sqrt{8 \cdot \ln 2} \cdot \hbar\omega \cdot \sqrt{S} \cdot \sqrt{\coth \frac{\hbar\omega}{2kT}} \tag{6}$$

where $\hbar\omega$ is the mean phonon energy. This equation can be used only when the parabolas of the ground state and the excited state have the same curvature [9]. Combining (5) and (6), we can find the Huang-Rhys-Pekar parameter S and phonon energy $\hbar\omega$ for the investigated materials and calculate the Stokes shift.

We apply this method to study the temperature dependence of the luminescence intensity of nanosized particles of the $SrAl_2O_4:Eu^{2+}$ phosphor obtained by combustion synthesis.

3.2 Excitation and emission spectra at room temperature

Figure 5 represents the mirror image relationship of the emission and excitation spectra of $SrAl_2O_4:Eu^{2+}$ at room temperature.

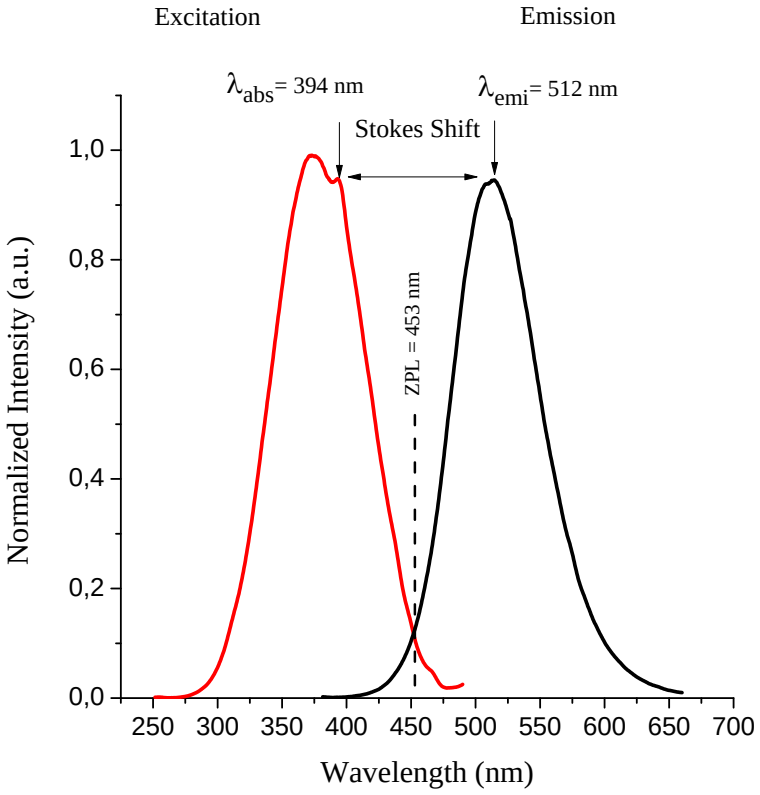

Fig. 5. Excitation (λ_{em}=512nm) and emission spectra ((λ_{exc}=325 nm) of the $SrAl_2O_4$: Eu^{2+} phosphor at room temperature.

The result shows that phosphor exhibits green emission band peaked at 512 nm. This emission is attributed to the typical $4f^6 5d \rightarrow 4f^7$ transition of Eu^{2+} ions in the $SrAl_2O_4$. No emission peaks of Eu^{3+} were observed in the emission spectra indicating that the Eu^{3+} ions in the samples have been completely reduced to Eu^{2+} ions. The excitation spectrum consists of two main bands with maxima at 375 and 394 nm. The zero-phonon line (ZPL) at the intersection of the emission and excitation is determined from Fig. 5 and corresponds to ZPL = 453 nm. The Stokes shift is also calculated from Fig. 5 and $\Delta E_s = (\lambda_{em} - \lambda_{abs}) = 118$ nm (5850 cm^{-1}).

Knowledge of the Stokes shift (ΔE_s = 5850 cm^{-1}) and FWHM ($\Gamma(T)$ = 3025 cm^{-1}) at T = 300 K from experimental emission and excitation spectra allows us to resolve graphically the system of equations (5) and (6) and to find S and $\hbar\omega$. An example of this solution for our case is shown in Fig. 6.

$$\frac{\Gamma(T)^2}{2.35^2}\frac{(2S-1)^2}{S\,\Delta E_S{}^2} = \coth\left(\frac{\Delta E_S}{(2S-1)}\frac{1}{2kT}\right) \tag{7}$$

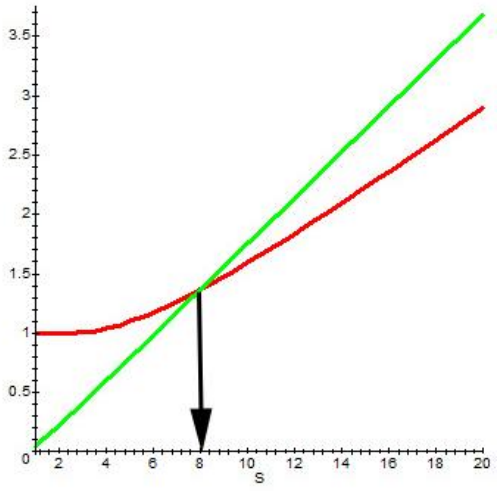

Fig. 6. Solution to equation (7).

Equations (7) and (5) give S=8 and $\hbar\omega$ =390 cm^{-1}. A similar consideration of the electron–vibrational interaction for Eu^{2+} in $SrGa_2S4$, $CaGa_2S_4$, and $BaGa_2S_4$ doped with Eu^{2+} was published recently [10, 11] with the values of S from 4 to 7 and $\hbar\omega$ values around 300 cm^{-1}. A higher value of the Huang–Rhys factor S=12 was demonstrated in [9, 12] and explained by a large Stokes shift (about 6500 cm^{-1}).

3.3 Low temperature measurements

The most interesting results for nanosized $SrAl_2O_4:Eu^{2+}$ were obtained from low temperature measurements. PLE and PL spectra are demonstrated in Fig. 7.

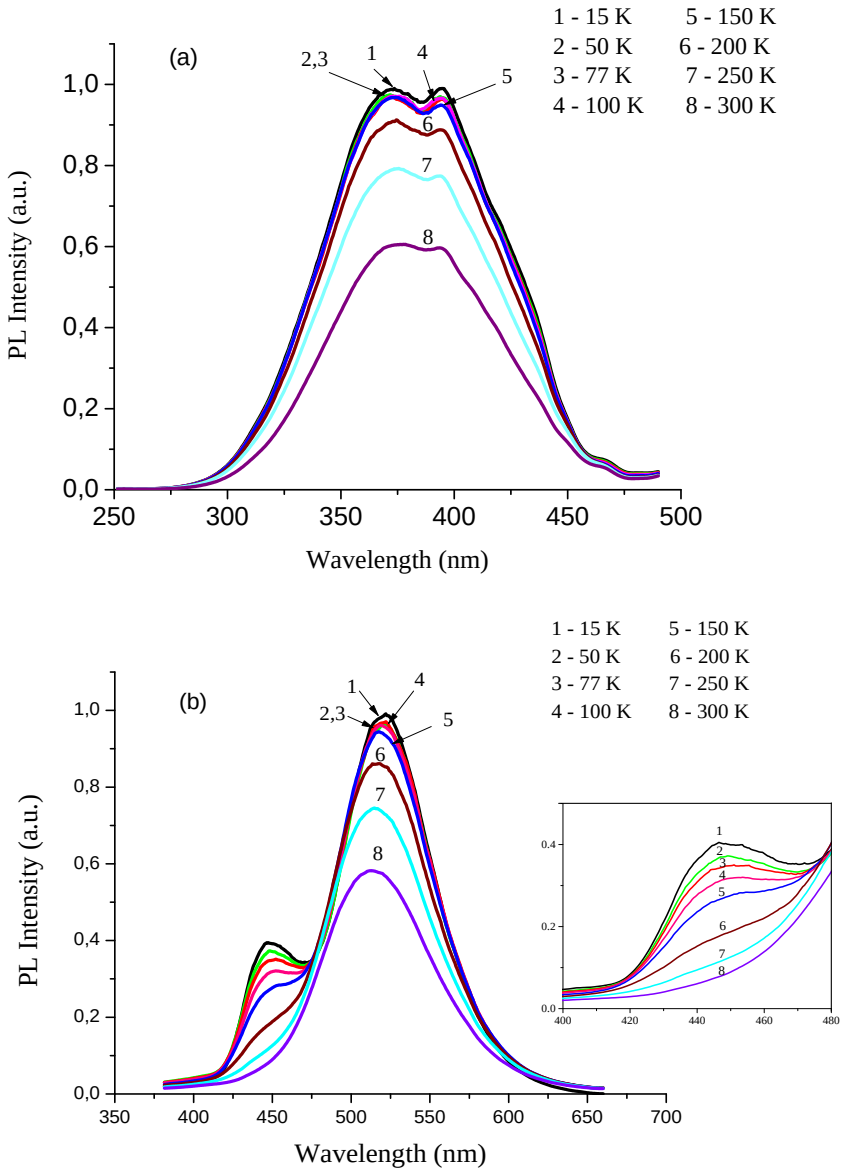

Fig. 7. Excitation (a) and emission (b) spectra of the $SrAl_2O_4$: Eu^{2+} phosphor measured at different temperatures.

Figure 7 shows the emission and excitation spectra of $SrAl_2O_4$:Eu^{2+} registered in a temperature region of 15 to 300 K.

The Eu^{2+} absorption (excitation) bands related to the $4f^7 \rightarrow 4f^6 5d$ transition are broad (Fig. 7a). This is related to the crystal field splitting of the Eu^{2+} energy levels as discussed above. The general diagram of the 5d levels splitting with characteristic emission and absorption transition is shown in Fig. 8. The 5d states of Eu^{2+} are split into two sets of the energy levels, which can be designated by t_{2g} (the lowest) and e_g (the highest) as shown in Fig. 8. The levels of the actual crystal field of low symmetry will split further. The emission transition is expected to occur only from the lowest 5d level, according to the general shape of the photoluminescence band.

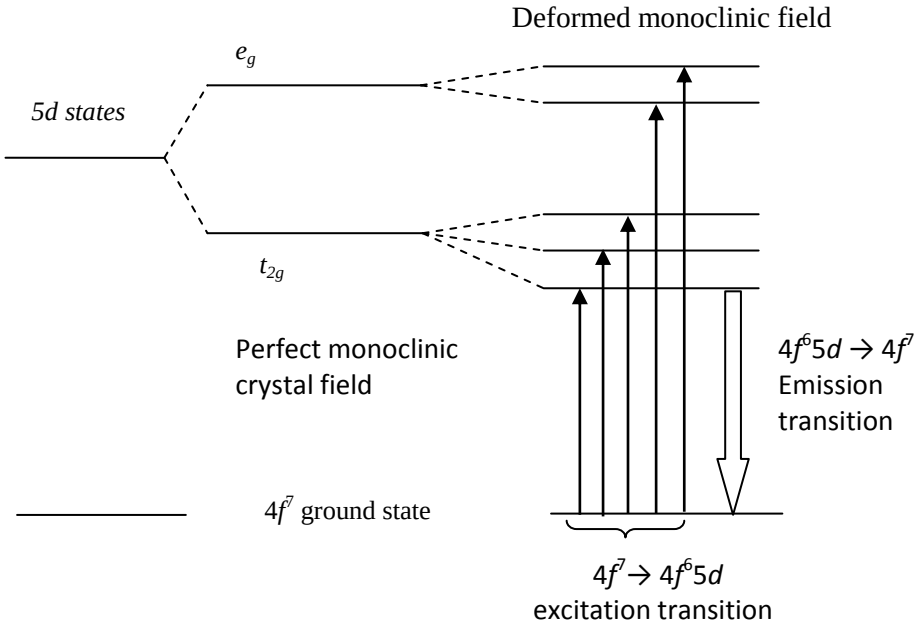

Fig. 8. Diagram of the $4f^7 \rightarrow 4f^6 5d$ absorption and $4f^6 5d \rightarrow 4f^7$ emission transitions in $SrAl_2O_4:Eu^{2+}$ [12].

It is well known that the $4f^6 5d$ state of Eu^{2+} is very sensitive to changes in crystal field strength, which leads to the splitting of the main levels into sublevels depending on strength. In low temperature experiments, this splitting of the absorption (excitation) band is clearly seen in Fig. 7a.

The emission spectra (Fig. 7b) consists of one band at 512 nm for the samples measured at room temperature, but low temperatures measurements show two bands centered near 450 and 512 nm (2.75 and 2.42 eV, respectively). The luminescence intensity of both bands decreases slowly in a temperature range of 15–150 K and decreases significantly when temperature increased above 150 K. At 250 K the "blue" band at 450 nm disappears. The wavelength of the emission maximum decreases from 522 to 512 nm, and the FWHM of the main band increases from 69 to 82 nm with increasing temperature. This temperature dependence of FWHM and calculated data from equation (6) are shown in Fig. 9. To overcome a small underestimation in (6), the scissor operator of 1.3 was used.

Based on crystallographic studies, the Eu^{2+} ions substitute two Sr sites present in the $SrAl_2O_4$ lattice system. It may be one of the causes of appearance of two bands. The luminescence at 512 nm is commonly ascribed to the parity-allowed electric dipole transition, $4f^6 5d^1 \rightarrow 4f^7$, of the Eu^{2+} ion [13]. The origin of the 450 nm emission is still under discussion. Poort et al. suggested that the 450- and 520-nm emission bands originate from the emission of the Eu^{2+} ion located at the two different crystallographic strontium sites [14]. Clabau et al. criticized this assignment and proposed that the 450-nm band arises from the charge transfer from oxygen to residual Eu^{3+} ion which takes place upon UV irradiation and is associated with a hole trapping at Sr^{2+} vacancies [15]. Holsa et al. consider this band as anomalous low-temperature luminescence and suggest that Eu^{2+} ion may exhibit this kind of unusual luminescence from a higher Eu^{2+} $5d$ state [16]. The Eu^{2+} luminescence ions are usually observed only from the lowest $4f^6 5d$ state because the higher excited states are not stable and can easily relax to the lowest state

which is located below the conduction band bottom. However, there is a possibility for luminescence at a higher Eu^{2+} $4f^6 5d$ state due to the absence of high energy lattice variation at low temperatures.

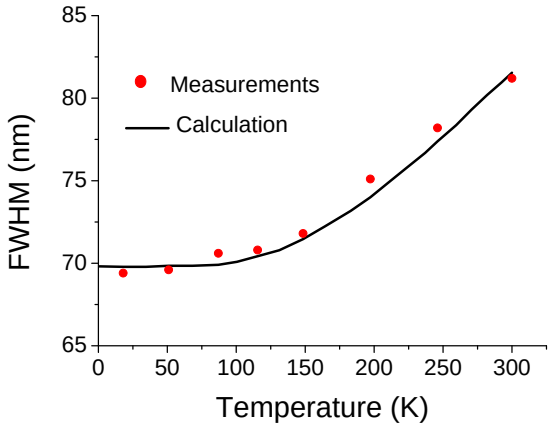

Fig. 9. Calculated (line) and experimental (circles) temperature dependence of the FWHM of the emission band measured under excitation at 325 nm.

Finally, an additional validation of reliability of the obtained values of S and $\hbar\omega$ is the emission band modeling. At a low temperature (T=15 K) in the single congiguration coordinate approximation, the intensity of the emission band can be calculated from the exact Pecar equation (1) or simplified equation (4) avalable at low temperatures. Good agrement with experimental measurements at low temperatures is demonstrated in Fig. 10.

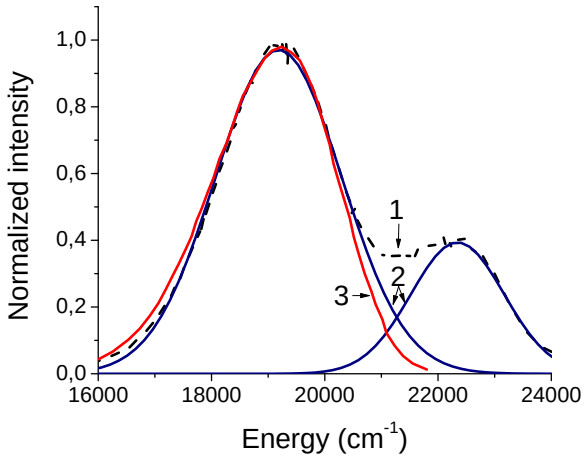

Fig. 10. (*1*) Normalized intensity of nanosized $SrAl_2O_4:Eu^{2+}$ at 15 K in an energy scale. (*2*) Decomposition of this intensity into two bands. (*3*) Calculated data for the main band and its comparison with experimental results.

This closeness between the experimental and theoretical values confirms the validity of the estimated parameters of electron-vibrational interaction for the nanosized $SrAl_2O_4:Eu^{2+}$ phosphor.

4. Conclusions

The nanosized green $SrAl_2O_4:Eu^{2+}$ phosphor was successfully synthesized by combustion synthesis. Luminescence properties at low temperatures and electron-vibrational interaction are reported. Broadband UV excited luminescence around 520 nm is attributed to $4f^6 5d \rightarrow 4f^7$ transition of Eu^{2+} ions in $SrAl_2O_4$. Another band at 450 nm was observed only at low temperature less than 150 K, and its nature is under discussion. For the first time, an analysis of the electron-vibrational interaction and crystal field splitting of the Eu^{2+} 5d states has been performed for the considered system. Stokes shift ΔE_s = 5850 cm^{-1} (118 nm), Zero-phonon line ZPL=22075 cm^{-1} (453 nm), Huang-Rhys-Pekar factor S=8, and effective phonon energy $\hbar\omega$ =390 cm^{-1} (7.9 nm) for the investigated material have been determined.

Acknowledgements

Financially support is acknowledged from Short Term Grant, University Sains Malaysia under grant no. 304/PBAHAN/60311036 and Post Graduate Grant Research under grant No. 1001/PBAHAN/8044033.

References

[1] C.K. Chang, D.L. Mao, and J.F. Shen, J. Alloys Compd. 348, 224 (2003).
[2] X. Yu, C. Zhou, X. He, et al., Mater. Lett. 58, 1087 (2004).
[3] R. Zhong, J. Zhang, S. Lu, and X.J. Wang, Appl. Phys. Lett. 88, 201916 (2006).
[4] K. Van den Eeckhout, P.F. Smet, and D. Poelman, Materials. 3, 2536 (2010)
[5] Y.M.Yen., S.Shionoya, and Y. Yamamoto H., 2, 2007, CRC Press, New York, P. 196 -197.
[6] D.R. Vij, Plenum Press. New York , 1998, P. 140 -141.
[7] Yu. E. Perlin and B.S. Tsukerblat., Elsevier, Amsterdam, 1984, P. 251-346.
[8] P. Henderson and G.Inbushch, Clarendon Press, Oxford, 1989.
[9] R.B. Jabbarov, C. Chartier, et al., J.Phys. Chem. Solids, 66, 1049 (2005).
[10] M. Nazarov, B. Tsukerblat, and D.Y. Noh, J. Lumin. 128, 1533 (2008).
[11] M. Nazarov, B. Tsukerblat, and D.Y. Noh, J. Phys. Chem. Solids. 69, 2605 (2008).
[12] K.S. Bartwal, H. Ryu, M.G. Brik, and I. Sildos, Opt. Mater. 32, 1329 (2010).
[13] V. Chernov, T.M.Piters, R.Melendrez, W.M.Yen, E.Cruz-Zaragoza, and M.Bartoza-Flores, Rad. measur. 42, 668 (2007).
[14] S.H.M. Poor, W.P. Blockpoel, and G.Blasse, Chem.Mater. 7, 1547 (1995).
[15] F. Clabau, X. Rocquefelte, S. Jobic, et al., Chem. Mater. 17, 3904 (2005)
[16] J. Holsa, H. Jungner, M. Lastusaari, and J. Niittykoski, J. Alloys Compd. 323, 326 (2001).

SYNTHESIS AND LUMINESCENCE OF $SrAl_2O_4$: Eu^{2+}, Dy^{3+}

A. Nor Nazida[1], M. N. Ahmad-Fauzi [1*], M. Nazarov [1,2], A. Azizan [1], and K. Shah Rizal[1]

[1]*School of Materials and Mineral Resources Engineering, Universiti Sains Malaysia, Engineering Campus, 14300 Nibong Tebal, Pulau Pinang, Malaysia*
[2]*Institute of Applied Physics, Academiei Str. 5, Chisinau, MD-2028 Republic of Moldova*
**e-mail: afauzi@eng.usm.my*

(Received 20 March 2011)

Abstract

This study systematically discusses the effects of the synthesis process of $SrAl_2O_4$:Eu^{2+}, Dy^{3+} in reducing the firing temperature and reducing the percentage of concentration of Eu_2O_3 and Dy_2O_3. The influence of firing temperature and rare earth doping on crystal structure, morphology, and its luminescent properties were analyzed by X-ray diffraction (XRD), Raman scattering, Photoluminescence excitation (PLE) and photoluminescence emission (PL) spectroscopy, and scanning electron microscopy (SEM). The emission intensity becomes stronger as the firing temperature increases from 1100°C to 1250°C. $SrAl_2O_4$:Eu^{2+}, Dy^{3+} firing at 1250°C shows the maximum photoluminescence intensity at 0.5 mol % Eu_2O_3 and 1 mol % Dy_2O_3 addition. A phase transformation from $SrAl_4O_7$ to $SrAl_2O_4$ and $Sr_4Al_{14}O_{25}$ is found with increasing firing temperature. The synthesized phosphors reveal the presence of the crystalline monoclinic structure of $SrAl_2O_4$ as a major phase (JCPDS card no. 74-0794) and the intermediate phase orthorhombic structure of $Sr_4Al_{14}O_{25}$. Small amount of doped Eu_2O_3 and Dy_2O_3 has almost no effect on the crystalline phase composition. The proposed firing temperature and mole concentration of the activator and co-activator is lower in comparison with other conventional solid state methods and allows us to obtain the $SrAl_2O_4$:Eu^{2+}, Dy^{3+} phosphor with improved properties.

1. Introduction

Nowadays, long lasting phosphorescence have attracted much attention in a variety of applications, such as lighting source, storage devices, medical instruments, pigments, arts and craft, etc. So far, a big number of different kinds of long persistence phosphor exist now, and most of them have been developed during the past two decades. In recent years, strontium aluminates, especially $SrAl_2O_4$ and $Sr_4Al_{14}O_{25}$ doped with rare earth ions, have been regarded as promising candidates due to their excellent luminescence properties. Several attempts were initially used for synthesis route, such as conventional solid state reaction, sol-gel method, combustion, and microwave heating synthesis. Typically, the synthesis process will be more complex to obtain a good phosphor that consists of high intensity and long persistence glowing properties in an efficient, cheap, and simple way. Solid state reaction process has been extensively used for phosphor synthesis, but this process often results in poor homogeneity leading to high calcination temperature, irregular morphology, and long calcination period [1]. It has been reported that strontium aluminate phosphors were generally prepared at high temperatures (1400–1600°C) for developing a well crystallized structure. Some synthesis and luminescence parameters from recent publications are shown in Table 1.

Table 1. Literature data of synthesis conditions and photoluminescence characteristics of $SrAl_2O_4:Eu^{2+}$, Dy^{3+}

Composition	Structure	Dopant	Temperature	Atmosphere	Spectra		Ref.
			(°C)		PL (nm)	PLE (nm)	
$Sr_4Al_{14}O_{25}$:Eu, Dy	$SrAl_2O_4$ $Sr_4Al_{14}O_{25}$	Eu^{2+} Dy^{3+}	1000- 5h 600- 1300, 5h	Air-prefired Annealing reduction		490	[2]
$SrAl_2O_4$:EuDy, Bx	$SrAl_2O_4$ $Sr_4Al_{14}O_{25}$	Eu^{2+} Dy^{3+}	1000-pre-heat 4h 1200-1300 , 3 h	reduction $10\%H_2+90\%N_2$	320-420	400-520	[3]
$Sr_{1-3}Al_2O_4$: Eu_xDy_y		Eu^{2+} Dy^{3+}	1300- 4h	5 $\%H_2$+95 $\%N_2$	420	520	[4]
	$SrAl_2O_4$ $SrAl_4O_7$	Eu^{2+} Dy^{3+}	1300	Mild reduction Carbon/urea vapor		480-530 640	[5]
$SrAl_2O_4$:EuDy	$SrAl_2O_4$ $Sr_4Al_{14}O_{25}$	Eu^{2+} Dy^{3+}	1300, 4 h	Mild reduction Atmosphere activator carbon		520	[6]
$SrAl_2O_4$:EuDy		Eu^{2+} 1 mol % Dy^{3+} 2 mol %	1250-1300, 6h -4 h	Reduction Atmosphere N_2 + 12% H_2		520	[7]
$SrAl_2O_4$:EuDy	$SrAl_2O_4$: EuDy		1100-1200	Soft-chemical 1-5% H_2 + 95% N_2	260-320	520	[8]

Based on this summary, the selection of firing temperature and atmosphere is important to determine the good photoluminescence spectra and structure as well as microstructure properties. In Table 1, we present a comparison of the properties of $SrAl_2O_4:Eu^{2+}$, Dy^{3+} prepared by different groups of researchers. Most of phosphors were preheated at a suitable temperature of about 1000°C to generate proper precursor powders that enhance the final phase formation. After that, the powders were annealed at a high temperature of 1300°C in a reducing atmosphere (Table 1).

In this study, we focus our attention on the reduction in the firing temperature to improve the luminescent properties by single firing in graphite crucible. A graphite crucible was used to promote the formation of a reducing atmosphere, and this can lower the temperature to save the cost and time. The unique physical and chemical properties of the lanthanide oxides activated by Eu^{2+} ions make them useful in a variety of applications. The emission of these materials is highly efficient, and their emission wavelength heavily depends on host lattice. In the $SrAl_2O_4$ host lattice, the main emission band of Eu^{2+} ions is centered near 520 nm. When another trivalent rare earth ion, such as Dy^{3+} ions, is incorporated into the system, they can enhance the luminescence properties and prolong the afterglow of phosphor. The main goal of this research is to improve the synthesis process, to reduce the firing temperature, and to optimize the concentrations of Eu^{2+} - Dy^{3+}ions in order to obtain the bright persistent phosphors with long-lasting afterglow.

2. Experimental

The conventional solid state reaction is mostly used for the preparation of bulk phosphors. Strontium aluminate phosphors doped with Eu^{2+} and co-doped with Dy^{3+} ($SrAl_2O_4:Eu^{2+}$, Dy^{3+}) were prepared by solid state reaction approach using strontium carbonate ($SrCO_3$; Aldrich, 99.9 %), aluminum oxide (Al_2O_3), europium oxide (Eu_2O_3; Aldrich, 99.99 %), and dysprosium oxide (Dy_2O_3; Aldrich, 99.99 %) as starting materials. A small amount (0.2 mol %) of H_3BO_3 was used as a flux. The raw powders were mixed according to the nominal composition of $SrCO_3$ and Al_2O_3 for the host lattice of $SrAl_2O_4$. To activate this host by Eu^{2+} and Dy^{3+}ions, Eu_2O_3 and Dy_2O_3 were used. The concentration of Eu^{2+} ions and Dy^{3+} ions was optimized separately. An appropriate amount of the starting materials was weighted and mixed. First, the dry milling was used for 30 min, and then a small amount of water was added in the wet-mixing machine for the homogeneity of mixing powders and ground for 30 min. The resulting slurry was dried at 150°C for 3 h to remove the water content. After fully dried, the mixed white powder was placed in a small alumina crucible and then fired consecutively at 1100°C, 1150°C, 1200°C, 1250°C, and 1300°C for 2 h in a mild reducing atmosphere. The physical parameters, such as heating rates of 10°C per minute, cooling rates of 10°C per minute, and a heating time of 2 h, were the same for all samples. The small alumina crucibles with powders were put in a big graphite crucible and then heated at fixed temperature 2 h. The graphite crucible was used to create a reducing atmosphere, to ensure a complete reduction of Eu^{3+} to Eu^{2+}, and to crystallize and form the luminescence centers. The mixing–milling process was used after calcination to obtain a smaller particle size and a homogenous mixture. A set of $SrAl_2O_4:Eu^{2+}$ crystals with different Eu^{2+} ion concentrations of 0.3, 0.5, 0.7, and 1 mol % was synthesized to study the effect of Eu^{2+} activation. Another set of $SrAl_2O_4:Eu^{2+}$, Dy^{3+} crystals with different Dy^{3+} ion concentrations of 1, 2.5, 5, and 10 mol % was also prepared**.**

Structure analysis and phase identification were carried out using XRD and Raman Spectroscopy. A Bruker D8 Advance X-ray Diffractometer with Cu-Kα radiation of wavelength 1.54 Å was applied. Data have been collected by step-scanning 2θ from 10° to 90° and 0.034 s counting time at each step at room temperature. The morphology was observed using a Zeiss Supra 35VP field emission scanning electron microscope. Before SEM observation, the phosphor particles were coated (a thickness of about 5 nm) with Pt-Pd using ion sputter. The photoluminescence excitation and emission spectra were recorded using an IHR 550 UV Fluorescence Spectrometer Horiba Jobin Yvon. All the samples were excited by 325 nm radiation from a pulsed Xenon lamp 450 W. The emission spectra were registered in a wavelengths range of 350 to 625 nm. For measuring the excitation spectra, the monochromator analyzer was set to the maximum wavelength of emission spectra.

Raman measurements were performed at room temperature by Raman Horiba Jobin Vynon HR800UV with excitation through a microscope using the 514.5-nm line of an Ar^+ laser, as well as by a RENISHAW Invia Raman Microscope using an excitation source of 633 nm by the combination of He and Ne sources with an exposure time of 20 s.

3. Results and Discussion

3.1 Effect of firing temperature on $SrAl_2O_4:Eu^{2+}$, Dy^{3+}

Since one of the objectives of this work is to study the effect of firing temperature, samples with the same composition were synthesized at different temperatures and analyzed by XRD. The

study of different firing temperatures is essential in this work. The main reason is to determine the optimum firing temperature which will be used for further phosphor characterization. The Rietveld analysis was performed to determine the structure. Figure 1 shows the XRD patterns of $SrAl_2O_4$:Eu^{2+}, Dy^{3+} annealed at different firing temperatures of 1100 to 1300°C for 2 h in an active carbon atmosphere. It was found that the XRD patterns in a temperature range of 1100 to 1150°C include two phases $SrAl_2O_4$ and $Sr_4Al_{14}O_{25}$, indicating the formation of mixed oxide phases. When the firing temperature was raised to 1200°C, the diffraction peaks of $SrAl_2O_4$, $Sr_4Al_{14}O_{25}$, and $SrAl_4O_7$ appear with the major phase of $SrAl_2O_4$. Moreover, as the firing temperature was increased from 1200 to 1250°C, the XRD peaks were sharper and the stable phases of $SrAl_2O_4$ and $Sr_4Al_{14}O_{25}$ with higher crystallinity could be obtained. The diffraction peak corresponding to $SrAl_4O_7$ disappeared. An increase in peak intensities indicates that the crystallinity also increases as well as the crystal symmetry and size. Two phases $SrAl_2O_4$ and $Sr_4Al_{14}O_{25}$ remain as major and secondary if the firing temperature increases from 1250°C up to 1300°C.

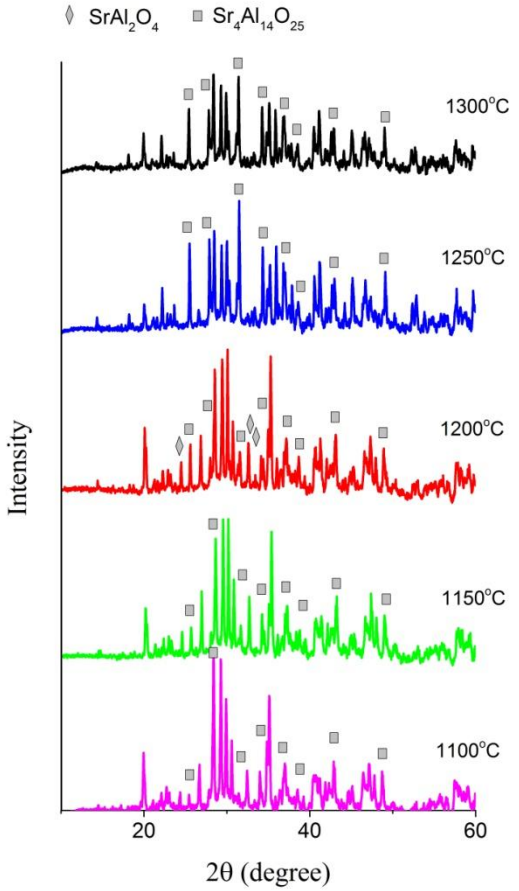

Fig.1. XRD patterns of phosphors at different temperatures.
[◊ = $SrAl_4O_7$, JCPDS - 25-1289; □ = $Sr_4Al_{14}O_{25}$, JCPDS - 52-1876, unmarked peaks belong to $SrAl_2O_4$, JCPDS - 74-0794].

3.2 Effect of Eu^{2+} and Dy^{3+} concentration on crystal structure

X-ray diffraction patterns of $SrAl_2O_4$:Eu^{2+}, Dy^{3+} obtained at 1250°C with different Eu^{2+} concentrations are shown in Fig. 2. The patterns match well with the characteristic diffraction peaks of strontium aluminate phosphor doped with Eu^{2+} and Dy^{3+} [9]. The major formed phase

$SrAl_2O_4$ is monoclinic and corresponds to standard JCPDS card data (74-0794). The secondary observed phase belongs to $Sr_4Al_{14}O_{25}$. This result indicates that the reaction conditions in this work are sufficient to obtain the $SrAl_2O_4$. Small changes of activator concentration do not show any effect on the phase formation.

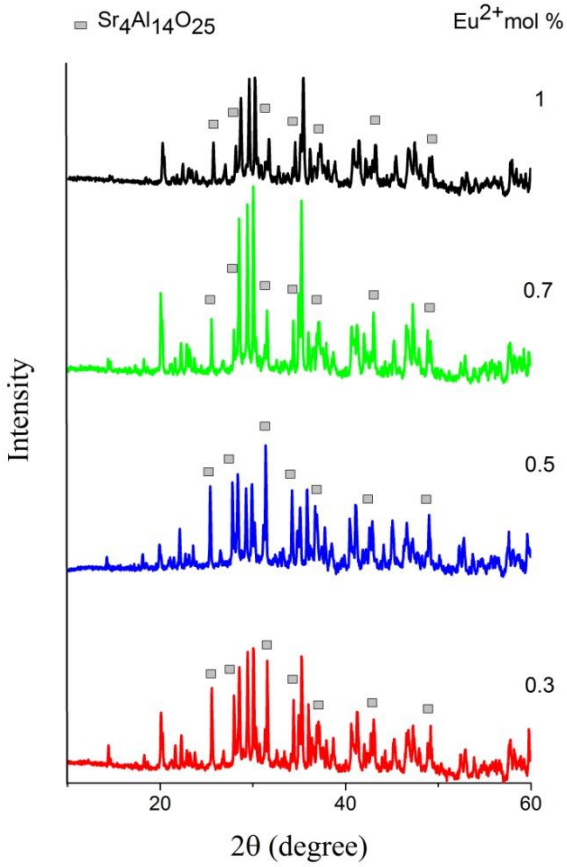

Fig. 2. XRD patterns of phosphors at different Eu^{2+} concentrations.
[□ = $Sr_4Al_{14}O_{25}$ - JCPDS , 52-1876, unmarked peaks belong to $SrAl_2O_4$, JCPDS - 74-0794].

Figure 3 depicts the XRD patterns of $SrAl_2O_4$, $SrAl_2O_4$:Eu^{2+} and $SrAl_2O_4$:Eu^{2+}, Dy^{3+} firing at 1250°C for 2 h. The XRD patterns show the monoclinic phase diffraction peaks of parent $SrAl_2O_4$ and secondary phase as octahedral $Sr_4Al_{14}O_{25}$. There is no much difference in XRD patterns in the system due to the replacement of Sr^{2+} by Eu^{2+} ions. In addition, a small amount of doped ions of Eu^{2+} and Dy^{3+} has almost no effect on the crystal structure of major phase and secondary phase of octahedral $Sr_4Al_{14}O_{25}$. By addition of Dy^{3+} ions, the intensity of XRD patterns increased indicating an increase in the crystallite size (see Table 2).

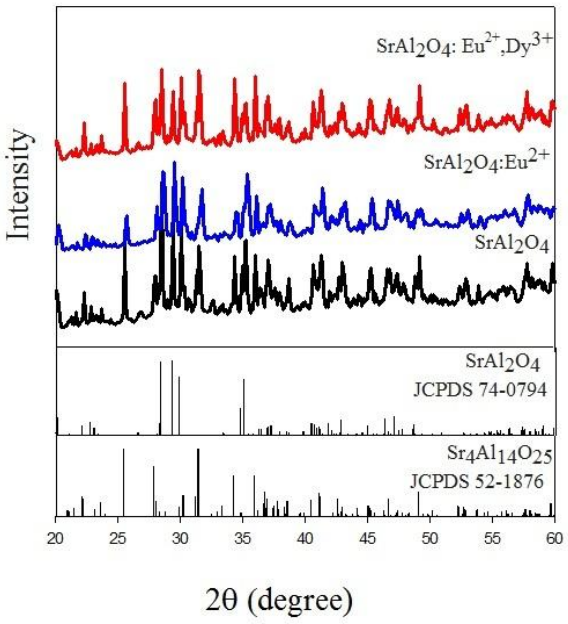

Fig. 3. XRD patterns of $SrAl_2O_4$, $SrAl_2O_4$:Eu^{2+} and $SrAl_2O_4$:Eu^{2+}, Dy^{3+}.

Table 2. Structural parameter of $SrAl_2O_4$, $SrAl_2O_4$:Eu^{2+} and $SrAl_2O_4$:Eu^{2+}, Dy^{3+} for monoclinic $SrAl_2O_4$

	$SrAl_2O_4$	$SrAl_2O_4$:Eu^{2+}	$SrAl_2O_4$:Eu^{2+}, Dy^{3+}
a (Å)	5.1549	5.1569	5.1564
b (Å)	8.8143	8.8217	8.8174
c (Å)	8.4378	8.4440	8.4397
β (°)	93.398	93.398	93.386
V ($Å^3$)	382.711	383.466	383.048
Crystallite size (Å)	913.4	726.6	964.8

Table 2 presents the variation of the lattice parameters and crystallite sizes of $SrAl_2O_4$, $SrAl_2O_4$:Eu^{2+} and $SrAl_2O_4$:Eu^{2+}, Dy^{3+} fired at 1250°C. It is evident from Table 2 that the corresponding lattice parameters (a), (b) and (c), as well as volume unit cells (V), were changed according the Vegard's law because of different activator ionic radius in comparison with the host lattice.

In order to enhance the understanding of the doping effect from the structural point of view, Raman scattering study is a very useful tool in investigating the lattice vibrational modes, which can provide details of lattice vibration changes. The Raman spectroscopy was applied in this work to complement the XRD data, particularly, when it concerns the doping and co-doping of our samples. Two lasers with 514.5 nm and 633 nm wavelengths were used. As the laser wavelength gets shorter, Raman scattering efficiency increases, but, at the same time, the risk of fluorescence also increases. Therefore, we used the 514.5-nm excitation to study only for the undoped host lattice of $SrAl_2O_4$ and 633 nm for the doped materials.

Raman spectrum presented in Fig. 4 was obtained in a spectral range of 100-1000 cm^{-1} using the 514.5-nm excitation wavelength from a continuous wave Ar^+ laser at room temperature. Incident light is focused on a sample through an optical microscope with a spatial resolution of < 2 μm in the backscattering geometry. We repeated these measurements several times from different points of the sample and registered the same spectra as shown in Fig. 4, which confirms the homogeneity of the prepared materials.

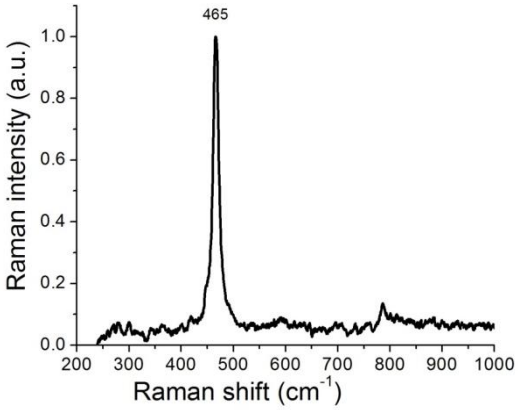

Fig. 4. Raman spectra of the $SrAl_2O_4$ host lattice fired at 1250°C and excited with the514.5 nm laser wavelength.

To a first approximation, we attribute modes at a frequency higher than 600 cm^{-1} to Al–O bond-stretching vibrations and the narrow low-frequency peaks below 250 cm^{-1} (not shown in Fig. 4) to tetrahedral librations or tilts. In the intermediate region, the assignment is impossible; by analogy with other compounds, we assign the most intense band at 465 cm^{-1} to the bending vibration of the O–Al–O angle [10]. This intermediate part of spectra is the most important, and this region (100-600 cm^{-1}) was measured carefully for all samples and shown in Fig. 5.

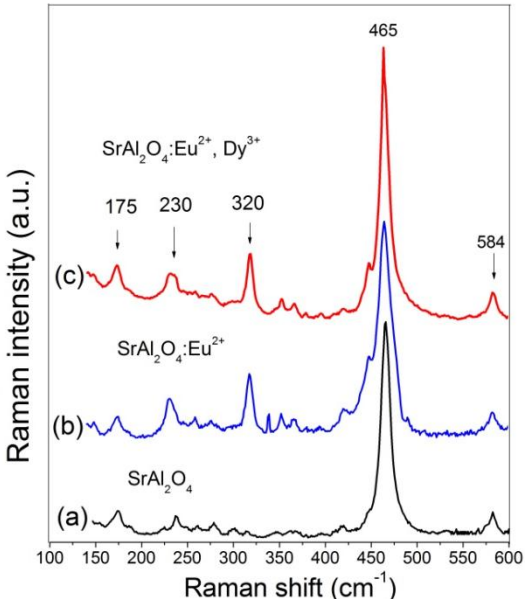

Fig. 5. Raman spectra of $SrAl_2O_4$, $SrAl_2O_4:Eu^{2+}$ and $SrAl_2O_4:Eu^{2+}$, Dy^{3+} fired at 1250°C and excited with the 633-nm laser wavelength.

The profiles (a,b,c) correspond to the Raman spectra of the $SrAl_2O_4$, $SrAl_2O_4:Eu^{2+}$ and $SrAl_2O_4:Eu^{2+}$, Dy^{3+} compositions, respectively. Theoretically, the Raman selection rules allow 81 active modes for monoclinic $SrAl_2O_4$ doped with Eu^{2+} [11]. However, as shown in Fig. 5, in the Raman spectra of Eu^{2+} and Dy^{3+} doped $SrAl_2O_4$, less than 14 active modes were observed, which is partially due to the possible overlap of some symmetry vibrations or the weak features of some Raman bands [12].

All spectra exhibit a ubiquitous 465-cm^{-1} band attributed to the bending of O–Al–O bonds in corner-sharing tetrahedra, indicating that the samples present very closely monoclinic structures.

The Raman spectra of $SrAl_2O_4$:Eu^{2+} and $SrAl_2O_4$:Eu^{2+}, Dy^{3+} are similar to the host $SrAl_2O_4$; however, they show several differences: one small new peak in the main band appears, some peaks especially at 230 and 320 cm^{-1} become stronger, and the width of strongest mode at 465 cm^{-1} has increased for doped phosphors. This result indicates that the lattice of the doped $SrAl_2O_4$ sample is considerably distorted. This is confirmed by the XRD results that show that the crystallite size for this phosphor totally decreases after doping with Eu^{2+}.

3.3 Morphology of $SrAl_2O_4:Eu^{2+},Dy^{3+}$ at different firing temperatures and activator concentrations

SEM study was carried out to investigate the surface morphology and the crystallite size of the synthesized samples. Figure 6 shows SEM images of $SrAl_2O_4:Eu^{2+}$, Dy^{3+} powders obtained at different firing temperatures. Crystal particles formed at lower firing temperature (a) and (b) show a smooth surface and a nonuniform formation of crystallites phosphor. It was observed that the samples fired at 1200°C (c) showed long needle-like crystals on the matrix surface, while the samples fired at 1250°C (d) formed small crystallite phosphor with varying sizes. With a further increase in the firing temperature to 1300°C (e), the surface matrix becomes smooth with solid matrix molten phosphor. Liquid phase sintering occurred at a high temperature because of the addition of flux H_3BO_3. This is believed to be associated with the Eu^{2+} ion content during heat treatment, which accelerates the formation of the crystallite of phosphor. Theoretically, the different shapes and sizes of the phosphor inhibit the absorption of the excitation energy and therefore reduce the emission energy intensity. Phosphor materials must have a narrow size distribution, non-agglomeration, and spherical morphology for good luminescence characteristics [13]. SEM characterization confirms that the optimum synthesis temperature for $SrAl_2O_4:Eu^{2+}$, Dy^{3+} in this study is 1250°C.

The microstructures of heated samples $SrAl_2O_4:Eu^{2+}$, Dy^{3+} with different Eu^{2+} concentrations are shown in Fig. 7. From this observation, we can say that their microstructure was quite different even though the phase form analyzed by XRD was the same. The sample with the lower concentration of activator (a) showed a nonuniform formation of crystallite phosphor. It was observed that the sample with the addition of 0.7 mol% Eu^{2+} (c) showed the homogenous needle-like crystal, while the samples with a high Eu^{2+} concentration of 1 mol % (d) are faceted crystals with varying sizes. This is associated with the Eu^{2+} ion content which accelerates the formation of phosphor crystallite. The multitude of different shapes and sizes of phosphor particles inhibits the absorption of excitation energy and therefore reduces the emission energy intensity.

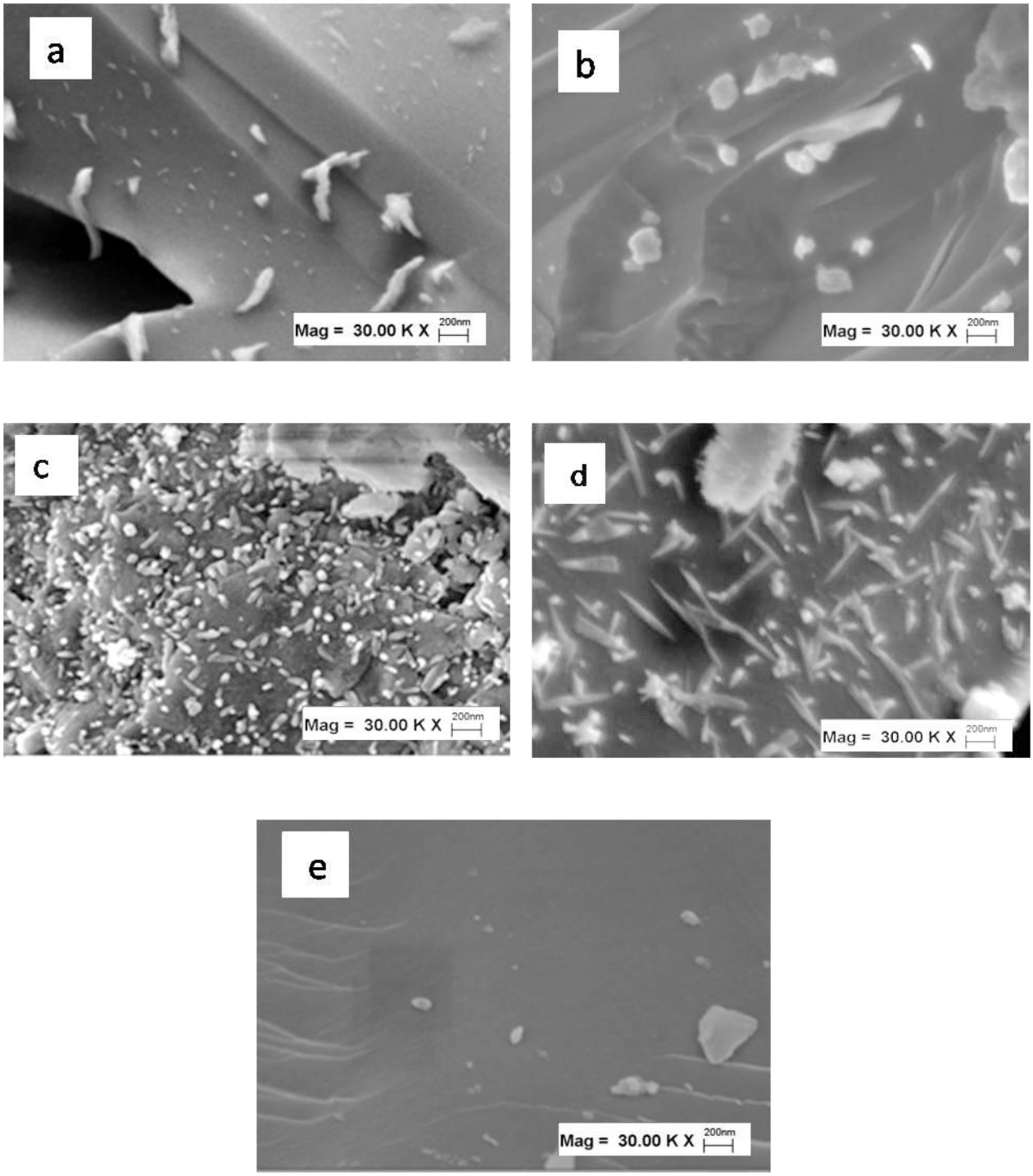

Fig. 6. SEM micrographs of $SrAl_2O_4:Eu^{2+}$, Dy^{3+} phosphor at different temperatures:
a) 1100°C, b) 1150°C, c) 1200°C , d) 1250°C, and e) 1300°C.

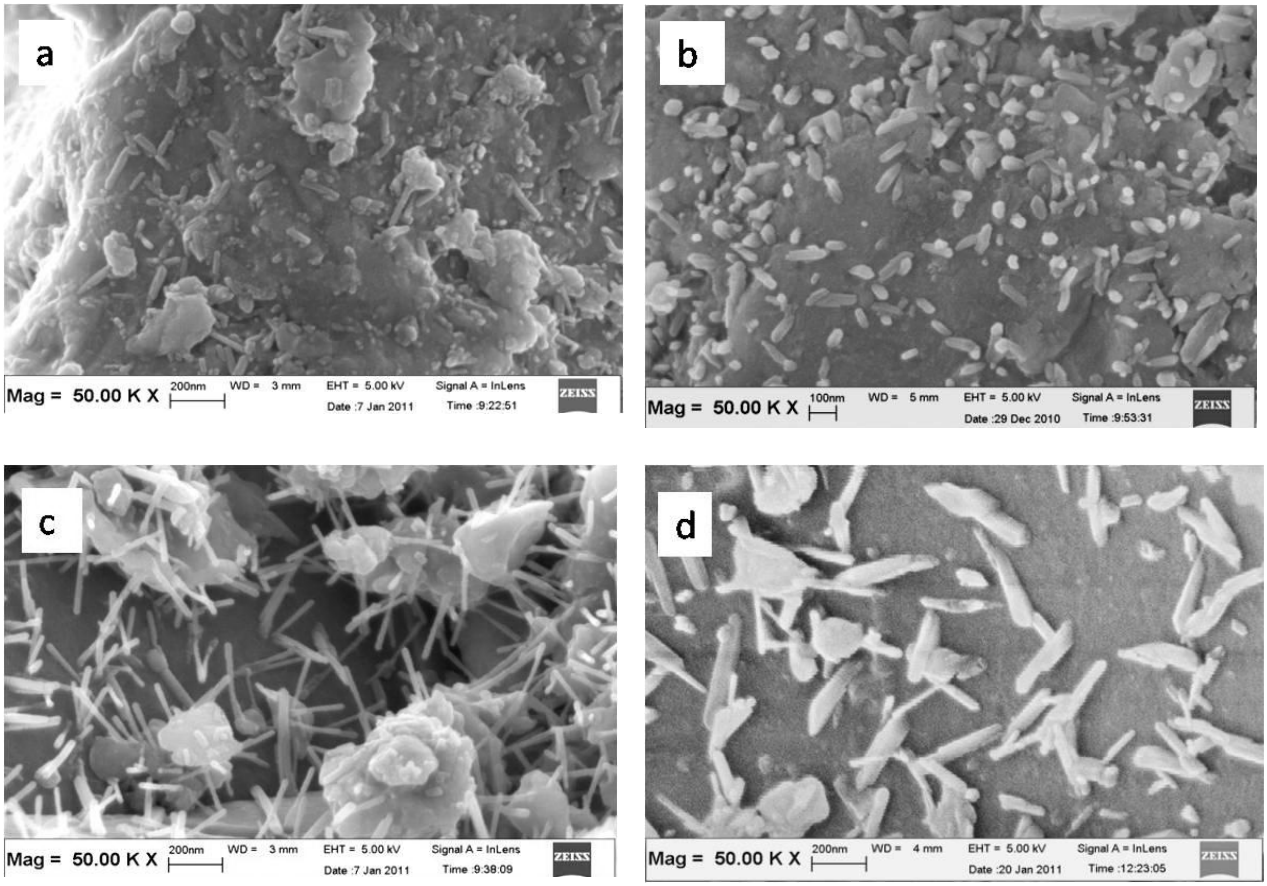

Fig. 7. SEM micrographs of $SrAl_2O_4:Eu^{2+}$, Dy^{3+} phosphor annealed at 1250°C with different Eu^{2+} concentrations: a) 0.3 mol % , b) 0.5 mol %, c) 0.7 mol %, and d) 1 mol %.

Figure 8 shows the morphology of $SrAl_2O_4$, $SrAl_2O_4:Eu^{2+}$ and $SrAl_2O_4:Eu^{2+}$, Dy^{3+} powders prepared at a firing temperature of 1250°C. All the samples show the formation of crystal structures of phosphor. For $SrAl_2O_4$ and $SrAl_2O_4:Eu^{2+}$, the crystal structures are clearer, longer, and inhomogeneous. The shape and size of the crystals are dissimilar. The double activated phosphor $SrAl_2O_4:Eu^{2+}$, Dy^{3+} shows the homogeneity of crystal structure. The shapes are around spherical morphology with homogeneous distribution.

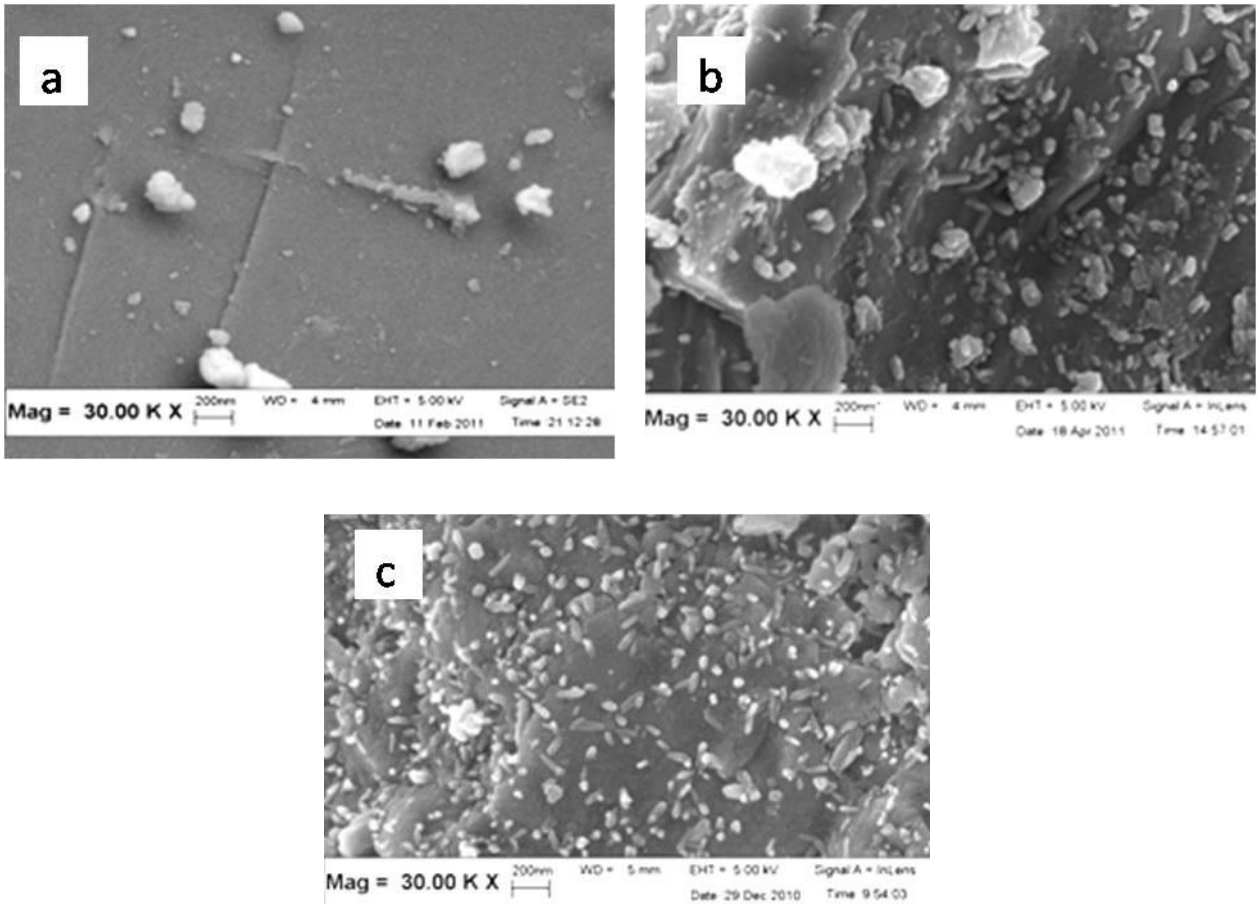

Fig. 8. SEM micrographs of phosphor at a temperature of 1250°C: (a) $SrAl_2O_4$, (b) $SrAl_2O_4:Eu^{2+}$, and (c) $SrAl_2O_4:Eu^{2+}$, Dy^{3+}.

3.4 Effect of activator concentrations and firing temperature on luminescence properties

The main goal in preparing persistent phosphor is the longest and the most intense afterglow emission. Therefore, the process of optimization of the activator concentration is very important. Figures 9 and 10 show the emission spectra of $SrAl_2O_4:Eu^{2+}$ with corresponding Eu^{2+} concentrations of 0.3, 0.5, 0.7, and 1 mol %. For the best sample of $Eu_{0.5}Sr_{0.95}Al_2O_4$ excited with the 325-nm wavelength, the emission band with maximum at 500 nm was registered and it agrees well with the reported spectra profiles in [5-6]. This emission is attributed to the $4f^6 5d^1 \rightarrow 4f^7$ transition in Eu^{2+} ions. No characteristic peaks of Eu^{3+} have been observed in the presented spectra. This means that the active carbon during firing can effectively reduce Eu^{3+} to Eu^{2+}. The Eu^{2+} ions are the luminescence centers for the phosphorescence. A further increase in the Eu^{2+} ion concentration up to 0.7 mol % gradually decreases the emission intensity due to the quenching effect.

There are two main parameters that characterize the persistent phosphors: brightness and long-lasting afterglow.

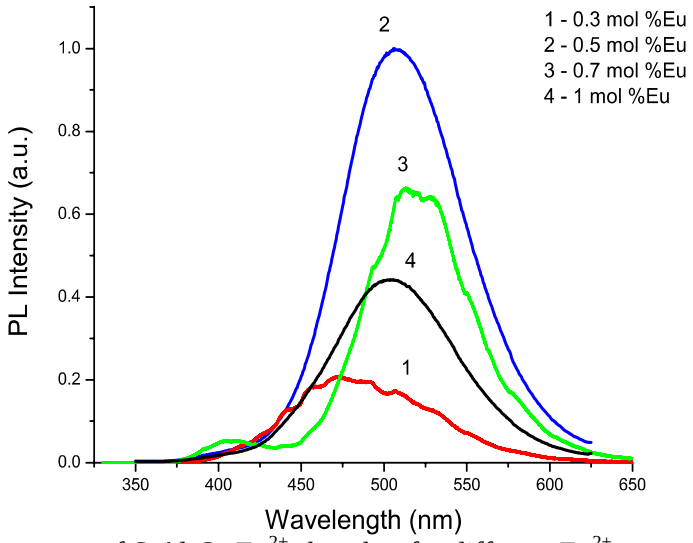

Fig. 9. Emission spectra of $SrAl_2O_4:Eu^{2+}$ phosphor for different Eu^{2+} concentrations.

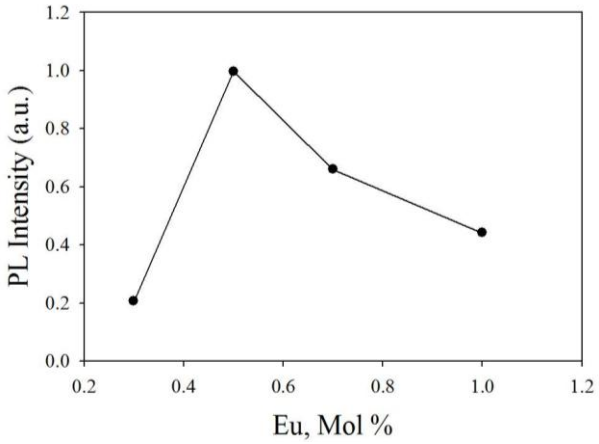

Fig. 10. PL intensity versus Eu concentration in $SrAl_2O_4:Eu^{2+}$.

By co-doping the green-emitting phosphor $SrAl_2O_4:Eu^{2+}$ (already showing a relatively strong and long-lasting afterglow by itself) with the rare earth element dysprosium Dy^{3+}, it is possible to create a material that emits bright light for hours after ending the excitation [14-15].

The luminescence (or phosphorescence for persistent phosphors) intensity of $SrAl_2O_4:Eu^{2+}$, Dy^{3+} doped with various amount of Dy^{3+} ions are presented in Fig. 11. If we increase the Dy^{3+} ion concentration from 0 to 1 mol %, the intensity also increases and attains maximum emission spectra Fig. 11 (2). Then, with a further increase in Dy^{3+} ions, it decreases as shown in Fig. 11. It is obvious that a higher concentration of Dy^{3+} ions in the host lattice will cause the concentration quenching process to decrease the phosphorescence intensity. We can confirm the role of Dy^{3+} ions as hole traps, because there are no emission spectra corresponding to the Dy^{3+} emission in all samples. Dy^{3+} ions also function as energy transporting media and induce the formation of hole traps associated with Sr^{2+} vacancies introduced because of charge compensation [16]. These trap centers generated during the phosphor excitation prolong the glowing times. The phosphorescence intensity depends on the density of traps located at suitable depths. It can be assumed from our experiments that a small amount of Dy^{3+} ions is sufficient to form trap defects in this matrix.

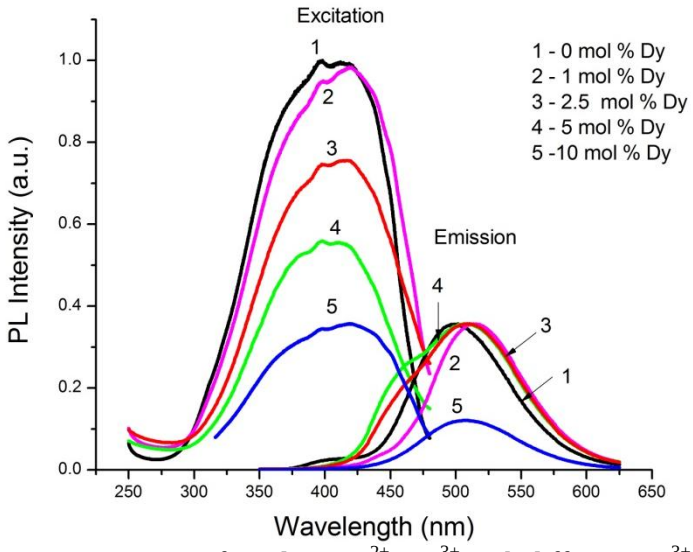

Fig. 11. Excitation and emission spectra of $SrAl_2O_4:Eu^{2+}$, Dy^{3+} with different Dy^{3+} concentrations.

To compare the experimental results, PLE and PL spectra for $SrAl_2O_4:Eu^{2+}$ (1) and $SrAl_2O_4:Eu^{2+}$, Dy^{3+} (2) are shown together in Fig. 12. The emission band peak for only Eu^{2+} doped sample is placed at 500 nm. The codoping of this sample with an optimized Dy^{3+} concentration shifts this peak to 508 nm. This shifting of emission peak is attributed to changes in the crystal field strength around Eu^{2+} ions, when Dy^{3+} ions are introduced. This observation is in good agreement with XRD data, which show that the crystallite size increased for $SrAl_2O_4:Eu^{2+}$, Dy^{3+} resulting in an increase in the crystal symmetry and thus enhancement of the crystal field strength. Two weak resolved bands in the excitation spectra at 398 nm and 419 nm were observed in both PLE spectra (1 and 2). These bands correspond to the crystal field splitting of the Eu^{2+} d-orbitals. We noted here that all the samples were synthesized at 1250°C in a reducing atmosphere in a graphite crucible that totally converted Eu^{3+} to the Eu^{2+} oxidation state. The emission spectra do not show any bands corresponding to Eu^{3+} or Dy^{3+} emissions in all the samples in a range of 350–650 nm. This also confirms that Dy^{3+} ions in the host lattice serve as hole or electron traps and energy transporting media.

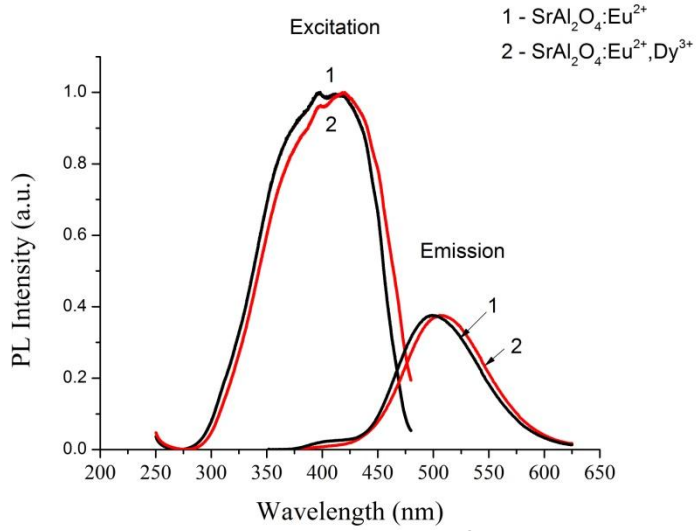

Fig. 12. Excitation and emission spectra for $SrAl_2O_4:Eu^{2+}$ (*1*) and $SrAl_2O_4:Eu^{2+}$, Dy^{3+} (*2*).

The firing temperature is another important parameter that affects the grain size and photoluminescence emission of phosphor. In order to study the role of firing temperature, we synthesized optimized $SrAl_2O_4$:Eu^{2+}, Dy^{3+} (0.5 mol % of Eu^{2+} and 1 mol % of Dy^{3+}) phosphor in the firing range (1100–1300°C). Figure 13 shows the effects of the firing temperature on PL spectra. The shape of spectra and PL intensity significantly changed with temperature variation. The emission spectra of $SrAl_2O_4$:Eu^{2+}, Dy^{3+} increase and shift when the temperature increases from 1100°C to 1250°C. However, their emission intensity is reduced, and the differences between all the samples fired at different temperatures indicate the different natures of Eu^{2+} surrounding [9]. Maximum luminescence was observed at 1250°C. This could probably be attributed to its better crystallinity. For samples fired at 1250°C, it was observed that the sharp emission spectrum peaked at 508 nm under the 325-nm excitation leads to the green luminescence. Poort et al. suggested that the 450 and 520 nm emission bands originate to the $4f^6 5d^1 \rightarrow 4f^7$ transition of Eu^{2+} ions located at the two different crystallographic strontium sites in $SrAl_2O_4$ [2, 17-18]. Two types of Sr^{2+} site are also present in our phosphors; one is surrounded by AlO_4 tetrahedra and the other by AlO_6 octahedra. The ionic radius of Sr^{2+} ($r_{Sr^{2+}}$ = 1.20Å) is quite similar to the ionic radius of Eu^{2+} ($r_{Eu^{2+}}$ = 1.01Å). Hence, the Eu^{2+} ions can easily substitute the Sr^{2+} ion site in the matrix phosphor [8]. However, for samples fired at 1150 and 1200°C, the emission spectra are at 491 nm. It is confirmed that the Eu^{2+} emission efficiency is very sensitive to firing temperature. At a lower temperature of 1100°C, the decrease in the emission intensity may be due to the small amount of Eu^{2+} ions diffused into the host lattice of $SrAl_2O_4$. At a high temperature of 1300°C, the emission intensity was totally reduced, and this is because of the rapid diffusion of Eu^{2+}, Dy^{3+} ions in the host lattice-grain boundary diffusion. The peak positions in the emission spectra depend on the nature of the Eu^{2+} surrounding; therefore, Eu^{2+} ions can emit different visible light in the various crystal fields. Figure 13 suggests that T = 1250°C is an optimum temperature for the best PL emission intensity.

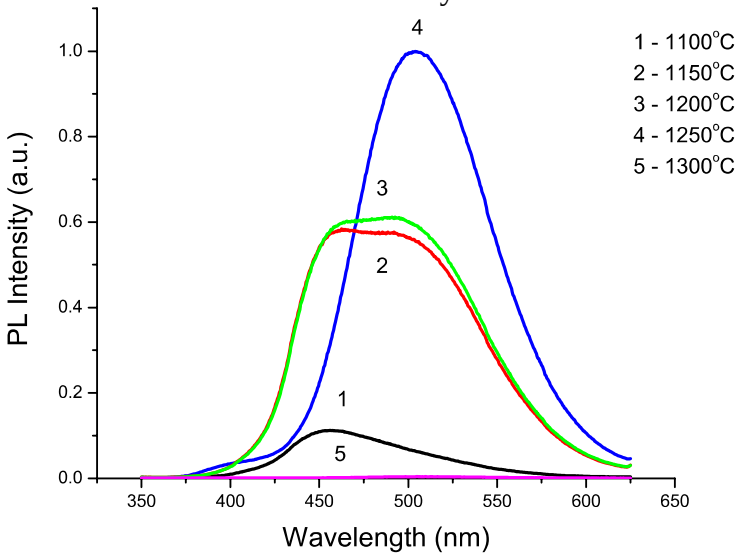

Fig. 13. Emission spectra of the phosphor samples at different firing temperatures.

In Figs. 14 and 15, we show the excitation and emission spectra for $SrAl_2O_4$:Eu^{2+} registered at room and low temperatures.

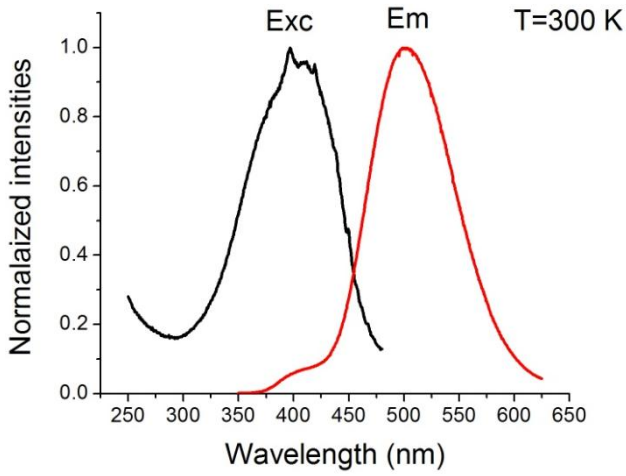

Fig. 14. Normalized excitation (λ_{em}=500 nm) and emission (λ_{exc}= 325 nm) spectra for $SrAl_2O_4:Eu^{2+}$ at room temperature.

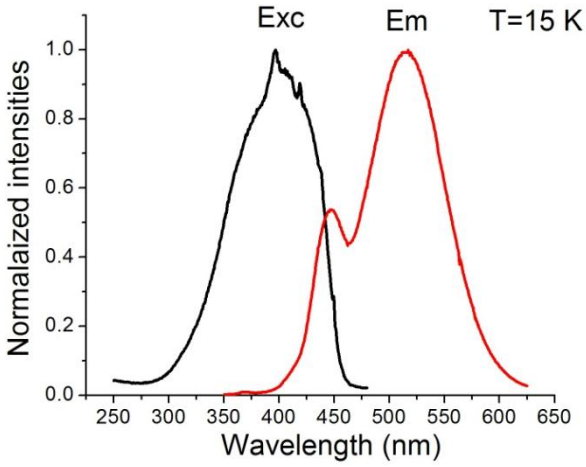

Fig. 15. Normalized excitation (λ_{em}=500 nm) and emission (λ_{exc}= 325 nm) spectra for $SrAl_2O_4:Eu^{2+}$ at 15 K.

One additional band around 450 nm in the emission spectrum was registered at a low temperature. The luminescence at 500 nm is commonly attributed to the parity-allowed electric dipole transition, $4f^6 5d^1 \rightarrow 4f^7$, of the Eu^{2+} ion [19]. The origin of the 450-nm emission is under discussion. Poort et al. suggested that the 450 and 520 nm emission bands originate from the emission of the Eu^{2+} ion located at the two different crystallographic strontium sites [20]. Clabau et al. criticized this assignment and proposed that the 450 nm band arises from the charge transfer from oxygen to residual Eu^{3+} ion that takes place upon UV irradiation and is associated with a hole trapping at Sr^{2+} vacancies [19]. Holsa et al. consider this band as anomalous low-temperature luminescence and suggest that Eu^{2+} ion may exhibit this kind of unusual luminescence from a higher Eu^{2+} 5d state [21]. This band needs a further more detailed examination.

4. Conclusions

Green phosphor $SrAl_2O_4:Eu^{2+}$, Dy^{3+} with improved properties was successfully synthesized by solid state reaction. The optimum firing temperature was greatly reduced to 1250°C. The results revealed the presence of a monoclinic structure of $SrAl_2O_4$ as a major phase and the intermediate phase identified as an orthorhombic structure of $Sr_4Al_{14}O_{25}$. It was found that the combination of 0.5 mol % Eu_2O_3 and 1 mol % Dy_2O_3 is the best for high photoluminescence effect in this system. A new luminescent band at a low temperature around 450 nm in the emission spectrum was observed and discussed.

Acknowledgements

This work was financially supported by Short Term Grant, Universiti Sains Malaysia, under grant No. 304/PBAHAN/60311036 and Post-Graduate Grant Research, 1001/PBAHAN/8044033 to conduct this research.

References

[1] C.H. Lu, and P.C. Wu, J. Alloys and Comp. 466, 457 (2008).
[2] T. Aitasalo, J. Holsa, H. Jungner, J.-C. Krupa, M. Lastusaari, J. Legendziewicz, and J. Niittykoski, Radiat. Meas. 38, 727 (2004).
[3] A. Nag, and T.R.N. Kutty, J. Alloys. Compd. 354, 221 (2003).
[4] X. Lu, W. Shu, Q. Yu, Q. Fang, and X. Xiong, Glass Phys. Chem. 33, 62 (2007).
[5] D. Haranath, V. Shanker, H. Chander, and P. Sharma, J. Phys. D Appl. Phys. 36, 2244 (2003).
[6] S.D. Han, K.C. Singh, T.Y. Cho, H.S. Lee, D. Jakhar, J.P. Hulme, C.H. Han, J.D. Kim, I.S. Chun, and J. Gwak, J.Lumin. 128, 301 (2008).
[7] T. Aitasalo, P. Dere, J. Holsa, H. Jungner, J.C. Krupa, M. Lastusaari, J. Legendziewicz, J. Niittykoski, and W. Strk, J Solid State. Chem. 171, 114 (2003).
[8] Y. Lin, Z. Zhang, F. Zhang, Z. Tang, and Q. Chen, Mater. Chem. Phys. 65, 103 (2000).
[9] R. Melendrez, O. Arellano-Tanori, M. Pedroza-Montero, W.M. Yen, and M. Barboza-Flores, J. Lumin. 129, 679 (2009).
[10] P. Escribano, M. Marchal, M. Luisa Sanjuán, P. Alonso-Gutiérrez, B. Julián, and E. Cordoncillo, J. Solid State Chem. 178, 1978 (2005).
[11] M.A. Salim, R. Hussin, M.S. Abdullah, S. Abdullah, N.S. Alias, S.A.A. Fuzi, M.N.M. Yusuf, K.M. Mahbor, Aip Conf. Proc. 17, 59 (2009).
[12] K.Liang, Y.Qi, C. Lu, J. Raman Spectrosc. 40, 2088 (2009).
[13] X. Yu, C. Zhou, X. He, Z. Peng, and S.P. Yang, Mater. Lett. 58, 2927 (2004).
[14] Abbruscato, V., J. Electrochem. Soc., 118, 930 (1971)
[15] Takasaki H., Tanabe S., and Hanada T., J. Ceram. Soc. Jpn., 104, 322 (1996).
[16] Y. Lin, Z. Tang, and Z. Zhang, Mater. Lett. 51, 14 (2001).
[17] T. Aitasalo, J. Holsa., H. Jungner, M. Lastusaari, and J. Niittykoski, J. Lumin. 94, 59 (2001).
[18] Y. Li, Y. Fang, N. Hirosaki, R.J. Xie, L. Liu, T. Takeda, and X. Li, J. Mater. 3, 1692 (2010).
[19] F. Clabau, X. Rocquefelte, S. Jobic, P. Deniard, M.H. Whangbo, A. Garcia, and T. Le Mercier, Chem. Mater. 17, 3904 (2005).
[20] S. Poort, W.Blokpoel, and G. Blasse, Chem.Mater. 7, 1547 (1995)
[21] J. Holsa, H. Jungner, M. Lastusaari, and J. Niittykoski, J. Alloys. Compd. 323, 326 (2001).

IMPROVEMENT OF PROPERTIES OF SILVER FILLED EPOXY COMPOSITES VIA PROCESSING METHOD

G. Suriati, M. Mariatti*, and A. Azizan

[1]*School of Materials and Mineral Resources Engineering, Engineering Campus, University Sains Malaysia, 14300 Nibong Tebal, Seberang Prai Selatan, Penang, Malaysia*

*(*Corresponding author: mariatti@eng.usm.my;*
Tel. No.: 604 5995262; Fax No.: 604 5941011)

(Received 12 April 2012)

Abstract

Conductive composites consisting of an epoxy matrix and silver flakes were fabricated, and mechanical, thermal and electric properties were investigated as a function of particle concentration and processing techniques. Scanning electron microscope (SEM) was utilized in an attempt to study the effect of the processing method on the distribution of silver flakes in the matrix. As observed by SEM, the use of a homogenizer enhanced the distribution of silver flakes with reducing the particle agglomeration due to the presence of shear force during mixing. The application of shear mixing during the fabrication of conductive polymer composites increased the electric conductivity, flexural modulus, and storage modulus of the silver filled epoxy composite.

Introduction

The demand for advanced materials, such as composite materials with better properties, to meet new requirements or to replace existing materials in a variety of applications, is incessantly increasing [1]. Nowadays, conductive polymer composites have received great attention as an alternative to current lead-solder system. As revealed by numerous researchers [2-5], polymer materials can attain electric conductivity either by synthesis of a polymer of definite chemical structure [6] or by the introduction of electrically conductive filler, such as metal powders, carbon black and graphite [7]. In an electrically conductive adhesive (ECA) which consists of a polymer and a conductive filler, the polymer resin will provide mechanical interconnection, while the conductive filler, which is normally silver flake, provides electric conductivity [8, 9]. For a composite material that consist of two different phases, such as ECA, the distribution of the filler which affects the interface bonding or adhesion between the filler and the matrix has a great influence on the properties of the composite [1]. Furthermore, the distribution of the filler in the polymer matrix depends on particle type and size, specific surface area, volume content of particles, and conditions of mixing [1, 2, 4, 7]. As is known, particle powders tend to agglomerate and stick together due to adhesive forces. Relative to particle mass forces, the adhesive forces increase with decreasing particle size. In order to obtain well dispersed fillers in the matrix, the way of combining the polymer matrix and the filler powder is important in influencing the final composite properties. Various methods, such as ultrasonic, homogenizer, mechanical stirrer and manual mixing, have been used in preparing the conductive composite as reported in previous works [11, 12].

In the present work, a mechanical method using a homogenizer has been compared with manual mixing (by hand) in producing the silver flake filled epoxy composite. The manual mixing method has been used and reported in previous works [9, 13]. Meanwhile, the using of a homogenizer was reported to introduce high shear forces during dispersion. This will break up the filler agglomerates and distribute the individual filler more homogeneously in the polymer [1]. Therefore, the purpose of this work is to examine and compare the effect of two types of different processing techniques on the filler dispersion and composite properties. Electric conductivity and flexural and thermal properties obtained in this study were also related with the morphology of the composites.

1. Experimental

2.1 Materials

The epoxy resin named EPON™ Resin 8281, supplied by Hexion Specialty Chemicals, Inc. was used as a matrix in this research. It is also chemically termed as Bisphenol-A-(epichlorohydrin). The curing agent used in the study is Polyetheramine D230 (PEA D230), supplied by BASF Corporation with a density of 0.946 g/ml at 298 K. Thirty two parts by weight of PEA D230 was added into 100 parts of EPON^{TM} Resin 8281 for curing process. Silver flakes with an average size of 4-8 μm and a density of 10.49 g/cm^3 were used as conductive filler. Filler loadings were varied from 0 vol % to 8 vol %.

2.2 Processing methods

In this study, two different processing techniques were employed to fabricate silver flake/epoxy composite: manual mixing and shear mixing. Manual mixing was carried out according to previous work [9] while for shear mixing, a homogenizer with 20000 rpm was introduced to improve the distribution of the filler in the epoxy matrix. Silver flakes were added into the resin and stirred for about 10 min followed by ultrasonication for 10 min in order to aid the dispersion of the filler in the epoxy. Then, the mixtures were evacuated at 35˚C for about 0.5 h to further remove the microbubbles and macrobubbles. After that, the mixtures were added with a curing agent and were stirred for other 10 min. Finally, the mixture was evacuated at room temperature before curing in an oven at 100°C for 1 h, which was followed by a post-cure at 125°C for 3 h.

2.3 Characterization

For conductivity test, we used an instrument named LCR Meter. The value of volume resistivity is defined as the electric resistance of a cube of material and determined according to (1) and (2):

$$V = IR_v \tag{1}$$

$$\rho_v = \frac{R_v A}{t} \tag{2}$$

where ρ_v is the volume resistivity, R_v is the volume resistance, A is the area of conductor, and t is the thickness of the sample pieces. Three-point bending tests were performed based on the standard test method, ASTM D 790-98. Rectangular cross section specimens with a length of 50

mm and a width of 12 mm were used in the testing. The testing was carried out with an Instron 3366 at room temperature with a crosshead speed of 5 mm/min while the sample's ratio of span length to thickness was maintained at 16 : 1. The fracture surface of the flexural test samples were observed using a Zeiss Supra 35VP Field Emission Scanning Electron Microscope (FESEM). Dynamic Mechanical Analysis was carried out by using a PelkinElmer DMA 8000 in a dual-cantilever mode at a temperature of 30-180°C. The thermal stability and the weight loss profile of silver/epoxy composites were examined using a PerkinElmer TGA 7. All TGA measurements were performed in a nitrogen atmosphere by heating the samples from 30-600°C at a heating rate of 10°C/min. The coefficient of thermal expansion of the composites was measured using a LINSEIS Dilatometer L75/1550. The specimens (20 mm x 4 mm x 1.8 mm) were tested at a temperature that changed from 30°C to 230°C at a heating rate of 3°C/min under an ambient atmosphere.

3. Results and discussion

3.1 Electric conductivity

As the properties of the polymer composite were affected by the dispersion of the filler in the polymer matrix, the use of different mixing techniques was expected to improve the distribution of the filler and hence enhance the electric conductivity of the polymer composite. A better dispersion of filler could result to better surface contacts which increase the current carrier from one particle to another [7]. The theory of percolation threshold indicated that the behavior of a material could change from insulator to conductor at a certain filler loading [3-5]. Figure 1 shows that the electric conductivity of silver flake filled epoxy composites prepared by manual and homogenizer mixing increased with increasing content of silver flakes. Both samples prepared by manual and homogenizer mixing demonstrate a percolation threshold at 6 vol %. The increase in electric conductivity with increasing content of silver flakes could be explained by the following. As the concentration of conducting particles increases, small particle agglomerates are first formed in the systems which then form conducting clusters [4]. As particles contact between these conducting clusters increase, the efficiency of current carrier is improved and furthermore increases the conductivity composites. It also can be seen in Fig. 1 that the conductivity of the samples prepared by shear mixing showed a higher conductivity compared to that of manual mixing. It has been reported that the interfacial resistance between fillers influences the electric conductivity of the composite [14]. Interfacial resistance is the resistance forming at a surface boundary between adjacent regions; in this case, between one particle and another. Our previous work [15] showed that a silver nanoparticle tends to form an aggregate and affects the distribution of the filler throughout the matrix as compared to a micron-sized filler. The poor distribution and agglomeration of silver flakes prepared by manual mixing subsequently increases the surface resistance and reduces the conductivity of the composites.

From the result of electric conductivity, the percolation threshold for both samples prepared by manual and shear mixing were achieved at 6 vol % loading of silver flakes. Below that point, the composite samples remain as insulator. The morphology of the samples observed by SEM (Fig. 2) shows that, at 4 vol % of silver flakes, the matrix content was dominant compared to the filler content. Hence, the metal-to-metal contacts are not sufficient to conduct the current throughout the sample. At a 6 vol % concentration, the conducting bridges, which are referred as to percolation threshold, are created across the single crystal. These bridges may be composed of single particles or of their aggregates. At this moment, the nonconducting system is transformed

into a conducting state. However, above the percolation threshold, which is 6 vol % of filler loading, the conductivity of the samples are remains unchanged, and this result is supported by previous works [5, 9, 16, 17].

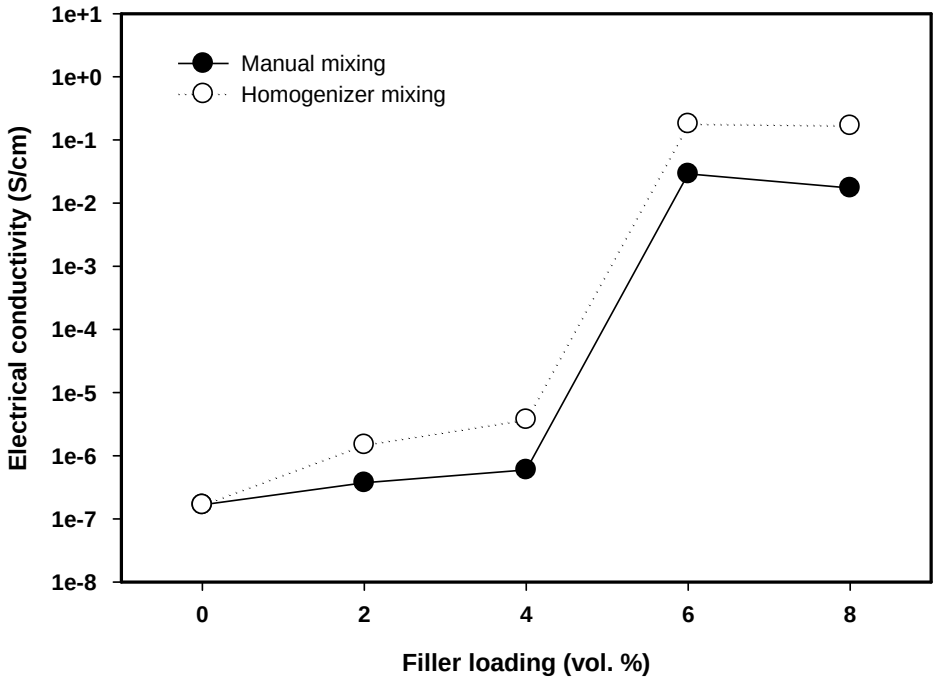

Fig. 1. Electric conductivity of the silver filled epoxy composite prepared by manual and homogenizer mixing.

The morphology of the samples depicted in Figs. 2b–2g show that the use of a homogenizer can break up the agglomeration of Ag fillers and subsequently reduced the size of Ag flake particles. At filler loadings of 4, 6, and 8 vol %, it can be seen that the use of a homogenizer gave a better dispersion of the filler (Figs. 2c, 2e, and 2g) compared to the samples prepared by manual mixing (Figs. 2b, 2d, and 2f), respectively. This observation might be due to the introduction of external shear forces generated by the homogenizer which could separate and break up the agglomeration of silver flakes to individual particles followed by better dispersion in epoxy resin compared to manual mixing. The samples prepared by manual mixing, especially at a high filler loading (Fig. 2d) also showed a higher agglomeration compared to the sample mixed with a homogenizer (Fig. 2e), which gave better distribution throughout the epoxy matrix.

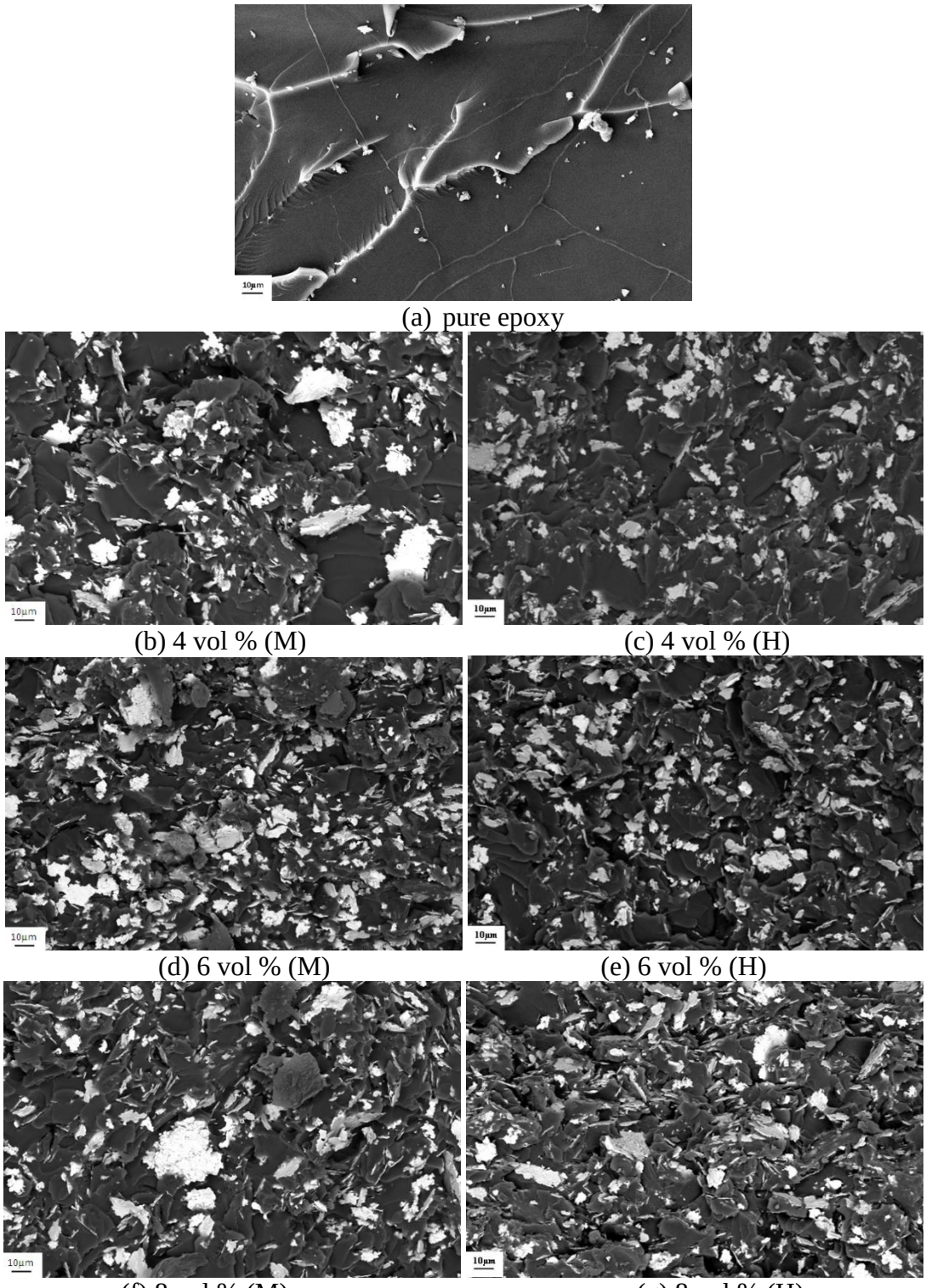

(a) pure epoxy

(b) 4 vol % (M) (c) 4 vol % (H)

(d) 6 vol % (M) (e) 6 vol % (H)

(f) 8 vol % (M) (g) 8 vol % (H)

Fig. 2. Fracture surface of pure epoxy and silver composites at different filler loading. (M) and (H) denote manual mixing and homogenizer mixing, respectively.

3.2 Flexural test

Figure 3 depicts flexural strength and flexural modulus for the silver filled epoxy composites prepared by manual and homogenizer mixing. It is evident from the figure that flexural strength for the composite mixed by a homogenizer at a low filler loading (e.g., 4 vol % and below) does not show any significant improvement and is slightly lower than that of the composite mixed by manual mixing. However, the deterioration in flexural strength at higher filler loading (6 and 8 vol %) for both processing method, which is even lower than unfilled epoxy, could be due to a number of reasons, such as weak interfacial bonding at the silver flakes and matrix interfaces and also a high aggregation of silver flakes with increasing amount of the filler. As the dispersion of the filler throughout the matrix affects the properties of the composite, it can be seen that composite mixed by a homogenizer shows an improvement at a higher filler loading (6 and 8 vol %) compared to those prepared by manual mixing at the same filler loading. From here, it can be seen that high shear forces introduced by the homogenizer were able to break up the particle agglomeration especially at high filler loading where the content of the filler is relatively high. The size distributions of Ag filler in the epoxy matrix (Fig. 4) for samples with 8 vol % of filler prepared by manual and homogenizer mixing were compared. The result clearly showed that silver flakes in the epoxy matrix prepared by manual mixing has a larger distribution which might be caused by agglomerations of the filler compared to the samples which prepared by homogenizer mixing at the same filler loading. The presence of these agglomerations could act as a stress concentrator which led to a decrease in the properties of the composites.

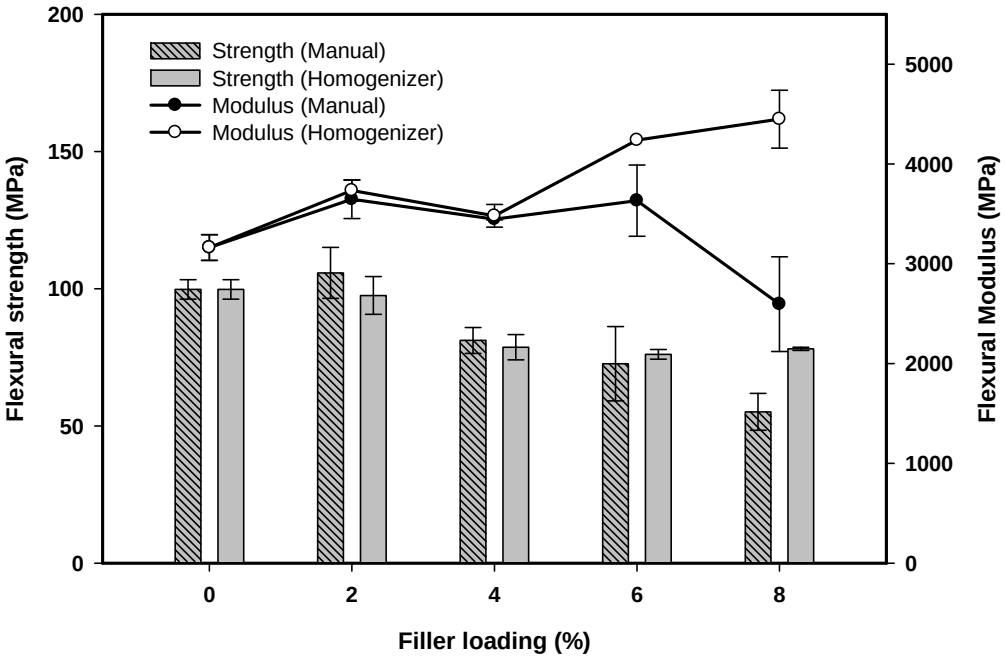

Fig. 3. Flexural strength and modulus at different filler loadings of silver flake filled epoxy composites prepared by different processing methods.

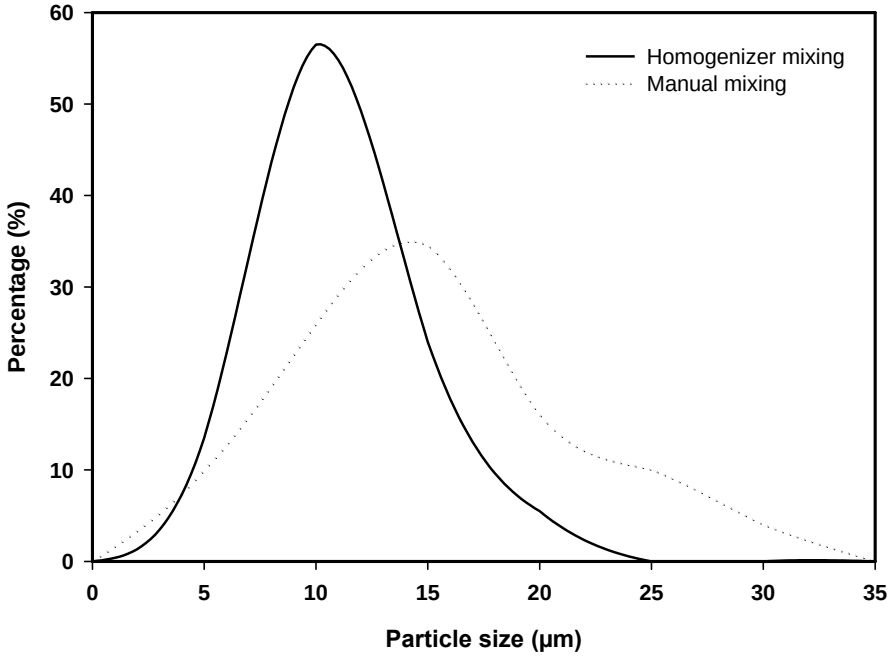

Fig. 4. Size distribution of silver flakes in epoxy matrix (8 vol %) calculated from the SEM image.

According to the rubber elasticity theory, there are four factors affecting the polymer composites elasticity [18]. The modulus of polymer composites could be controlled by the degree of cure, the presence of a solvent, strain induced crystallization, and the effect of fillers. Theoretically, the modulus of a composite material increases with increasing filler loading. The addition of rigid particles to the polymer matrix can easily improve the modulus since the rigidity of an inorganic filler is generally much higher than that of an organic polymer. Hwang [18] reported that the modulus of polymer composite materials increased with an increase in the filler content and a decrease in the filler size. However, despite this factor, it was reported that the size and distribution of filler particles also play an important role. From the result in Fig., we can see that the sample at 8 vol % prepared by manual mixing undergoes a significant decrement of flexural modulus at a higher filler content which is not quite pronounced for the sample prepared by homogenizer mixing. This observation might be due to the filler agglomeration, because at this loading, a high amount of the filler also could increase the viscosity and hence reduce the process ability. The presence of agglomeration subsequently increased the size of filler lumps which then act as a stress concentrator when it is subjected to load. In addition, although most of the composites (except the sample of 8 vol % prepared by manual mixing) exhibit a higher modulus than pure epoxy, they however show final failure at a much lower strain than the pure epoxy.

3.3 Dynamic Mechanical Analysis (DMA)

Figures 5 and 6 depict the storage modulus (E') – and tan delta – temperature profile for unfilled epoxy and silver flake filled epoxy composites prepared by manual and homogenizer mixing, respectively. The curves show a general shape where the storage modulus is much higher

below T_g of the polymer but falls steeply above T_g. In this study, composite samples have a higher storage modulus than the unfilled sample, which proved that the addition of silver particles could reinforce the epoxy matrix. Figure 5 shows that both composites prepared by manual and homogenizer mixing at high filler loading (8 vol %) have a higher value of storage modulus than that at a low filler loading (4 vol %). This observation can be caused by the following. It was believed that an increase in silver filler loading increases the stiffness of the resulted composites and thus increases the storage modulus. Moreover, an increase in storage modulus at a higher filler loading could also be due to the reduction of matrix mobility in the vicinity of the Ag filler as a result of the polymer adsorption onto the filler surfaces. According to Teh et al. [19] and Heimann et al. [20], an increase in storage modulus could also be due to a higher level of crosslink density. It is evident from Fig. 5 that the samples prepared by homogenizer mixing have a higher storage modulus than the samples prepared by manual mixing. However, at a low filler content (4 vol %), the differences in storage modulus between these two mixing techniques are not so apparent compared to the samples prepared at a higher filler content (8 vol %). This observation can be related to the degree of filler agglomeration and filler dispersion in epoxy matrix. It can be suggested that, at a low filler loading, the silver filler could be dispersed well in the epoxy matrix regardless of the mixing technique used. Moreover, at a low filler loading (4 vol %), the agglomeration of the filler is not quite pronounced compared to the composite at a higher filler loading (8 vol %). As the filler content increased, it was believed that the filler-filler interaction is higher than the filler-matrix interaction, which furthermore resulted to the formation of a filler agglomerate in the epoxy matrix. A higher filler-filler interaction furthermore could reduce the crosslink density of the composite and thus result in a decrease in the storage modulus. Therefore, it can be seen that the technique to disperse the filler is very important in order to break up agglomeration and improve the dispersion of the filler.

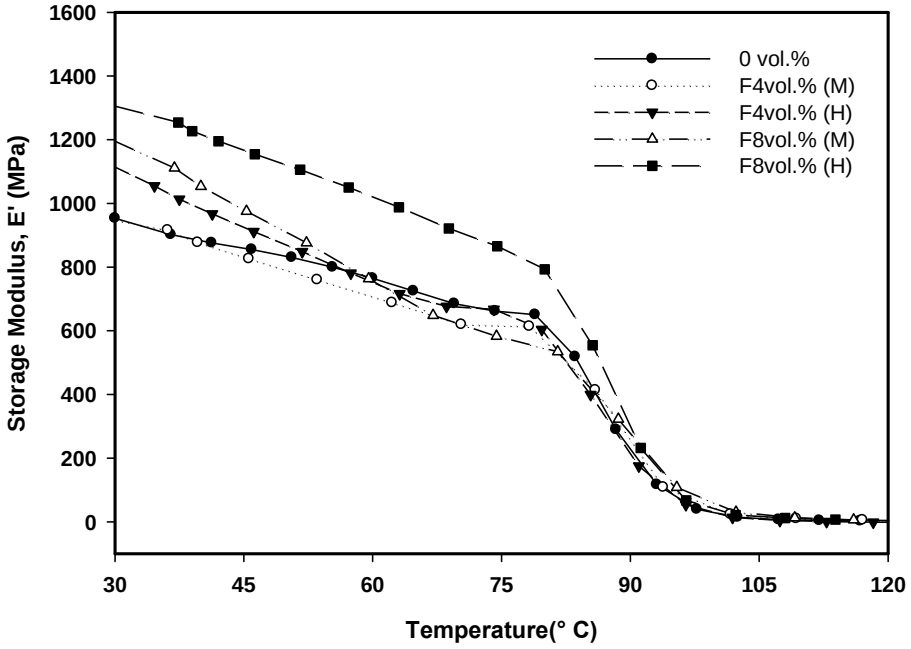

Fig. 5. Storage modulus of the silver flake filled epoxy composite prepared by manual (M) and homogenizer (H) mixings.

Figure 6 shows that tan delta peaks for composite samples are shifted to a higher temperature, which indicates a higher value of T_g compared to the unfilled samples. In general, an increase in T_g is attributed to a good adhesion between the polymer and the reinforced particles; hence, the particles can restrict the segmental motion of cross-links under loading [21]. However, in this study, the T_g value did not show any trend except an increase in the T_g value for the composite sample compared to the unfilled one. A reduction in the T_g value, especially for the samples prepared by manual mixing, are most probably due to the agglomeration of the filler, which leads to imperfect interfacial adhesion. The agglomerated lumps of filler particles would eventually affect the van der Waals interaction between the polymer chains and reduce the crosslinking of the matrix. In addition, a weak filler-matrix interaction could subsequently increase the mobility of the polymer chain when subjected to load and resulted in a decrease in the T_g value of the composites. This observation is supported by Yasmin et al. [13]: the T_g value is also affected by the degree of particle dispersion that includes size, homogeneity, orientation, and spacing between particles.

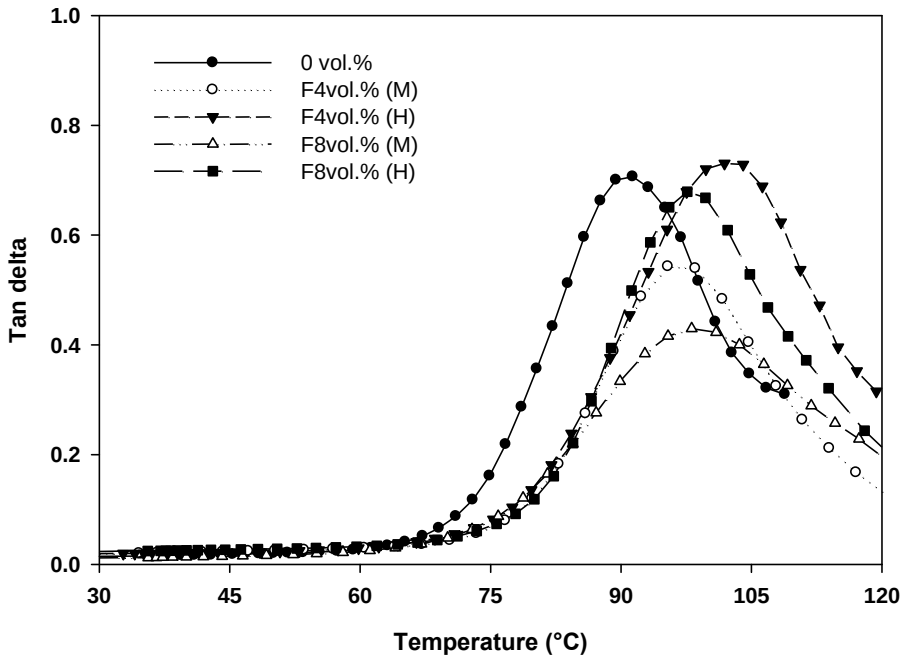

Fig. 6. Tan delta of silver flake filled epoxy composite prepared by manual (M) and homogenizer (H) mixings.

3.4 Coefficient of Thermal Expansion (CTE) Analysis

The differences in CTE between the chip and substrate makes flip chip assemblies vulnerable to thermally induced strains and often result in joint failure. One of effective solutions for this problem is to use a low CTE of the ECA material that mechanically couples the severely mismatched CTE of the chip and the substrate and provides a significant enhancement in assembly reliability [18]. The results of the dilatometer analysis of silver flake filled epoxy composites listed in Table 1 showed that the value of CTE before the glass transition temperature T_g is lower than the value of CTE after T_g. This typical trend is due to an insufficient energy supplied to cause more polymer chains to rotate or mobilize and thus allowing low dimension changes to occur [11]. The reduction in the CTE of the composite sample compared to the

unfilled samples was mainly related to a reduction in the molecular mobility of the macromolecular chains around the silver filler.

Table 1. CTE of the silver flake filled epoxy composite prepared by manual mixing. Values in brackets represent homogenizer mixing

Filler loading (vol %)	CTE before T_g, α_1 (ppm/K)	CTE after T_g, α_2 (ppm/K)
0	84.3	254
4	53.79 (52.45)	177.00 (176.95)
8	45.89 (47.27)	153.57 (167.25)

It is evident from Table 1 that CTE before and after T_g of the sample prepared by manual mixing at 4 vol % has a comparable value with the sample prepared by homogenizer mixing. However, at 8 vol %, the sample prepared by manual mixing shows a much lower value, especially CTE after T_g, than that of the sample prepared by homogenizer mixing. The result obtained could be related to the degree of silver flake dispersion throughout the epoxy matrix. As the dispersion state of the filler in the epoxy matrix influences the thermal properties of the composite behavior, it is necessary to point out that inhomogeneous distribution of the filler particles with considerable agglomerations could be noticed, especially for the sample prepared by manual mixing at a high filler content. For this sample, it can be suggested that the presence of agglomerations of silver flakes obstructs the expansion of the polymer chain, which in turn is lower the CTE value. On the other hand, a better dispersion with a low agglomeration of the filler in the sample prepared by homogenizer mixing could distribute the heat more efficiently compared to the sample that has a higher degree of filler agglomeration.

3.5 Thermogravimetry Analysis (TGA)

Figure 7 illustrated the TGA curves of silver flakes filled epoxy composites. It is observed that the systems seem to be stable up to 300°C, which is suitable to be used for electronic packaging where the application temperature is around 150-200°C. The percentage of weight loss of the samples increased as the temperature increased. The close-up of TGA curves at a temperature of 30°C to 350°C showed that, at a temperature of 320°C, all composite samples experienced ~2-3% weight loss, which can be referred to the volatile component, such as moisture, solvent evaporation, etc. Result shows that, at a low filler content (4 vol %), the sample prepared by homogenizer mixing has a lower value of residue than the sample prepared by manual mixing. However, an anomalous result could be observed for the samples with a higher filler content, which is 8 vol %. The result shows that the sample prepared by manual mixing had a higher residue than the sample prepared by homogenizer mixing. This might be related to the uneven distribution of the filler and the presence of agglomeration or lumps of silver flakes in the composites that furthermore increase the residue content of the samples. Moreover, under close observation (Fig. 7), the samples prepared by homogenizer mixing show a higher thermal stability than the samples prepared by manual mixing at any given filler content. This suggests that the sample prepared by homogenizer mixing provides a better surface interaction between the filler and the matrix and minimum particles to particle interaction. The reason for lowering the thermal stability of the samples prepared by manual mixing can be the perturbation of silver

lumps to the structure of the polymer. The presence of any perturbation could weaken the van der Waals interaction between the polymer chains which reflects the stability of the polymer [10].

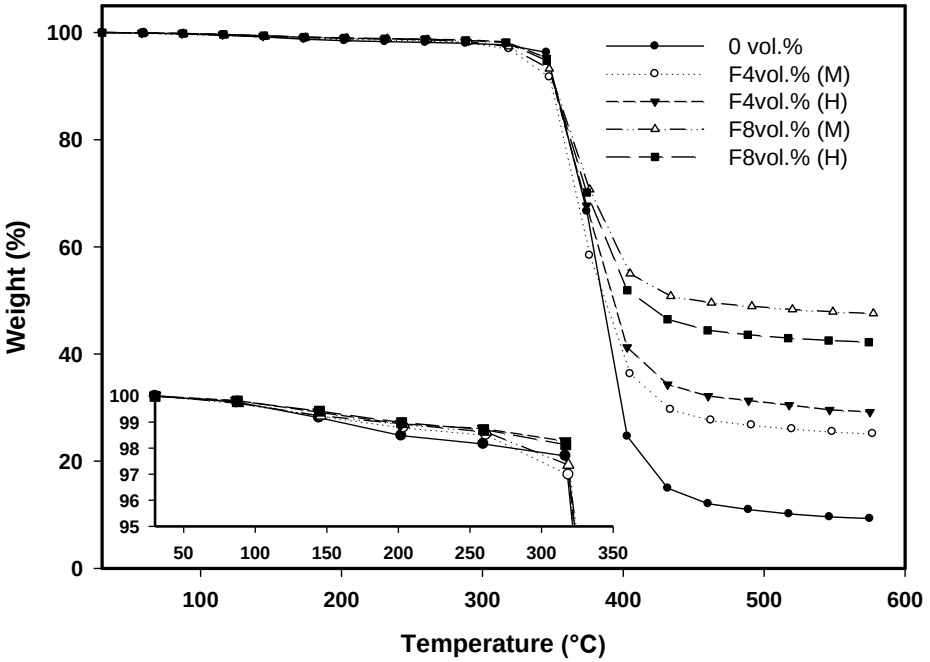

Fig. 7. TGA curve of the silver flake filled epoxy composite prepared by manual (M) and homogenizer (H) mixings.

4. Conclusions

The results of this study indicate that silver filled epoxy composites prepared by the aid of a homogenizer has a higher conductivity compared to the samples prepared by manual mixing. The result was achieved due to a better distribution of the filler throughout the epoxy matrix, which allows better contact and furthermore increases the current carrier in the system. It is also evident that the external shear force generated by the homogenizer subsequently separates and breaks up the silver flake agglomeration and improves the flexural properties of the composite samples. In addition, the thermal properties of the composite prepared by homogenizer mixing show a slightly higher thermal stability, a lower CTE, and a higher T_g compared to the composite prepared by manual mixing.

Acknowledgements

The authors gratefully acknowledge the grant support from the Ministry of Higher Education, Malaysia through FRGS grant and National Science Foundation (NSF). We thank the staff of the School of Materials and Mineral Resources, USM for their help during the experimental measurements and useful discussions.

References

[1] F. Haupert and B. Wetzel, Springer, 45-60, (2005).
[2] D. L. Markley, Q. K. Tong, D. J. Magliocca, and T. D. Hahn in Int. Symp. on Advanced Packaging Materials, (1999).
[3] V. I. Roldughin and V.V. Vysotskii, Prog Org Coat 39, 81-100, (2000).
[4] S. Kumar, T, Rath, R. N. Mahaling, C. S. Reddy, C. K. Das, K. N, Pandey, R. B. Srivastava, and S. B. Yadaw, Mat Sci Eng B 141, 61-70, (2007).
[5] H. P. Wu, X. J. Wu, M. Y. Ge, G. Q. Zhang, Y. W. Wang, and J. Jiang, Compos. Sci. Technol. 67, 1182-1186, (2007).
[6] M. Bouguettaya, N. Vedie, and C. Chevrot, Synthetic Met 102, 1428-1431, (1999).
[7] V. E. Gul, The Netherlands, 1-26, (1996).
[8] Y. Li and C. P. Wong, Mat. Sci. Eng. R 51, 1-35, (2006).
[9] D. I. Tee, M. Mariatti, A. Azizan, C. H. See, and K. F. Chong, Compos. Sci. Technol. 67, 2584-2591, (2007).
[10] N. Chisholm, H. Mahfuz, V. K. Rangari, A. Ashfaq, and S. Jeelani, Compos. Struct. 67, 115-124, (2005).
[11] K. L. Chan, M. Mariatti, Z. Lockman, and L. C. Sim, J. Mater. Sci. Mater. Electron. 21, 772-778, (2010).
[12] S. Khairul Anuar, M. Mariatti, A. Azizan, N. Chee Mang, and W. T. Tham, J. Mater. Sci. Mater. Electron., DOI 10.1007/s10854-010-0207-7, (2010).
[13] A. Yasmin, J. J. Luo, and I. M. Daniel, Compos. Sci. Technol. 66, 1179-1186, (2006).
[14] L. Fan, B. Su, J. Qu, and C. P. Wong, Int. Symp on Advanced Packaging Materials, 193-199, (2004).
[15] G. Suriati, M. Mariatti, and A. Azizan, J. Mater. Sci. Mater. Electron. 22, 56-63, (2011).
[16] Y. P. Mamunya, V. V. Davydenko, P. Pissis, and E. V. Lebedev, Eur. Polym. J. 38, 1887-1897, (2002).
[17] H. Jiang, K. Moon, Y. Li, and C. P. Wong, Electronic Components and Technology Conference, (2006).
[18] J. S. Hwang, Microelectron. Reliab. 48, 645-651, (2008).
[19] P. L. Teh, M. Jaafar, H. M. Akil, K. N. Seetharamu, A. N. R, Wagiman, and K. S. Beh, Polym. Adv. Technol. 19, 308-315, (2008).
[20] M. Heimann, M. Wirts-Ruetters, B. Boehme, and K.-J., Wolter, Electronic Components and Technology Conference, (2008).
[21] S. N. Goyanes, P. G. König, and J. D. Marconi, J. Appl. Polym. Sci. 88, 883-892, (2003).

FABRICATION OF SCREEN-PRINTING PASTES OF CARBON POWDERS FOR DYE-SENSITIZED SOLAR CELLS

J. O. Ozuomba[1], L. U. Okoli [2], A. J. Ekpunobi [3], and P. I. Ekwo[3]

[1]Department of Industrial Physics, Madonna University, Elele, Rivers State, Nigeria
e-mail: okanandu@yahoo.com; 08033267967
[2]Department of Physics, Federal College of Education, Technical, Umunze, Anambra, Nigeria
[3]Department of Physics and Industrial Physics, Nnamdi Azikiwe University, Awka, Nigeria

(Received 3 April 2012)

Abstract

A preparation technique of screen-printing pastes of carbon has been disclosed in order to fabricate nanocrystalline layers without cracking and pealing-off over 6.8-μm thickness for the counter electrodes of dye-sensitized solar cells (DSSCs). A well blended mixture of powdered activated carbon, natural graphite powder, and a colloidal sol produced the screen-printing pastes. A DSSC fabricated with the carbon electrode whose TiO_2 photo-electrode was sensitized with *anthocyanin* local dye gave a photoconversion efficiency of 1.01%.

1. Introduction

Dye-sensitized solar cells (DSSCs) are currently attracting academic and commercial interest as regenerative low-cost alternatives to conventional solid state devices [1, 2]. A DSSC is composed of a dye-sensitized nanocrystalline titanium(IV) oxide photoelectrode, a counter electrode, and a redox electrolyte in between [3]. Light incident on the transparent photo-electrode excites the dye in the cell from the ground state, whereby an electron is formed [4]. The photo-excited dye molecules inject electrons into the conduction band of TiO_2, whereby the combined action of redox species in the electrolyte and the counter electrode reduce the oxidized dye molecules back to their original state [4, 5]. Generally, DSSCs consist of platinized counter electrodes fabricated by deposition of platinum on a transparent conducting oxide (TCO) substrate using thermal decomposition, sputtering, or electrodeposition of H_2PtCl_2 [3, 6, 7]. Platinum is relatively expensive, and the deposition techniques usually employed are costly and sophisticated [7].

Carbonaceous materials are quite attractive to replace platinum due to their high electronic conductivity, low cost, high total surface area, porosity, high temperature stability, and chemical resistance [6-9]. The development of simpler deposition methods will lower the cost of DSSC and enable the fabrication of large-scale DSSC devices.

Hence, we have developed a procedure which takes less than 24 h to fabricate and deposit high quality screen-printing carbon paste electrodes. Optimization of the electrical properties of the carbon electrodes was achieved through doctor blading and DSSC fabricated with the carbon electrode achieved a photoconversion efficiency of 1.01%.

2. Material and Methods

2.1. Reagents and solutions

Tin(II) chloride, carboxy ethyl cellulose (NATROSOL), 25% hydrochloric acid, powdered activated carbon (PAC) and a kind of natural graphite powder (NGP) were used. High purity de-ionized water was used to prepare the solutions at a temperature of 25 ± 2^0C. The chemicals were of analytical grade and used without further purification.

2.2. Apparatus

Ainsworth DE – 100, Max 100g, e = 0.0001g chemical balance, electric hot plate, Carbolite 201 tubular furnace, wooden clamp, 500 W electric bulb, no. 90 polyester mesh and its mounting frame, blue emulsion, sensitizer, squeegee, fluorine-dope tin oxide (FTO) glass substrate, substrate holder, film, UV filter, hot air blower, carbolite 201 tubular furnace, acetone and methanol.

2.3. Fabrication of screen-printing pastes through sol-gel technique

We dissolved 12 g of tin(II) chloride in 50 ml of deionized water and titrated with about 1 ml of 25% HCl. The solution became colourless and there was a noticeable fall in temperature. Then 2 g of Natrosol was dissolved in 50 ml de-ionized water and stirred properly. We mixed the two solutions under permanent stirring. This mixture was heated to 300^0C using a hot-plate technique. The stirring continued as the heating lasted for about 39 s. The resulting solution (about 16 ml) was allowed to stay for about 12 h at room temperature. It was further heated on the following day for about 7 min to get a polymeric colloidal sol of about 12 ml. The resulting solution was our "binder." Eighteen grams of powdered activated carbon PAC were ground in a porcelain mortar for about 30 min. The screen-printing carbon pastes were obtained by hand mixing certain proportions of the well-blended PAC and the binder.

2.4. Deposition of carbon electrode through screen-printing

The first step was to prepare the photoresist by hand mixing the blue emulsion and sensitizer in the ratio of 2 : 1. Then we applied the photoresist onto a small portion of the mesh. The squeegee was used to rub it uniformly (front and back) on the mesh and it was allowed to stay for 2 min. A hot air blower was used to fasten the drying process. The film in form of a dark image imprinted on a sheet of tracing paper has been designed. The shape of the film determines the shape of the screen and, hence, that of the electrode. We placed the tracing paper on the top of the photoresist and set the mesh 40 cm below the source of radiation. The ultraviolet radiation filter (glass shield) was placed on the top of the film, while a 500-W electric bulb was switched on. After about 5 min, the UV filter and the film were removed and the mesh was placed beneath a water tap. The tap was slightly opened and water was allowed to gently run on the top of the photoresist. The spot covered by the dark image on the tracing paper was washed away by the water thereby forming a sharp image (screen) on the mesh. The mesh can be allowed to dry naturally, but we used a hot air blower to fasten the drying process.

The photoresist is soluble in water, but when radiant light passes through it for some time, it will become insoluble. Hence, it was possible to wash off the area that formed our screen because the dark design on the tracing paper served as an absorber surface. With the help of the substrate holder, we positioned the FTO at a short distance beneath the screen with the conducting side facing upward. A small amount of the carbon paste was dispensed onto the upper surface of the screen using the squeegee, and the squeegee was used to squeeze the paste across the screen surface. This is a single layer deposition. Double layer deposition can be achieved by

running another stroke of the carbon paste using the squeegee, and the thickness of the deposited carbon electrode increases with multiple deposition. Before deposition, the glass substrate was cleaned with acetone, then methanol and etched through plasma treatment for 1 min. The entire mesh was washed with acetone at the end of screen printing and the entire process can be repeated. Meanwhile, the particular screen can be washed with water after usage so that it can be used again but it is advisable to imprint many dark films on a sheet of tracing paper so as to obtain many screens.

2.5. Thermal treatment

A hot air blower was used to dry the carbon counter electrode for about 3 min immediately after deposition. Using an electric hot plate, the carbon electrode was subjected to thermal annealing at 150^0C for 5 min. Immediately after annealing, the electrode was sintered at 200^0C for about 15 min using a carbolite 201 tubular furnace.

2.6. Optimization of electrical properties

The sheet resistance of the carbon electrode was reduced to a very low value by preparing another carbon paste using equal mixtures of PAC and NGP and applying doctor blading deposition technique [10]. This method is very similar to screen-printing, except that the mesh has no role to play. The carbon paste was deposited directly onto the FTO glass substrate using a squeegee. The thickness of the film was determined by covering the four edges of the glass substrate with a masking tape, while thicker films were obtained using multiple layers of the masking tape. Carbon films prepared through this blade method were subjected to the same thermal treatment.

3. Results and discussion

The quantity of carbon and binder which formed our carbon paste was varied in the ratio of 0.133 g/ml to 1.2g/ml, while the sheet resistance of the fully sintered electrode varied from 1.99 x 10^4 Ω /square to 543.35 Ω /square (Table 1). It is true that we achieved a significant reduction in the sheet resistance, but there was need for further reduction since we obtained the sheet resistance of the FTO glass substrate of14.55 Ω/square. The carbon concentration must be further increased, but a bottleneck would be the ability of the thick carbon paste to pass through the mesh. At this stage, we resorted to the blade deposition technique.

Table 1. Electrical characterization of carbon electrode deposited through screen printing

Quantity of carbon (g)	Quantity of binder (ml)	Concentration (g/ml)	Sheet resistance (Ω/square)
0.20	1.50	0.133	$1.99x10^4$
0.30	0.40	0.750	$1.02x10^3$
0.80	1.00	0.800	893.75
0.50	0.50	1.000	599.47
0.30	0.25	1.200	543.35

The results of electrical characterization of carbon electrode deposited through the blade method are shown in Table 2. The quantity of carbon and binder which formed our carbon paste was varied from 1.2 g/ml to 4.0 g/ml, while the sheet resistance of the fully sintered electrode

varied from 212.137 to 60.713 Ω/square. This was another breakthrough in the sheet resistance reduction, yet further optimization was required taking into account the low resistivity of the FTO glass substrate. We found that the 4.0 g/ml carbon electrode was pealing after sintering, so we considered 3.0g/ml for further optimization since it was stable.

Table 2. Electrical characterization of carbon electrode deposited through blade method

Quantity of carbon (g)	Quantity of binder (ml)	Concentration (g/ml)	Sheet resistance (Ω/square)
0.60	0.50	1.20	212.137
1.00	0.50	2.00	139.520
1.40	0.50	2.80	90.289
1.50	0.50	3.00	66.594
1.00	0.25	4.00	60.713

The carbon paste electrode comprising 3.0 g of powdered activated carbon per milliliter of binder was considered for further optimization through multiple layer deposition by doctor blading. We obtained the sheet resistance for double and triple layer deposition of 50.998 Ω/square and 36.954 Ω/square, respectively (Fig. 1). This was another breakthrough in our research work, which implies that the thicker the electrode, the lower the resistivity [3, 4, 9]. Meanwhile, we observed little cracks on the three-layered electrode, and we still need to go further to match the impedance of the counter electrode with that of the FTO glass substrate.

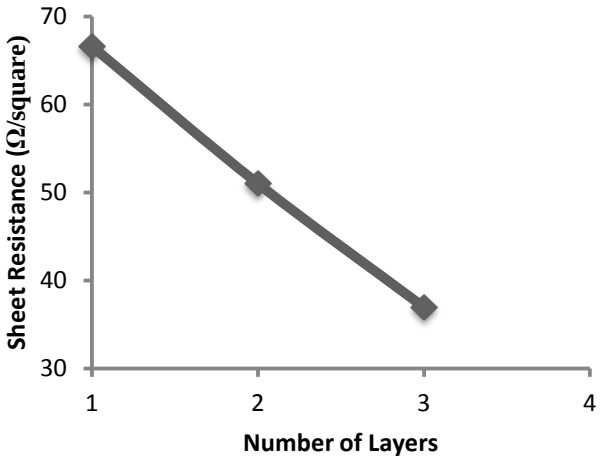

Fig. 1. Sheet resistance versus number of layers for 3.0g/ml PAC electrode

Since we need a carbon counter electrode with a lower sheet resistance, we fabricated another carbon paste with a well blended mixture of equal amount of PAC and NGP. The effect of graphite on the sheet resistance is shown in Fig. 2. The single, double, and triple layer deposition gave stable electrodes. The triple layer deposition was able to reduce the sheet resistance to 15.400 Ω/square. This result confirmed not only the fact that the thicker the electrode, the lesser the sheet resistance, but also that graphite has high electrical conductivity [7, 10].

So, we were successful in matching the sheet resistance of the counter electrode to that of

the FTO glass substrate which is 14.55 Ω/square. The electrode is expected to exhibit optimal performance when deposited on the substrate. Electrode characterization using a Dektak stylus 7.0 surface profiler gave the film thickness for the single, double, and triple layer PAC-NGP electrodes to be 5.26, 6.31, and 6.82 μm, respectively.

A DSSC of active surface area 1.8 cm^2 was fabricated with a titanium dioxide photoelectrode and sensitized with *chlorin* dye. *Chlorin* is a local dye fabricated from bahama grass [9, 11]. Figure 3 depicts the current-voltage characteristics of the DSSC at the illumination intensity of 100 W/m^2 using an Oriel class A solar simulator. The cell parameters were the following: open circuit voltage (0.44 V), short circuit photocurrent (3.9 mA/cm^2), fill factor (0.59), and photoelectric conversion efficiency (1.01%) [9]. The results can be compared to those obtained by Waita *et al.* using platinum as the counter electrode [3].

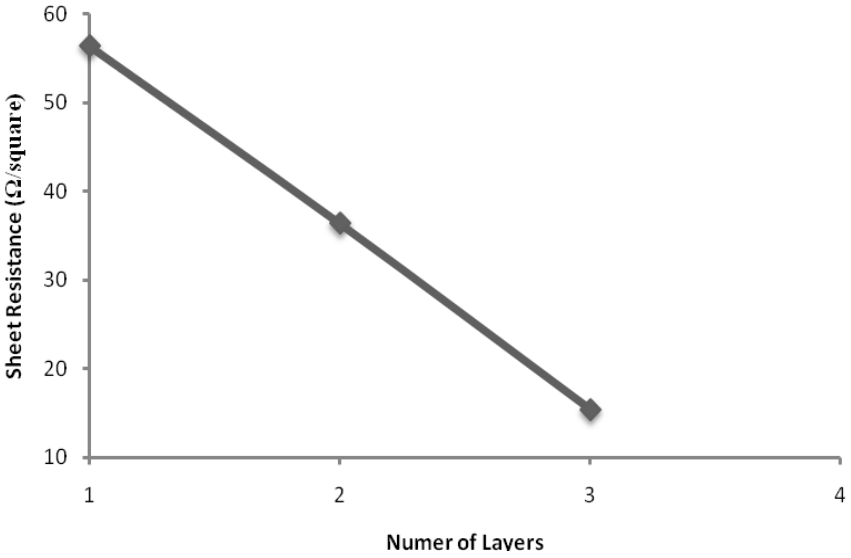

Fig. 2. Sheet resistance versus number of layers for 3.0g/ml PAC-NGP eletrode

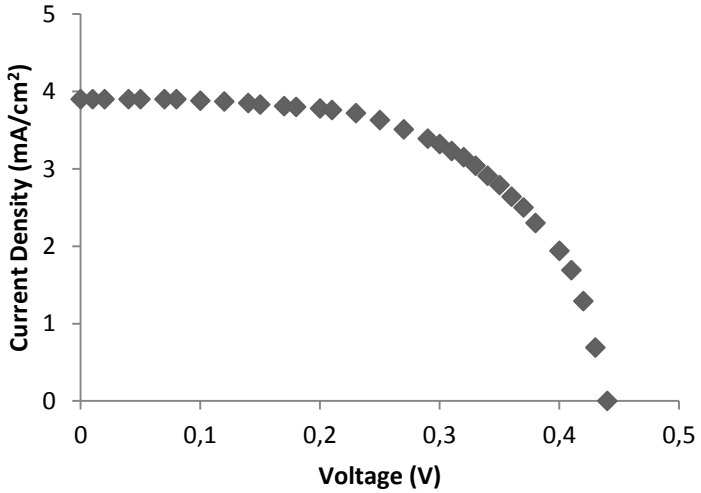

Fig. 3. The I-V curve for cell sensitized with *chlorin* dye

4. Conclusions

Screen printing pastes from carbon powders were successfully fabricated through a sol-gel technique. Stable carbon paste electrodes with a very low sheet resistance were obtained. A DSSC fabricated with the carbon electrode achieved a photocurrent conversion efficiency of 1.01%. This methodological investigation can contribute not only to the development of cheaper DSSCs, but also to the encouragement of production of large-scale DSSC devices.

References

[1] B. O'Regan and M. Gratzel, Nature, 353, 737 (1991).
[2] M. Gratzel, Nature, 414, 338 (2001).
[3] S. M. Waita, J. M. Nwabora, B. O. Aduda, G. A. Niklasson, S. Lindquist, and C. Granqvist, African J. Sci. Technol. l 7, 106 (2006).
[4] J. O. Ozuomba, A. J. Ekpunobi, and Ekwo P. I., Dijest J. Nanomater. Biostruct. 6, 1043 (2011).
[5] N. R. Neale, N. Kopidakis, J. van de Lagemaat, and A. J. Frank, Tailoring the Interface to Improve V_{oc} in Dye-Sensitized Solar Cells, Conference paper NREL/CP-590-37056, Colorado, 1-2 (2004).
[6] Z. Huang, X. Liu, K. Li, D. Li, Y. Luo, H. Li, W. Song, L. Chen, and Q. Meng, Electrochem. Commun. 9, 596 (2007).
[7] G. Wang, L. Wang, W. Xing, and S. Zhuo, Mater. Chem. Phys. 123, 690 (2010).
[8] Z. Kavaliauskas, L. Marcinauskas, and P. Valatkevicius, Enhanced Capacitance of Porous Carbon Electrodes through Deposition of Small Amounts of NiO, Proceedings of the VII International Conference ION, Poland, 66 (2010).
[9] J. O. Ozuomba and A. J. Ekpunobi, Res. J. Chem. Sci. 1, 76 (2011).
[10] E. Sabio, E. Gonzalez, J. F. Gonzalez, C. M. Gonzalez-Garcia, A. Ramiro, and J. Ganan, Carbon 42, 2285 (2004).
[11] J. O. Ozuomba, A. J. Ekpunobi, and P. I. Ekwo, Chalcogenide Lett. 8, 155 (2011).

COMBUSTION SYNTHESIS AND CHARACTERIZATION OF NANOSIZED POWDER $SrAl_2O_4:Eu^{2+}$ PHOSPHOR

S. C. M. Calyn[1], M. Nazarov [1,2], A. Nor Nazida[1], and M. N. Ahmad-Fauzi [1*]

[1] *School of Materials and Mineral Resources Engineering, University Sains Malaysia, Engineering Campus, 14300 Nibong Tebal, Pulau Pinang, Malaysia*
[2] *Institute of Applied Physics, Academiei str. 5, Chisinau, MD-2028 Republic of Moldova*
**e-mail: afauzi@eng.usm.my*

(Received 20 April 2012)

Abstract

A stoichiometric $SrAl_2O_4:Eu^{2+}$ nanosized powder was synthesized by combustion synthesis using urea at 500°C. The crystal structure, element and phase composition, and particle size were analyzed with the aim to study the properties of nanosized $SrAl_2O_4:Eu^{2+}$ green phosphor and its application. X-ray Diffraction pattern revealed that the $SrAl_2O_4:Eu^{2+}$ crystallizes were a major phase, and $Sr_4Al_{14}O_{25}$ as a secondary phase with a small amount of the dopant has no effect on the crystal structure of $SrAl_2O_4$. Crystalline structure can be observed and enhanced by calcination at 1000ºC with 2-h soaking time in a reductive atmosphere. Nucleation of particles occurs and forms a needle-like structure for $SrAl_2O_4$ and a star-like structure for $SrAl_2O_4:Eu^{2+}$. This structure is unstable and agglomerates during calcination at 1000°C to form a stable specific flower-like structure which enhances the glowing effect of the samples.

1. Introduction

Strontium aluminate oxides are commonly prepared by the conventional solid state reactions (SSR) which require a long reaction time of 2-6 h in a high temperature range of 1200-1600°C. Furthermore, high calcination temperature are also required to induce sintering and aggregation of particles. Milling process was also required in SSR resulting in a reduction of the particle size and a decrease in the luminescent properties. However, by using combustion synthesis, phosphor powders can be prepared in a simpler, safer, more energy saving way and within a shorter time [1]. Combustion synthesis can produce more homogeneous products compared to the solid state reaction method due to good mixing of starting materials and relatively low reaction temperature [2]. There are numerous publications; some of them referring to the combustion synthesis are shown in Table 1.

Theoretically, an ideal combustion is a process in which all the fuel burns completely. It involves burning the entire carbon (C) to carbon dioxide (CO_2), the entire hydrogen (H) to water vapor (H_2O) and all the nitrates (NO_3) to nitrogen (N_2) or nitrogen dioxide (NO_2). Combustion synthesis process has low temperatures, fast heating rate, and short characteristic reaction time. It has been widely used as an efficient and facile method for synthesizing and processing advanced ceramics (structural and functional), catalysts, composites, alloys, intermetallics, and nanomaterials [9]. It also plays an important role to produce complex oxides ceramics, such as aluminates, ferrites, and chromites [10]. Combustion synthesis route provides low density mass reducible to very fine particles up to submicron region. Oxidizing atmosphere prevails in combustion process [5]. The concept of combustion synthesis is the exothermicity of redox

(reduction-oxidation or electron transfer) chemical reaction between metal nitrate precursor and a fuel like urea at a relatively low temperature. The excessive heat required during combustion process completes in the reaction in short time producing small particles with high crystallinity. Combustion synthesis can be divided depending on the nature of the reactants: elements or compounds (solid, liquid, or gas) and the exothermicity (adiabatic temperature). The advantages of the combustion synthesis are the following [9]: simple usage of equipment, high purity products, stabilization of metastable phases, and the formation of products with nearly any size and shape. Useful oxide materials can be prepared by a rapid heating of aqueous solutions containing metal nitrates (oxidizer) and fuels like urea/hydrazides [carbon hydrazine (CH), oxalyl dihydrazide (ODH), malonic acid dihydrazide (MDH), tetra formal tris azine (TFTA), etc.]. The purposes of using fuels are as follows: they are a source of C and H, which will combust to form CO_2 and H_2O and liberating heat, they form complexes with the metal ions providing a homogeneous mixture of cations in solution or gel.

Table 1. Comparison of properties of $SrAl_2O_4:Eu^{2+}$, Re^{3+} powders by various methods

Composition	Type of Combustion	Type of Fuel	Mixing	Combustion	Spectra		Ref.
					PL(nm)	PLE(nm)	
$SrAl_2O_4:Eu^{2+}$, Dy^{3+}, Tb^{3+}	Combustion	Urea	70°C – 4 h	400-900°C – 5 min	335	513	[1]
$Sr_{0.97}Al_2O_4$: $Eu_{0.01}$,$Dy_{0.02}$	Solution Combustion	Glycine		500°C – 3 min	242	513	[3]
$SrAl_2O_4:Eu^{2+}$, Dy^{3+},Gd^{3+}	Combustion	Urea	70°C – 4 h	600°C – 5 min	348	515	[4]
($Sr_{0.98}Eu_{0.02}$, $Dy_{0.04}$) Al_2O_4	Modified combustion	Urea		400-600°C – 5 min	337	529, 667	[5]
$SrAl_2O_4:Eu^{2+}$, Dy^{3+},0.10M Dy^{3+}& Eu^{3+}	Gel combustion synthesis	Urea + ammonium acetic	85°C	6000°C – 5 min	320	511	[6]
$Sr_{0.97-x}Al_2O_4$: $Eu^{2+}_{0.01}$, $Dy^{3+}_{0.02}$, Yb^{3+}_{x}	Solution Combustion	Urea	80°C – 2 h	600°C – 10 min	355	513	[7]
$Sr_{0.97}Al_2O_4$: $Eu_{0.01}$,$Dy_{0.02}$	Combustion	Urea	70°C – 4 h	540°C – 5 min	365	516	[8]

There are numerous publications discussing the combustion synthesis. The main goal of this research is to improve the properties of $SrAl_2O_4:Eu^{2+}$ by the combustion method with a lower combustion temperature in order to produce nanoparticle powder for different applications.

2. Experimental

2.1 Sample Preparation

$SrAl_2O_4:Eu^{2+}$ phosphor was prepared by combustion synthesis. The starting material included: aluminum nitrate ($Al(NO_3)_3.9H_2O$; Systerm, 98%), strontium nitrate ($Sr(NO_3)_2$; Aldrich, 99%), europium oxide (Eu_2O_3; Aldrich, 99.99%) and urea ($CO(NH_2)_2$; Systerm, 99%). Small amount of acid boric (H_3BO_3; Fisher, 100.04%) were used as flux and small amounts of urea were used as reducer and fuel. Figure 1 below shows the flow chart of $SrAl_2O_4:Eu^{2+}$ powders synthesis.

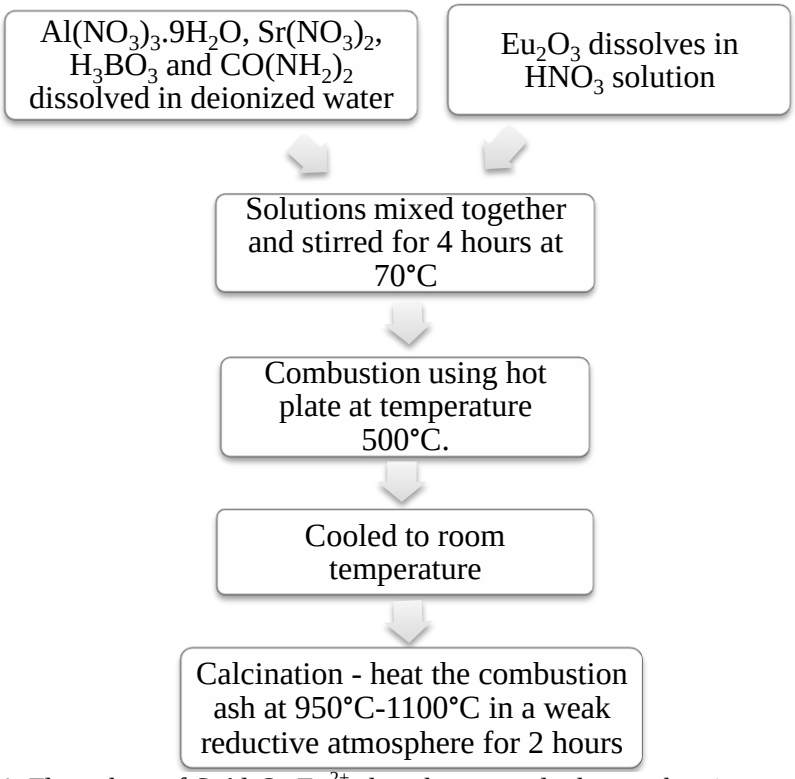

Fig.1. Flow chart of $SrAl_2O_4:Eu^{2+}$ phosphors powder by combustion synthesis.

There are four stages to describe the combustion synthesis.

Stage I: Composition of raw materials

The stoichiometric quantities of raw materials were calculated and weighed by using high precision mass balance. The composition of the acid boric was set as 0.08 mol %. Each raw material $Al(NO_3)_3.9H_2O$, $Sr(NO_3)_2$, H_3BO_3 and $CO(NH_2)_2$ was dissolved into 20 ml of deionized water to obtain a transparent solution. Wet mixing was used to obtain a homogeneous mixture. Deionized water is selected instead of distilled water due to the removal of the mineral ions, such as cations from sodium, calcium, iron, copper and anions from chloride and bromide, which will influence on the experiment result [11]. Eu_2O_3 was dissolved with a minimum amount of the HNO_3 solution to convert into $Eu(NO_3)_3$ according to the equation

$$Eu_2O_3 + 6HNO_3 \rightarrow 2\ Eu(NO_3)_3\ + 3H_2O \quad (1)$$

Stage II: Mixing

The two solutions were mixed together and stirred using a magnetic bar for several hours at 75°C to obtain a viscous gel solution. The mixing temperature was set in a range between 70°C to 80°C in this project due to several reasons. Firstly, according to the MSDS, aluminum nitrate has a fairly low melting point (73°C) but a high boiling point or decomposition temperature (135°C). The heating of aluminum nitrate above its melting point encourages the formation of a homogeneous solution. Furthermore, it can dissolve acid nitric which has a low boiling point (83°C).

Stage III: Combustion synthesis

The mixed viscous gel obtained continues for combustion reaction. In this project, combustion is done by using a hot plate instead of a furnace. White combustion ash was obtained in 3-5 min by combusting the precursor gel at a temperature of 500°C. Initially, the solution boiled and underwent dehydration followed by decomposition with emission of large amounts of gasses (oxides of carbon, nitrogen, and ammonia). Later, the viscous gels spontaneously start to burn and burn slowly without flame (smouldering combustion), thus producing white fine powder. The entire process takes less than 5 min. When heated at 500°C, the powder was held for a few minutes to ensure the combustion reaction was complete. The chemical equation of combustion is complicated and not yet verified; however, the brief equation can be shown as follows:

$$2Al(NO_3)_3.9H_2O + Sr(NO_3)_2 + CO(NH_2)_2 + Eu(NO_3)_3 + 1.5O_2 \rightarrow SrAl_2O_4 : Eu^{2+} + 20H_2O + 5N_2 + 14.5O_2 + CO_2 \quad (2)$$

Next, the combustion ash was cooled to room temperature.

Stage IV: Calcination step

The final pigment synthesis is done by heating the combustion ash at 950°C -1100°C in a weak reductive atmosphere for 2 h to obtain $SrAl_2O_4:Eu^{2+}$ phosphor. The weak reductive atmosphere was created by using a graphite crucible to inhibit further oxidation.

2.2 Characterization techniques

Phase identification was carried out using a Bruker, D8 Advance X-ray Diffraction (XRD) instrument with Cu-Kα radiation of a wavelength of 1.54 Å. Data were collected by step-scanning 2θ from 10° to 90° and 0.034 s counting time at each step at room temperature. The morphology and topography of the samples were observed by using a Zeiss Supra 35 VP scanning electron microscope (SEM). The samples were placed on the pin mount specimen holders with the help of a double-sided tape. The samples were coated with a few nanometer-thick gold palladium layer by using Sputter Coater Polaron SC 515 before SEM observation. Energy-dispersive X-ray spectroscopy (EDX) is known as a chemical microanalysis technique used with SEM. EDX was used to investigate the presence of elements of phosphors in a pre-captured SEM micrograph qualitatively and quantitatively.

The particle sizes of the samples were determined by a NANOPHOX (NX0064) Particle

Size Analyser. It used the photon cross-correlation spectroscopy (PCCS) technique for the simultaneous measurement of particle size and stability in a range of about 1 nm to 10 μm in opaque suspensions and emulsions. The key principle of PCCS is the 3D cross correlation technique based on dynamic light scattering. PCCS is using two separate beams with the same measuring volume for the illumination to create two separate speckle patterns. The time decay of the particles caused by Brownian motion is used to evaluate the size of nanoparticles and is shown in Fig. 2. The Brownian motion results from impacts of the thermal movement of the molecule in a suspending fluid.

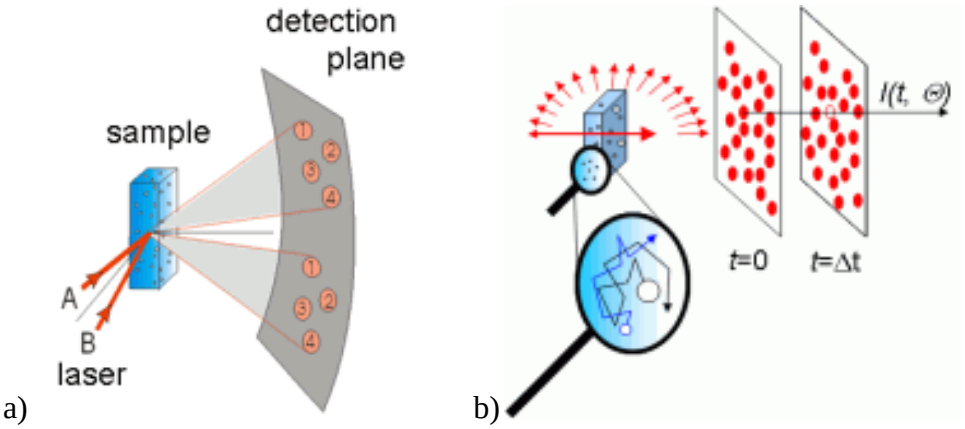

Fig. 2. (a) PCCS is using two separate beams with the same measuring volume to create two separate speckle patterns. (b) Brownian motion of the particles.

It is important to note that only singly scattered light is valid in evaluation of PCS theory. Any contribution of multiple scattered lights will affect the results and misinterpretations. Thus, PCS required highly diluted suspensions in order to avoid multiple scattering. Sensitivity will focus on the impurities in the liquid instead of the low concentration of particles. Very pure liquid and a clean room environment are required for the preparation and operation. For the sample preparation method, a small amount of the sample was dispersed in deionized water and stirred for 15 min using a magnetic bar. Then, it was vibrated for another 15 min by using an Ultrasonic bath.

3. Results and Discussion

3.1 X-ray Diffraction (XRD) analysis

XRD is a non-destructive analytical method used for identification and quantitative determination of the various crystalline forms (known as phase) present in samples. The phase identification is important because the phosphorescent powders properties are strongly dependent on the structure. Identification can be achieved by comparison of the XRD pattern – 'diffractogram' obtained from samples with an internationally recognized database. The diffractogram show the phases present (peak position), phase concentrations (peak heights), amorphous content (background bump), and crystalline size/strain (peak width).

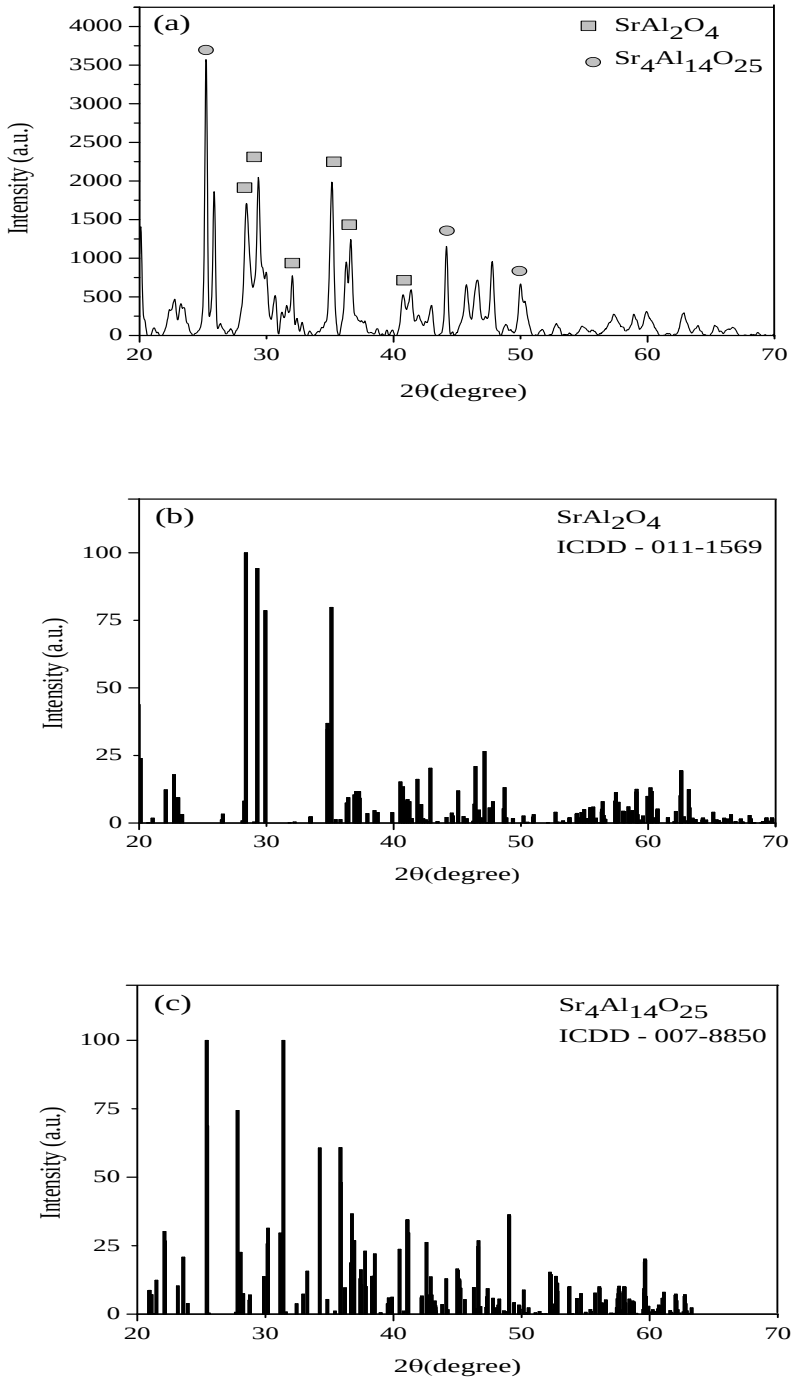

Fig. 3. (a) XRD for $SrAl_2O_4$:Eu^{2+}, (b) theoretical XRD for monoclinic $SrAl_2O_4$ taken from ICDD file no. 011-1569 and (c) orthorhombic $Sr_4Al_{14}O_{25}$ taken from ICDD file no. 007-8850.

A typical X-ray diffraction pattern of the stoichiometric $SrAl_2O_4$: Eu^{2+} powder prepared at 1000°C in a graphite crucible is shown in Fig. 3. We can observe that the product of combustion is multiphase and contains characteristic peaks of monoclinic $SrAl_2O_4$ phase as a major phase and

orthorhombic $Sr_4Al_{14}O_{25}$ as a secondary phase. The different peaks can be indexed to the $SrAl_2O_4$ (ICSD - 011-1569) and $Sr_4Al_{14}O_{25}$ (ICSD - 007-8850) (ICSD: inorganic crystallographic structure database). No other products or starting materials are observed, which shows that a small amount of doped rare earth ions does not influence the $SrAl_2O_4$ phase composition.

3.2 SEM analysis

Microscopy and topography analysis on phosphorescent powders was done through scanning electron microscopy (SEM). The main idea is to observe any crystallize phases present in the samples.

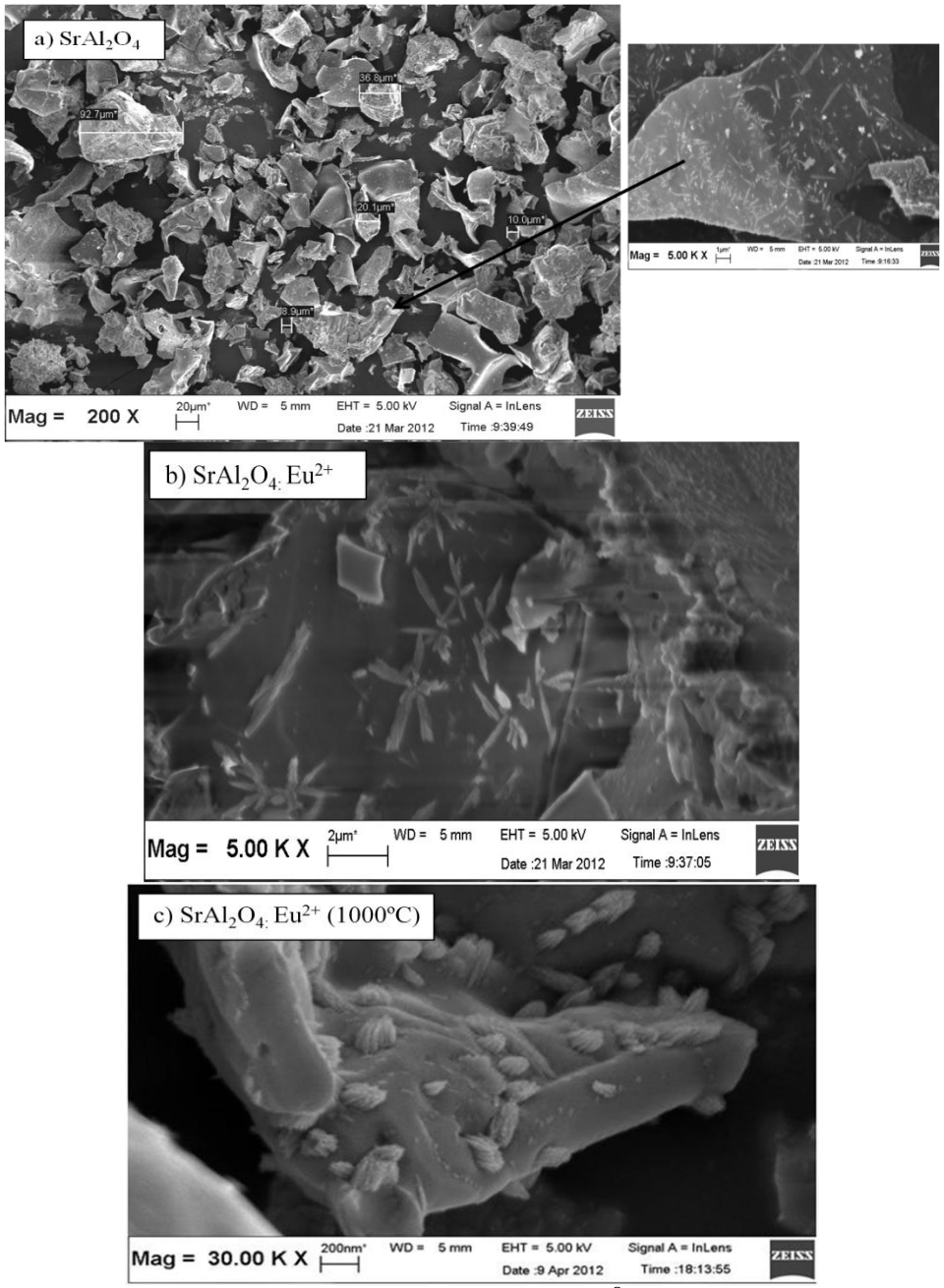

Fig.4. a) Sample $SrAl_2O_4$ before calcinations, b) Sample $SrAl_2O_4$: Eu^{2+} before and c) after calcinations at temperature 1000°C.

Figure 4a depicts the morphology of the host material $SrAl_2O_4$ without adding any activator and co-activator, while Figs. 4b and 4c show the $SrAl_2O_4$:Eu^{2+} samples with an addition of europium activator. Figure 4a represents the particle size distribution obtained from SEM for sample $SrAl_2O_4$ before calcinations. It is evident from the figure that an irregular structure at various sizes and lengths was obtained. All the samples show the formation of crystal structures of phosphor. The homogenous distribution and size of a star-like structure on the matrix surface shows the activator ions were homogenously dispersed throughout the phosphor matrix. In the case with an additional amount of Eu, sample $SrAl_2O_4$: Eu^{2+} (Fig. 4 (b)) has higher crystallite or star-like particles compared to sample $SrAl_2O_4$. The particles connected together form a larger network of star-like structure. The crystal structure has a clear, longer, and equal size in each leg of the star-like particles. After calcinations at 1000°C with 2-h soaking, the structure of the star-like particles of sample $SrAl_2O_4$: Eu^{2+} are closed and stacked together to form a flower-like structure with a better crystal (Fig. 4(c)).

The possible mechanism of the flower-like structure can be described as shown in Fig. 5. Generally, the crystal growth process involves two parts: nucleation and growth. The particles undergo nucleation at the initial state. With an increase in temperature, the grains become compressed and finer. The needle shape and star-like structure appear after 500°C. This structure is unstable and agglomerates during calcinations at 1000°C to form a stable specific flower-like structure [12, 13].

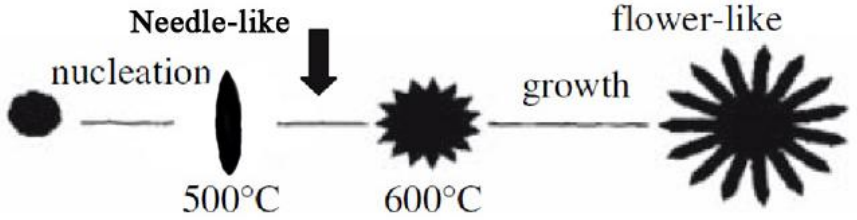

Fig. 5. Scheme to illustrate the possible mechanism of the flower-like structure of $SrAl_2O_4$: Eu^{2+} [12].

3.3 Energy-dispersive X-ray Spectroscopy (EDX) Analysis

EDX is used to characterize the elemental composition of the phosphor powder. The EDX results in Table 2 indicate the presence of a small amount of europium for sample $SrAl_2O_4$: Eu^{2+}.

Table 2. Overall EDX results of sample $SrAl_2O_4$, $SrAl_2O_4$: Eu^{2+} (before calcinations) and $SrAl_2O_4$: Eu^{2+}, annealed at 1000°C

Samples / Element	**Al**		**Sr**		**Eu**		**O**	
	Wt%	**At%**	**Wt%**	**At%**	**Wt%**	**At%**	**Wt%**	**At%**
$SrAl_2O_4$	26.22	23.35	32.19	08.83	-	-	10.78	21.57
a) $SrAl_2O_4$: Eu^{2+}	27.92	24.94	30.00	08.25			35.29	53.17
b) $SrAl_2O_4$: Eu^{2+} (after)	19.92	24.96	49.18	18.98	04.88	01.09	26.02	54.98

Table 2 shows that the content of aluminum is stable throughout the combustion and calcinations processes. The content of the europium element is examined after calcination and indicates that the content of europium distributed to the grain boundary phase and grain surface diffuse into the host lattice by rapid grain boundary diffusion [14]. The oxygen content increases upon the addition of europium in the sample and is very high, which can be due to the large amount of oxygen supplied during combustion and calcinations processes. No carbon and

nitrogen are present in the EDX analysis, which indicates that the combustion synthesis is complete.

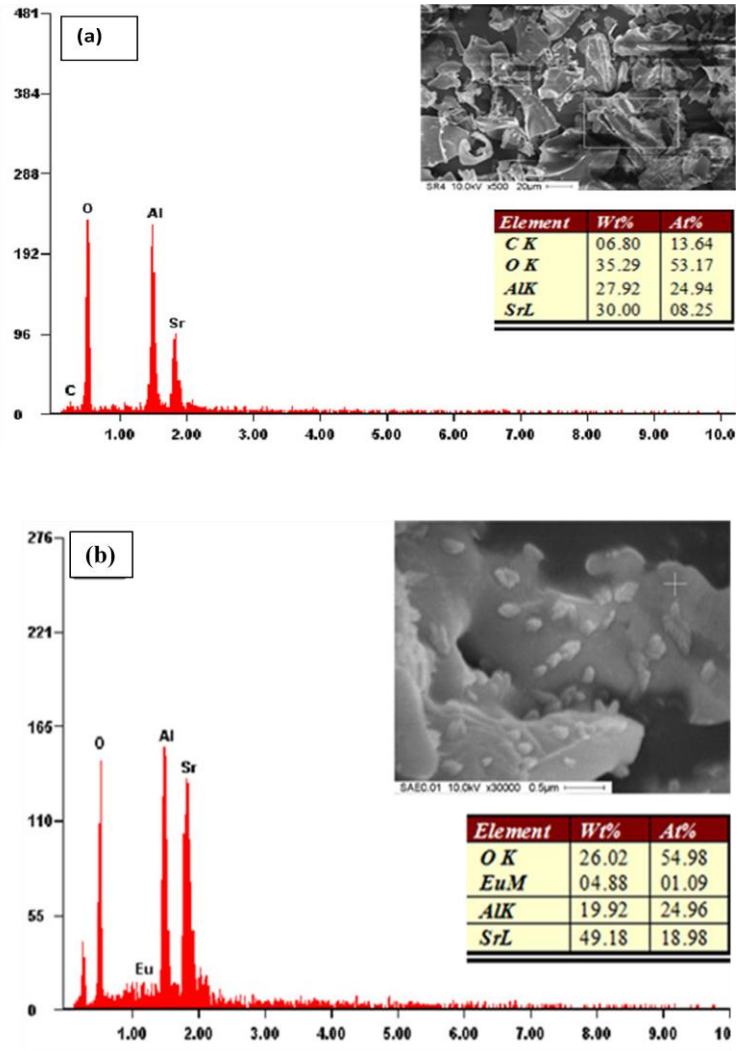

Fig. 5. EDX results of sample $SrAl_2O_4$: Eu^{2+} before (a) and after calcination (b).

3.4 Particle size analysis

The particle size of the samples was measured to justify the presence of a nanosize powder in this project. Table 3 below shows the particle analysis for samples $SrAl_2O_4$ (after calcinations) and $SrAl_2O_4$: Eu^{2+} before and after calcinations. The average size, x_{50} will be used as a reference.

Table 3. Particle size analysis data for samples $SrAl_2O_4$ and $SrAl_2O_4$: Eu^{2+} before and after calcinations

Samples	x_{10} (nm)	x_{50} (nm)	x_{90} (nm)	SMD (nm)	VMD (nm)
$SrAl_2O_4$	81.19	84.14	89.39	84.54	84.61
$SrAl_2O_4$: Eu^{2+}	44.15	51.62	60.02	51.27	51.98
$SrAl_2O_4$: Eu^{2+} (after)	112.65	132.21	154.26	131.29	133.20

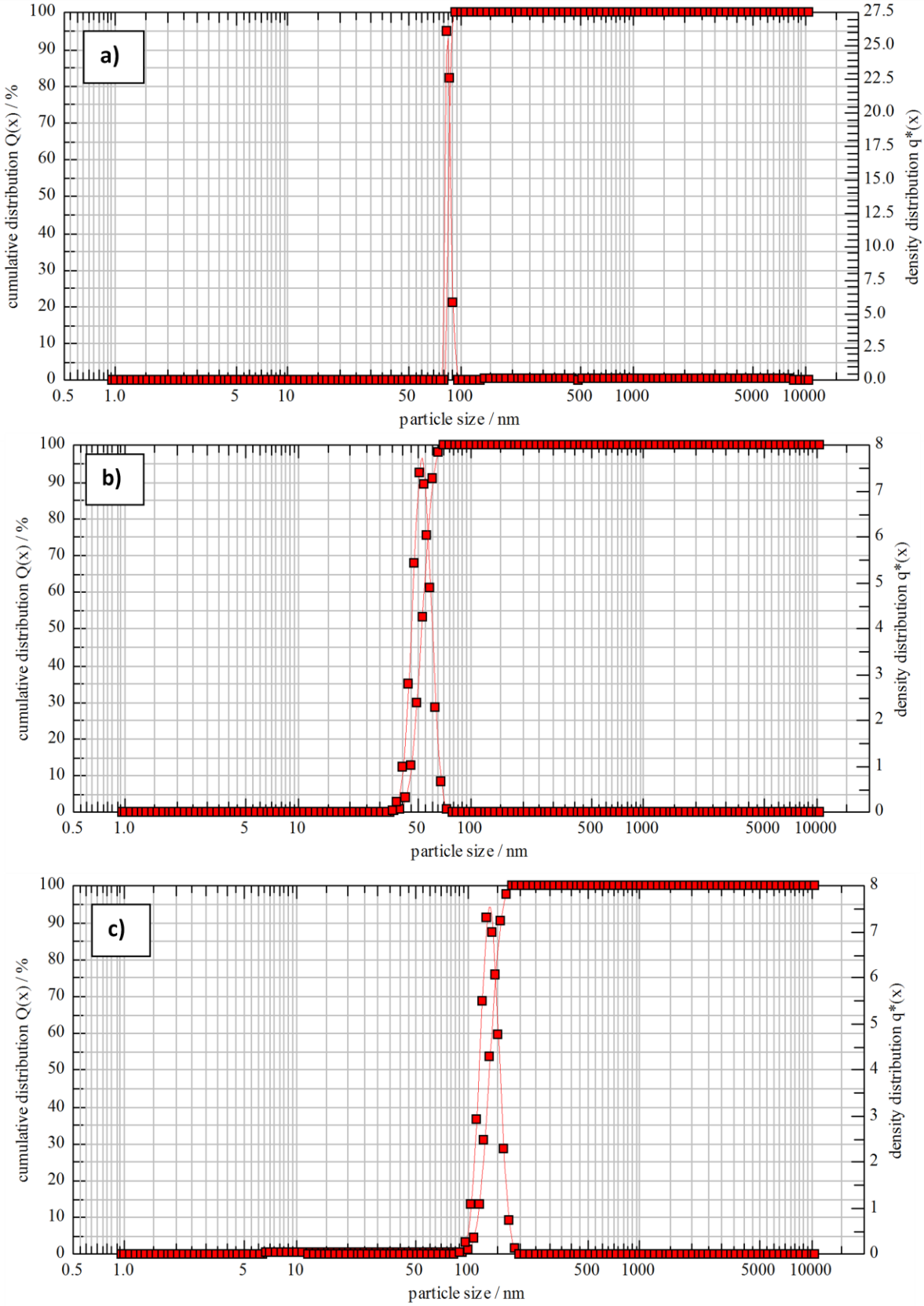

Fig. 6. Graph of particle size analysis for sample a) $SrAl_2O_4$, b) $SrAl_2O_4$: Eu^{2+} before and c) $SrAl_2O_4$: Eu^{2+} after calcinations.

The results show that all the samples achieve nanoparticle size except for sample $SrAl_2O_4$: Eu^{2+} after calcination. The particle size ranges from 81 to 89 nm for $SrAl_2O_4$, while for $SrAl_2O_4$:Eu^{2+}, it is 44 to 60 nm before the calcination processes take place. This can be explained from SEM analysis where europium was homogeneously dispersed throughout the phosphor matrix to produce a crystalline phase. The crystalline formation helps to produce a powder with a finer particle size. Furthermore, we should emphasize that the particle size distribution for $SrAl_2O_4$ has a narrow range which does not exceed 10 nm compared to $SrAl_2O_4$: Eu^{2+}. However, for sample $SrAl_2O_4$: Eu^{2+} after calcination, we observed an increase in the particle size after heating at a higher temperature due to grain grow. Excessive sintering and aggregation of particles occurs, and thus the particle size increases.

There is another method which can be used to determine the particle size. XRD pattern parameters were used to determine the average particle size by using Scherrer equation: $D_{hkl}=k\lambda / (\beta\cos\theta)$, where D_{hkl} is the size of the crystal particles, k is equal to 0.89, β is the full-width at half maximum (FWHM), and θ is the Bragg angle that corresponds to the peak analyzed. The XRD results were used to compare with the particle size PCCS analysis. Figure 7 shows one of the parts taken from the XRD data from 28 to 36 degree. The particle size of each peak was calculated as shown in the equation below, and it indicates an average grain diameter of the particles.

$$D_1 = \frac{k\lambda}{(\beta_1 \cdot \cos\theta_1)} = \frac{0.89 \times 0.15405\text{nm}}{\left(\frac{0.2534 \cdot \pi}{180}\right) \cdot \cos(14.209)} = 31.79\ \text{nm}$$

$$D_2 = \frac{k\lambda}{(\beta_2 \cdot \cos\theta_2)} = \frac{0.89 \times 0.15405\text{nm}}{\left(\frac{0.1807 \cdot \pi}{180}\right) \cdot \cos(14.677)} = 44.64\ \text{nm}$$

$$D_3 = \frac{k\lambda}{(\beta_3 \cdot \cos\theta_3)} = \frac{0.89 \times 0.15405\text{nm}}{\left(\frac{0.3374 \cdot \pi}{180}\right) \cdot \cos(17.575)} = 48.40\ \text{nm}$$

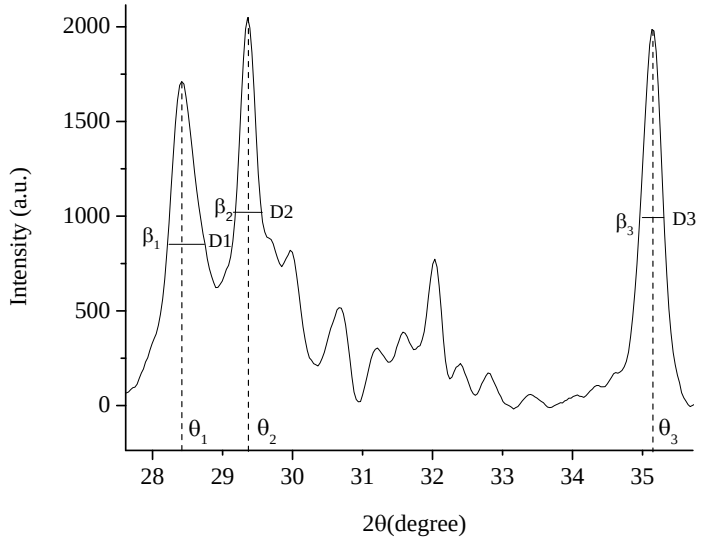

Fig. 7. Particle size of sample $SrAl_2O_4$: Eu^{2+} (1000°C) estimated from XRD measurement.

The particle sizes calculated from the Scherrer equation are in the range of 31 to 48 nm. It

has lower values compared to the results obtained using a Nanophox particle size analyzer. By comparing both methods, particle size calculated is approximate with the result obtained from Nanophox, which is more accurate referring to the grain growth when temperature is increased.

4. Conclusions

$SrAl_2O_4:Eu^{2+}$ phosphor was successfully synthesized by combustion at 500°C with calcinations at 1000°C under a reductive atmosphere. The characteristic peaks of monoclinic $SrAl_2O_4$ (ICDD - 011-1569) phase as a major phase and orthorhombic $Sr_4Al_{14}O_{25}$ (ICDD - 007-8850) as a secondary phase were obtained from X-ray diffraction analysis. No other products or starting materials are observed, which shows that a small amount of doped rare earth ions does not influence the $SrAl_2O_4$ phase composition. For scanning electron microscopic analysis, homogenous distribution and size of the flower-like structure on the matrix surface was observed; this shows that the activator ions were homogenously dispersed throughout the phosphor matrix leading to the higher excitation and emission. The particle-size analysis results implied that the phosphor powder has an average size of 50 nm before and 132 nm after calcinations. The applied combustion synthesis and calcination at low temperatures in comparison with traditional methods give promising results, and nanosized phosphors with improved properties can find a large application.

Acknowledgements

Financial support is acknowledged from Final Year Project, University Sains Malaysia, and Post Graduate Grant Research under grant no. 1001/PBAHAN/8044033.

References

[1] H. Song, and D. Chen, J. Lumin., 22 (6), 554, (2007).
[2] E. Shafia, M. Bodaghi, and M. Tahriri, Curr. Appl Phys., 10 (2), 596 (2010).
[3] T. Peng, H. Yang, et al., Mater. Lett., 58 (3), 352 (2004).
[4] H. Song, D. Chen, et al., Displays, 29 (1), 41 (2008).
[5] H. Chander, D. Haranath, et al., J. Cryst. Growth, 271 (1), 307 (2004).
[6] R. Zhang, G. Han, et al., Mater. Chem. Phys., 113 (1), 255 (2009).
[7] R. Chen, Y. Wang, et al., J. Lumin., 128 (7), 1180 (2008).
[8] S. Nguyen Manh, V. Le Thi Thao, et al., J. Phys. Conf. Ser., 187 (1), 012017 (2009).
[9] K.C. Patil, S.T. Aruna, and T. Mimani, Curr. Opin. Solid State Mater. Sci., 6 (6), 507 (2002).
[10] X. Yu, C. Zhou, et al., Mater. Lett., 58 (6), 1087 (2004)
[11] J.J. Moore and H.J. Feng, Prog. Mater Sci., 39 (4). 243 (1995).
[12] H. Ji, G. Xie, et al., J. Sol-Gel Sci. Technol., 44 (2), 133 (2007).
[13] P. Zhang, M. Xu, et al., J. Sol-Gel Sci. Technol., 43 (1), 59 (2007).
[14] Y.Liu, and C.-N. Xu, J. Phys. Chem. B, 107 (17), 3991 (2003).

INVESTIGATION OF THE EFFECT OF AN EQUALIZING RESISTOR ON THE PARALLELING VOLTAGE SOURCES BY PROJECTIVE GEOMETRY

A. A. Penin and A. S. Sidorenko

Institute of Electronic Engineering and Nanotechnologies, Academy of Sciences of Moldova, Academiei str. 3/3, Chisinau, MD-2028 Republic of Moldova
e-mail: aapenin@mail.ru, anatoli.sidorenko@kit.edu

(Received 17 February 2012)

Abstract

The method of current sharing of limited capacity voltage sources operating in parallel by equalizing resistors is considered. The effect of equalizing resistors is investigated on uniform distribution of relative values of currents when the actual loading corresponds to the capacity of a specific source. Necessary concepts for quantitative representation of operating regimes of sources are introduced using projective geometry.

1. Introduction

The basic problem of paralleled voltage sources is current sharing among these modules. Various approaches of current distribution are known [1]. In the most simple droop method, the equalizing resistors are used [2–4] including lossless passive elements [5]. Usually, the equality of module parameters, i.e., an open circuit voltage and internal resistance, is provided. Therefore, the distribution of currents means the equality of these currents. On the other hand, a scatter of module parameters, the use of voltage sources with different capacity determines the nonuniformity of current distribution. Therefore, it is natural to understand a uniform loading of sources in relative sense when the actual loading corresponds to the capacity of the source [6]. The analysis of this power supply system with a variable equalizing resistor for a given load leads to the introduction of some concepts for the quantitative representation of operating regimes and system parameters.

2. Analysis of paralleling voltage sources

Consider voltage sources E_1, E_2 in Fig. 1. Resistors R_{i1}, R_{i2} are internal resistances of these voltage sources; equalizing resistors R_{e1}, R_{e2} provide current distribution for a given load R_0.

The circuit in Fig. 1 is described by the following system of the equations

$$\begin{cases} E_1 = I_1(R_{i1} + I_1 R_{e1} + R_0) + I_2 R_0 \\ E_2 = I_1 R_0 + I_2(R_{i2} + I_2 R_{e2} + R_0) \end{cases}. \tag{1}$$

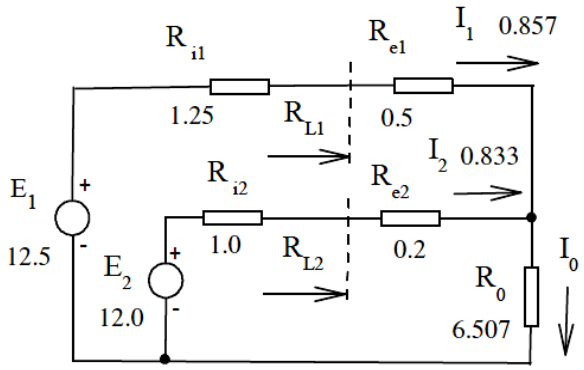

Fig. 1. Paralleling of voltage sources.

The variants of normalized parameters of a loading regime of the first source (used in different areas of electrical engineering, radio engineering, and power electronics) look like

$$m_1 = \frac{R_{L1}}{R_{i1}} = \frac{I_1^M}{I_1} - 1,\ J_1 = \frac{I_1}{I_1^M}, \tag{2}$$

here the maximum current of the source corresponds to the short circuit current

$$I_1^M = \frac{E_1}{R_{i1}}. \tag{3}$$

Similar considerations can be done for the second source:

$$m_2 = \frac{R_{L2}}{R_{i2}} = \frac{I_2^M}{I_2} - 1,\ J_2 = \frac{I_2}{I_2^M}.$$

Then we have

$$I_1 = \frac{I_1^M}{m_1 + 1} = \frac{E_1}{(m_1 + 1)R_{i1}}, I_2 = \frac{E_2}{(m_2 + 1)R_{i2}}.$$

Let us write expressions which associate the parameters of source loadings in the form $m_2(m_1)$ and $J_2(J_1)$ with the variable equalizing resistor R_{e1} for a given load. It follows from (1) that

$$E_2 = \frac{E_1}{(m_1 + 1)R_{i1}} R_0 + \frac{E_2}{(m_2 + 1)R_{i2}} (R_{i2} + R_{e2} + R_0).$$

Then we obtain

$$m_2(m_1) = \frac{\frac{R_{e2} + R_0}{R_{i2}} m_1 + \frac{R_{e2} + R_0}{R_{i2}} + \frac{E_1}{E_2}\frac{R_0}{R_{i1}}}{m_1 - \left(\frac{E_1}{E_2}\frac{R_0}{R_{i1}} - 1\right)} = \frac{\alpha m_1 + (\delta + \alpha + 1)}{m_1 - \delta}, \tag{4}$$

$$J_2(J_1) = -\frac{\delta + 1}{\alpha + 1} J_1 + \frac{1}{\alpha + 1}. \tag{5}$$

The plots of these dependences are presented in Fig. 2.

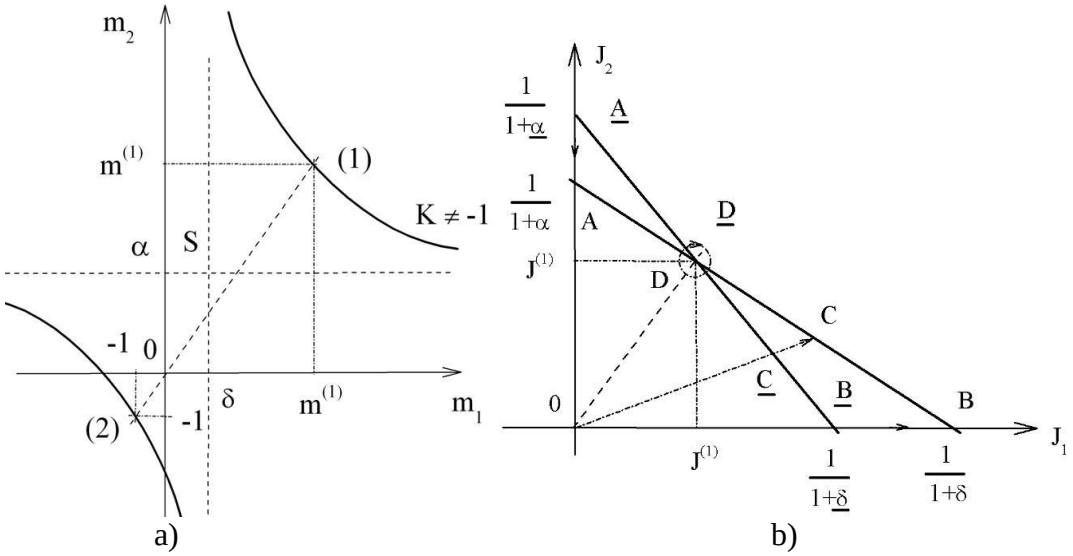

Fig. 2. Correlated changes of the source loadings parameters:
(a) as a hyperbole $m_2(m_1)$ for a given non-uniformity loading factor K;
(b) as a straight line $J_2(J_1)$ for two different systems.

Expression (4) corresponds to a hyperbole and (5) corresponds to a straight line. The desirable operating regime corresponds to the straight lines on these plots, $m_2 = m_1$, $J_2 = J_1$. The crossing of this straight line with the hyperbole gives two points of equal loading of sources $m^{(1)}, m^{(2)}$. The working area (load consumes energy) corresponds to the first point $m^{(1)}$. The second point corresponds to a condition when the voltage sources relatively equally consume energy. The points of equal loading are fixed points of the projective transformations $m_1 \to m_2, J_1 \to J_2$ as shown in Fig. 3. These transformations differ from the ones for the variable load case [6].

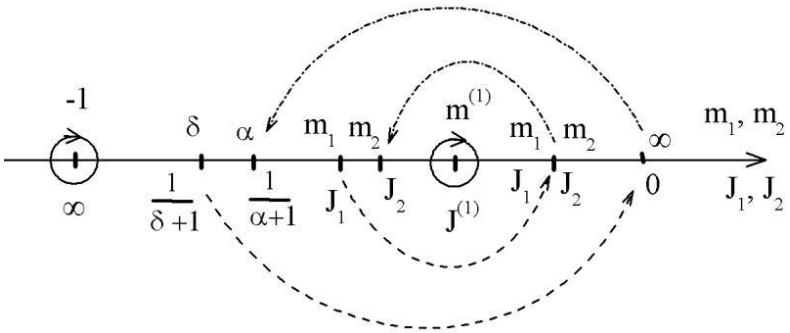

Fig. 3. Display of projective transformations of points $m_1 \to m_2$, $J_1 \to J_2$.

Let us find the fixed points $m = m_1 = m_2$. In this case, expression (4) leads to a quadratic one:

$$m^2 - (\delta + \alpha)m - (\delta + \alpha + 1) = 0 .$$

The solution gives two roots

$$m^{(1)} = \delta + \alpha + 1, \;\; m^{(2)} = -1 , \tag{6}$$

that correspond to two fixed points of transformation (5):

$$J^{(1)} = \frac{1}{\delta + \alpha + 2}, \;\; J^{(2)} = \infty . \tag{7}$$

For the second fixed point, the currents $I_2, I_1 \to \infty$. Though this case is not physically feasible, its mathematical description allows introducing some necessary characteristics of the circuit.

Similarly to [6], ***it is possible to introduce two concepts; one of them defines the circuit: how much the source loadings can differ. The second concept defines deviations of actual loadings from a fixed point in the relative form.*** In this case, it is possible to compare running regimes of different circuits.

For introduction of these characteristics, we use a number of concepts of projective geometry [7] applied in the circuit theory [8]. The characteristic of positioning of two points, concerning the chosen points (as the special case, it is the fixed points $m^{(1)}$, $m^{(2)}$) is the cross ratio of these four points

$$(m^{(2)} \;\; m_2 \;\; m_1 \;\; m^{(1)}) = \frac{m_2 - m^{(2)}}{m_2 - m^{(1)}} \div \frac{m_1 - m^{(2)}}{m_1 - m^{(1)}}, \tag{8}$$

where points $m^{(2)}, m^{(1)}$ are extreme or base. It is also known that the cross ratio corresponding to fixed points does not depend on values of running points m_1, m_2. Therefore, we accept for simplification of calculations that $m_1 = \infty$. Then

$$(m^{(2)} \;\; m_2(\infty) \;\; \infty \;\; m^{(1)}) = \frac{m_2(\infty) - m^{(2)}}{m_2(\infty) - m^{(1)}} = -\frac{\alpha + 1}{\delta + 1} = K ,$$

$$K = -\frac{\alpha + 1}{\delta + 1} = -\frac{E_2}{E_1} \cdot \frac{R_{i1}}{R_{i2}} \left(1 + \frac{R_{i2} + R_{e2}}{R_0} \right) < 0 . \tag{9}$$

The obtained expression is defined only by the circuit parameters and characterizes the ability of a circuit to equal loading of sources, which corresponds to the first introduced concept. This expression is referred to as the ***non-uniformity loading factor*** K. The negative value of K shows that points m_1, m_2 are located on different sides from fixed point $m^{(1)}$. For the variable load case, these points are located on the one side from the fixed point, and a similar factor takes place: $K > 0$ [6].

Equation (8), taking into account (9), gives the possibility to express the dependence $m_2(m_1)$ using only two parameters of the circuit, namely $m^{(1)}$ and K. Let us present (8) as

$$K = \frac{m_2 + 1}{m_2 - m^{(1)}} \div \frac{m_1 + 1}{m_1 - m^{(1)}} . \tag{10}$$

From here

$$m_2 = \frac{-\dfrac{1+Km^{(1)}}{1-K}m_1 + m^{(1)}}{m_1 - \dfrac{K+m^{(1)}}{1-K}} = \frac{-(1+Km^{(1)})m_1 + (1-K)m^{(1)}}{(1-K)m_1 - (K+m^{(1)})}, \quad \delta = \frac{K+m^{(1)}}{1-K}. \tag{11}$$

3. Comparison of loading regime of different circuits

Let us obtain a normalized representation of dependence $m_2(m_1)$. For this purpose, we consider the cross ratios for variables m_1 and m_2, using their conformity, according to transformation (4). Therefore, the cross ratios are equal among themselves:

$$(-1\, m_1 \;\; m^{(1)} \;\; \delta) = (-1\, m_2 \;\; m^{(1)} \;\; \infty).$$

The cross ratio is a relative expression and gives a necessary normalization of the variables. Therefore, any variations of relative expressions for variables m_1 and m_2 are excluded.

Let us present each cross ratio as

$$(-1\, m_1 \;\; m^{(1)} \;\; \delta) = \frac{m_1+1}{m_1 - \dfrac{K+m^{(1)}}{1-K}} \div \frac{m^{(1)}+1}{m^{(1)} - \dfrac{K+m^{(1)}}{1-K}} = \frac{m_1+1}{m_1 - \dfrac{K+m^{(1)}}{1-K}} \cdot \frac{-K}{1-K},$$

$$(-1\, m_2 \;\; m^{(1)} \;\; \infty) = \frac{m_2+1}{m_2-\infty} \div \frac{m^{(1)}+1}{m^{(1)}-\infty} = \frac{m_2+1}{m^{(1)}+1}.$$

Then, we have the equation

$$\frac{m_2+1}{m^{(1)}+1} = \frac{m_1+1}{m_1 - \dfrac{K+m^{(1)}}{1-K}} \cdot \frac{-K}{1-K}.$$

The left side of this expression represents a normalized value and prompts how it is possible to write the similar value in the right side. Therefore,

$$\frac{m_2+1}{m^{(1)}+1} = \frac{-\dfrac{K}{1-K}\dfrac{m_1+1}{m^{(1)}+1}}{\dfrac{m_1+1}{m^{(1)}+1} - \dfrac{1}{1-K}}. \tag{12}$$

Similarly, we have for (5)

$$\frac{J_2}{J^{(1)}} = \frac{J_1}{J^{(1)}K} - \frac{1-K}{K}. \tag{13}$$

It should be noted that expressions (12) and (13) obviously set a deviation of running parameters of loading from the equal loading regime in the form of normalized values. But it is not enough for comparison of deviations for the circuits with different values of parameter K. Using the example of the most simple relation (13), we will show why it is so. Let us consider

two circuits with different values of parameters $K, \underline{K}$, but with identical value $J^{(1)} = 1$. Characteristics of the circuits in the form of straight lines are presented in Fig. 2b. Loading regimes can be considered identical if the conformity of characteristic regime points takes place (shown by arrows) upon a change in the load. This follows from similarity principles [9]. Then, the projective transformation takes place and it is set by the center at point 0 and by three pairs of characteristic regime points: A, B, D and $\underline{A}, \underline{B}, \underline{D}$. The points $D, \underline{D}$ coincide and correspond to the fixed point $J^{(1)}$. The point of a running regime C corresponds to the point $\underline{C}$. For this projective transformation, the invariant in the form of a cross ratio is carried out $(A\,C\,D\,B) = (\underline{A}\,\underline{C}\,\underline{D}\,\underline{B})$.

Here, the points A, B and $\underline{A}, \underline{B}$ are base, and the points $D, \underline{D}$ are unit ones.

Therefore, this cross ratio can be accepted as an equal deviation of running points C, $\underline{C}$ from the unit points. Further, we display points A, C, D, B on the axis of currents J_1. Then, we obtain the deviation for the first source:

$$\Delta_1 = (0 \;\; J_1 \;\; J^{(1)} \;\; (1-K)J^{(1)}) = \frac{J_1}{J_1 - (1-K)J^{(1)}} \cdot K \;, \tag{14}$$

and the other form is

$$\Delta_1 = \left(0 \; J_1 \; J^{(1)} \; \frac{1}{\delta + 1}\right) = \frac{J_1}{J_1 - \dfrac{1}{\delta + 1}} \cdot \frac{-\alpha - 1}{\delta + 1} \tag{15}$$

The deviation for the second source is expressed similarly:

$$\Delta_2 = \left(0 \; J_2 \; J^{(1)} \; \frac{1}{\delta + 1}\right).$$

Thus, the deviations include the circuit parameters and are not simply the normalized values as $J_1 / J^{(1)}$, $J_2 / J^{(1)}$.

With the aim to show the presented reasons, we will consider a special case, $K = -1$. Then, expressions (13) and (14) became

$$\frac{J_2}{J^{(1)}} = 2 - \frac{J_1}{J^{(1)}}, \; \Delta_1 = \frac{\dfrac{J_1}{J^{(1)}}}{2 - \dfrac{J_1}{J^{(1)}}} = \frac{2 - \dfrac{J_2}{J^{(1)}}}{\dfrac{J_2}{J^{(1)}}} = \frac{1}{\Delta_2}.$$

Thus, the deviations look like usual proportions and normalized values.

Taking into account the conformity between various definitions of loading parameters, the deviation is expressed in the invariant form through the cross ratio for the variable m_1

$$\Delta_1 = \left(0 \; J_1 \; J^{(1)} \; \frac{1}{\delta + 1}\right) = (\infty \; m_1 \; m^{(1)} \; \delta) = \frac{m^{(1)} - \delta}{m_1 - \delta} = \frac{1 + \alpha}{m_1 - \delta} \;. \tag{16}$$

The values of the deviations at the characteristic points are presented in Fig. 3. In particular, the deviation $\Delta^{(2)}$ for the second fixed point, $m^{(2)} = -1$, is equal to parameter K.

Again we will consider a special case, $K=-1$. Then, from (11), we obtain

$$m_2=\frac{\frac{m^{(1)}-1}{2}m_1+m^{(1)}}{m_1-\frac{m^{(1)}-1}{2}}=\frac{\delta m_1+m^{(1)}}{m_1-\delta},\ \alpha=\delta.$$

The points m_1, m_2 are symmetries concerning $m^{(1)}$ and bear the special name of harmonic conjugate points in projective geometry. In particular, the point $m_1=\delta$ corresponds to the point $m_2=\infty$ and vice versa. In addition, for the hyperbole in Fig. 2a, the center S will be on the straight line of equal loading.

Let us calculate deviations using (16). The deviation for the second fixed point, $\Delta^{(2)}=-1$, from the point $m^{(2)}$ concerning the base points is harmonic conjugate one to a unit point $m^{(1)}$.
In turn, the deviation for the second source is

$$\Delta_2=\left(\infty\quad m_2\ m^{(1)}\ \delta\right)=\frac{1}{\Delta_1}.$$

We introduce the hyperbolic metric which defines the distances of the running regime points to the fixed point, $r_1=Ln\Delta_1$, $r_2=Ln\Delta_2$, $r_1=-r_2$. From here, the physical sense of value $K=-1$ follows: deviations of sources are equal in quantity, but are opposite in sign (this can be of practical use for all the equalizing resistor values).

Example. Consider the given circuit in Fig. 1.
Maximum currents of a source by (3), $I_1^M=10$, $I_2^M=12$. Parameters of the loading regime by (2), $m_1=10.66$, $J_1=0.0857$, $m_2=13.4$, $J_2=0.0694$.
Expressions of the loading regime of sources by (4), (5)

$$m_2=\frac{6{,}707m_1+12{,}13}{m_1-4{,}422},\quad J_2=-0{,}703J_1+0{,}13.$$

First fixed points by (6), (7), $m^{(1)}=12{,}13$, $J^{(1)}=0{,}0761$. Non-uniformity loading factor by (9), $K=-1{,}421$. Deviations for the sources by (16), $\Delta_1=1{,}2345$, $\Delta_2=0{,}802=1/1{,}246$.
The distances of the running regime points to the fixed point
$r_1=Ln\Delta_1=0{,}2106$, $r_2=Ln\Delta_2=-0{,}2206$.
The deviation for the second source is greater than for the first one.

4. Conclusions

We have proposed the concept of a nonuniformity loading factor for voltage sources which quantitatively characterizes the ability of a circuit for equal loading of sources. This factor makes it possible to compare different circuits.

We have introduced the concept of deviation of the running regime from the regime of

equal loading in a relative form for voltage sources. It gives the possibility to compare the deviations of the regime of the sources being parts of single or different supply systems.
Geometrical interpretation provides a validation for the introduction and definition of the proposed concepts.

References

[1]. Huang Y. and Tse C. K., IEEE Transactions on Circuits and Systems I: Regular Papers. 54, 5, 1099 (2007).
[2]. Irving B. T. and Jovanović M. M., Proceedings of 15th Annual IEEE Applied Power Electronics Conference, p. 235 (2000). http://www.deltartp.com/dpel/dpelconferencepapers/06_3.pdf
[3]. Kim J.W., Choi H. S., and Cho B. H., IEEE Transactions on Power Electronics 7, 1, 25 (2002). http://pearlx.snu.ac.kr/Publication/IEEE0202.pdf
[4]. Villarejo J. A., De Jodar E., SOTO F., and Jimenez J., Proceedings of the 7th WSEAS International Conference on Circuits, Systems, Electronics, Control and Signal Processing (CSECS'08), p.114, 2008. http://www.wseas.us/e-library/conferences/2008/tenerife/CD-CSECS/papers/CSECS18.pdf
[5]. Wang J. B., Advances in Power Electronics. v. 2011 (2011). Article ID 713250. doi:10.1155/2011/713250. http://www.hindawi.com/journals/ape/2011/713250/
[6]. Penin A.A., Elektrichestvo 11, 32 (1999).
[7]. Glagolev N. A., Proektivnaya geometriya, Nauka, Moskva, 1963.
[8]. Penin A. A., Wseas Transactions on Circuits and Systems 10, 5, 157 (2011). http://www.wseas.us/e-library/transactions/circuits/2011/53-346.pdf.
[9]. Venikov V.D. , Teoria podobiya i modelirovaniya, Vysshaya Shkola, Moskva, 1976.

EVOLUTION OF CONVECTIVE CLOUDS IN TERMS OF THE GENERAL SYSTEMS THEORY

G. S. Burundukov, E. I. Potapov, Yu. A. Stepanyatov, and A. V. Khomenko

Special Service for Active Influences on Hydrometeorological Processes of Republic of Moldova, Chisinau

(Received 24 April 2012)

Abstract

Some features (laws) of the evolution of convective clouds fit into and are summarized in terms of a simple "resource−consumer" Lotka – Volterra model. Based on this model, taking into account the revealed system-wide patterns, we analyze the possibility of an impact on convective clouds to control their intensity (redistribution of precipitation, hail suppression).

1. Introduction

Previous studies of the development of convective clouds [2, 3] have shown that the use of the nonconventional approach (model) in which an individual convective cloud is regarded as an open evolving system is promising.

A system is a set of interacting elements (Bertalanffy L. von [4]). According to this definition, we consider a convective cloud (*Cb, Cu cong*.) as a set of interacting convection elements (CEs), and a cloud convective cell (CC) is none other than a dominant CE.

The evolution of *Cb* (*Cu cong*) is the evolution of a "complex whole," of a system. Systems and laws of their evolution are the subject matter of the general systems theory (GST).

The main idea of the GST is the principle of isomorphism of the laws governing the functioning of system objects regardless of their nature. In line with this principle, the basis of our approach is the use of the Lotka – Volterra model versions to study the evolution of *Cb* (*Cu cong*) [2, 3, 13, 14].

2. Lotka – Volterra Model

The Lotka – Volterra model describes, in particular, the evolution of the "consumer-resource" system; in our case, the "*Cb* (*Cu cong*.) – resource" system. By the resource we mean wet subcloud air (water vapor) which is used by the cloud ("consumer") during its evolution. It is the water vapor that provides the dynamics of growth (development) of the cloud in the exothermic processes of phase transitions.

The Lotka – Volterra model in one of its versions can be written through the following system of equations:

$$dR/dt = Q - aMR, \quad (1)$$

$$dM/dt = bMR - cM, \quad (2)$$

where dR/dt and dM/dt are the time variation of the amount of resource R in the system (interpreted as the change in the water vapor mass in the atmospheric boundary layer in a neighborhood of the cloud) and the respective change in the mass M (integrated water content) of the cloud; *a* and *b* are the coefficients that determine the efficiency of "assimilation" of the

resource by the cloud; *c* is the specific rate of the natural dissipation of the cloud (*a*, *b*, and *c* are positive constants); *Q* is the rate of resource inflow from the outside (in [13, 14], M and R are used with the dimension of density rather than mass).

3. Evolution of a Cloud–Resource System on a Nonrenewable Resource

Figure 1 shows the features of evolution of model clouds on a nonrenewable resource (the resource isolation of the system, Q = 0) versus the initial amount of the resource: in the first case (black) R1 = 1500 arb. units; in the second case (green) R2 = 2000 arb. units.

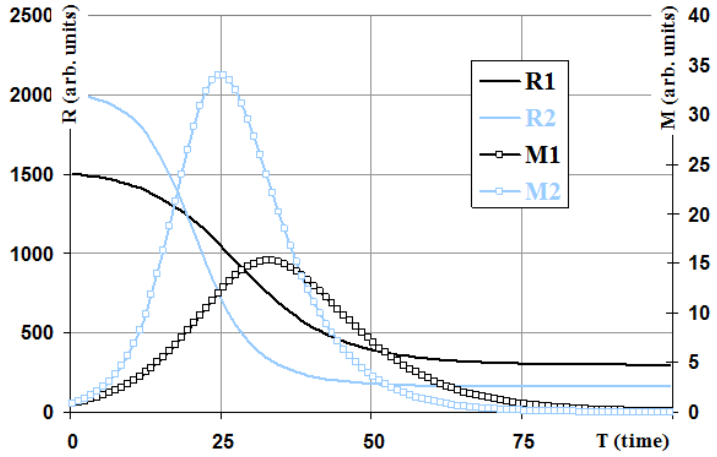

Fig. 1. Evolution of model clouds in the version of a nonrenewable resource (the resource isolation of the system) versus the initial amount of resource in the system. Initial conditions: R1 = 1500 arb. units, R2 = 2000 arb. units; M1 = M2 = 0.9 arb. units of mass (integrated water content) of the cloud.

"Time" in iteration steps is plotted along the horizontal axis; the resource mass in the system and the cloud mass in arbitrary units are plotted along the vertical axes on the left and on the right, respectively. At the initial stage of evolution, the growth of cloud masses occurs exponentially. The cessation of growth and the subsequent dissipation of the cloud are the result of a decrease in the amount of the resource in the cloud–resource system.

The pattern of evolution of *Cb* (*Cu cong*.) changes depending on the initial amount of the resource in the system. With a larger amount of the resource, the cloud develops faster and achieves a larger mass at its maximum, while the time of the growth phase decreases. The growth rate of the cloud → maximum value of its parameters relationship [6, 10] is known to be used for assessing the possibility of transition of the cloud into a hail-hazardous state [11].

This evolution of the model cloud is interpreted as the evolution of a single-cell cloud (the presence of a single mass maximum in the evolution of the cloud). The finiteness of the resource is the cause of the termination of the evolution of the model cloud. We assume that the suppression of the influent upward flow by precipitation is not a necessary condition for the dissipation of the cloud. The evolution of a deep convective single-cell cloud is a rapid process; this causes a reduction in the time limit for making decisions on the impact on the cloud at its higher power at the growth peak.

4. Evolution of the Cloud–Resource System with a Constant Resource Inflow

According to the model experiment, the resource is constantly flowing into the system ($Q > 0$). Ten arbitrary units of the resource mass are added per iteration step in the R1 version and 30 arbitrary units for R2 (Fig. 2).

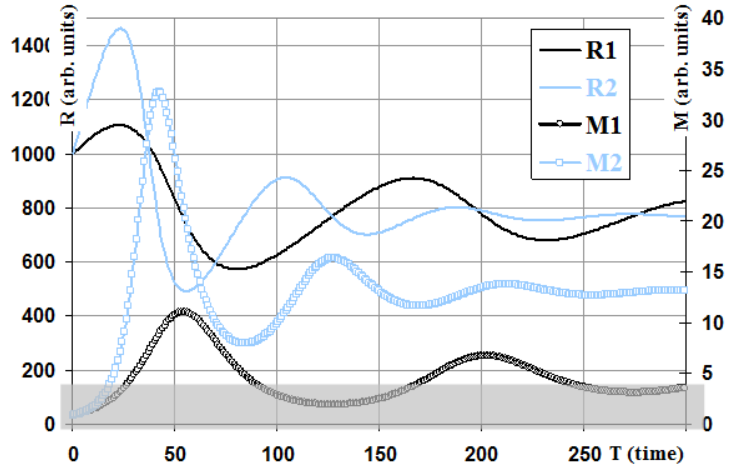

Fig. 2. Evolution of model clouds with a constant resource inflow into the system: in the R1 version, 10 arb. units of resource mass per iteration step are added; in the R2 version, 30 arb. units. Initial conditions: R1 = R2 = 1000 arb. units of resource mass; M1 = M2 = 0.9 arb. units of mass (integrated water content) of the cloud.

The main feature of evolution in this case is the occurrence of an oscillation mode in the system: out-of-phase oscillations of the masses of the cloud and the resource occur (at a constant inflow of the resource). An increase in the amount of the resource in the system is observed in the phase of minimum cloud mass.

The studies of the evolution of *Cb* fields [1, 15] showed that the periods of minimum parameters of the dominant *Cb* (in terms of the model, they are the resource growth stages in the evolving system) are accompanied by the formation of new convective entities (*Cb*, *Cu cong*.). In storm-hail processes in this period, a more frequent formation of new radio echoes was observed; in mesoscale *Cb* complexes, the frequent formation of new radio echoes and structural rearrangements of radio echo fields were observed; for the *Cb* scales (with a decrease in its parameters), an increase in the cloud canopy area was revealed, i.e., the formation of new cloud CEs (Khomenko, 2008). Thus, we can apparently state the similarity of processes in the evolution of convective systems of different scales (scale invariance).

As the resource inflow increases (Fig. 2, R2 version), the cloud grows at a higher rate and achieves a greater mass at its maximum. At the same time, the oscillation frequency of the cloud mass and the resource amount in the system increases. Radar observations (MRL-5) revealed different periods of formation of new CCs in multicell clouds of 15 to 25 min [8].

The evolution with an oscillatory variation in the model cloud mass is interpreted as the evolution of a multicell cloud with the sequential formation of new CCs in the cloud.

According to simulation results, the growth of another CC in the cloud is possible with a sufficient amount of available resource. We assume that the occurrence of the outflow of the cold

air in the surface layer, which results from the precipitation from the previous CC ("trigger mechanism"), is not a necessary condition for the generation of new CCs in the cloud.

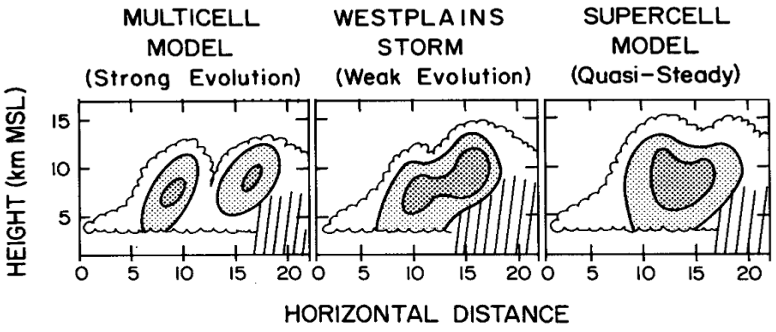

Fig. 3. Fragment of a schematic diagram of evolution of three types of storms taken from [18].

Taking into account the sensitivity threshold of the MRL, we find that a multicell cloud can be identified as a time-sequential formation of single-cell clouds: in Fig. 2 (M1 version), we shaded the conventionally unrecordable integrated water content (<4 arb. units).

Based on the solution to equations (1) and (2) in the form of spatial waves of M and R in [13], we assume that an increase in the resource inflow leads, in addition to an increase in the frequency of formation of new cells (Fig. 2), to a decrease in the distance between the formed cells. Thus, increasing the resource inflow to the cloud resource system, we can simulate the known sequence of conventional typing of *Cb*: single-cell, multicell, supercell clouds. The transition of a multicell cloud into a supercell cloud will occur through an intermediate structure of "weak evolution" [18] (see Fig. 3).

Note that the resource inflow into the cloud can be implemented through its displacement over the field of the uniformly (as an idealization) distributed resource. The rate of movement of the cloud relative to the resource field (wet air of the sub cloud layer of the atmosphere) and, therefore, the magnitude of the resource inflow will be higher for greater vertical wind shear within the troposphere. It is known that the intensity of *Cb* increases (with a change in its structure) with increasing vertical wind shear [12, 16].

The decrease in the amplitude of oscillations of mass and resource over time in the versions under discussion (Fig. 2) occurs at a constant magnitude of the resource inflow. An increase in the inflow over time can lead to an increase in the amplitude, and the fluctuations in the resource inflow into the cloud–resource system can cause resonance effects.

The difficulty of describing the evolution of a cloud lies in the fact that the space distribution of the resource is nonuniform. This is evidenced, in particular, by the nonuniform distribution of temperatures of dry and wet bulb thermometers in the surface layer. It is shown that the spatial localization of hail processes is attributed to this nonuniformity [5].

We assume that the oscillations of the cloud parameters are a combination of (a) natural oscillations of the cloud–resource system (self-oscillations at a constant resource inflow) and (b) the nonuniformity of the spatial distribution of the resource and, as a consequence, the nonuniformity of the resource influx into the cloud that is moving relative to the field of the resource.

The foregoing suggests that some of the observed features of the evolution of *Cb* fit (are summarized) into the terms of the used model and can be explained by it.

5. Impact on a Convective Cloud (CC, CE): Nonrenewable Resource

One of the effects of impact on *Cb* (*Cu cong*.) via the seeding of its super-cooled part with an ice-forming agent (AgI, etc.) is the stimulation of convection and, as a consequence, an increase in the mass of the cloud. This effect is theoretically substantiated and confirmed by full-scale experiments. It is used as a basis for the implementation of relevant programs of the artificial increase in precipitation from *Cb* (*Cu cong*.) [7]. It is this effect that is used by us in the modeling of the evolution of a cloud during impact (the model gives the possibility to simulate this effect).

Figure 4 depicts the results of these model experiments on impacts:

(a) No impact was conducted. Clouds that develop on a common resource enter into a competitive interaction (limit one another in growth). Cloud 2 is formed 10 iteration steps later than cloud 1 (given by the model for all the cases under discussion); as a consequence, it develops not so rapidly and achieves a lower mass. In this case, the ratio of the masses of the clouds at the stage of their maximum development is **2.8**. The clouds achieve their mass maxima simultaneously in the 76th iteration step.

(b) An impact on cloud 1 in order to stimulate its growth was carried out in the 30th iteration step (indicated by a red arrow); in this step, a mass of 0.4 arb. units (stimulus value is constant in all the versions) was added to the cloud. As a result, the ratio of the masses of the clouds is **3.2**. The growth of the mass of cloud 1 is accompanied by a loss in the mass of cloud 2. The maximum mass is achieved in step 75.

(c) An impact on cloud 2 was carried out in the 30th iteration step. The mass ratio of the clouds is **2.1**. An increase in mass of cloud 2 and a loss in the mass of cloud 1 take place. The maximum mass is achieved in step 75.

(d) An impact on cloud 2 was carried out in the 15th iteration step. The mass ratio of the clouds is **1.2**. The maximum mass is achieved in step 73.

According to the results of the simulation experiment:

- The effect of the impact on a cloud in a complex of competing clouds is shown as a stimulation of the cloud exposed to the impact, and the magnitude of the cloud reaction is not proportional to the value of the stimulus. The impact is accompanied by a redistribution of the influent resource between the clouds of the complex with respective changes in the masses of the clouds (it is assumed that the spatial redistribution of precipitation also occurs in this case).
- The period of growth (time to the maximum mass of the clouds) decreases.
- The earlier (at the growth stage) the impact is carried out and the higher the stimulus value, the greater these effects (as obtained in experiments with varying stimulus value).

The authors of [17] analyze the possible hail suppression techniques and give preference to an active impact for redistributing the resource (using our terminology) between competing clouds. The simulation results confirm that this approach to impacts on *Cb* (*Cu cong*.) is promising.

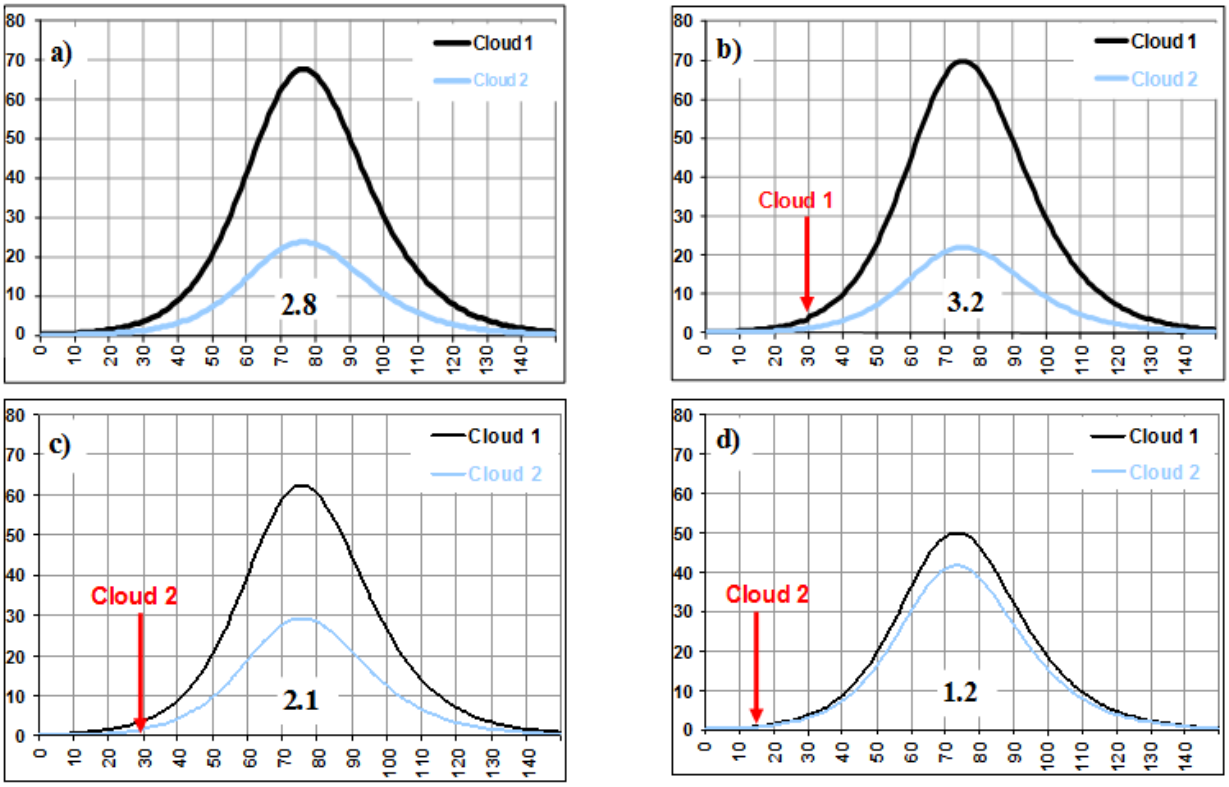

Fig. 4. Simulation of a stimulating impact on a convective cloud. The mass (integrated water content) of the clouds in arb. units is plotted along the vertical axis; "time" in iteration steps is plotted along the horizontal axis. See the text.

6. Evolution Link (Time Unit Cell of System Evolution)

Zhirmunskii and Kuz'min [9], based on the generalization of the features of development of different systems, introduce the notion of a time unit cell of system evolution, i.e., an evolution link (Fig. 5a). The total period of an evolving system is the sequence of these links. The minimum possible lifetime of the system is the duration of a link. It has two components: a growth phase and a rearrangement phase (critical period). The rearrangement phase is of particular interest. By the assumption of the authors, in this period, the system is most sensitive to an external impact. Small fluctuations in the rearrangement phase can significantly change the trajectory of the evolution of the system.

Figure 5b shows the behavior of the parameters of a hail cloud as of August 5, 2008, where H45 is the height of the upper boundary of the isosurface of 45 dBZ, which is the parameter used to estimate the hail hazard (intensity) of the cloud, and S45 canopy is the area of the cloud canopy in the contour of 45 dBZ.

If we consider the period of decrease in H45 (from 15:45 to 15:52) as a rearrangement phase in an evolution link of the cloud system, then this rearrangement consists in an increase in the canopy area, i.e., an intensification of formation of new CEs and the formation of another CC. According to the model, these periods are characterized by an increase in the amount of the resource in the cloud–resource system (in Fig. 2, ~60 to the 100th iteration step for R2). The increased sensitivity of the cloud system in this phase of development becomes clear: this is the "sensitivity" of new convective entities (CEs) which are in a competitive interaction between

each other (see the conclusions of previous section 4).

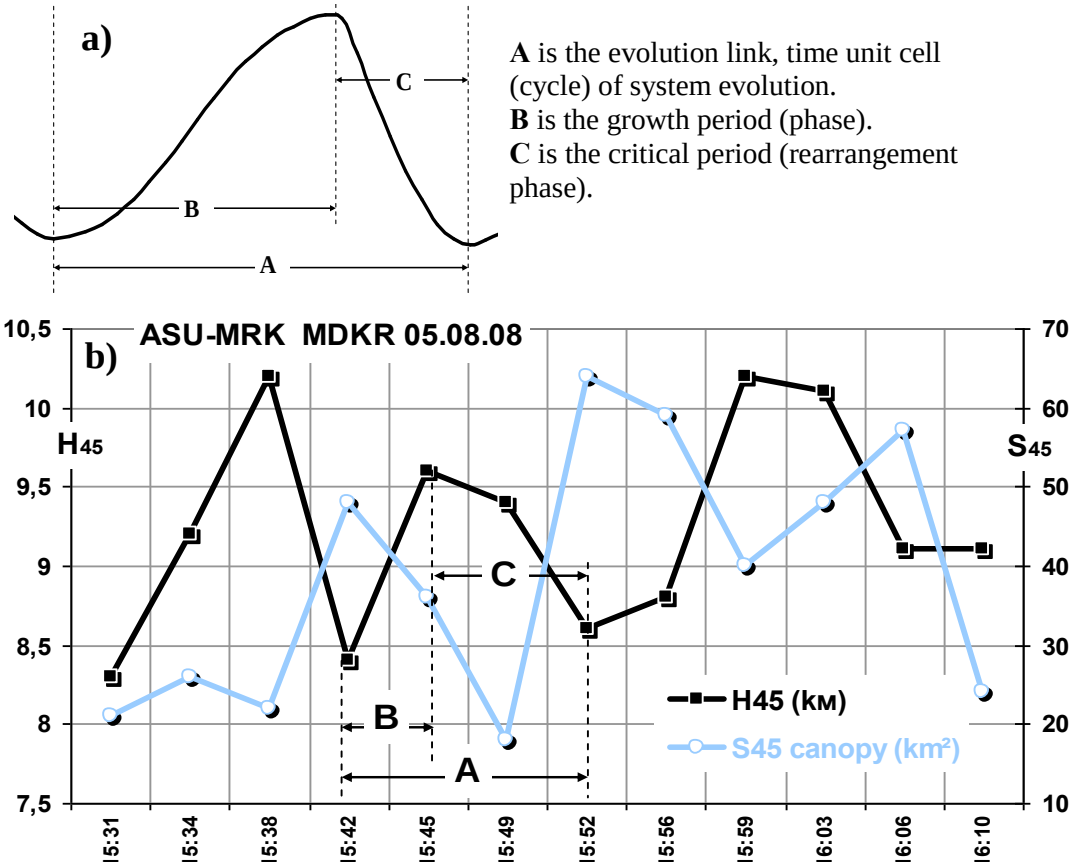

Fig. 5. (a) Evolution link, time unit cell (cycle) of system evolution; diagram according to [9]. (b) Behavior of parameters (H45 and S45 canopy) of a real hail cloud according to the
ASU-MRL archives as of August 5, 2008. Time period: **A** is interpreted as a cloud evolution link: **C** is the cloud structure rearrangement.

7. An Alternative Concept of Active Impacts on *Cb* (*Cu cong*) to Suppress Hail

Based on the used approach (method) for describing the evolution of a convective cloud, we formulate some proposals on a possible alternative concept of active impacts (AIs) on *Cb* (*Cu cong*) to suppress hail. The AI problem reduces to the prevention of the formation of a dominant CE (hail CC) through the redistribution of the resource inflowing into the cloud between competing CEs (CC, *Cb*, *Cu cong*.).

This can be achieved in the following ways:

- Seeding the supercooled cloud volumes with an ice-forming reagent in order to locally stimulate the convection.
- Seeding the periphery of the cloud (the region of newly formed CEs in their initial development stage).

- Seeding the formed satellite clouds.
- Abandoning the seeding (stimulation) of the cloud volume responsible for the formation of a dominant CC which, in its natural evolution, can achieve a hail stage.
- Impacting the cloud in the phases of its structural rearrangements (a decrease in parameters, an increase in the canopy area, the possible formation of satellite clouds); in this case, the periodicity of seeding is determined by the frequency of generation of new cells in the cloud and the increase in the canopy areas (periodicity of rearrangement phases).

The intended effects of impact:

- A failure/destruction of the space-time structure of the cloud;
- An increase in the precipitation field area;
- A decrease in the kinetic energy of falling solid precipitation.

Some of the represented proposals are being implemented in the AI practice, for example, seeding the periphery of *Cb* (new CEs).

Conclusions

We summarize the foregoing in the form of a brief sequence.

- Based on the fact that a cloud is a complex entity (system), we use the capabilities of the GST.
- Based on the principle of isomorphism, we employ one of the versions of the Lotka – Volterra model to describe/study the evolution of *Cb* (*Cu cong*.).
- It is shown that, in terms of the selected model, it is possible to summarize and explain a number of dissimilar facts derived at different times by different researchers in the observations of the evolution of convective clouds (the descriptive component of the model is satisfactory).
- The possibility of an AI on *Cb* (*Cu cong*.) to suppress hail has been explored (simulation experiments). The results show that an AI can be advantageous through the redistribution of the resource between competing CEs (CC, *Cu cong*., *Cb*) via local convection stimulation. According to the results of simulation experiments, a possible alternative concept of AIs has been formulated.
- Based on the concepts of a link as a time unit cell of system evolution and the rearrangement phase in this link (system-wide pattern), we have specified the methodological issues of the alternative concept of AIs.

In this study, we do not discuss the complex processes occurring in a convective cloud; we put an emphasis on describing the "behavior" of a cloud as an active entity (complex object, system) which, in its evolution, interacts with the external environment, i.e., a medium that exhibits specific properties and contains resources of "vital importance" for the cloud, and with similar convective entities which are competitors for the resource.

References

[1] Abdullaev S.M and Matyushkin A.A., Trudy Vsesoyuznogo seminara "Aktivnye vozdeistviya na gradovye processy i perspektivy usovershenstvovaniya l'doobrazuyushchikh reagentov dlya praktiki aktivnykh vozdeistvii," Moscow, Gidrometeoizdat, 1991, pp. 102-108.

[2] Burundukov G.S., in Aktivnoe vozdeistvie na gradovye processy v Moldove, Chisinau, Protivogradovaya sluzhba Respubliki Moldova, 2004, pp. 29-47.

[3] Burundukov G.S., Potapov E.I., Garaba I.A., Plyusnin S.D., Zasavitskii E.A., Abshaev M.T., and Abshaev A.M., Meteorologiya i gidrologiya, 2, 88 (2011).
[4] Geides M.A. Obshchaya teoriya sistem (sistemy i sistemnyi analiz), Globus-Press, 2005, 202 p.
[5] Goral' G.G., Trudy VGI, 61, 26 (1985).
[6] Dadali Yu.A., Trudy VGI, 41, 53 (1978).
[7] Dennis A., Izmenenie pogody zasevom oblakov, Moscow, Mir, 1983, 272 p.
[8] Dinevich L.A., Livshic E.M., Starostin A.N., and Shvecov V.S., Tez. dokladov 7-go vsesoyuznogo soveshchaniya po radiometeorologii, Moscow, Gidrometeoizdat,1986, p. 114.
[9] Zhirmunskii A.V. and Kuz'min V.I., Kriticheskie urovni v razvitii prirodnyh system, Leningrad, Nauka, Leningradskoe otdelenie, 1990, 224 p.
[10] Livshits E.M. Nekotorye rezul'taty issledovaniya evolyutsii konvektivnykh radiolokatsionnykh yacheek. Problemnye voprosy aktivnogo vozdeistviya na atmosfernye processy, Kishinev, Shtiintsa, 1986, pp. 76-88.
[11] Imamdzhanov H.A., Usmanov I., and Kiyaev A.E. Protivogradovye raboty v Uzbekistane i ikh ekonomicheskaya effektivnost'. Doklady nauchno-prakticheskoi konferentsii, Nal'chik, 2007, Pechatnyi dvor, 2011, pp. 57-61.
[12] Mal'bakhova N.M., Trudy VGI, 80, 99 (1991).
[13] Svirezhev Yu.M., Nelineinye volny, dissipativnye struktury i katastrofy v ekologii, Moscow, Nauka, 1987, 368 p.
[14] Svirezhev Yu.M. and Logofet D.O., Ustoichivost' biologicheskikh soobshchestv, Moscow, Nauka, 1978, 352 p.
[15] Ryazantsev N.A. and Starostin A.N., Opyt ispol'zovaniya sputnikovoi i radiolokatsionnoi informatsii dlya sverkhkratkosrochnogo prognoza evolyutsii oblakov. Aktivnye vozdeistviya na atmosfernye processy v Moldavii, Kishinev, Shtiintsa, 1989, pp. 102-111.
[16] Shvetsov V.S., Sposob otsenki intensivnosti kuchevo-dozhdevogo oblaka. Problemnye voprosy aktivnogo vozdeistviya na atmosfernye processy, Kishinev, Shtiintsa, 1986, pp. 60-69.
[17] Aleksis N.M. and Telenta B., Technological Feasibility of Hail Suppression Hypotheses, 6th WMO Scientific Conference on Weather Modification, Paestum, Italy, 1994, pp. 147-150.
[18] Foot G.B. and Frank W.M., J. Atmos. Sci., 40, 3, 686 (1983).